UNIVERSITÉ
DE LORRAINE

AVERTISSEMENT

Ce document est le fruit d'un long travail approuvé par le jury de soutenance et mis à disposition de l'ensemble de la communauté universitaire élargie.

Il est soumis à la propriété intellectuelle de l'auteur. Ceci implique une obligation de citation et de référencement lors de l'utilisation de ce document.

D'autre part, toute contrefaçon, plagiat, reproduction illicite encourt une poursuite pénale.

Contact : ddoc-theses-contact@univ-lorraine.fr

LIENS

Code de la Propriété Intellectuelle. articles L 122. 4
Code de la Propriété Intellectuelle. articles L 335.2- L 335.10
http://www.cfcopies.com/V2/leg/leg_droi.php
http://www.culture.gouv.fr/culture/infos-pratiques/droits/protection.htm

THÈSE

Presentée à

l'université de Lorraine

École Doctorale Lorraine de Physique et Chimie Moléculaires

par **Rawiwan BANCHATHANAKIJ**

pour obtenir le grade de

Docteur

Spécialité : Physique de la matière condensée

Rheophysical properties of fluorinated nonionic micellar phases : link with mesoporous materials

---

Soutenue le 12 juillet 2012

Devant la commission d'examen composée de :

Rapporteurs :

Christian WAGNER	Professeur, Universität des Saarlandes
Frédéric PIGNON	Chargé de Recherche CNRS, LR, Grenoble

Examinateurs:

Christophe BARAVIAN	Professeur, Institut National Polytechnique de Lorraine
Jean-François WAX	Maître de Conférences, Université de Lorraine
Blaise NSOM	Professeur, Université de Bretagne Occidentale
Jean-François LE MEINS	Maître de Conférences, Université de Bordeaux 1

Directeur de thèse

Jean-Paul DECRUPPE	Professeur, Université de Lorraine

Co-directeur de thèse

Marie-José STEBE	Directrice de Recherches CNRS, Université de Lorraine

---

Laboratoire de Chimie et Physique - Approche Multi-échelles des Milieux Complexes

(LCP-A2MC) 1 Bd. Arago 57078 METZ cedex 03

The majority of this work has been done in the research group of Complex fluids, in the Laboratoire de Chimie et Physique - Approche Multi-échelles des Milieux Complexes (LCP-A2MC, Metz), Université de Lorraine. This project is also a collaboration with the research group of Physical Chemistry of Colloids, Laboratoire Structure et Réactivité des Systèmes Moléculaires Complexes (SRSMC, Nancy), Université de Lorraine.

Foremost, I would like to express my sincere gratitude to my director Prof. Jean-Paul DECRUPPE for the continuous support of my Ph.D study and research for his patience, motivation, enthusiasm, and knowledge. Throughout the three years in Metz at LCP-A2MC, his big supports and guidance helped me in all the time of research, encouragement for participation in international conferences, summer school and writing of this thesis.

I am also deeply grateful to my co-director, Ms. Marie-Jose STEBE, for her warm supports especially at the beginning of this study at SRSMC. Thanks for giving me a good basic knowledge to work properly on these surfactant systems and always suggest some detailed and constructive comments during my Ph.D work. Thanks to Jean-Luc BLIN for the fruitefull discussions we had.

I would like to thank the rest of my thesis committee: Prof. Christian WAGNER and Mr. Frédéric PIGNON, for accepting to be the reviewer and giving a very nice feedback. I also gratefully acknowledge Mr. Jean-François LE MEINS, Mr. Jean-François WAX, Prof. Christophe BARAVIAN and Prof. Blaise NSOM, for their valuable suggestions, insightful comments, and very good questions.

I wish to thank Mr. Olivier GREFFIER and Ms. Lydiane BECU, for their essential assistances in research. With their enthusiasm and great efforts to teach and explain things clearly and simply, I always work in a warm atmosphere in LCP-A2MC. Many thanks for Mr. Jean-Pierre GOBEAU, a very kind and active technician in our laboratory. I am grateful especially to Mr. Olivier GREFFIER for his encouragement, incisive advices, and lots of good ideas; not only about work, but also about my daily life and made my stay delightfully in France.

My sincere thanks also goes to Institut Laue-Langevin (ILL), Mr. Peter LINDNER and the team at the D11 line, for providing a chance and proficient operation for the small angle neutron scattering experiment in Grenoble.

I would like to thank Ms. Sandra LEROUGE, Laboratoire Matière et Systèmes Complexes (MSC), for allowing us to continue studying on the rheological measurements in Paris, as the rheometer in our laboratory was not working properly.

The nonionic fluorinated surfactants used in this work are kindly provided by DuPont de Nemours Belgium.

I am grateful for the financial support in this thesis provided by French Ministry of Higher Education and Research (MESR).

Many thanks to the French group of Rheology (GFR), for giving me financial support during my participation in an international conference in Gothenburg, Sweden.

I express my deep appreciation to Ms. Pranee INPRAKHON, Deputy Head, Department of Biotechnology, Mahidol University, for encouraging me to grab the great opportunity for doing this Ph.D project here in France.

I thank the members, fellow colleagues and labmates in LCP-A2MC group. Special thanks to Clarice, Al-Saleh, Mouas, Filsan and Kareem, for all your enthusiastic helps in every single thing, especially about my poor French skill. I will never forget such a warm and fun environment we shared during these almost four years. My sincere appreciations go for the former members in SRSMC group as well. Na DU, my first mentor in my Ph.D life, our friendship will never end even we are far apart. Thanks Kévin for all supports and also his good sense of humour. Special mention must be addressed to Florentin MICHAUX, for the supportive experimental data, stimulating discussions and giving some guidance on my work with his kindness.

Furthermore, I thank the friends I made in France. Though I do not have enough space to list all names here, but I wish to thanks for our great friendships and very good taking care. In particular, Manuela, Jay, Ble, Nyu, and Joe, who always be with me whenever I want, Thanks a million.

Due to my research abroad, it would have been impossible for me to finish this work without an encouragement and supports from my family. My gratitude and deepest appreciation are to my father, mother and my sisters for their love, kindness, understanding, patience and being great motivation throughout my study.

Rawiwan Banchathanakij

Table of Contents

Abbreviations .... **i**

General introduction **3**

Chapter I. Literature reviews **11**

1.1 Surfactant based system 11

1.1.1 Organized molecular system (OMS) 11

1.1.2 Phase behaviour 16

1.1.3 Fluorinated surfactants 21

1.2 Mesoporous material 22

1.2.1 Mechanisms of formation 24

1.2.2 Cooperative Templating Mechanism (CTM) 25

1.2.3 Nonionic surfactant for mesoporous material preparation 28

1.2.4 Nonionic fluorinated surfactant for preparation of mesoporous materials 30

1.2.5 Various fluorocarbon solubilization and oil incorporation in systems 35

1.2.6 Effect of salts and ethanol additions on the cloud point of nonionic, hydrogenated or fluorinated surfactant systems 37

1.3 Rheology of micelles 40

1.4 Context of study 43

1.4.1 Study of $R_7^F(EO)_8$-based system 43

1.4.2 Study of $R_8^F(EO)_9$-based system 44

1.4.3 Objectives 45

References 46

Chapter II. Materials and Experimental Methods **55**

2.1 Materials: Surfactant solutions 55

2.2 Rheometry 57

2.2.1 Rotational rheometer and shearing cells 58

2.2.2 Flow experiments 61

2.2.3 Zero shear viscosity measurement 61

2.2.4 Dynamic viscoelastic measurement 62

2.3 Polarized light microscopy 64
2.4 Flow birefringence 65
  2.4.1 The polarimetric bench 65
  2.4.2 The measuring cell 66
  2.4.3 The optical measurements. Principle of flow birefringence measurement 68
  2.4.4 Measurement protocol 69
    2.4.4.1 Determination of the angle of extinction 69
    2.4.4.2 Determination of the birefringence intensity 70
2.5 Small Angle Neutron scattering 71
  2.5.1 Devices and experiments 71
  2.5.2 Definition of the measured quantities in a SANS experiment 73
  2.5.3 Extraction of the spectra 74
References 76

Chapter III. Phase diagram of $R_7^F(EO)_8$ and $R_8^F(EO)_9$ surfactant-based systems 81

3.1 $R_7^F(EO)_8$ surfactant based system 81
  3.1.1 Phase diagram of $R_7^F(EO)_8$ in water 81
  3.1.2 Phase diagram of $R_7^F(EO)_8$ in sodium iodine (NaI) 83
3.2 $R_8^F(EO)_9$ surfactant based system 85
  3.2.1 Phase diagram of $R_8^F(EO)_9$ in water 85
  3.2.2 Phase diagram of $R_8^F(EO)_9$ in sodium cloride (NaCl) 86
References 88

Chapter IV. Rheophysics of nonionic fluorinated surfactant based system 93

4.1 System I - $R_7^F(EO)_8$ in water 94
  4.1.1 Rheological properties 94
    4.1.1.1 Steady state rheological behaviour 94
    4.1.1.2 Dynamic rheological behaviour 99
    4.1.1.3 Stress cycle 104
    4.1.1.4 Evolution of the zero shear viscosity with the concentration of surfactant (wt%) 106

4.1.2 Flow birefringence 109
4.1.3 Small angle scattering experiments 111
4.1.3.1 SANS at rest 113
4.1.3.2 SANS under flow 118
4.2 System II - $R_7^F(EO)_8$ in NaI 124
4.2.1 Rheological properties 124
4.2.1.1 Steady state rheological behaviour 124
4.2.1.2 Dynamic rheological behaviour 128
4.2.2 Flow birefringence 133
4.3 System III - $R_8^F(EO)_9$ in water 134
4.3.1 Steady state rheological behaviour 134
4.3.2 Dynamic rheological behaviour 137
4.3.3 Flow birefringence 138
4.4 System IV - $R_8^F(EO)_9$ in 3M NaCl 138
4.4.1 Steady state rheological behaviour 138
4.4.2 Dynamic rheological behaviour 141
4.4.3 Flow birefringence 142
References 146

Chapter V. Discussion 151
5.1 Molecular organization of $R_7^F(EO)_8$ system at equilibrium 151
5.1.1 $R_7^F(EO)_8$ in water 151
5.1.2 $R_7^F(EO)_8$ in 1M NaI solution 153
5.2 Formation of hybrid hexagonal mesophase: link to the rheological behaviours 155
5.2.1 $R_7^F(EO)_8$ in water 155
5.2.2 $R_7^F(EO)_8$ in 1M NaI solution 155
5.3 $R_7^F(EO)_8$ -water vs $R_7^F(EO)_8$ -1M NaI systems 156
5.4 Comparison between flow birefringence, rheology and SANS 159
5.4.1 $R_7^F(EO)_8$ in water 159
5.4.2 $R_7^F(EO)_8$ in 1M NaI solution 163

5.5 Molecular orientation of $R_8^F(EO)_9$ system 163
5.5.1 $R_8^F(EO)_9$ in water 163
5.5.2 $R_8^F(EO)_9$ in 3M NaCl solution 164
5.6 Comparison between two nonionic fluorinated surfactant systems 165
References 167

Conclusion **173**
Appendix **179**
List of Tables **185**
List of Figures **187**

Résumé (Abstract) **193**

Abbreviations

OMS	Organized Molecular System
CTM	Cooperative Templating Mechanism
CMC	Critical Micellization Concentration
HLB	Hyphophile-Lipophile Balance
LCT	Lower Consolute Temperature
LCB	Lower Consolute Boundary
CP	Cloud point
CPP	Critical Packing Parameter
POE	Polyoxyethylene
EO	Oxyethylene groups
MCM	Mobil Crystalline Materials
SBA	Santa Barbara Amorphous type materials
FSM	Folded-Sheet Mesoporous materials
IUPAC	International Union of Pure and Applied Chemistry

Direct (1) and reverse (2) Phases :

L_1, L_2	micellar solutions
I_1, I_2	micellar cubic phases
V_1, V_2	bicontinuous cubic phases
H_1, H_2	hexagonal phases
L_α	lamellar phase

Products :

$R_7^F(EO)_8$	$C_7F_{15}C_2H_4(OC_2H_4)_8OH$
$R_8^F(EO)_9$	$C_8F_{17}C_2H_4(OC_2H_4)_9OH$

Rhelogical measurements

σ	Shear stress, Pa
$\dot{\gamma}$	Shear rate, 1/s
Ω	Angular velocity
η	Apparent viscosity, Pa.s
κ	Consistency coefficient, Pa s^n
n	Flow behaviour index, -
$\dot{\gamma}_c$	Critical shear rate, 1/s
ω	Angular frequency, rad/s
γ	Strain, %
LVR	Linear viscoelastic region
G'	Storage modulus, Pa
G''	Loss modulus, Pa

G_0 : Plateau modulus, Pa
η_0 : Zero shear viscosity, Pa.s
τ_R : Relaxation time, second
τ_break : Breaking time, second
τ_rep : Reptation time, second
ω^* : Angular frequency at the minimum loss modulus (G''_min), rad/s
ξ_H : Hydrodynamic correlation length, metres
T : Temperature, K or °C
k_B : Boltzmann's constant, 1.38 10^{-23} SI
η' : Complex viscosity, Pa.s
σ_M : Maximaun shear stress, Pa
σ_m : Minimun shear stress, Pa
ϕ_{mass} : Mass fraction, weight percent (wt %)
t_w : Flow time of pure water, second
t_s : Flow time of solution, second

Flow birefringence

n_1, n_2 : reflective index, -
Δn : birefringence intensity, -
χ : Extinction angle, °
$\vec{\omega}$: Vorticity axis
$\vec{v}$: Velocity axis
λ : Wavelength, metres
δ : Phase shift or retardance
e : Thickness of the medium
I_0 : Incident light intensity
I_α : Transmitted intensity
ϕ : Phase angle, °
C : Stress optical coefficient, Pa^{-1}

Small Angle Neutron Scattering (SANS)

$\vec{q}$: Scattering wave vector, Å^{-1}
θ : Scattering angle, °
$A(\vec{q})$: Total scattering amplitude
V : Scattering volume
$\rho(\vec{r})$: Scattering length density
b_i : Scattering length
$\dfrac{d\Sigma}{d\Omega}$: Differential scattering cross section per unit volume, cm^{-1}
$\vec{\omega}$: Vorticity direction
$\vec{V}$: Tangential velocity direction

$I_{\parallel}$: Scattered intensity in the direction parallel to the tangential velocity $\vec{V}$

$I_{\perp}$: Scattered intensity in the direction parallel to the vorticity $\vec{\omega}$

q^* : Wave vector at the correlation peak, Å^{-1}

ξ : Correlation distance, Å

N_{ag} : Aggregation number

A, B : Dimension of the particle

A_{phobe}, B_{phobe} : Dimensions of the hydrophobic core

L_A, L_B : Length of hydrophilic and hydrophobic parts of the micelle

p : Ellipticity

α : Number of water molecule per surfactant molecule

S : Polar head surface at the hydrophilic / hydrophobic interface

Introduction générale

Au cours des dernières années, la synthèse de matériaux mésoporeux innovants a subi une croissance explosive et un développement constant par suite de leur large domaine d'applications et de leurs propriétés structurales uniques[1] [2]. Ces caractéristiques uniques offrent d'excellentes opportunités pour la création de matériaux ordonnés à fonctionnalités spécifiques telles que l'arrangement régulier des canaux, le contrôle systématiques du diamètre des pores entre 2 et 50 nm ou la grande surface spécifique qui peut dépasser $1000 m^2.g^{-1}$. Toutes ces propriétés les rendent particulièrement utiles dans les domaines tels que la catalyse, l'adsorption, la biochimie ou encore comme support pour l'immobilisation d'enzymes telles que les lipases utilisées dans la fabrication de bioréacteurs enzymatiques réutilisables[3]. Le méthode de synthèse des matériaux mésoporeux via un processus sol-gel est habituellement utilisée par suite de son faible coût et de sa relative simplicité[4]. Le matériau est obtenu à partir de systèmes moléculaires organisés (SMO) qui sont utilisés modèles de charpente[1] [2] [4]. Ainsi l'addition à la phase micellaire d'un précurseur, la silice, conduit à des interactions entre la silice et les structures formées par les tensioactifs favorisant la formation d'une mésophase hybride organique-inorganique. A l'heure actuelle, il est communément admis que ce mécanisme repose sur l'auto assemblage de molécules de tensioactifs et du précurseur inorganique ; ce mécanisme est appelé Cooperative Templating Mechanism (CTM) ou encore cooperative self assembling mechanism[1] [5] [6].

Il apparaît que les caractéristiques des matériaux fabriqués telles que la structure, le diamètre des pores sont fortement liées aux propriétés des tensioactifs utilisés dans le processus de fabrication[3] [7] [8] [9]. Par exemple, dans un article traitant du design structural de matériaux mésoporeux à base de silice par un mécanisme de contrôle du paramètre d'agrégation (packing parameter) d'un mélange de molécules amphiphiles [$C_nH_{2n+1}(OCH_2CH_2)_x$-OH), n = 12-18, x = 2-100], Stucky et al. [8] ont montré qu'une corrélation existe entre la structure finale et le rapport du volume de la tête hydrophile (V_A) au volume de la partie hydrophobe (V_B) du tensioactif. L'utilisation de tensioactifs fluorés et hydrogénés a également permis de mettre en évidence que le mécanisme d'auto assemblage des molécules est favorisé lorsque la limite de la courbe de démixtion est déplacée vers les hautes températures et que la température de changement de phase est éloignée de la température à laquelle la silice est ajoutée à la solution micellaire[3].En effet des tamis hexagonaux ont été obtenu avec $C_8F_{17}C_2H_4(OC_2H_4)_9OH$ [$R_8^F(EO)_9$]; en milieu aqueux les molécules de tensioactif s'assemblent spontanément en micelles dans une gamme de concentration de 5 à 25 % en masse et jusqu'à une température de plus de 80°C[10]. Par contre, dans les mêmes conditions de synthèse, i.e. pH, rapport molaire tensioactif/silice, température et durée de la synthèse, seules des structures vermiculaires sont obtenues avec $C_7F_{15}C_2H_4(OC_2H_4)_8OH$ [$R_7^F(EO)_8$][11]. Ce système présente un point de trouble proche de la température ambiante et un matériau mésoporeux ordonné n'est obtenu que lorsque des additifs qui ont pour effet de repousser le point de trouble vers les hautes températures, sont ajoutés[3]. Des travaux précédents faisant appel aux techniques de diffusion dynamique de lumière et de diffusion de neutrons aux petits angles, ont montré que les micelles de $R_8^F(EO)_9$ressemblent à des sphéroïdes tandis que celles de $R_7^F(EO)_8$ auraient plutôt une forme allongée. Ceci pourrait expliquer pourquoi on obtient des matériaux mésoporeux ordonnés avec $R_8^F(EO)_9$ et des structures vermiculaires tubulaires désordonnées avec $R_7^F(EO)_8$. Dans ce travail, nous décrivons et analysons le comportement sous écoulement de solutions aqueuses formées avec ces deux systèmes de tensioactifs. Plusieurs techniques expérimentales seront utilisées : rhéologie, biréfringence d'écoulement et diffusion de rayonnement. A l'aide des données recueillies, nous tenterons d'apporter un éclairage supplémentaire quant à la faculté de ces tensioactifs à former des matériaux mésoporeux ordonnés.

General introduction

Due to a wide range of application and unique structural properties[1] [2], the synthesis of advanced mesoporous materials has undergone an explosive growth and has been continuously developed in these recent years. The particular characteristics provide excellent opportunities for the creation of ordered material with additional functionality, such as dimensional channel arrangement, a systematic pore diameters ranging from 2 to 50 nm, including a high specific surface area which is greater than 1000 $m^2.g^{-1}$. All of these features make them suitable for use in various fields as catalysis, adsorption, biochemistry, or as a support for enzyme immobilization, such as lipase, in order to design a stable and reusable enzymatic bioreactors [3]. The synthesis method of mesoporous materials via a sol-gel process has been classically employed because of its economy and the relative simplicity[4]. The material is obtained from organized molecular systems (OMS) which are used as framework templates[1] [2] [4]. Thus the addition of a silica precursor to the micellar phase leads to the interactions between silica and the structures formed by surfactants, driving the formation of a hybrid organic-inorganic mesophase. Today it is well-accepted that this mechanism is based on the self-assembling of surfactant molecules and inorganic precursors, which is named Cooperative Templating Mechanism (CTM) or cooperative self-assembling mechanism [1] [5] [6] .

It appears that the characteristics of the recovered materials, such as the structure and the pore diameter, are strongly related to the properties of the surfactant used for their preparation [3] [7] [8] [9]. For example in a paper dealing with the structural design of mesoporous silica by micelle-packing control using blends of amphiphiles [$C_nH_{2n+1}(OCH_2CH_2)_x$-OH), n = 12-18, x = 2-100], Stucky and co-workers [8] have established a correlation between the final structure and the ratio between the volume of the hydrophilic head group (V_A) and the hydrophobic part (V_B) of the surfactant. This scale can be extended to the polyoxyethylene fluoroalkyl ethers family [3]. Using both hydrogenated and fluorinated systems, it has also been evidenced that the self assembly mechanism is favoured if the lower consolute boundary is shifted toward high temperatures and if the phase separation temperature is moved away from the temperature at which the silica source is added to the micellar solution [3]. As a matter of fact, hexagonal molecular sieves have been obtained with $C_8F_{17}C_2H_4(OC_2H_4)_9OH$ $[R_8^F(EO)_9]$; the surfactant is self assembling in micelles in aqueous solution in a concentration range of around 5-25 wt.% and up to temperatures above 80°C [10]. By contrast, in the same conditions of synthesis - i.e. pH, surfactant / silica molar ratio, hydrothermal temperature and duration - only wormhole-like structures are recovered with $C_7F_{15}C_2H_4(OC_2H_4)_8OH$ $[R_7^F(EO)_8]$[11]. This system has a cloud point quite close to room temperature, the mesopore ordering occurs only when additives are added to shift the cloud point towards high temperatures [3]. Previous works like Dynamic Light Scattering experiments and SANS analysis indicate that $R_8^F(EO)_9$ micelles should be spheroid whereas those of $R_7^F(EO)_8$ have rather an elongated shape. This might explain why ordered mesoporous materials are recovered when $R_8^F(EO)_9$ micelles are used as building blocks while $R_7^F(EO)_8$ micelles give rise to wormhole like structure. In this work, we describe and analyze the behaviour under flow of aqueous systems prepared with these two surfactants. Several experimental techniques will be used: rheology, flow birefringence and try to shed light on the difference of behaviour between the two systems.

Chapitre I.

Généralités et situation bibliographique (résumé)

Le premier chapitre est divisé en quatre parties principales qui proposent une synthèse des connaissances actuelles sur les propriétés des tensioactifs servant à la préparation des matériaux mésoporeux à base de silice.

La première partie présente des généralités sur les tensioactifs et les systèmes qu'ils sont susceptibles de former en solution.

La seconde partie est consacrée aux matériaux mésoporeux ; on y aborde les méthodes de préparation à partir de solutions de tensioactifs, les structures obtenues.

Dans la troisième partie, quelques éléments de rhéologie des solutions micellaires sont résumés.

La dernière partie expose l'objet de ce travail

1.1 Les tensioactifs

Les tensioactifs ont la propriété de modifier la tension superficielle du solvant dans lequel ils sont mis en solution. Leurs molécules sont amphiphiles et composées de deux groupes d'atomes liés chimiquement. L'un des groupes est hydrophile tandis que l'autre est hydrophobe. Les tensioactifs sont classés en quatre groupes distincts : anioniques, cationiques, zwitterioniques et non ioniques. Les deux tensioactifs qui font l'objet de ce travail appartiennent à la dernière catégorie.

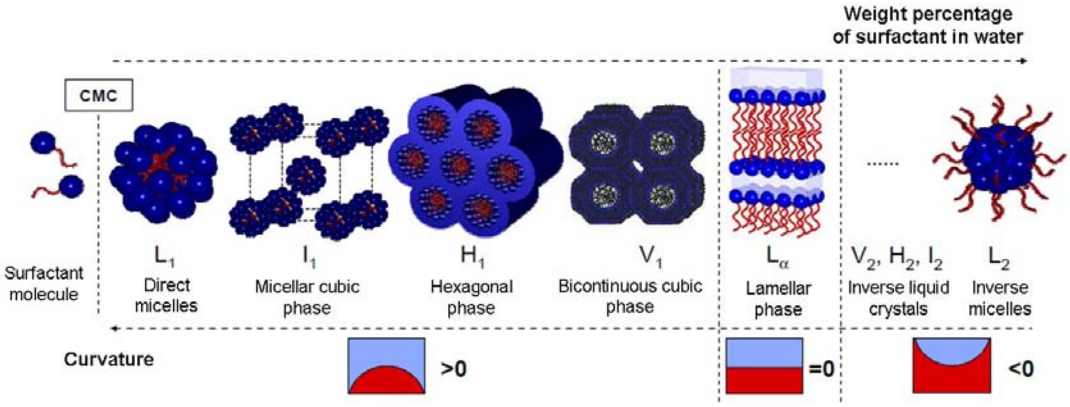
Weight percentage of surfactant in water
CMC
Surfactant molecule
L1
Direct micelles
I1
Micellar cubic phase
H1
Hexagonal phase
V1
Bicontinuous cubic phase
Lα
Lamellar phase
......
V2, H2, I2
Inverse liquid crystals
L2
Inverse micelles
Curvature
>0
=0
<0

Figure I.1 Différents formes de micelles et phases micellaires. Les parties hydrophobes sont en bleu et les éléments hydrophobes en rouge.

En solution, le plus souvent aqueuse, les molécules de tensioactifs peuvent s'associer en édifices complexes tels que micelles, phases lamellaires, cristaux liquides dont une représentation schématique est donnée sur la figure 1.1.

La structure précise des micelles et des phases lamellaires dépend des conditions de température, de concentration en tensioactif, de salinité du solvant mais également de caractéristiques microscopiques telles que : structure moléculaire, taille des têtes polaires, longueur des chaines hydrophobes. Dans ce travail, nous avons utilisé des tensioactifs fluorés. Les conditions de température et concentration sont telles que ces tensioactifs non ioniques forment une phase de micelles directes dénommée phase L_1 . Cette phase est isotrope au repos.

Le diagramme de phases est caractérisé par la présence de la courbe de miscibilité dont un point remarquable est le point de trouble[,1] [2] .

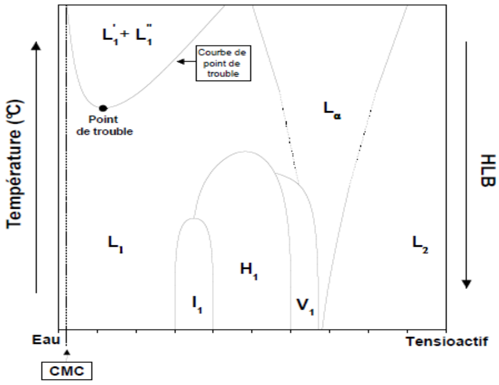

Figure I.2. Diagramme de phase idéal d'un tensioactif.

La figure I.2 en est une représentation caractéristique. Dans le domaine des basses et moyennes concentrations en tensioactif, la courbe de miscibilité sépare la phase L_1 d'une région diphasique où coexistent deux phases L'_1 et L'', respectivement riche et pauvre en micelles.

1.2 Les Matériaux mésoporeux

Les matériaux mésoporeux sont des structures présentant des pores agencés plus ou moins régulièrement et de dimensions comprises entre 2 et 200nm. Les plus anciens ont été découverts aux XVIIIe siècles ; ce sont les zéolithes qui ont une distribution de taille étroite et uniforme. Leur importance en tant qu'adsorbants a largement contribué au développement de la synthèse de ces composés et une réelle avancée a lieu en 1992 lorsque Mobil Oil a réussi la synthèse des composés mésoporeux M41S. Différentes techniques ont été utilisées : auto assemblage, procédé sol-gel, traitement des aluminosilcates. Dans ce travail, nous n'aborderons que la méthode qui consiste à utiliser des solutions micellaires de tensioactifs comme modèles. Deux voies de synthèse sont alors utilisées : la première, CTM (Cooperative Templating Mechanism) est une copie d'une phase micellaire L_1 tandis que pour la seconde, LCT (Liquid Crystal Templating), le principe est le même mais la phase initiale est un cristal liquide.

Ces deux voies de synthèse sont représentées schématiquement sur la figure I.3.

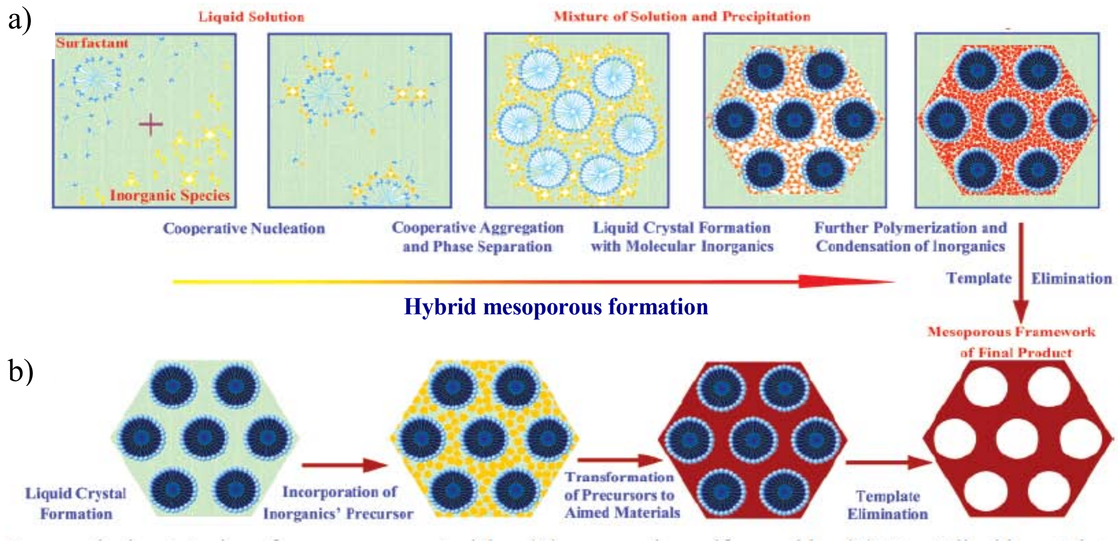
a)
Liquid Solution
Mixture of Solution and Precipitation
Surfactant
Inorganic Species
Cooperative Nucleation
Cooperative Aggregation and Phase Separation
Liquid Crystal Formation with Molecular Inorganics
Further Polymerization and Condensation of Inorganics
Template Elimination
Hybrid mesoporous formation
Mesoporous Framework of Final Product
b)
Liquid Crystal Formation
Incorporation of Inorganics' Precursor
Transformation of Precursors to Aimed Materials
Template Elimination

Figure I.3. Deux voies de synthèse des matériaux mésoporeux : (a) auto assemblage coopératif sur phase micellaire, (b) copie d'un modèle cristal liquide.

Le mécanisme de formation des matériaux mésoporeux, lorsqu'il est réalisé à partir d'une solution micellaire comporte trois étapes. La première étape consiste en la formation d'une mésophase organique-inorganique. Elle résulte de l'interaction entre les micelles de tensioactif et la silice, précurseur inorganique. Puis s'opère la condensation du précurseur à la surface extérieure de la micelle. C'est la condensation intramicellaire. Il y a ensuite formation d'une phase hexagonale hybride par condensation intermicellaire avant traitement thermique qui a pour effet d'éliminer le tensioactif.

Dans la phase de préparation, la molécule de tensioactif joue un rôle crucial et le choix judicieusement du rapport longueur des chaines hydrophiles et lipophiles permet de déterminer la structure du matériau mésoporeux. On utilisera de préférence des tensioactifs non-ioniques plutôt qu'ioniques en raison de leur plus grande stabilité thermique et de la facilité avec laquelle leur extraction du squelette inorganique est réalisée [3], [4], [5].

Les travaux afférents aux effets de l'addition de sels, d'huiles et d'éthanol sont également mentionnés. Il ressort de ces études que l'addition de sels a pour effet de déplacer la courbe de miscibilité et que la structure des matériaux mésoporeux est d'autant plus régulière que la température à laquelle la silice est ajoutée est éloignée de la température de changement de phase.

1.3 Rhéologie des micelles

Les grandeurs caractéristiques des micelles L_c, longueur de contour, l_p, longueur de persistance et ξ_H, longueur de corrélation sont introduites dans ce paragraphe. Elles influent sur les propriétés rhéologiques des solutions micellaires.

Dans ce paragraphe, une attention particulière est portée aux fluides Maxwelliens viscoélastiques dont on verra l'importance lors de l'analyse des résultats expérimentaux. La relaxation de ces fluides est monoexponetielle avec un seul de temps de relaxation.

$$\tau_R = \sqrt{\tau_b \tau_{rep}}$$

avec τ_b, τ_{rep}, respectivement les temps de cassure et recombinaison et le temps de reptation.

Les travaux des groupes de Shrestha [6] et de Sharma [7] sont décrits de façon succincte. Ils portent sur l'étude du comportement rhéologique de solutions de tensioactifs fluorés, de mélanges de tensioactifs et de systèmes ternaires eau/tensioactif/huile en relation avec la formation de matériaux mésoporeux.

1.4 Objet du travail

Ce paragraphe décrit l'objet du travail constituant le corps de cette thèse. Il s'agit d'établir l'existence éventuelle d'une relation entre la structure des micelles de tensioactifs fluorés et la faculté de ces solutions à conduire à la formation de matériaux mésoporeux ordonnée. Les deux tensioactifs fluorés connus pour conduire à la formation de matériaux mésoporeux ordonnés par le mécanisme CTM dans certaines conditions de température, de concentration et de salinité sont présentés. Il s'agit de $R_7^F(EO)_8$ et de $R_8^F(EO)_9$ en présence ou non de sel NaI ou NaCl.

Bibliographie

[1] D. J. T. Mitchell, G. J. T., L. Waring, T. Bostock and M. P. McDonald, *Journal of the. Chemical Society-Faraday Transactions I* **1983**, *79*, 975-1000.

[2] J. S. Sjöblom, P.; Danielsson, I. In Nonionic Surfactant Physical Chemistry, *Nonionic Surfactant Physical Chemistry*, M. Dekker, New York, **1987**, p. 369.

[3] A. E. C. Palmqvist, *Current Opinion in Colloid & Interface Science* **2003**, *8*, 145-155.

[4] M. Kruk, M. Jaroniec, C. H. Ko and R. Ryoo, *Chemistry of Materials* **2000**, *12*, 1961-1968.

[5] S. Ruthstein, V. Frydman, S. Kababya, M. Landau and D. Goldfarb, *The Journal of Physical Chemistry B* **2003**, *107*, 1739-1748.

[6] L. K. Shrestha, S. C. Sharma, T. Sato, O. Glatter and K. Aramaki, *Journal of Colloid and Interface Science* **2007** *316*, 815–824.

[7] K. S. Sharma, S. R. Patil and A. K. Rakshit, *Colloids and Surfaces A: Physicochemical and Engineering Aspects* **2003**, *219*, 67-74.

Chapter I. Literature Reviews

1.1 Surfactant based systems

Surfactants are surface active agents, defined as a compound that can greatly reduce the surface tension of water. Surfactant molecules are amphiphilic; that is, they possess hydrophilic (water-soluble) groups chemically bounded to hydrophobic (oil-soluble) groups. A typical hydrophobic group is non-polar and usually consists of aliphatic or aromatic hydrocarbon chains, frequently called a surfactant “tail”. The hydrophilic part consists of polar groups which usually interact strongly with water, often called the “head”. Therefore, they are located at the interface between water and oil. Surfactants can be generally classified into four groups by the presence of formally charged groups in their head, which are anionic (carboxylic, sulfonic, phosphates and phosphoric salts), cationic (amines, ammonium salts), Zwitterionic (amino acid salts, betaines) and nonionic surfactants (ethers, esters, amides, block polymers).

1.1.1 Organized molecular system (OMS)

It is well known that surfactants can spontaneously self-organize into a variety of different types of aggregates in aqueous solution as given in Figure I.1. These structural aggregates vary depending on surfactant concentration, temperature, and a change in curvature of the interface between hydrophilic and hydrophobic areas. The continuous medium is usually water and the structures formed are called direct micelles (subscript 1 in the following picture) (part hydrophobic forming the core structure, the hydrophilic part being in contact with water) the curvature of which is defined as positive. These structures allow solubilisation of hydrophobic compounds in the core of the structure such as oils. The increase in the proportion of surfactant leads to a decrease of the curvature and to the formation of reverse structures (subscript 2) with a negative curvature via a structure with zero curvature.

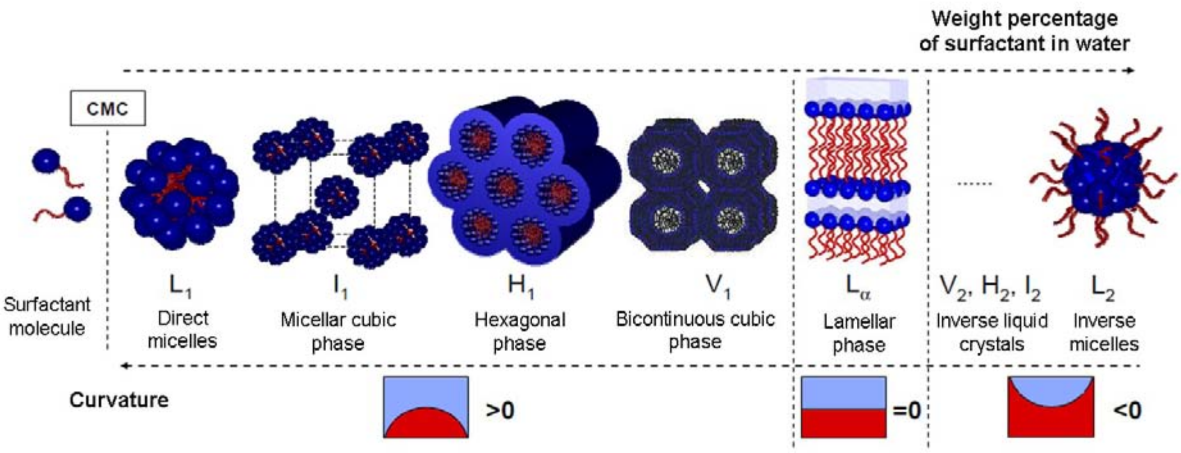
Weight percentage of surfactant in water
CMC
Surfactant molecule
L_1
Direct micelles
I_1
Micellar cubic phase
H_1
Hexagonal phase
V_1
Bicontinuous cubic phase
L_α
Lamellar phase
V_2, H_2, I_2
Inverse liquid crystals
L_2
Inverse micelles
Curvature
>0
=0
<0

Figure I.1 Schematic and curvature of OMS: the sequence of weight percentage dependent phase of surfactant in water. The blue and red areas are hydrophilic and hydrophobic, respectively [3].

In aqueous solution, the surfactants self-assemble in order to hide their hydrophobic part from the water, while the hydrophilic head group remains immersed in the water. At very low weight percentages of surfactant, the molecules are preferentially adsorbed at the surface of the solution. As the concentration increases, this adsorption becomes stronger until saturation is reached; the molecules are then packed close together with strong lateral interactions occurring between the hydrophobic chains which tend to stick up out of the water and a few molecules are solubilized into water until saturation. Then a self-assembling process gives rise to the formation of “direct micelles” (denoted as L_1) above the critical micellar concentration (CMC) when the temperature is above the Kraft temperature. They are structures in which the hydrophobic portions of the surfactant molecule associate together to form regions from which the solvent, water, is excluded. The hydrophilic head groups remain on the outer surface to maximize their interaction with the water and with the oppositely charged ions (called counterions). A significant fraction of the counterions remain strongly bound to the head groups so that the lateral repulsive force between those groups is greatly reduced. When the surfactant concentration is above the CMC, the micelles are at first spherical and, upon increasing the concentration, they become more distorted in shape like cylindrical, worm-like or disk-shaped micelles. The precise structure of the micelle depends on the temperature and concentration but also on the details of the molecular structure: size of head group, length and number of hydrocarbon chains, presence of branches, double bonds or aromatic rings, etc. Due to the

CMC at which micelles form in the solution, some physical characteristics can be marked by quite sharp changes in slope when various transport and equilibrium properties (such as surface tension, solubility or conductivity) are plotted against concentration as in Figure I.2.

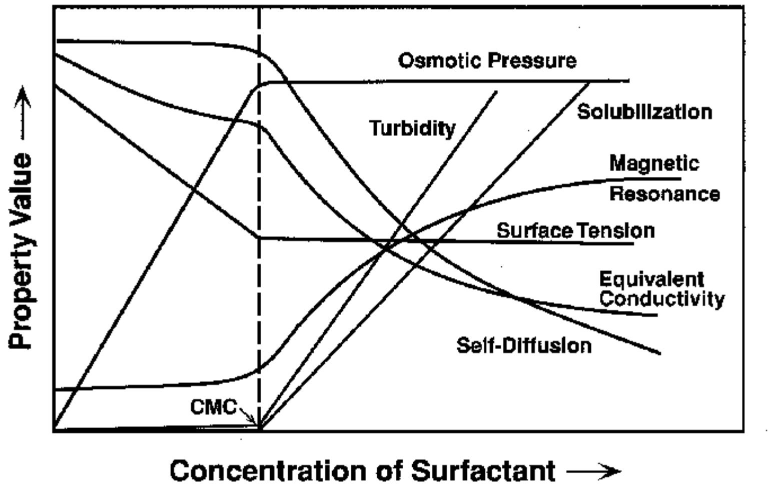

Figure I.2 Onset of micellization observed by sudden change in measured properties of solution at characteristic surfactant concentration, critical micellization concentration (CMC) [12].

At very high surfactant concentration, inverse micelles (L_2) are formed; the continuous medium formed by the alkyl chains is non polar and the hydrophilic parts and the water are eventually grouped in the center of the aggregates and therefore the curvature is negative. These micellar phases are characterized by their absence of long-range order, and optical isotropy and often low viscosity. Some systems which show a more hydrophobic behaviour also show a sponge phase (denoted L_3), usually in the dilute region. The L_3 phase is bicontinuous and multiple connected, but the structure is disordered lacking long-range order. It is known that this kind of structure is composed of two interpenetrating continuum. Therefore, this whole variety of structures affects the surfactant properties such as surface tension, adsorption, stability, solubility, and temperature dependence, etc.

For concentrations of surfactant intermediate between the direct and reverse micelles concentrations, the solutions generally form “liquid crystals” (or mesophase). They are stable from a thermodynamical point of view and exhibit a long-range order, highlighted by a high viscosity and by specific optical properties. Such aggregates can form cubic (V), hexagonal (H) and lamellar (L_α) phases. Some of these mesophases exhibit anisotropic properties. Their repeat distance can be measured by small angle X-ray diffraction. These organizations can have a uni-, bi- or three-dimensional order. In case of uni- and bi-dimensional mesophases, they exhibit anisotropic properties and appear iridescent under polarized light. Furthermore, the observation under polarized light microscopy can reveal specific textural characteristics of organization, arising from stacking faults in the molecular arrangement. They may form in both polar or non-polar solvents and may consist of direct and reverse systems. The basic polymorphic varieties of lyotropic liquid crystal include the following three mesophases:

- Hexagonal phase (H_1 / H_2) – bidimensional structure

At higher amphiphile concentrations, the micelles fuse to form cylindrical aggregates of indefinite length, and consequently can arrange in some conditions into long-ranged hexagonal arrays. It is known as the normal topology hexagonal phase with positive curvature, thus generally denoted by the symbol H_1. Whereas an inverse topology hexagonal phase (denoted H_2) has water within the cylindrical aggregates and the hydrocarbon chains fill the voids between the hexagonally packed cylinders. This mesophase does not flow as easily as micellar solution due to its higher viscosity. Thin films of both normal and inverse topology hexagonal phases exhibit birefringence under a polarizing microscope, giving rise to characteristic optical textures. Typically these textures are smoke-like, fan-like or mosaic in appearance (Figure I.3).

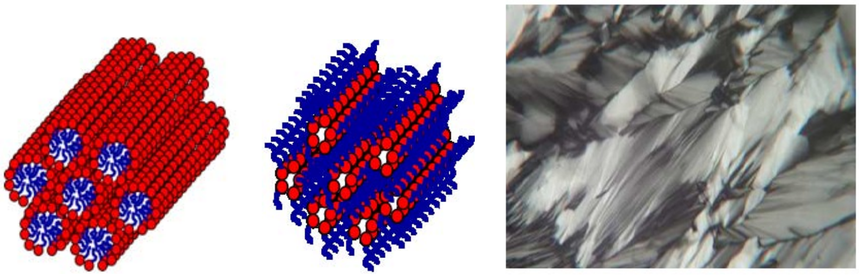

Figure I.3 Schematic models and texture of hexagonal phase [3].

- Lamellar phase (L_α) – unidimensional structure

At concentrations of amphiphile higher than those leading to direct hexagonal phases, the surfactants assemble into a lamellar structure (denoted L_α). The lamellar phases consist of stacks of surfactant bilayers separated by thin water layers. In these systems, the water and surfactant molecules are free to move in the x-y planes. Thus this characteristic feature leads to a decrease of the viscosity compared to hexagonal phases. The viscosity drop is caused by the layer structure of this phase allowing an easy slipping of the planes. The changes in microstructural conformation of the lamellar phase can be induced during shear [13]. Lamellar phases exhibit long range smectic order and show characteristic birefringent textures when observed under polarizing light microscope. The morphological features of the liquid crystal textures are unique with respect to their phases and are often used for phase recognition purposes. Lamellar structures may give mosaic, oily streaks, Maltese cross textures (Figure I.4). However, a gradual morphological transition between these textures can be found depending on the water content in the system.

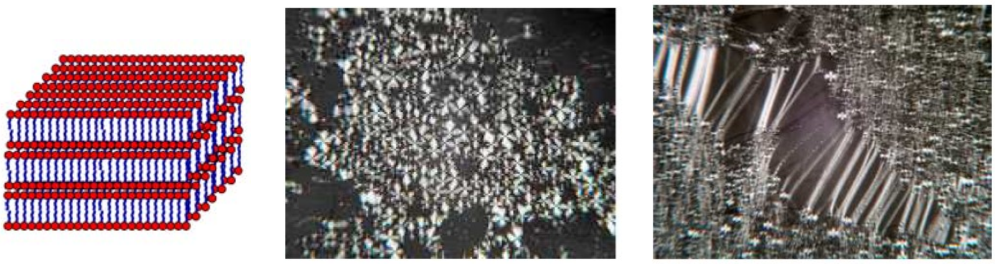

Figure I.4 Schematic model and texture of lamellar phase [3].

- Cubic phases (I_1 / V_1) – tri-dimensional structure

The simplest cubic liquid crystal phase that is formed by spherical micelles is the direct micellar cubic phase, denoted by the symbol I_1. Micelles can be arranged on a simple cubic, body-centered or face-centered cubic arrangement. These mesophases are optically isotropic phases but are different from micellar solutions by their very high viscosity. When thin film samples of this phase are viewed under a polarising microscope, they appear dark and featureless.

However, for most amphiphiles that consist of a single hydrocarbon chain, one or more phases having complex architectures are formed at concentrations that are intermediate between those required to form a hexagonal phase and those that lead to the formation of a lamellar phase. Often this intermediate phase is a bicontinuous cubic phase (V_1).

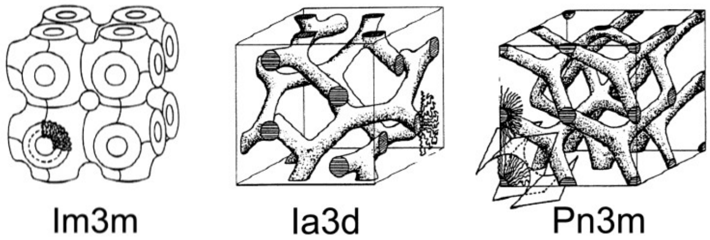

Figure I.5 Bicontinuous cubic phases (*Ia3d* and *Pn3m*), *Im3m*.

1.1.2 Phase behaviour

In order to better understand the initial preparation step of mesoporous material by nonionic surfactant templating method, we have focused on the properties of nonionic surfactants. The hydrophilic part of nonionic surfactant is often formed by several oxyethylene groups, EO. The C_mH_{2m+1} $(OC_2H_4)OH$, $[C_m(EO)_n]$ compounds consist of an alkyl chain of m carbons linked to a polyoxyethylene with n oxyethylene groups. They are commercially available with many combinations of values of n and m, which leads to a variety of mesophases in water. The binary phase behaviours of several $C_m(EO)_n$ have been reviewed as a function of surfactant volume fraction and micelle curvature [14]. When the number of EO units increases, with the fixed C_{12}-chain length, there are two phenomena. First, the importance of the stability range of mesophases follows the expected sequence: lamellar phase (L_α), direct bicontinuous cubic phase (I_1), direct hexagonal phase (H_1) and direct micellar phase (L_1). Large head groups and low temperatures are in favour of I_1 and H_1 phases, while small head groups and high temperature rather lead to L_α and L_2. Therefore, at low to medium temperature, increasing temperature suggests a decrease in surface area per molecule at the micelle surface. On heating, the EO groups are dehydrated and phase separation is observed at high temperature and low surfactant concentrations.

The phase sequence can be modified by modulating the hydrophilic character of the surfactant, by adjusting the Hyphophile-Lipophile Balance (HLB). According to Griffin's method in 1949 [15], the HLB number for nonionic surfactants can be calculated as

$$HLB = 20 * (M_{hydrophile} / M_{surfactant})$$

where $M_{hydrophile}$ / $M_{surfactant}$ is the ratio of the molecular weight of the surfactant to the hydrophilic part of surfactant. This yields an HLB range of 1-20. This HLB number is widely used, but only to compare the surfactants within a given series. The phase behaviour of nonionic surfactants is affected by their HLB value. For example, for the series of hydrogenated compounds [$C_m(EO)_n$] a surfactant having an HLB value below 10 is said to be hydrophobic and one can predict that it will not form structures in water, but rather lamellar and reverse structures. The surfactant is hydrophilic if it has an HLB value greater than 12, and is balanced if its HLB lies between 10 and 12.

The phase sequences presented below correspond to surface called "hydrophilic" having a high HLB (over 10) and thus forming direct micelles in water, the *sine qua non* condition for the preparation of mesoporous materials through the cooperative self-assembly mechanism. The phase diagram in Figure I.6 shows the influence of temperature, concentration and HLB values on the phase behaviours. The phase sequence in this case is limited to the partial sequence L_1-I_1-H_1-V_1-L_2-L_α.

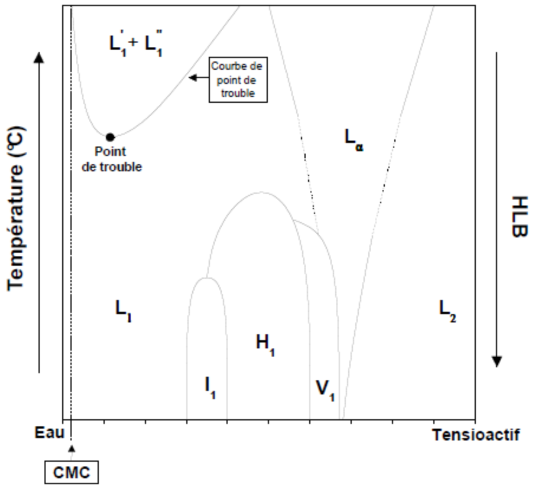

Figure I.6 The ideal phase diagram of most surfactant as a function of temperature and HLB values.

For the [$C_m(EO)_n$] compounds, the nature of the liquid crystal phases is particularly sensitive to the HLB. A very hydrophilic surfactant forms mostly liquid crystal phases hexagonal and cubic symmetry. This is the case of the system formed by the hydrogenated surfactant $C_{16}(EO)_{12}$ (HLB = 14.2) (Figure I.7a), which has mostly hexagonal and cubic phases, while the lamellar field is very limited. With a more hydrophobic surfactant, such as $C_{16}(EO)_8$ (HLB = 12.4) (Figure I.7b), a wide field for lamellar phases is found at higher concentrations of surfactant.

In addition, the combined area of hexagonal and cubic liquid crystal phases appears at lower temperature. A system having a lower HLB still shows only lamellar liquid crystal in water.

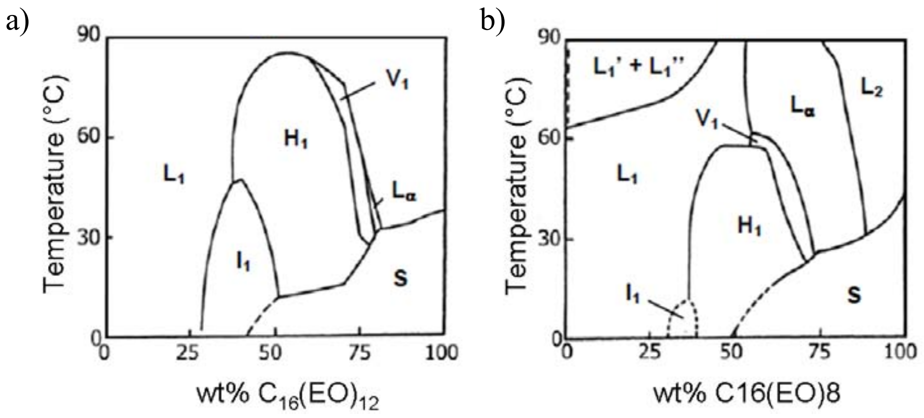

Figure I.7 Phase diagram of hydrogenated surfactants a) $C_{16}(EO)_{12}$ and b) $C_{16}(EO)_8$ [14].

In addition, nonionic surfactants are characterized by the presence of a solubility curve also called miscibility curve [14] [16]. This curve separates the area of direct micelles (L_1) from a two-phase field consisting of two micellar phases, one poor in micelle (L_1') and the other rich in micelles (L_1''). The minimum of the solubilisation curve corresponds to the lower critical temperature (LCT noted for Lower Consolute Temperature). This critical point is also known as the cloud point (noted as CP), because of the appearance of the micellar solution which becomes highly turbid. This phase separation in systems containing surfactants is often explained too simply by the effect of the dehydration of the polyoxyethylene (POE) chains occurring at the cloud point temperature, due to a decrease in the number of hydrogen bonds [17]. This dehydration has been suggested to be induced by the conformational change of the POE chain associated with temperature rise [18].

Moreover, two separate mechanisms are proposed for this phase separation (the cloud point) of nonionic surfactant-water systems. One, involving intermicellar van der Waals attractions between micelle cores, operates at low temperatures, while the second, involving intermicellar EO-EO interactions occurs at high temperatures [14].

The simplest model for describing self-assembly in surfactant solutions is “the critical packing parameter”. The packing parameter is admitted to be able to predict the possible microstructures for a given surfactant structure and the dependence of the microstructure on the amounts and types of solvent present, on temperature, on salinity, and so on. This issue was first addressed in 1980 by Tanford, and later on in 1992 by Israelachvili, Mitchell and Ninham who compared the relative bulkiness of the polar and nonpolar parts of the surfactant molecule. As in Figure I.8, Israelachvili and coworkers illustrate this principle [19]: Conical molecules with bulky head groups attached to slender tails form spherical micelles; cylindrical molecules with heads and tails of equal bulkiness form bilayers; a wedge-shaped molecules with tails bulkier than their heads form inverted micelles containing the heads in their interior. A simple dimensionless molecular parameter that controls the shape of the aggregates is the molecular 'packing parameter' g which is defined in equation I.1; g depends on the molecular geometry of the surfactant molecules, such as the number of carbon atoms in the hydrophobic chain, the degree of chain saturation, the size and charge of the polar head groups.

$$g \cong V/a_0 l_c \qquad \text{(equation I.1)}$$

where V is the effective volume of the hydrophobic tail, a_0 is the area of the surface that the head group occupies, and l_c is the critical hydrophobic chain length "the maximum effective length of the tail" [20]. When $V/a_0l_c \leq 1/3$, the spherical micelles are expected; when $1/3 \leq V/a_0l_c \leq 1/2$, cylinders are favoured; for $V/a_0l_c \approx 1$, bilayers should form; and for V/a_0l_c value higher than 1, we expect inverse structures. Moreover, the cubic phases can be also expected when $1/2 \leq V/a_0l_c \leq 2/3$ or when $1 \leq V/a_0l_c \leq 3/2$.

The effects of the solution parameters, including ionic strength, pH, co-surfactant concentration and temperature, are included implicitly in V, a_0 and l_c [19]. The maximum effective tail length (l_c) and the tail volume V of the saturated hydrocarbon chain n_c carbon atoms are estimated as (Tanford, 1980 [21]):

$$l_c \approx (1.54 + 1.256\, n_c) \qquad \text{(equation I.2)}$$

$$V \approx (27.4 + 26.9\, n_c)\ \text{Å}^3 \qquad \text{(equation I.3)}$$

The head-group area (a_0) is harder to estimate because it is not constant for a given molecule, but depends on the solvent environment. For example, at low ionic strength, the head groups of ionic surfactant repel each other more strongly and therefore occupy a larger effective area on the aggregate's surface than they do at the high ionic strength. Thus, as the ionic strength is decreased, a_0 increases; leads to a decrease in packing parameter, V/a_0l_c, therefore the transitions from cylindrical to spherical micelles can occur. However, a_0 can be obtained from the measurements of surface tension versus surfactant concentration by using the Gibbs adsorption equation [22].

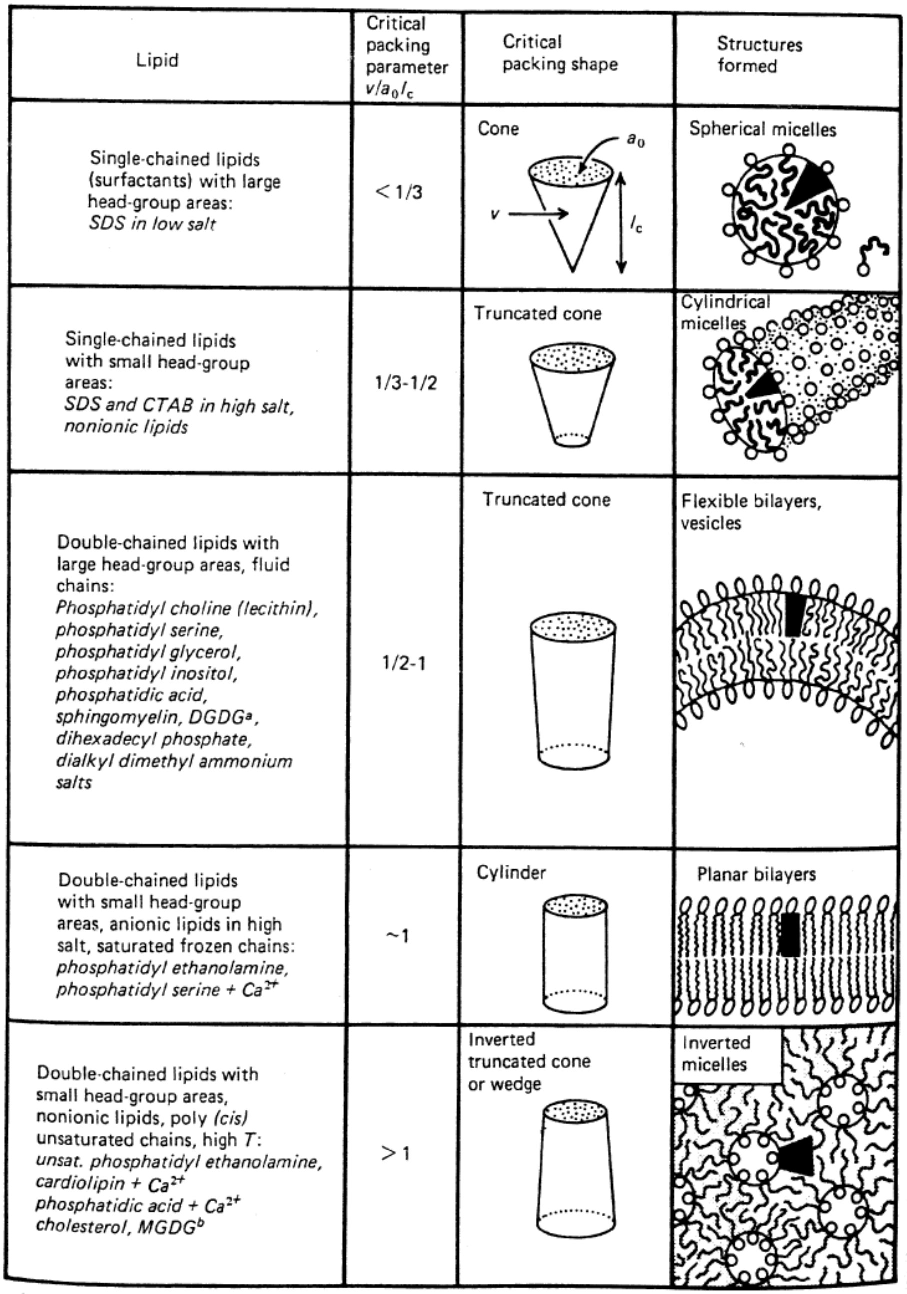

Lipid	Critical packing parameter v/a_0l_c	Critical packing shape	Structures formed
Single-chained lipids (surfactants) with large head-group areas: *SDS in low salt*	$< 1/3$	Cone	Spherical micelles
Single-chained lipids with small head-group areas: *SDS and CTAB in high salt, nonionic lipids*	1/3-1/2	Truncated cone	Cylindrical micelles
Double-chained lipids with large head-group areas, fluid chains: *Phosphatidyl choline (lecithin), phosphatidyl serine, phosphatidyl glycerol, phosphatidyl inositol, phosphatidic acid, sphingomyelin, DGDG*[a]*, dihexadecyl phosphate, dialkyl dimethyl ammonium salts*	1/2-1	Truncated cone	Flexible bilayers, vesicles
Double-chained lipids with small head-group areas, anionic lipids in high salt, saturated frozen chains: *phosphatidyl ethanolamine, phosphatidyl serine +* Ca^{2+}	~1	Cylinder	Planar bilayers
Double-chained lipids with small head-group areas, nonionic lipids, poly *(cis)* unsaturated chains, high *T*: *unsat. phosphatidyl ethanolamine, cardiolipin +* Ca^{2+} *phosphatidic acid +* Ca^{2+} *cholesterol, MGDG*[b]	> 1	Inverted truncated cone or wedge	Inverted micelles

[a] DGDG, digalactosyl diglyceride, diglucosyl diglyceride.
[b] MGDG, monogalactosyl diglyceride, monoglucosyl diglyceride.

Figure I.8 Packing shapes of surfactants and the structure they form [19].

Moreover, the phase transitions also reflect a decrease in surface curvature from the cubic (*Pm*3*n*) over the hexagonal to the lamellar phase. Spherical aggregates are preferentially formed by varying surfactants possessing large polar head groups. On the other hand, if the head groups are small and packed tightly, the aggregation number increases, resulting in rod-like or lamellar aggregates.

The experimental confirmation of the shape of the micelles was made some years later. The first results of small angle neutron scattering (SANS), small angle X-ray and light scattering showed that at the equilibrium, micelles can adopt different forms such as spherical [23], cylindrical [24].

1.1.3 Fluorinated surfactants

Due to the specific characteristics of fluorine and its high electronegativity, the fluorinated compounds have properties quite different from their hydrogenated analogues. Accordingly, with a very stable C-F bond, fluoride compounds exhibit superior chemical resistance and thermal stability, compared with hydrogenated ones [25]. This stability is due to a good interaction between 2s and 2p orbitals of fluorine and carbon. The size of the fluorine atom (van der Waals radius = 1.47 Å) is also larger than the hydrogen atom, and corresponds to the optimal size to fit into a carbon chain. The average volumes of CF_2 and CF_3 groups are 38 $Å^3$ and 92 $Å^3$, respectively, while, 27 $Å^3$ and 54 $Å^3$ for CH_2 and CH_3 groups. The low polarizability of fluorine atoms is the result of the existence of weak Van der Waals interactions, between fluorinated chains and low cohesion energy density in fluorocarbon liquids [26]. These weak interactions are responsible for most of the specific properties of fluorinated compounds such as low surface tension, wetting force, a high vapour pressure, high compressibility and gas solubility. Thus, larger quantities of gas (CO_2, O_2, CO, N_2, H_2, He) can be dissolved in fluorocarbons in oil or water. Moreover, their melting temperatures are higher than those of their hydrogenated analogues, while their boiling temperatures are lower and higher densities. The refraction indices of fluorocarbons are the lowest ever known for an organic solvent. Fluorinated surfactants can lower the surface tension of water down to a value half of what is attainable by using hydrocarbon surfactants. For nonionic surfactant, the existence of hydrophobic chains with the fluorinated groups (1 CF_2 equivalent to 1.7 CH_2 in terms of hydrophobicity) leads to a critical micellar concentration smaller than that of a hydrogenated compound of the same chain length. Despite the difference in hydrophobicity, the phase behaviour of fluorinated surfactant is similar to that of hydrogenated surfactants.

1.2 Mesoporous materials

Ordered porous materials are high-performance materials as catalysts or highly selective adsorbents; but in addition they provide excellent opportunities for the creation of materials with additional functionality. According to the standards set forth in the IUPAC definition [27], porous materials are classified by the following ranges of pore diameters [28]:

- Microporous Materials: pore diameters of less than 2 nm
- Mesoporous Materials: pore diameters ranging from 2 nm to 50 nm
- Macroporous Materials: pore diameters of greater than 50 nm

Among the porous materials, one of the oldest members is zeolite. Zeolites are hydrated crystalline aluminosilicates, which have a narrow and uniform microporous size distribution. Zeolites were discovered from the mineral ‘stilbit’ in 1756 by Cronsted [29]. They have extensively attracted the attention due to their structural characteristics and capabilities [23]. Approximately at the same time, the preparation of mesostructured silica was independently investigated by scientists from the Mobil Oil Corporation [1] and by Kuroda’s group [24] in the early 1990’s. However, a significant breakthrough in the mesoporous materials research has come when Mobil Oil Corporation’s scientists disclosed the M41S Type silica-based compounds and analogues in 1992. The discovery of the M41S family of mesoporous silica helped in the zeolite synthesis by providing methodologies to expand the pore size into the mesopore range.

The synthesis of mesoporous silica material was achieved by several synthetic pathways, such as self-assembly, templated self-assembly, sol-gel processing, dealumination of Al-rich aluminosilicates, spray drying method and etc. However, in our study, we will focus on the mesoporous material preparations via surfactant templating process.

Mesoporous silica materials made by the use of self-assembled surfactants as templates have attracted a lot of interest in recent years. Since, the formation of M41S mesostructured silica, this route of synthesis immediately attracted attention and this “surfactant-templated synthesis of mesoporous materials” has become a new field of research in materials science community.

Combined with the sol-gel chemistry, the difference depends on the surfactant concentration. Two mechanisms can lead to the formation of the ordered material. The first one is the self-assembly mechanism by Cooperative Templating Mechanism (CTM); in this case the building blocks are the micelles, so the CTM occurs at low surfactant concentrations. The second approach to the preparation of ordered mesostructures utilizes the liquid crystal phase and is labeled as the direct liquid crystal templating (LCT) pathway.

For synthesis of M41S, they used the self-assembly mechanism involving the dissolution of a surfactant species in the pre-hydrolysed inorganic pre-cursor. The mechanism is strongly influenced by electrostatic and steric interactions between the solvent molecules, the inorganic species and the self assembled organic surfactants. The most important family member of M41S is a hexagonal MCM-41 (Mobil Composition of Matter No.41). This material showed a highly ordered hexagonal array of unidimensional pores. It has a relatively large diameter ranging from 2-10 nm with a very narrow pore size distribution. A typical feature is its extremely high surface areas in excess of 200 – 1000 m^2/g, and a specific pore volume of up to 1.3 ml g^{-1} [28] [30] [31].

The excitement at the discovery of the hexagonal MCM-41 induced related research and gave rise to analogous mesoporous structures with different pore orientations, most notably MCM-48 (cubic) and MCM-50 (lamellar) [30] [31]. MCM-48 is a cubic phase with Ia3d symmetry consisting of an enantiomeric pair of nonintersecting three-dimensional channel systems that are mutually intertwined. MCM-50 is in unstable phases, which collapse during template removal. Therefore, MCM-41 has proven to be more stable and easier to synthesize than the other two members and has thus been more extensively studied and applied to various applications.

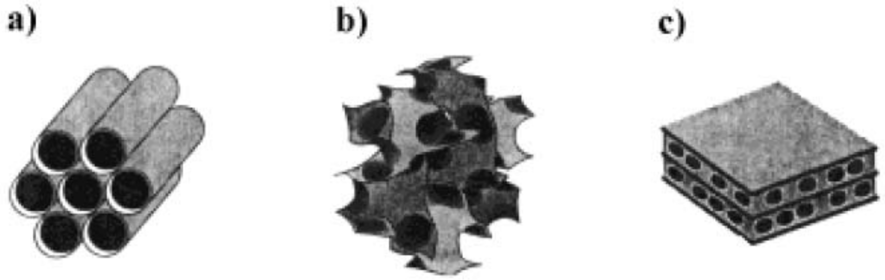

Figure I.9 Illustrations of mesoporous M41S materials: a) MCM-41 b) MCM-48 and c) MCM50 [32].

1.2.1 Mechanisms of formation

The detailed mechanistic studies have allowed the precise control of the structure and of the pore diameter in these materials, so that the systems are virtually tunable for a desired application [33]. The pore arrangement and morphology of the mesostructured materials, i.e., hexagonal, cubic, lamellar, or wormhole-like structure, is affected by several physicochemical factors; such as the molecular structure of the surfactant, the silica/ surfactant molar ratio [1] [34] [35], the pH value of the solution, the heating duration, and the temperature [34] [36], including the optimisation of relative kinetics and interactions between the inorganic and organic components of the synthesis [37].

Different mechanisms have been proposed to explain the formation of these materials. According to Mobil researchers, M41S type materials are formed through an LCT (liquid crystal templating) mechanism [1], in which aggregates of template molecules in combination with silicate species form a supramolecular structure. Later, based on the studies of different authors, this mechanism was modified to lead to the CTM (cooperative templating mechanism) [8] [38] [39].

A large number of studies have been carried out to investigate the formation and assembly of mesostructures on the basis of surfactant self-assembly. Two main pathways, that are cooperative self-assembly and "true" liquid-crystal templating processes, seem to be effective in the synthesis of ordered mesostructures, as shown in Figure I.10.

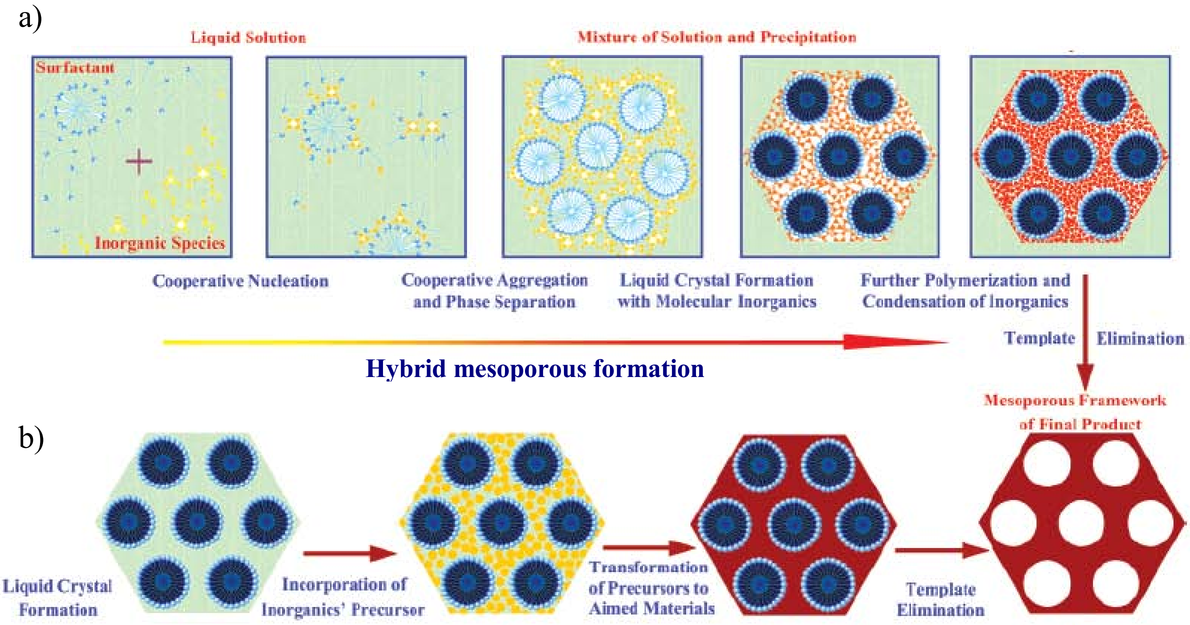
a)
Liquid Solution
Mixture of Solution and Precipitation
Surfactant
Inorganic Species
Cooperative Nucleation
Cooperative Aggregation and Phase Separation
Liquid Crystal Formation with Molecular Inorganics
Further Polymerization and Condensation of Inorganics
Template Elimination
Hybrid mesoporous formation
Mesoporous Framework of Final Product
b)
Liquid Crystal Formation
Incorporation of Inorganics' Precursor
Transformation of Precursors to Aimed Materials
Template Elimination

Figure I.10 Two synthesis strategies of mesoporous materials:
(a) cooperative self-assembly, (b) "true" liquid-crystal templating process [40].

1.2.2 Cooperative Templating Mechanism (CTM)

This pathway is established on the basis of the interactions between silicates and surfactants to form inorganic-organic mesostructured composites. When the mesoporous material is prepared from a micellar solution, it is today well-accepted that the formation of these materials occurs through the cooperative templating mechanism [5] [38] [39].

It consists of 3 steps. In the initial step, the interactions between silica and isolated spherical or cylindrical micelles drive to the formation of an organic–inorganic mesophase. Then, the condensation of the inorganic precursor at the external surface of the micelles occurs (intramicellar condensation) [39] [41] [42]. Finally, the self-organization of micelles surrounded by silica is gradually occurred to form a hybrid hexagonal mesophase (intermicellar condensation). The hydrothermal treatment at higher temperature completes the assembly of micelles and the polymerization of the silica source.

However, some disagreement concerning the first step of the CTM mechanism appears and numerous investigations were carried out in order to better understand how the surfactant and the inorganic precursor could affect the formation of the hybrid mesophase. Even if the debate concerning the initial step of the CTM mechanism is still opened, it is admitted that the interactions between surfactant and inorganic precursor are responsible for the mesoporous materials formation. It appears that this step is strongly affected by the behaviour of surfactant in the synthesis solvent.

According to a microscopic model introduced by Israelachvili et al. [20] as mentioned in Section 1.1.2, the relative stabilities of different aggregate shapes and the corresponding mesophase structures can be predicted as in Table I.1 In classical micelle chemistry, mesophase transition occurs when the packing parameter g is increased above some critical values.

Table I.1 Surfactant packing parameter g, expected structure and examples for such structures.

g	Expected structure	Example
1/3	cubic (*Pm3n*)	SBA-1
1/2	hexagonal (*p6*)	MCM-41, FSM-16, SBA-3
1/2 - 2/3	cubic (*Ia3d*)	MCM-48
1	lamellar	MCM-50

The mechanism of cooperative self-assembly considers the interactions on the surfactant/inorganic species interfaces. In 1993, Monnier and Huo et al. [43] gave a formula of the free energy in the whole process:

$$\Delta G = \Delta G_{\text{inter}} + \Delta G_{\text{wall}} + \Delta G_{\text{intra}} + \Delta G_{\text{sol}}$$

in which ΔG_{inter} is the energy associated with the interaction between inorganic walls and surfactant micelles, ΔG_{wall} is the structural free energy for the inorganic frameworks. ΔG_{intra} is the van der Waals force and conformational energy of the surfactant, and ΔG_{sol} is the chemical potential associated with the species in solution. For the surfactant-templating assembly of mesostructured silicates, ΔG_{sol} can be regarded as a constant in a given solution system. Therefore, the key factor is the interaction between surfactant and inorganic species, such as the matching of charge density. The more negative ΔG_{inter} is, the more easily the assembly process can proceed. Elaborate investigations on mesoporous materials have been focused on understanding and utilizing the inorganic organic interactions [5] [30].

As described above, this cooperative self-assembly process results from the electrostatic interactions or H-bonding between inorganic and organic interface of the inorganic precursor and the surfactants. It appears that the characteristics of the recovered materials, such as the structure and the pore diameter, are strongly related to the properties of the surfactant used for their preparation. For ionic surfactants templating procedure, the silicate species in solution play a more active role in directing the formation of the organic-inorganic mesophase through a charge balance with the surfactant ions.

The way to produce three dimensional periodic biphasic arrays by using the self assembling of the S^+ and I^- ions or by using the reverse charge matching (S^-I^+) has been described by Ciesta et al. [28] [44], S is the surfactant species and I is the silicate.

In addition, a mechanism involving a third ion (X^- or M^+) is often used to combine the surfactant and the silicate : X^- = halogenide anions, under acidic conditions and M^+ = alkaline cations, in basic media) [5]. The more recent procedures often use this synthesis pathway in which the surfactant and silicate species are both cationic and their interaction is mediated by an anionic species in acidic conditions.

Other synthesis routes rely on nonionic surfactants, where the main interactions between the template and inorganic species are H-bonding or dipolar. Under neutral conditions, mesostructures are formed by neutral (S^0) [45] or nonionic surfactants (N^0) [46]. In this approach (N^0I^0 or S^0I^0) hydrogen bonding is considered to be the driving force for the formation of the mesophase. In case of superacid conditions (pH < 2), silica source will charge positively because of the presence of H+, ($S^0H^+X^-I^+$).

Table I.2 Synthesis routes to mesoporous materials with the emphasis on silicates [40]

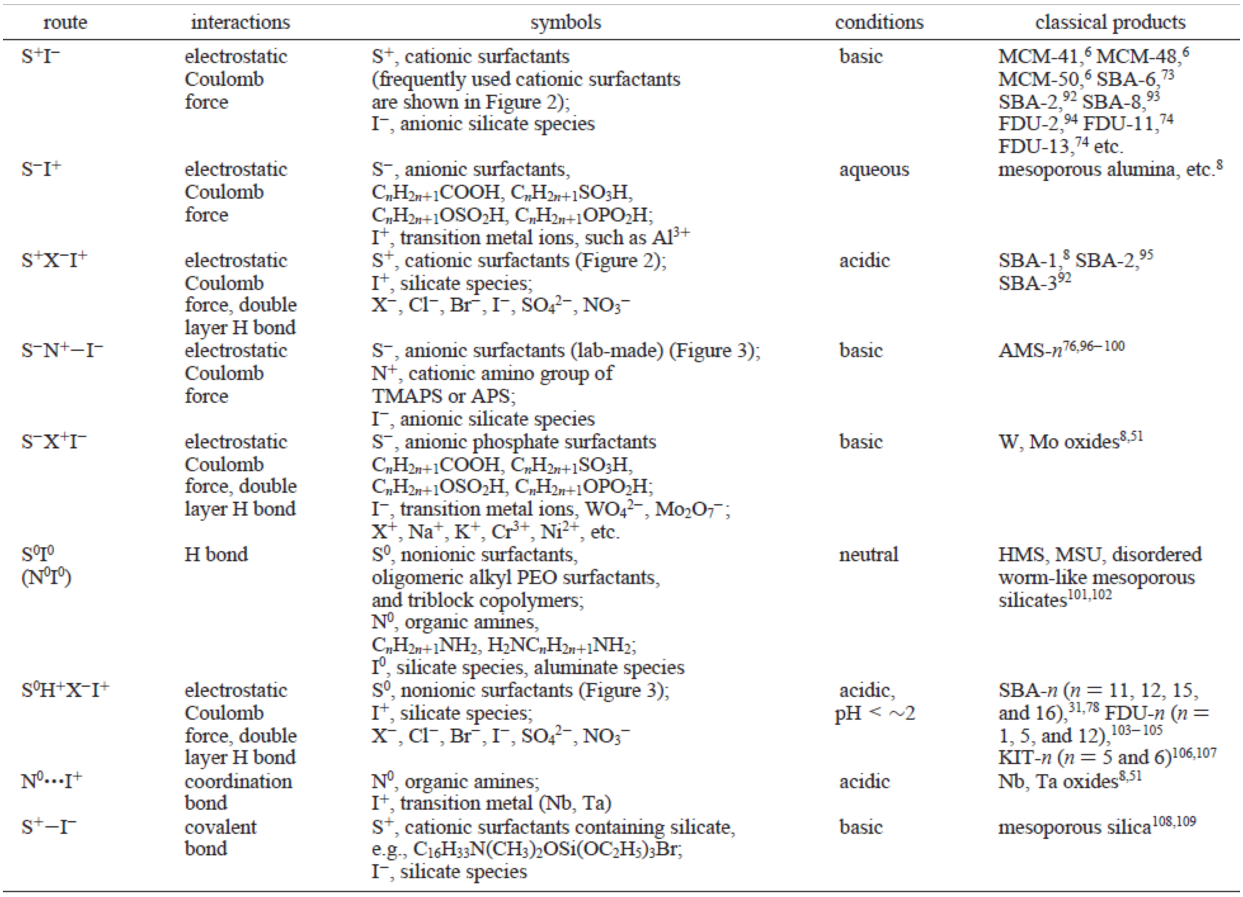

route	interactions	symbols	conditions	classical products
S^+I^-	electrostatic Coulomb force	S^+, cationic surfactants (frequently used cationic surfactants are shown in Figure 2); I^-, anionic silicate species	basic	MCM-41,[6] MCM-48,[6] MCM-50,[6] SBA-6,[73] SBA-2,[92] SBA-8,[93] FDU-2,[94] FDU-11,[74] FDU-13,[74] etc.
S^-I^+	electrostatic Coulomb force	S^-, anionic surfactants, $C_nH_{2n+1}COOH$, $C_nH_{2n+1}SO_3H$, $C_nH_{2n+1}OSO_2H$, $C_nH_{2n+1}OPO_2H$; I^+, transition metal ions, such as Al^{3+}	aqueous	mesoporous alumina, etc.[8]
$S^+X^-I^+$	electrostatic Coulomb force, double layer H bond	S^+, cationic surfactants (Figure 2); I^+, silicate species; X^-, Cl^-, Br^-, I^-, SO_4^{2-}, NO_3^-	acidic	SBA-1,[8] SBA-2,[95] SBA-3[92]
$S^-N^+{-}I^-$	electrostatic Coulomb force	S^-, anionic surfactants (lab-made) (Figure 3); N^+, cationic amino group of TMAPS or APS; I^-, anionic silicate species	basic	AMS-*n*[76,96–100]
$S^-X^+I^-$	electrostatic Coulomb force, double layer H bond	S^-, anionic phosphate surfactants $C_nH_{2n+1}COOH$, $C_nH_{2n+1}SO_3H$, $C_nH_{2n+1}OSO_2H$, $C_nH_{2n+1}OPO_2H$; I^-, transition metal ions, WO_4^{2-}, $Mo_2O_7^-$; X^+, Na^+, K^+, Cr^{3+}, Ni^{2+}, etc.	basic	W, Mo oxides[8,51]
S^0I^0 (N^0I^0)	H bond	S^0, nonionic surfactants, oligomeric alkyl PEO surfactants, and triblock copolymers; N^0, organic amines, $C_nH_{2n+1}NH_2$, $H_2NC_nH_{2n+1}NH_2$; I^0, silicate species, aluminate species	neutral	HMS, MSU, disordered worm-like mesoporous silicates[101,102]
$S^0H^+X^-I^+$	electrostatic Coulomb force, double layer H bond	S^0, nonionic surfactants (Figure 3); I^+, silicate species; X^-, Cl^-, Br^-, I^-, SO_4^{2-}, NO_3^-	acidic, pH < ~2	SBA-*n* (*n* = 11, 12, 15, and 16),[31,78] FDU-*n* (*n* = 1, 5, and 12),[103–105] KIT-*n* (*n* = 5 and 6)[106,107]
$N^0\cdots I^+$	coordination bond	N^0, organic amines; I^+, transition metal (Nb, Ta)	acidic	Nb, Ta oxides[8,51]
$S^+{-}I^-$	covalent bond	S^+, cationic surfactants containing silicate, e.g., $C_{16}H_{33}N(CH_3)_2OSi(OC_2H_5)_3Br$; I^-, silicate species	basic	mesoporous silica[108,109]

Firouzi and coworkers suggested a model [38] that makes use of the cooperative organization of inorganic and organic molecular species into three dimensional structure of material. In this model, the properties and structure of a system are determined by dynamic interplay among ion-pair of inorganic and organic species, so that different phases can be readily obtained through small variations of controllable synthesis parameters, including mixture composition and temperature. Nucleation, growth, and phase transitions may be directed by the charge density, coordination, and steric requirements of the inorganic and organic species at the interface and not necessarily by a preformed structure. A specific example is presented in which organic molecules in the presence of multiply charged silicate oligomers self-assemble into silicatropic liquid crystals. The organization of these silicate-surfactant mesophases is investigated with and without interfacial silicate condensation to separate the effects of self-assembly from the kinetics of silicate polymerization. By including the inorganic component, Stucky et al. [38] [47] expanded the model to the ternary NaOH/cetyltrimethylammoniumbromide (CTAB)/tetraethoxysilane (TEOS) system and created a synthesis-space diagram of mesophase structures. Additionally, Vartuli and co-workers [48] studied the effect of surfactant/silica ratios on the formation of mesostructures. Obviously, the ratio is a critical variable in the mesophase formation and by, varying the surfactant/silica molar ratio from 0.5 to 2.0, products with hexagonal, cubic (*Ia*3*d*), lamellar and uncondensed cubic octamer composite structures were obtained.

1.2.3 Nonionic surfactant for mesoporous material preparation

Nonionic polyoxyethylene alkyl ether surfactants $C_m(EO)_n$ may contain polyoxyethylene chains, either block copolymers of the polyoxyethylene–polyoxypropylene–polyoxyethylene type (often referred to as EO–PO–EO polymers), fatty alcohol ethoxylates, C_mH_{2m+1}–$(EO)_n$, with m typically being 12–18 and n being 5–8. They have been widely studied in much physicochemical data, such as micelle formation, intermicellar interaction, clouding phenomenon, structural studies, and phase behaviour in various solvents. These surfactants have become commercially available, and they are used as emulsifiers, wetting agents, detergents, or solubilizers.

In all the preparation methods, the crucial tools for controlling the mesostructure are the surfactant molecules. Tuning the hydrophilic and/or the lipophilic chain lengths allows determining the mesostructure of the materials. Nonionic surfactants have the advantage, compared to ionic surfactants, that they can be easily removed from the inorganic framework by solvent extractions or soft thermal treatments, because of weak hydrogen bond interactions between nonionic organic molecules and inorganic species, instead of stronger covalent or ionic interactions [37] [49] [50]. For instance, Pluronic, nonionic surfactants copolymers consisting of blocks of poly(ethylene oxide) (EO) and poly(propylene oxide) (PO), have been extensively used in the preparation of mesoporous materials, with controlled pore size and morphology. The materials are often calcinated to remove the Pluronic molecules.

During the middle 1990s, nonionic surfactants have been widely employed as templates (structure-directing agents) for the preparation of mesoporous molecular sieves. In 1995, Attard et al. [51] reported the first syntheses of mesoporous molecular sieves through the N_0I_0 pathway by using $C_{12}(EO)_8$ and $C_{16}(EO)_8$. The assembly of the mesostructure is based on the hydrogen bonding interactions between the oxygen atoms of the nonionic oxyethylene group (N_0) and the hydrogen atoms of the neutral inorganic precursor (I_0). The obtained ordered materials with hexagonal channel arrangement exhibit pore sizes up to 3.0 nm. Then, Stucky and coworkers [8] reported new cubic cage-structured (Im3m), cubic (Pm3m), 3-d hexagonal ($P6_3/mmc$), 2-d hexagonal (p6mm), lamellar (L_α) mesoporous silica and possibly continuous L_3 sponge, mesophases by using commercially available nonionic alkylethylene oxide oligomeric surfactants and poly(alkylene oxide) block copolymer surfactants in strong acid media. They suggested that surfactants with short EO segments tend to form lamellar mesostructured silica at room temperature. The EO/PO ratio of the copolymers has a large effect on the formation of the silica mesophase: lowering the ratio of the triblock copolymer moieties promotes the formation of lamellar mesostructured silica, while higher ratios favor cubic mesostructured silica. The assembly of the inorganic and organic composite materials appears to occur by a double-layer hydrogen-bonding $(S^0 H^+)(X^-I^+)$ pathway involving cationic silica species that are present in the strong acid conditions. The assembly rate r increases with increasing concentration of $[H^+]$ and $[Cl^-]$, according to the kinetic expression $r = k[H^+]^{0.31}[Cl^-]^{0.31}$. Pinnavaia group [45] [46] [52] have successfully synthesized the wormhole-like MSU (Michigan State University) mesoporous silica structure by using organic amines, nonionic oligomeric surfactants and triblock copolymers under neutral conditions. They proposed the N^0I^0 or S^0I^0 mechanism involving hydrogen-bonding interactions between the hydrated silicate oligomers (I^0) derived from TEOS, nonionic surfactant (N^0) or amines (S^0). Moreover, this disordered material showed a uniform pore size distribution and high thermal and hydrothermal stabilities.

The nonionic surfactants have most often been used under acidic rather than under neutral conditions. The hydrophilic–lipophilic balance (HLB) of these surfactants is strongly affected by the temperature, which makes it possible to govern the type of liquid crystal structure formed in water solutions by temperature adjustments. Kipkemboi and coworkers have demonstated how the mesostructure obtained with EO–PO–EO block copolymers as structure directing agents, is influenced by the temperature and by the hydrophilic domain length [7]. An increase in temperature leads to dehydration of the polyoxyethylene (EO) chains, causing a reduction of the size of this block. This results in a change of the spontaneous curvature of the surfactant film. Increasing the temperature will, for low surfactant concentrations, lead to a transition from less elongated to more elongated micelles and for high surfactant concentration to a transition from micellar cubic, via hexagonal and lamellar, to bicontinuous cubic liquid crystals. One would expect that the temperature-controlled mode of self-assembly in solution would be transferred to the corresponding structures in the mesoporous material. Shrinkage of the hydrophilic domains of the templating surfactant means that the volume where the silica wall is being formed is reduced. This would be expected to lead to thinner walls of the mesoporous material. It is now experimentally verified that this is true, i.e., an increase in temperature for systems based on surfactants containing polyoxyethylene chains leads to a decrease of the wall thickness. The mesopore diameter is only slightly affected by variations in temperature, however, because it is governed by the size of the hydrophobic domain, i.e., the PO block, which is little influenced by the temperature [7].

1.2.4 Nonionic fluorinated surfactant for preparation of mesoporous materials.

As their hydrogenated analogues, fluorinated surfactants are used in various domains, $C_mF_{2m+1}C_2H_4(OC_2H_4)_nOH$. Indeed, due to their high stability, they can support strong temperature and severe pH conditions. The substitution of hydrogen atoms by fluorine ones enhances the chemical and thermal stability of the surfactant. For example the energy of the C-F bond is 552 kJ mol^{-1} instead of 338 kJ mol^{-1} for the C-H bond [53]. In 1972, Shinoda and coworkers suggested [54] that the presence of fluorine atoms also strongly affects the properties of the surfactant and particularly its hydrophobicity and its critical micellar concentration (cmc). Then, the comparative studies of nonionic hydrogenated and fluorinated surfactant properties have been reported by the Stébé team since 1988. For nonionic surfactant, they state that one CF2 group is equivalent to 1.7 CH_2 groups [26], which triggers lower cmc’s. As an instance if the headgroup is not changed, a fluorinated surfactant with 7 carbon atoms has the same cmc as a hydrogenated one with 11 carbon atoms. As a consequence of the high hydrophobicity, fluorinated surfactants can decrease the surface tension of water from 30-40 to 15-20 mN.m^{-1}. The phase behaviour of fluorinated surfactants is quite similar to the hydrogenated ones [26] [55]. However, some differences can be found, and a comparative study [26] of fluorinated and non-fluorinated based systems has emphasized that lamellar liquid crystals and larger aggregates are preferentially formed with fluorinated surfactants. This difference in behaviour has been ascribed to the fluorinated chain rigidity and to the higher value of the headgroup area (CF group) of fluorinated surfactants.

The aggregate structures in fluorinated surfactants have been described by Israelachvili and coworkers [20], as in hydrogenated surfactants, in terms of the value of the critical packing parameter (CPP). The fluorocarbon chains are bulkier than the hydrocarbon chain with the volume V of -CF_2 and terminal -CF_3 being 0.041 and 0.084 nm^3, respectively compared with 0.027 and 0.037 nm^3, for hydrocarbon analogues [21]. Moreover, the self-assembly in fluorinated surfactant systems were reviewed by Maura Monduzzi in 1998 [56]. The effect of a F chain lead to an increase of the hydrophobic interactions and a decrease in surface tension and cmc values. F chains are generally responsible for an increase of the chain volume, because of a higher cross-sectional area of the CF group and weaker van der Waals interactions among the F chains. These results in an increase of the critical packing parameter (CPP) value, so that interfacial curvature increases, thus allowing important variations of the phase behaviour to occur in comparison with the corresponding hydrogenated surfactants. As a general comment, it is worth noting that H/F mixed systems always give interesting microstructural features. Fluorinated surfactants allow cosolubilization of water and perfluoroalkanes [57] [58], and the specific property of fluorocarbon to dissolve high quantities of oxygenandcarbon dioxide make them very attractive for biomedical applications such as oxygen vectorization for instance [59] [60].

Stébé's team also compared [61] the structural property of aqueous nonionic fluorinated micellar solution, depending upon the chemical structure of surfactant polar head. The results obtained by intrinsic viscosity and small-angle scattering showed the correlation between the micelles shape and the critical concentration. They were in complete agreement with the molecular surfactant structure. A bulky voluminous polar head is compatible with spherical micelles, whereas a long linear chain promotes elongated micelles. Therefore, to form a spherical aggregate, fluorinated surfactants with very large headgroups are needed to balance the effect of the bulky fluorocarbon chain [61].

The formation of mesostructured silica with another series of nonionic fluorinated surfactants $C_8F_{17}SO_2(C_3H_7)N(C_2H_4O)_nH$ (abbreviated $C_8F_{17}(EO)_n$) (Figure I.11) via the self-assembly precipitation method in acidic aqueous solutions was reported in 2006 by

Esquena and coworkers [62]. $C_8F_{17}(EO)_n$ forms elongated micelles and liquid crystals in water. The optimal poly(ethylene oxide) chain length to obtain well-ordered mesostructured materials is 10 units of ethylene oxide. The concentration of surfactant required to obtain well-ordered mesoporous materials is very low (1 wt% at 25°C related to binary phase diagram), and the pore walls are thick (>20 Å). Two-dimensional hexagonal (p6mm) mesostructures are obtained at HCl concentrations higher than 0.1 M, whereas disordered worm-like mesostructured silica are formed at lower HCl concentrations. They possess high specific surface areas (~1000 m^2/g), very homogeneous inner pore diameters, and robust thick walls. Their work demonstrated that fluorinated surfactants are very appropriate for the preparation of mesostructured materials with relatively small pore diameters and thick pore walls.

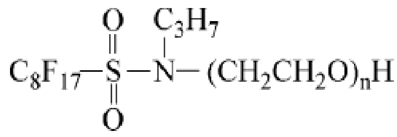

$$C_8F_{17}-\overset{\overset{\displaystyle O}{\|}}{\underset{\underset{\displaystyle O}{\|}}{S}}-\overset{\overset{\displaystyle C_3H_7}{|}}{N}-(CH_2CH_2O)_nH$$

Figure I.11 Molecular structure of perfluoroalkyl sulfonamide ethoxylate, $C_8F_{17}EO_n$ [63].

According to the work of Sharma's team in 2006 [63], the $C_8F_{17}EO_n$ nonionic surfactant is so far the only one known to form a highly viscoelastic solution of wormlike micelles in a surfactant water binary system. The mixed system of highly hydrophilic nonionic fluorinated surfactants $C_8F_{17}EO_{20}$ and a hydrophobic amphiphile $C_8F_{17}EO_1$ (cosurfactant) in aqueous solution was studied. Addition of $C_8F_{17}EO_1$ reduces the interfacial curvature of the aggregates and induces one-dimensional micellar growth. With successive addition of $C_8F_{17}EO_1$, the viscosity increases rapidly to form viscoelastic solutions, then decreases after the maximum, and ultimately, a phase separation occurs. The dynamic rheological behaviour of the viscoelastic solutions can be described by Maxwell's model at low-shear frequency, which is the typical behaviour of wormlike micellar solution. Increasing surfactant or cosurfactant concentration in the mixed nonionic system increases the extent of one-dimensional micellar growth which is mainly attributed to the decrease in the spontaneous curvature of the aggregates and consequently a progressive increase in the energy cost for the formation of the hemispherical end caps of the aggregates. Addition of a small amount of fluorinated oils to the wormlike micellar solution disrupts the network structure and decreases the viscosity sharply. It was found that perfluoropolyether oil, (F-$(C_3F_6O)_{21}CF_2CF_2COOH$), PFE, decreases the viscosity more effectively than the perfluorodecalin (PFD). The difference in the effect of oil on the rheological properties was explained in terms of the solubilisation site of the oils in the hydrophobic interior of the cylindrical aggregates, and their ability to induce rod-sphere transition. Hence, PFE which is solubilised in the core of the hydrophobic interior of the cylindrical aggregate increases the spontaneous interfacial curvature more effectively and stabilizes the end caps. PFD, which is preferentially solubilised in the palisade layer shows a lower extent of viscosity drop.

Hence, the formation and rheological behaviour of a viscoelastic wormlike micellar solution of $C_8F_{17}EO_{10}$ in aqueous solution was focused by Achraya and co-workers [64]. The temperature-induced viscosity growth in a water-surfactant binary system at various concentrations was investigated. They suggested that fluorinated surfactants tend to form aggregates with low curvature, such as cylindrical aggregates, at a solution condition where hydrocarbon surfactants would form spherical aggregates. This $C_8F_{17}EO_{10}$ forms flexible cylindrical aggregates in water even at low-surfactant concentrations and low temperature. With an increase in the surfactant concentration, these cylindrical micelles undergo one-dimensional growth and form very long and flexible wormlike micelles which entangle and form a network making a viscoelastic solution. With successive increases in the surfactant concentration, the aggregates loose the flexibility and transform into hexagonal liquid crystalline phases. An increase in the temperature of the nonionic surfactant system reduces the interfacial curvature and induces micellar growth, which is mainly attributed to the progressive increase in the energy cost for the formation of the hemispherical end caps of the aggregates. Therefore, the viscosity increases with temperature. Above a certain temperature, the viscosity begins to decrease, not because of the shrinking of micelles but because the system tends to eliminate the free ends by forming micellar joints in the network and such changes in the microstructure result in a decrease in the viscosity and stress relaxation time (τ_R), retaining the network structure. Variations of the rheological parameters are in agreement, and SAXS provides a direct evidence of such microstructural changes. The temperature at which the viscosity begins to decrease, gradually shifts toward lower values when the surfactant concentration increases because both have similar effects on the interfacial curvature. The rheological parameters, viscosity at low shear rate (η_o) and shear modulus (G_o), show scaling relationships with the surfactant concentrations with exponents greater than the values predicted by the living-polymer model, but the exponent of stress relaxation time (τ_R) is in agreement with the theory. Finally, dynamic light scattering measurements indicate the presence of fast-relaxation modes, associated with micelles, and medium and slow modes, associated with transient networks. The disappearance of the slow mode and the predominance of the medium mode as the temperature is increased gives support to the conclusions derived from SAXS and rheometry.

Based on the application of low dielectric constant materials, the hybrid fluorocarbon–silica materials consisting of micronsized spherical particles with hexagonal nanostructure were synthesized by sol–gel hydrolytic polycondensation using the same surfactant $C_8F_{17}EO_{10}$ as a structure-directing agent [65]. The prepared material is thermally stable and, more interestingly, has a very low dielectric constant (2.15), which is almost independent on frequency. Rodríguez Abreu and coworkers also studied the formation of hybrid fluorocarbon–silica nanocomposites by the self-assembly of this fluorinated surfactant and aminoalkoxysilane coupling agents [66]. The material possesses a lamellar nanostructure, silica layers in the materials are very thin, and contain a relatively high concentration of attached aminopropyl groups. Interestingly, the materials are thermally stable, hydrophobic and show a low dielectric constant (~2.8), which is almost independent on frequency, as predicted by the Maxwell–Wagner model.

The phase behaviour and self-assembled structures of perfluoroalkyl sulfonamide ethoxylate ($n = 20$), $C_8F_{17}EO_{20}$ a nonionic fluorocarbon surfactant in an aqueous system has also been investigated by Shrestha and coworkers in 2008 [67]. $C_8F_{17}EO_{20}$ forms spherical micelles in the dilute region and different liquid crystal phases depending on the temperature and composition under L_1 phase. The fluorocarbon micellar structure induced by temperature or composition change and the addition of fluorocarbon co-surfactant $C_8F_{17}SO_2N(C_3H_7)(CH_2CH_2O)H$ (abbreviated as $C_8F_{17}EO_1$) has been systematically studied. The SAXS data were analyzed by indirect Fourier transformation (IFT) and generalized indirect Fourier transformation (GIFT) depending on the volume fraction of the surfactant and complemented by plausible model calculations, supporting that the temperature favours one-dimensional micellar growth. A drastic modulation in the micellar structure is observed upon reducing the hydrophilic headgroup size of the surfactant. Namely, the globular type of micelles observed with $C_8F_{17}EO_{20}$ transforms into long cylindrical micelles with $C_8F_{17}EO_{10}$ at 25 °C. On the other hand, concentration does not lead to any significant changes in the micellar structure over a wide concentration range (1-25 wt %) at 25 °C.

Micellar growth leading to the formation of viscoelastic wormlike micelles in the ternary mixture of $C_8F_{17}EO_{20}$/water/$C_8F_{17}EO_1$ is confirmed by SAXS and rheometry.

1.2.5 Various fluorocarbon solubilization and oil incorporation in systems

It is known that addition of chemicals such as oils, affects the self-aggregation behaviour of surfactants. Oil incorporation can strongly affect the phase behaviour of surfactant/water systems as investigated by Blin and Stébé in 2004 [10]. The effect of perfluorodecalin (PFD) addition on the nonionic fluorinated surfactant $CF_3(CF_2)_7C_2H_4(OC_2H_4)_9OH$/water system was investigated. L_1 micellar phase, hexagonal (H_1), and cubic (I_1) liquid crystals were identified. Phase behaviour and SAXS measurements proved that the liquid crystals phase (H_1, I_1) can swell by addition of PFD, whereas only 1% of oil can be incorporated into the hydrophobic core of micelles (L_1). PFD can be used as an effectively swelling agent to enlarge the pore size of mesoporous materials. The preparation of mesoporous materials from the micellar phase shows that the pores increase in size despite the low incorporation of PFD in the L_1 phase. This behaviour is explained by the swelling of a hexagonal hybrid mesophase (surfactant-silica) and can be related to PFD incorporation in hexagonal liquid crystal H_1.

They also investigated the ability of perfluorocarbons to be used as organic auxiliaries in the preparation of large pore mesostructured silica [68]. To better understand the influence of these perfluorocarbons and to shed some light on the mechanism of pore size enlargement, they have studied the effect of various fluorocarbon addition on the surfactant phase behaviour and the ternary $C_8F_{17}C_2H_4(OC_2H_4)_9OH$/oil/water systems have been investigated. Perfluorodecalin ($C_{10}F_{18}$, PFD), Perfluoroheptane (C_7F_{16}, PFH) and Perfluorooctane (C_8F_{18}, PFO) can be effectively used as expander since they increase the pore size from 4.0 to 6.8 nm. However, if the oil content is too high (>2.5 wt %), the pore size enlargement occurs but the hexagonal structure is lost and recovered materials adopt a wormhole-like structure. PFD and PFH can swell the rod of the hexagonal liquid crystal phase whereas no effect on the hydrophobic radius of the rod is noted when PFO was added. They suggested that PFD is truly incorporated into the core of the rods (swelling effect), involving a channel swelling, while the value of the cross-sectional area remains constant. On the contrary, PFO molecules only penetrates between the hydrophobic chains of the hybrid mesophase, no swelling of the channel occurs neither in the structure nor in the pore diameter The value of the cross-sectional area increases with the addition of PFO, whereas the one of the hydrophobic radius remains constant.

Amaki and coworker also reported the effect of oil on a nonionic fluorinated surfactant $C_8F_{17}EO_{10}$ in aqueous system by using SAXS [69]. The addition of a small amount of perfluoropolyether (PFE) oil, $(C_3F_6O)_{21}COOH$, modulate the shape and size of micelles. Long cylindrical micelles eventually transform into globular like particles. The onset of the cylinder-to-sphere transition in the structure of the micelles in the surfactant/water/oil system is probably due to the amphiphilic nature of the oil, which tends to increase the spontaneous curvature. The lipophilic part of the oil tends to reside in the micellar core, whereas, the hydrophilic part goes close to the polar head group of the surfactant so that effective cross-sectional area per surfactant molecules increases and as a result spherical micelles tend to form. Perfluorodecalin (PFD) also decreases size of the micelles but its effect is poor compared to the PFE oil. Due to structural transition of the micellar structure, the rheological properties of the surfactant/water/oil systems were significantly modified. The viscosity of the solution decreases dramatically (four orders of magnitude by incorporating 1 wt% PFE). Thus, this research highlighted the possible routes to the structural control of the fluorinated micelles by tuning temperature, surfactant concentration and added fluorinated oils. According to their above mentioned results, they also studied the structural transition of viscoelastic wormlike micelles induced by oils [70]. The micellar solution of the $C_8F_{17}EO_{20}$ can solubilise a significant amount of $C_8F_{17}EO_3$, and the solubility increases with increasing $C_8F_{17}EO_{20}$ concentration. With successive addition of $C_8F_{17}EO_3$ to the aqueous $C_8F_{17}EO_{20}$ solution, viscosity increases rapidly, and a viscoelastic solution is formed. The viscoelastic solution can be fitted to Maxwell's model typical of wormlike micelles. With further addition of $C_8F_{17}EO_3$, the viscosity decreases, and phase separation occurs. Addition of PFE oil to the viscoelastic solution decreases the viscosity monotonically until phase separation. On the other hand, when PFD oil is added, viscosity first decreases and attains a limiting value before excess oil phase separates out. The viscosity decrease in water/surfactant/oil systems is possibly caused by the microstructural transition in the network structure. SAXS measurements were performed to complement the rheological data. It has been found that the $C_8F_{17}EO_3$ reduces the interfacial curvature of the aggregates and induces one-dimensional growth of the $C_8F_{17}EO_{20}$ micelles. On the other hand, when PFE is added, a wormlike-sphere type transition is more likely to occur.

1.2.6 Effect of salts and ethanol additions on the cloud point of nonionic, hydrogenated or fluorinated surfactant systems

The cloud point (CP) on the lower consolute boundary (LCB), is the lowest temperature at which the appearance of the micellar solution becomes turbid. In the case of $C_m(EO)_n$ surfactant, this phenomenon is related to the fact that water around the polyoxyethylene chain is more structured than bulk water [16] and it is associated with a strong entropy dominance [71]. Indeed, the ethylene headgroups are highly hydrated, so they are characterized by low entropy. When two micelles approach each other, their hydration spheres overlap and some water molecules are freed. As a consequence, the entropy is increased and this phenomenon becomes more important at the CP. On the other hand, to explain the clouding phenomenon in the case of polyethylene oxide solutions Karlström [72] [73] proposed a model where the conformational adaptation to the environment provides the mechanism of changing the free energy of interaction. In general, nonionic surfactants having a longer POE chain consequently have a higher CP, meaning a greater capacity to hydrate. The CP strongly depends on the hydrophilic-lipophilic balance (HLB) of the surfactant, and for a given hydrophobic chain length, its value increases with the number of EO units [14] [74]. For example, in a paper dealing with polyoxyethylene-type nonionic surfactants, Tiddy and co-workers [14] found, for the $C_{12}(EO)_n$ family, that changing n from 4 to 12 involves a shift of the lower consolute temperature from 4 to 98°C. The CP is also modified by the presence of additives [63], which affects the intermicellar interactions. A similar effect can be obtained with alcohol, and it is reported [75] that the addition of butanol (0.6 mol.L^{-1}) to the $C_{12}(EO)_5PO_4$-water system lowers the CP of about 10 °C, while methanol (1 mol.L^{-1}) increases the CP of 3 °C. Moreover, it is well-known that the presence of salts strongly modify the surface and the bulk properties of nonionic surfactant solutions [63] [76] [77] [78]. Therefore, salts affect the CMC as well as the position of the lower consolute boundary. Depending on the electrolyte, the lower consolute boundary can be shifted either toward higher (salting in) or lower (salting out) temperature. As an example, NaF, NaCl, and NaBr decrease the cloud point of $C_{12}(EO)_{10}$, whereas NaI shifts the temperature position of the boundary in the opposite way [63].

In 2006, Michaux et al. focused on the relation between the position of the lower consolute boundary of various nonionic surfactants in water and the properties of the final products [3]. Depending on the features of the phase diagram, they looked for either a salting out or a salting in effect. For $C_7F_{15}C_2H_4(EO)_8$ surfactant/water system, the phase diagram presented a cloud point at 34°C and the addition of NaI shifted the lower consolute boundary toward higher temperatures (salting in effect). While only disordered mesostructured are recovered from the $C_7F_{15}C_2H_4(EO)_8$/water system, well-ordered mesostructure are synthesized from an aqueous solution of sodium iodide. However, the pore ordering was lost if the temperature at which the silica precursor was added was near the phase separation temperature. By contrast, for the fluorinated $C_8F_{17}C_2H_4(EO)_9$ or the hydrogenated $C_{12}H_{25}(OC_2H_4)_8$ surfactants, NaCl involves a shift of the lower consolute boundary toward lower temperatures (salting out effect). In a 3 $mol.L^{-1}$ HCl solution, the phase separation temperatures of the surfactant solutions at 10 wt % are 48 and 36 °C, respectively for $C_8F_{17}C_2H_4(EO)_9$ and $C_{12}H_{25}(OC_2H_4)_8$ instead of a temperature higher than 90 °C and 75 °C for the salt-free solutions. As regards the mesoporous materials preparation, an hexagonal structure with uniform pore diameter was obtained from the $C_8F_{17}C_2H_4(EO)_9$ /water or the $C_{12}H_{25}(OC_2H_4)_8$ /water systems, but the presence of HCl leads to the loss of the pore ordering. However, the pore ordering is also affected by the ratio between the volume of its hydrophilic head group (V_A) and its hydrophobic part (V_B).

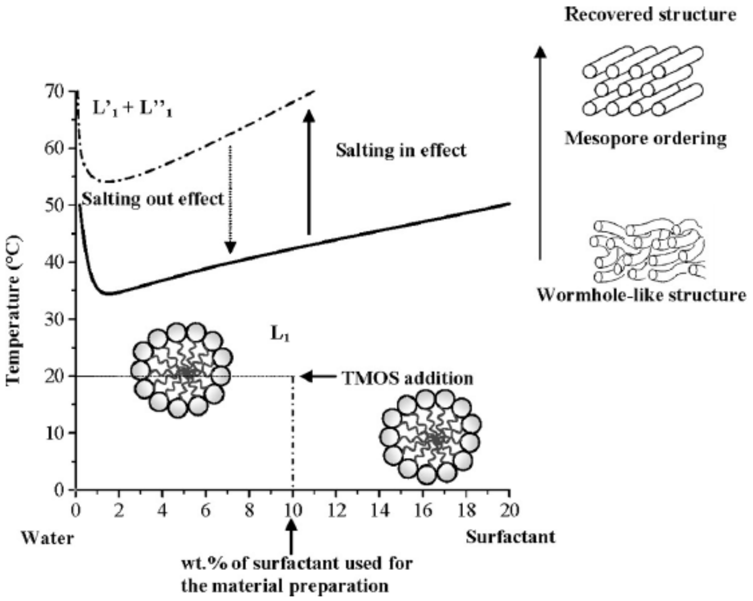
Recovered structure
L'₁ + L''₁
Salting in effect
Mesopore ordering
Salting out effect
Wormhole-like structure
L₁
TMOS addition
Temperature (°C)
0
10
20
30
40
50
60
70
0
2
4
6
8
10
12
14
16
18
20
Water
Surfactant
wt.% of surfactant used for the material preparation

Figure I.12 The influence of salt on the shift of the lower consolute boundary [3].

Finally, for all the investigated systems, they concluded as in Figure I.12 that the lower consolute boundary was shifted by adding salts. For material preparation, the results clearly evidenced that the cooperative self-assembly mechanism is favoured if the lower consolute boundary is shifted toward high temperatures and if the phase separation temperature is moved away from the temperature at which the silica source is added to the micellar solution. The higher the difference between the phase separation temperature and the temperature at which the silica precursor is added to the surfactant solution, the better the mesopore ordering is [3].

A time dependent sphere-to-rod micellar growth in the aqueous medium of the triblock copolymer $EO_{20}PO_{70}EO_{20}$ (P123) on approaching their cloud points was found by Ganguly and co-workers [79]. They reported that the rate of micellar growth increases with increase in temperature, but quite interestingly, it can be rather dramatically induced when the copolymer solutions are subjected to heat cycling, i.e., heating them to the phase separation and subsequently cooling them back to below their cloud point. They observed a kinetically restricted micellar growth has been attributed to the slow dynamics of the micellar restructuring processes essential to arrive at the temperature dependent equilibrium structure. It has been suggested that the improvement in the micellar growth rate upon heat cycling is due to overcoming of the activation energy associated with the micellar restructuring process. In the presence of water-structure-making salts like NaCl, salts reduce the sphere-to-rod transition temperature and help in forming wormlike micelles at room temperature upon similar heat cycling.

Recently, the influence of alcohol released during the hydrolysis of the inorganic precursor have been studied by Zimny and co-workers [80] in nonionic fluorinated surfactant-based systems. Methanol molecules interact with the EO units of the surfactant; upon addition of methanol, the L_1 micellar phase grows, H_1 and L_α liquid crystals progressively melt with the increase of the alcohol content. The CP curve of surfactant can be shifted to high temperatures upon addition of alcohol. Due to the shift of the cloud point curve, the hexagonal structure of the mesostructured silica obtained can be lost when increasing the content of methanol, leading to a wormhole-like structure. They confirm that the CTM mechanism is unfavoured if the cloud point temperature is close to the temperature at which the materials are prepared.

1.3 Rheology of micelles

In hydrocarbon-surfactant systems, the cylindrical micelles are often observed at solution conditions where spherical micelles are expected. Disordered solutions of spherical micelles are not particularly viscoelastic, or even viscous, unless the volume fraction of micelles becomes high enough. The micellar viscosity is higher than that of hard-sphere suspensions because of micellar ellipsoidal shape fluctuations and electrostatic repulsions. As cylindrical micelles grow, their total length can eventually exceed their persistence length, they then become semi flexible ‘wormlike’ micelles. These long chains can overlap in three-dimensional networks to give viscoelastic materials. Their physical properties depend on their flexibility and reversibility of the structures. At the surfactant concentration higher than a certain critical concentration, the aqueous solution is transformed from a low-viscosity Newtonian fluid to a highly viscoelastic solution. This remarkable change in rheological properties induces the considerable attention from theoreticians [81] [82] [83] [84] [85] [86] [87] and experimentalists [88] during the past decade in the context of complex fluids.

When the packing properties of amphiphiles, or in other words, when the spontaneous curvature of the micelle favours the formation of cylindrical aggregates, the molecules packed at the hemispherical ends have excess free energy in comparison to the molecules at the cylindrical part. This excess free energy, called “end cap energy”, is the thermodynamical driving force for the linear growth of cylindrical micelles. The system can reduce the free energy by reducing the number of free ends, that is, by end-to-end fusion of several short cylindrical aggregates to form a long aggregate. When the number density of the wormlike aggregates exceeds a certain threshold value, they entangle with each other to form a transient network and exhibit viscoelastic properties.

In all these systems, the structures of the aggregates at various scales (shapes, sizes, flexibility, internal molecular arrangement) are directly affected by a slight modification of the chemical constitution of the solvent, thus providing a way to modify the macroscopic behaviour of these materials (i.e., stability, mechanical, optical and thermal properties).

Hydrogen bonding, coordination bonding and various electron transfer processes are the most common “driving forces” for the 1D aggregation (fiber axis growth) and for the cross-sectional extension (junction zone growth). When the chain-like aggregates are integrating in dynamically disordered zones (called in the following “entanglement” by analogy with polymers), the mechanical cohesion on long time scales cannot be insured, the network is transient and the sample is a viscoelastic fluid.

The average chain length or the molecular weight distribution is also a thermal equilibrium and according to the nature and the strength of the monomer-monomer interaction within the chain, a kinetically breaking/recombination process can exist. This process can be in competition with the dynamics of motion of the individual chains and defines the “life time” of the chains by contrast to the “ordinary” polymers (unbreakable chains).

For micellar solution of surfactant at high enough concentrations, the micelles can entangle with each other, like the entanglements in concentrated solutions of long synthetic polymers. The entangled wormlike micelles increase the viscosity of fluids like polymer, and pronounced viscoelastic effects can occur. These giant wormlike micelles can break and re-form. Hence, it was sometime called “equilibrium polymers” or “living polymer” [89], because their length distribution is not fixed by chemical synthesis, but can vary reversibly in response to changes in concentration, salinity, temperature and even flow.

The wormlike micelles break and reconnect fairly rapidly. At equilibrium, the typical time for breakage of a micelle must equal the time for reconnection. For quantitative rheological measurement, two key structural features which controls their rheological response is the contour length L_c (a measure of the end to end distance) and the persistence length l_p (a measure of the flexibility of the micelle). The elasticity of the system is impacted by the hydrodynamic correlation length ξ_H of the worm like micelle. Stress relaxation can take place by reptation, and also by breaking and reforming, processes controlled by two characteristic time, the reptation time τ_rep and the breaking time τ_break.

- When $\tau_\mathrm{break} > \tau_\mathrm{rep}$, the micelles behave very much like unbreakable polymers, with exponential polydispersity and the stress relaxation takes the form: $\sigma(t) \sim \exp[-(t/\tau_{rep})^{1/4}]$

- If $\tau_\mathrm{break} < \tau_\mathrm{rep}$, the relaxation time is given by $\tau_\mathrm{R} \sim (\tau_\mathrm{break}\tau_\mathrm{rep})^{1/2}$, obtained from the cross-over of G' and G''.

When the fluid behaves like a Maxwell fluid with a single relaxation time, the viscoelastic properties of the sample are described by the two modulii, the storage modulus G' and and the loss modulus G'', function of the angular frequency ω.

$$G' = G_0 \frac{\omega^2 \tau_R^2}{1 + \omega^2 \tau_R^2}$$

$$G'' = G_0 \frac{\omega \tau_R}{1 + \omega^2 \tau_R^2}$$

The zero shear viscosity (η_0) in this case can be linked to the plateau modulus (G_0) by the simple equation : $\eta_0 = G_0.\tau_R$. The hydrodynamic correlation length (ξ_H) can be extracted from the plateau modulus: $\xi_H^3 = k_B T / G_0$; where k_B is Boltzmann constant and T is temperature in Kelvin.

If the persistence length is estimated or extracted (from high frequency rheology or small angle scattering technique), then it can be fully characterized the entanglement length (l_e) through: $l_e \approx \xi_H^2 / l_p^2$

Amaki's team [90] have reported the rheological behaviour of micellar solution of highly hydrophilic nonionic fluorinated surfactant, perfluoroalkyl sulfonamide ethoxylate ($C_8F_{17}EO_{20}$) at relatively low surfactant concentration with less hydrophilic surfactant $C_8F_{17}EO_{10}$ in aqueous system. Above the critical micellar concentration, the surfactant, $C_8F_{17}EO_{20}$ forms small spherical micelles in water and the viscosity of the solution remains constant regardless of the shear rate, i.e., the solutions exhibit Newtonian behaviour. Then, addition of $C_8F_{17}EO_{10}$ to the dilute solution of $C_8F_{17}EO_{20}$ leads to a decrease in the effective cross-sectional area per amphiphile at the interface and induces one dimensional micellar growth leading to the formation of viscoelastic short-haired wormlike micelles. Mixing the hydrophilic $C_8F_{17}EO_{20}$ with $C_8F_{17}EO_{10}$ resulted in higher viscosities at certain temperature and concentration, due to an increase in the rigidity of the surfactant layer so that micellar branching might be prevented. The oscillatory-shear rheological behaviour of the viscoelastic solution can be described by Maxwell model at low frequency. GIFT analysis of the SAXS data highlighted the one-dimensional micellar growth with increase in the $C_8F_{17}EO_{10}$ concentration and thus supports the rheological data.

In the aspect of rheological behaviour of hydrocarbon surfactant systems, there are some reports on the effect of oil addition and it was found that the effect depends on the nature of the oil. Little is known about the effect of oil in the wormlike micellar solution in fluorinated surfactant system. Sharma and coworkers [63] have studied the phase behaviour and formation of self-assemblies in the ternary sytem of water/fluorinated surfactant ($C_8F_{17}EO_{10}$)/perfluoropolyether (PFE) oil $(C_3F_6O)_{21}COOH$. At low surfactant concentration, the transformation of the viscoelastic surfactant solution into a low viscosity Newtonian liquid with increasing solubilisation of polymeric oil is attributed to a rod-sphere transition. On the other hand, at high surfactant concentration, the phase sequence H_1–V_1–L'_α occurs by incorporating polymeric oil, which suggests that the curvature changes from positive to zero. As suggested by rheological measurements, worm-like micelles are present in $C_8F_{17}EO_{10}$ aqueous solutions but a rod-sphere transition takes place by solubilisation of PFE oil. The surfactant $C_8F_{17}EO_{10}$ acts as a structure directing agent for the preparation of hexagonal mesoporous silica by the precipitation method. The addition of PFE oil induces the formation of larger but disordered pores.

1.4 Context of study

1.4.1 Study of $R_7^F(EO)_8$-based system

The phase behaviour of a fluorinated surfactant $C_7F_{15}C_2H_4(EO)_8$ in water has been investigated since 2006 [91] (Figure I.13). They continued studying the relationship between the cloud point curve of fluorinated surfactant and the structures of mesoporous materials in the final products [9]. On their batch of $C_7F_{15}C_2H_4(EO)_8$ solution, the cloud point is situated at 19°C for 2 wt% of surfactant. Using this surfactant, mesoporous materials have been synthesized with micellar solution prepared either at 10°C (below the CP) or at 40 °C (above the CP). Results showed that whatever the syntheses conditions, only a wormhole-like structure is recovered, from this templating surfactant. They also noted an increase in the pore diameter when the temperature of the micellar solution preparation is increased or when the concentration of the surfactant is raised. The first tendency is the resulted of a variation of the aggregation number of micelles (L_1 phase). The second tendency can be explained by a change in the micelle shapes. CTM is not favoured if the cloud point is too low. They also noted an increase in the pore diameter when the temperature of the micellar solution preparation is increased or when the concentration of the surfactant is raised.

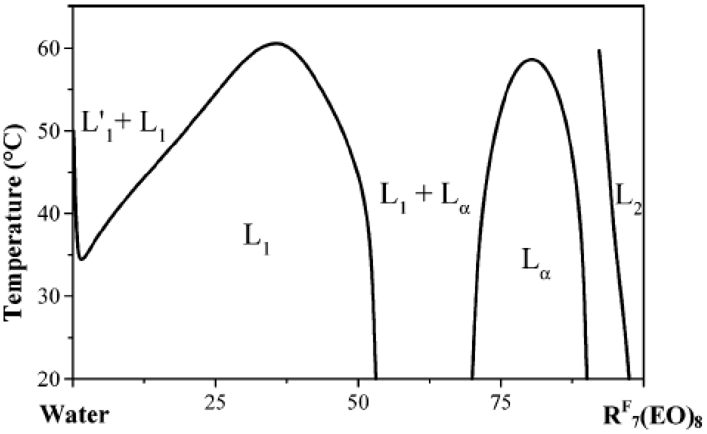

Figure I.13 Temperature-composition phase diagram of $C_7F_{15}C_2H_4(OC_2H_4)_8OH$, $R^F{}_7(EO)_8$ in water [91].

Based on the above system, they also focus on the relation between the position of the lower consolute boundary of various nonionic surfactants in water and the properties of the final products [92]. Depending on the features of the phase diagram, they looked for either a salting out or a salting in effect. For $C_7F_{15}C_2H_4(EO)_8$ surfactant/water system, the phase diagram presented a cloud point at 34°C and the addition of NaI shifted the lower consolute boundary toward higher temperatures (salting in effect). While only disordered mesostructured are recovered from the $C_7F_{15}C_2H_4(EO)_8$/water system, well-ordered mesostructure are synthesized from an aqueous solution of sodium iodide. However, the pore ordering was lost if the temperature at which the silica precursor was added was near the phase separation temperature.

1.4.2 Study of $R_8^F(EO)_9$-based system

The use of nonionic fluorinated surfactants in the preparation of ordered mesoporous molecular sieves are also reported by Stébé and coworkers in 2004 [93]. They investigated the phase behaviour of a fluorinated surfactant $[F(CF_2)_8C_2H_4(OC_2H_4)_9\text{-}OH]$, $R_8^F(EO)_9$ in water (as in Figure I.14) and synthesized the ordered mesoporous material via a CTM-type mechanism. The materials with a hexagonal channel array at 80°C were obtained in a wide range of nonionic fluorinated surfactant concentrations (5-20 wt %). However, decreasing the hydrothermal temperature or increasing the surfactant concentration leads to the formation of a wormhole-like mesostructure in the final product. At high temperature, the channel arrangement is governed by the surfactant behaviour in solution, whereas at lower temperature, the silica condensation and polymerization become the driving force. An increase in the pore diameter is noted with the rise in heating temperature. This phenomenon is the result of a change in aggregation number with temperature. A change in micelle shape is assumed to explain the variation of the pore diameter with surfactant concentration. The prepared materials exhibit higher degrees of organization and higher pore diameters, compared to analogous hydrogenated surfactants.

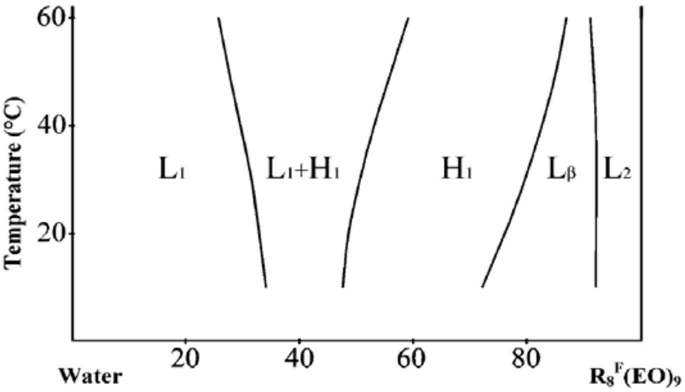

Figure I.14 Temperature-composition (wt%) phase diagram of $R_8^F(EO)_9$[93].

1.4.3 Objectives

According to the literature reviews above, we have investigated the thermodynamical structural parameters controlling the formation of micellar solution of nonionic fluorinated surfactant $R_7^F(EO)_8$ and $R_8^F(EO)_9$ in aqueous system. The influences of temperature, concentration of surfactant, salt addition have been studied under equilibrium and non-equilibrium conditions. As in previous works on preparation of mesoporous material in $R_7^F(EO)_8$-water system, we cannot obtain an ordered material unless shifting the miscibility curve by adding NaI salt addition. In order to understand this issue, we are focusing on a detailed study of the $R_7^F(EO)_8$ micellar phase by non-equilibrium techniques (rheology and rheo-optics). Thus, the influence of the distance to the miscibility curve on the rheophysical properties is also investigated by addition of NaI and NaCl in the $R_7^F(EO)_8$ and $R_8^F(EO)_9$-systems, respectively. Finally, we also shed light on the different behaviours between these two surfactant systems.

References

[1] C. T. Kresge, M. E. Leonowicz, W. J. Roth, J. C. Vartuli and J. S. Beck, *Nature* **1992**, *359*, 710-712.

[2] A. Rousset, *L'actualité chimique* **2005**, *288*, 15-25.

[3] F. Michaux in *Contribution des tensioactifs fluorés à la synthèse de matériaux mésoporeux. Application à la conception d'un bioréacteur., Ph.D thesis* Nancy Université, Nancy, **2009**.

[4] C. J. Brinker and G. W. Scherer, *The physics and chemistry of sol-gel processing.*, Academic Press, SanDiego, **1990**.

[5] Q. Huo, D. I. Margolese, U. Ciesla, P. Feng, T. E. Gier, P. Sieger, R. Leon, P. M. Petroff, F. Schuth and G. D. Stucky, *Nature* **1994**, *368*, 317-321.

[6] P. T. Tanev, M. Chibwe and T. J. Pinnavaia, *Nature* **1994**, *368*, 321-323.

[7] P. Kipkemboi, A. Fogden, V. Alfredsson and K. Flodstrom, *Langmuir* **2001**, *17*, 5398-5402.

[8] D. Zhao, Q. Huo, J. Feng, B. F. Chmelka and G. D. Stucky, *Journal of the American Chemical Society* **1998**, *120*, 6024-6036.

[9] J. L. Blin, R. Bleta and M. J. Stébé, *Journal of Colloid and Interface Science* **2006**, *300*, 765–773.

[10] J. L. Blin and M. J. Stébé, *The Journal of Physical Chemistry B* **2004**, *108*, 11399-11405.

[11] R. Bleta, J. L. Blin and M. J. Stebe, *The Journal of Physical Chemistry B* **2006**, *110*, 23547-23556.

[12] R. R. Klimpel, *Instructional module on introduction to chemicals used in particle systems*, NSF Engineering Research Center for Particle Science & Technology, Gainsville, FL, **1997**, p. 29.

[13] Bemi, G. M, Lawrence, J. C, Machin and D, *A review of the rheology of the lamellar phase in surfactant systems*, Elsevier, Amsterdam, PAYS-BAS, **2002**, p. 27.

[14] D. J. T. Mitchell, G. J. T., L. Waring, T. Bostock and M. P. McDonald, *Journal of the. Chemical Society-Faraday Transactions I* **1983**, *79*, 975-1000.

[15] W. C. Griffin, *Journal of the Society of Cosmetic Chemists 1*, 311-326.

[16] J. S. Sjöblom, P.; Danielsson, I. In Nonionic Surfactant Physical Chemistry, *Nonionic Surfactant Physical Chemistry*, M. Dekker, New York, **1987**, p. 369.

[17] W. N. J. Maclay, *Journal of Colloid Science* **1956**, *11*, 272-285.

[18] K. Tasaki, *Journal of the American Chemical Society* **1996**, *118*, 8459-8469.

[19] J. N. Israelachvili and *Intermolecular and surface forces*, Academic Press, London, **1991**, p. 450.

[20] J. N. Israelachvili, D. J. Mitchell and B. W. Ninham, *Journal of the Chemical Society, Faraday Transactions 2: Molecular and Chemical Physics* **1976**, *72*, 1525-1568.

[21] C. Tanford in *The Hydrophobic Effect: Formation of Micelles and Biological Membranes*, *Vol.* John Wiley & Sons, New York, **1980**.

[22] A. Herb Craig, B. Chen Liang and M. Sun Wei, *Structure and Flow in Surfactant Solutions* **1994**, *578*, 153-166.

[23] J. E. R. V. Chiola, C.D. Vanderpool, US Patent No. 3 556 725, **1971**.

[24] T. Yanagisawa, T. Shimizu, K. Kuroda and C. Kato, *Bulletin of the Chemical Society of Japan* **1990**, *63*, 988-992.

[25] P. D. I. Fletcher in *Specialist Surfactants*, (Ed. I. D. Robb), Blackie Academic and Professional, London, **1997**, p. 104.

[26] J. C. Ravey and M. J. Stébé, *Colloids and Surfaces A: Physicochemical and Engineering Aspects* **1994**, *84*, 11-31.

[27] I. M. o. S. a. Terminology, *Pure appl. Chem.* **1972**, *31*, 578.

[28] U. Ciesla and F. Schüth, *Microporous and Mesoporous Materials* **1999**, *27*, 131-149.

[29] X. S. Zhao, G. Q. Lu and G. J. Millar, *Industrial & Engineering Chemistry Research* **1996**, *35*, 2075-2090.

[30] J. Y. Ying, C. P. Mehnert and M. S. Wong, *Angewandte Chemie International Edition* **1999**, *38*, 56-77.

[31] A. Corma, *Chemical Reviews* **1997**, *97*, 2373-2420.

[32] J. C. Vartuli, C. T. Kresge, W. J. Roth, S. B. McCullen, J. S. Beck, K. D. Schmitt, M. E. Leonowicz, J. D. Lutner and E. W. Sheppard, *Advanced Catalysts and Nanostructured Materials: Modern Synthesis Methods*, Academic Press, New York, **1996**, p. 1-19.

[33] J. S. Beck and J. C. Vartuli, *Current Opinion in Solid State and Materials Science* **1996**, *1*, 76-87.

[34] J. L. Blin, A. Léonard and B. L. Su, *The Journal of Physical Chemistry B* **2001**, *105*, 6070-6079.

[35] N. R. B. Coleman and G. S. Attard, *Microporous and Mesoporous Materials* **2001**, *44-45*, 73-80.

[36] E. P. Barrett, L. G. Joyner and P. P. Halenda, *Journal of the American Chemical Society* **1951**, *73*, 373-380.

[37] A. E. C. Palmqvist, *Current Opinion in Colloid & Interface Science* **2003**, *8*, 145-155.

[38] A. Firouzi, D. Kumar, L. M. Bull, T. Besier, P. Sieger, Q. Huo, S. A. Walker, J. A. Zasadzinski, C. Glinka, J. Nicol and a. et, *Science* **1995**, *267*, 1138-1143.

[39] Y. S. Lee, D. Surjadi and J. F. Rathman, *Langmuir* **1996**, *12*, 6202-6210.

[40] Y. Wan and D. Zhao, *Chemical Reviews* **2007**, *107*, 2821-2860.

[41] X.-B. Lu, W.-H. Zhang, J.-H. Xiu, R. He, L.-G. Chen and X. Li, *Industrial & Engineering Chemistry Research* **2003**, *42*, 653-656.

[42] O. Regev, *Langmuir* **1996**, *12*, 4940-4944.

[43] S. F. Monnier A., Huo Q., Kumar D., Margolese D., Maxwell R.S., Stucky G.D., Krishnamurty M., Petroff P., Firouzi A., Janicke M., Chmelka B.F., *Science* **1993**, *261*, 1299-1303.

[44] U. Ciesla, D. Demuth, R. Leon, P. Petroff, G. Stucky, K. Unger and F. Schuth, *Journal of the Chemical Society, Chemical Communications* **1994**, 1387-1388.

[45] P. T. Tanev and T. J. Pinnavaia, *Science* **1995**, *267*, 865-867.

[46] S. A. Bagshaw, E. Prouzet and T. J. Pinnavaia, *Science* **1995**, *269*, 1242-1244.

[47] G. D. Stucky, A. Monnier, F. Schuth, Q. Huo, D. Margolese, D. Kumar, M. Krishnamurty, P. Petroff, A. Firouzi, M. Janicke and B. F. Chmelka, *Molecular Crystals and Liquid Crystals Science and Technology. Section A. Molecular Crystals and Liquid Crystals* **1994**, *240*, 187 - 200.

[48] J. C. Vartuli, K. D. Schmitt, C. T. Kresge, W. J. Roth, M. E. Leonowicz, S. B. McCullen, S. D. Hellring, J. S. Beck and J. L. Schlenker, *Chemistry of Materials* **1994**, *6*, 2317-2326.

[49] M. Kruk, M. Jaroniec, C. H. Ko and R. Ryoo, *Chemistry of Materials* **2000**, *12*, 1961-1968.

[50] S. Ruthstein, V. Frydman, S. Kababya, M. Landau and D. Goldfarb, *The Journal of Physical Chemistry B* **2003**, *107*, 1739-1748.

[51] G. S. Attard, J. C. Glyde and C. G. Goltner, *Nature* **1995**, *378*, 366-368.

[52] E. Prouzet and T. J. Pinnavaia in *Assembly of mesoporous molecular sieves containing wormhole motifs by a nonionic surfactant pathway: control of pore size by synthesis temperature*, Angew Chem Int Ed. 36 **1997**, p. 516-518.

[53] E. Kissa, *Fluorinated Surfactants Synthesis properties Applications*, Dekker, New York, **1994**.

[54] K. Shinoda, M. Hato and T. Hayashi, *The Journal of Physical Chemistry* **1972**, *76*, 909-914.

[55] H. Hoffmann, J. Ravey and M. Stébé in *Phase and structure behaviour of fluorinated nonionic surfactant systems*, *Vol. 73* Springer Berlin / Heidelberg, **1987**, p. 127-133.

[56] M. Monduzzi, *Current Opinion in Colloid & Interface Science* **1998**, *3*, 467-477.

[57] J. C. S. Ravey, M. J.; Oberthür R. , *In Surfactant in solution; Mittal, K. L., Bothorel, P Vol. 6, p 1421.*, Plenum, New York, **1987**.

[58] G. Mathis, P. Leempoel, J. C. Ravey, C. Selve and J. J. Delpuech, *Journal of the American Chemical Society* **1984**, *106*, 6162-6171.

[59] J. G. Riess, *Chemical Reviews* **2001**, *101*, 2797-2920.

[60] M. H. A. Hamza, G. Serratrice, M. J. Stébé and J. J. Delpuech, *Journal of the American Chemical Society* **1981**, *103*, 3733-3738.

[61] C. El Moujahid, J. C. Ravey, V. Schmitt and M. J. Stébé, *Colloids and Surfaces A: Physicochemical and Engineering Aspects* **1998**, *136*, 289-297.

[62] J. Esquena, C. Rodríguez, C. Solans and H. Kunieda, *Microporous and Mesoporous Materials* **2006**, *92*, 212-219.

[63] K. S. Sharma, S. R. Patil and A. K. Rakshit, *Colloids and Surfaces A: Physicochemical and Engineering Aspects* **2003**, *219*, 67-74.

[64] D. P. Acharya, S. C. Sharma, C. Rodriguez-Abreu and K. Aramaki, *The Journal of Physical Chemistry B* **2006**, *110*, 20224-20234.

[65] C. Rodríguez-Abreu, P. M. Botta, J. Rivas, K. Aramaki and M. A. L. Quintela, *Colloids and Surfaces A: Physicochemical and Engineering Aspects* **2007**, *298*, 284-286.

[66] C. Rodríguez-Abreu, P. M. Botta, J. Rivas, K. Aramaki and M. A. López Quintela, *Journal of Non-Crystalline Solids* **2008**, *354*, 1074-1079.

[67] R. G. Shrestha, L. K. Shrestha, S. C. Sharma and K. Aramaki, *The Journal of Physical Chemistry B* **2008**, *112*, 10520-10527.

[68] J. L. Blin and M. J. Stébé, *Microporous and Mesoporous Materials* **2005**, *87*, 67-76.

[69] L. K. Shrestha, S. C. Sharma, T. Sato, O. Glatter and K. Aramaki, *Journal of Colloid and Interface Science* **2007** *316*, 815–824.

[70] S. C. Sharma, R. G. Shrestha, L. K. Shrestha and K. Aramaki, *The Journal of Physical Chemistry B* **2009**, *113*, 1615-1622.

[71] R. Kjellander, *Journal of the Chemical Society, Faraday Transactions 2: Molecular and Chemical Physics* **1982**, *78*, 2025-2042.

[72] G. Karlstroem, A. Carlsson and B. Lindman, *The Journal of Physical Chemistry* **1990**, *94*, 5005-5015.

[73] G. Karlstroem, *The Journal of Physical Chemistry* **1985**, *89*, 4962-4964.

[74] T. Inoue, H. Ohmura and D. Murata, *Journal of Colloid and Interface Science* **2003**, *258*, 374-382.

[75] C. Jin-Ling and M. Jian-Hai, *Colloid Journal* **2002**, *64*, 550-555.

[76] H. Schott, *Journal of Colloid and Interface Science* **1997**, *189*, 117-122.

[77] K. Weckström and M. Zulauf, *Journal of the Chemical Society, Faraday Transactions 1: Physical Chemistry in Condensed Phases* **1985**, *81*, 2947-2958.

[78] K. Weckström and A. C. Papageorgiou, *Journal of Colloid and Interface Science* **2007**, *310*, 151-162.

[79] R. Ganguly, M. Kumbhakar and V. K. Aswal, *The Journal of Physical Chemistry B* **2009**, *113*, 9441-9446.

[80] K. Zimny, J. L. Blin and M. J. Stébé, *Journal of Colloid and Interface Science* **2009**, *330*, 456-462.

[81] M. E. Cates, *Macromolecules* **1987**, *20*, 2289-2296.

[82] M. E. Cates, T. C. B. McLeish and G. Marrucci, *EPL (Europhysics Letters)* **1993**, *21*, 451.

[83] M. E. Cates, *The Journal of Physical Chemistry* **1990**, *94*, 371-375.

[84] N. A. Spenley, M. E. Cates and T. C. B. McLeish, *Physical Review Letters* **1993**, *71*, 939-942.

[85] M. Doi and S. F. Edwards, *Journal of the Chemical Society, Faraday Transactions 2: Molecular and Chemical Physics* **1978**, *74*, 560-570.

[86] M. Doi and S. F. Edwards, *Journal of the Chemical Society, Faraday Transactions 2: Molecular and Chemical Physics* **1978**, *74*, 918-932.

[87] M. Doi and S. F. Edwards, *Journal of the Chemical Society, Faraday Transactions 2: Molecular and Chemical Physics* **1979**, *75*, 38-54.

[88] H. Rehage and H. Hoffmann, *Molecular Physics* **1991**, *74*, 933-973.

[89] C. Oelschlaeger, G. Waton, E. Buhler, S. J. Candau and M. E. Cates, *Langmuir* **2002**, *8*, 076-3085

[90] S. C. Sharma, C. Rodriguez, L. K. Shrestha and K. Aramaki, *J. Col. Int. Sci.* **2007**, *314*, 223-229.

[91] J. L. Blin, R. Bleta, J. Ghanbaja and M. J. Stébé, *Microporous and Mesoporous Materials* **2006**, *94*, 74-80.

[92] F. Michaux, J. L. Blin and M. J. Stébé, *Langmuir* **2008**, *24*, 1044-1052.

[93] J. L. Blin, P. Lesieur and M. J. Stébé, *Langmuir* **2004**, *20*, 491-498.

Chapitre II.

Méthodes expérimentales et tensioactifs

Le second chapitre comporte deux parties principales : la première est dédiée à la présentation des tensioactifs fluorés et à la méthode de préparation des solutions et la seconde est consacrée à la description des techniques expérimentales employées au cours de ce travail à savoir : rhéométrie, microscopie en lumière polarisée, biréfringence d'écoulement et diffusion de neutrons aux petits angles.

2.1 Les tensioactifs

Deux tensioactifs fluorés fournis par la société DuPont sont utilisés sans purification supplémentaire au cours de ce travail. Leurs caractéristiques sont résumées dans le tableau II.1.

Table II.1 Caractéristiques physiques des tensioactifs fluorés.

Label	Formula	ρ $(g.ml^{-1})$*	M $(g.mol^{-1})$	Vmol $(cm^3.mol^{-1})$
$R_7^F(EO)_8$	$C_7F_{15}C_2H_4(OC_2H_4)_8OH$	1.35	744	551
$R_8^F(EO)_9$	$C_8F_{17}C_2H_4(OC_2H_4)_9OH$	1.39	870	626

* La densité est donnée à 20°C

La longueur des chaines hydrophiles (EO) et hydrophobes (R) n'est pas fixe mais suit une distribution gaussienne avec une moyenne de 8 et 9 pour les groupes oxyethylene ($-OC_2H_4$) et 7 et 8 pour les chaines fluorées. Pour la suite, on utilisera la notation simplifiée $R_7^F(EO)_8$ et $R_8^F(EO)_9$ pour designer les deux tensioactifs.

Le diagramme de phase des systèmes binaires tensioactif/H_2O est établi par observation directe d'une série d'échantillons en lumière polarisée à l'aide d'un microscope.

2.2 Techniques expérimentales

2.2.1 Rhéologie

Les mesures rhéologiques ont été réalisées à l'aide de deux appareils permettant de réaliser des écoulements permanents et dynamiques. Il s'agit du RFS III de TA Instruments fonctionnant à déformation imposée et du Physica MCR 501 de Anton Paar opéré en déformation ou contrainte imposées RFS III géométrie du cône : diamètre = 50 mm, angle = 0.02 rad et gap = 50 µm

- Physica MCR 501 géométrie du cône : diamètre = 50 mm, angle = 1° et gap = 103 µm
- Physica MCR 501 géométrie de Couette : diamètre intérieur= 26.5 mm diamètre extérieur = 29 mm et gap = 1.25mm

Afin de caractériser leurs propriétés viscoélastiques, les échantillons sont soumis à plusieurs types d'écoulement de cisaillement : balayage en taux de cisaillement constants, sollicitations dynamiques dans le domaine linéaire et cycles de contrainte. On obtient ainsi les différents rhéogrammes, les modules *G*' et *G*'' ainsi que l'évolution de la viscosité apparente en fonction du temps.

2.2.2 Microscopie en lumière polarisée

L'échantillon est placé entre polariseurs linéaires croisés, l'observation est visuelle. Une phase isotrope ne modifie pas la polarisation de la lumière transmise, le champ d'observation reste noir, l'extinction est conservée ; par contre une phase anisotrope transmets une lumière elliptique qui rétablit l'éclairement. On peut ainsi mettre en évidence l'apparition de phases optiquement anisotrope au repos.

2.2.3 Biréfringence d'écoulement

Sous l'action d'un gradient de cisaillement, les solutions de particules asymétriques peuvent devenir optiquement anisotropes. Elles présentent de la biréfringence d'écoulement caractérisée quantitativement par une orientation moyenne définie par l'angle d'extinction χ

et par l'intensité de la biréfringence Δn différence entre deux indices principaux de réfraction.

La solution à étudier est cisaillée en cellule de Couette placée entre polariseurs croisés. L'extinction est rompue sous écoulement ; χ et la différence de phase induite δ sont déduits de l'analyse des deux signaux par une méthode de zéro (méthode de Sénarmont):

$$I_\alpha = I_0 \sin^2 \frac{\phi}{2} \sin^2 2(\chi - \alpha)$$

et

$$I = \frac{I_0}{4}\left[1 - \cos(2\phi - \delta)\right]$$

L'extinction est rétablie en tournant l'analyseur d'un angle α ou ϕ. Les signaux I_α et I sont alors annulés et on trouve ainsi $\chi = \alpha$ et $\delta = 2\phi$.

2.2.4 Diffusion de neutrons

Les expériences de diffusion de neutrons ont été effectuées dur la ligne D11 de l'Institut Laue Langevin de Grenoble. Elles n'ont pu être réalisées que sur une partie des systèmes étudiés par les autres techniques par suite d'une allocation de temps de faisceau trop courte.

L'échantillon est soumis au flux de neutrons dans un dispositif de Couette en quartz de diamètres extérieur et intérieur égaux à 50 et 48 mm. Le dispositif de cisaillement est contrôlé par un rhéomètre Bohlin (CV0120) fonctionnant à déformation imposée. Rhéologie et diffusion peuvent ainsi se dérouler simultanément.

La longueur d'onde des neutrons est de 6 Å avec une résolution de 10%. Les données brutes sont recueillies sur un détecteur bidimensionnel de 100x100cm avec une résolution de 128 points dans chaque direction. Deux distances d'acquisition ont été choisies : 2.5 et 8m permettant ainsi au vecteur d'onde de couvrir l'intervalle [$8.84\times10^{-3} - 2.71\times10^{-1}$ Å^{-1}].

Les données brutes recueillies sur le détecteur sont corrigées à l'aide des logiciels de l'ILL avant le tracé des courbes d'intensité et l'analyse des résultats.

Chapter II. Materials and experimental methods

This chapter is dedicated to the presentation of the materials and of the experimental techniques used to study the physical characteristics of fluorinated micellar systems. In the first part, we shall describe the fluorinated surfactants and the way to prepare the solutions used for the determination of the phase diagram. The second part is dedicated to the different experimental techniques used in this work: rheometry, polarizing microscopy, flow birefringence and small angle neutron scattering.

2.1 Materials: the surfactant solutions

The nonionic surfactants studied in this work are supplied by the company DuPont and are used without any further purification. The hydrophilic part consists of a series of oxyethylene groups ($-OC_2H_4-$) while the hydrophobic part is a linear fluorinated alkyl chain. Table II-1 shows their physico-chemical characteristics. In the case of fluorinated surfactant, the presence of a spacer making the link between the hydrophilic and hydrophobic part is necessary. This spacer may consist of one or several methylene groups or functional groups. For the surfactants studied in this work, the spacer consists of two methylene groups.

Table II.1 Physical- data of the fluorinated surfactants.

Label	Formula	Density, ρ (g.ml^{-1})*	Mass, M (g.mol^{-1})	Molar volume, V_{mol} (cm^3.mol^{-1})
$R_7^F(EO)_8$	$C_7F_{15}C_2H_4(OC_2H_4)_8OH$	1.35	744	551
$R_8^F(EO)_9$	$C_8F_{17}C_2H_4(OC_2H_4)_9OH$	1.39	870	626

* The density is given at 20°C

Concerning the hydrophilic chain moiety, it has a Gaussian chain length distribution. Thus, the subscript (8 or 9) of the formula corresponds to an average value of the number of the oxyethylene groups (-OC_2H_4-). The hydrophobic part also has different chain lengths and the distribution of the number-average molecular weight allows us to calculate the average length of the hydrophobic chains. It turns out that the average number of fluorinated carbon is 7 for $R_7^F(EO)_8$ and 8 for $R_8^F(EO)_9$. Although the raw material is a mixture of several chain lengths, in the following we shall use the simple designation $R_7^F(EO)_8$ and $R_8^F(EO)_9$ to represent these molecules.

For the preparation of a series of samples at different concentrations, the necessary amounts of surfactant are carefully weighed (± 0.01g) and then dissolved in the required amount of water or salt solution under magnetic stirring. The solutions are then stored at room temperature for several days in well-closed glass vials to avoid evaporation and to reach the thermodynamic equilibrium prior to any measurement.

The phase diagrams of the surfactant/water binary systems are established by direct visual observation with a polarizing microscope of a series of samples prepared in the concentration range 0.5-50 wt % for the surfactant $R_7^F(EO)_8$ in water and in NaI aqueous solutions (0.5 and 1 M) as described in F. Michaux thesis [1]. For $R_8^F(EO)_9$ in water or in NaCl aqueous solutions (1.5 and 3 M), a series of samples in the range of 0.5-30 wt% were prepared and the phase diagrams also established in the same way.

Before each observation, the sample is left at rest during 20 minutes at least in a water bath at each controlled temperature. The different phases were merely identified by visual observation between crossed linear polarizers in natural white light. Each sample is characterized by the number of phases present in the vessel, their optical characteristic (isotropic or anisotropic) and appreciating qualitatively its viscosity. The temperature at which the surfactant solutions turned opaque is observed visually in order to plot the lower consolute boundary (phase separation). The liquid crystalline phase domains are subsequently identified by direct observation of the texture under an optical microscope equipped with crossed polarizers.

Although the phase diagram of various surfactant/water or surfactant/water/salt solutions are already reported, we found it necessary to check it again since the samples were prepared with a different new batch of the surfactant.

2.2 Rheometry

Rheometry is the experimental technique used to study the rheological properties of matter. Rheology is the "science of deformation and flow of matter" and aim at describing the way in which materials respond to applied stresses or strains. It was introduced by Bingham in 1920 to name the new scientific developments trying to explain the behaviour of viscoelastic matter.

Complex fluids show mechanical properties which are intermediate between those of ordinary viscous fluids and simple elastic solids; they often have long structural or molecular relaxation times [2]. Depending on the time evolution of their characteristics, they can be described by a large variety of models (see Figure II.1).

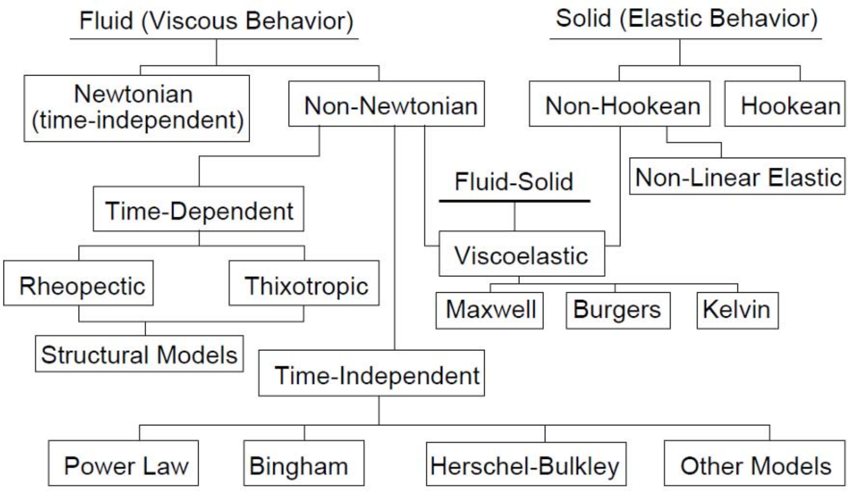
Fluid (Viscous Behavior)
Solid (Elastic Behavior)
Newtonian (time-independent)
Non-Newtonian
Non-Hookean
Hookean
Non-Linear Elastic
Fluid-Solid
Time-Dependent
Viscoelastic
Rheopectic
Thixotropic
Maxwell
Burgers
Kelvin
Structural Models
Time-Independent
Power Law
Bingham
Herschel-Bulkley
Other Models

Figure II.1 Simple classification of rheological behaviours [3]

Rheological measurements are performed on rheometers, apparatus designed to subject the sample to different kinds of solicitations (steady or time dependent). The collected data are then used to draw the rheogram $\sigma(\dot{\gamma})$ or the viscosity curve $\eta(\dot{\gamma})$. In this study, the experiments are performed in shearing devices of the rotational type which can be operated either in stress or strain controlled mode.

2.2.1 Rotational rheometer and shearing cells

The test fluid is sheared between two surfaces, one is usually fixed while the second is rotated under stress or strain controlled conditions. The velocity gradient in the sample is related to the dimensions of the cell and to the angular velocity of the moving plate. The three principal and mostly used shearing cells are sketched in figure II.2: (a) the Couette cell built with coaxial cylinders, (b) cone-plate, (c) parallel plates (See Figure II.2).

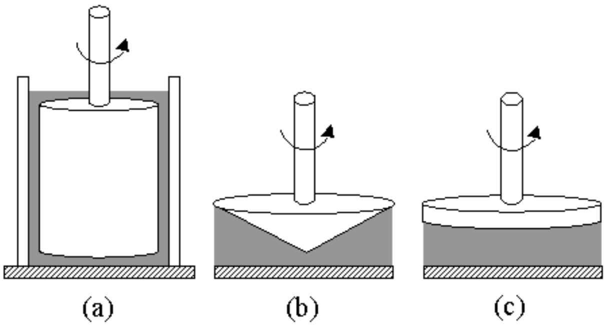

Figure II.2 Schematic diagram of basic tools for the rotational rheometer: (a) coaxial cylinders, (b) cone-plate, (c) parallel plates

Due to its large surface in contact with fluid, the Couette cell is the most widely used system when working with low viscosity samples.

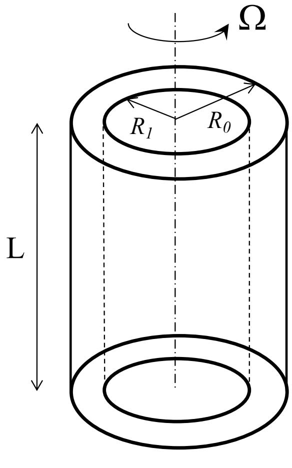

Figure II.3 Schematic view of a concentric cylinder rheometer [4].

The shear stress and the shear rate are not exactly constant in the annular gap of the device. However, in the small gap and curvature approximation, the stress and velocity gradient will only depend on the geometrical dimensions of the cylinders. In that case:

$$\sigma = \frac{M}{4\pi L}\frac{R_0^2 + R_1^2}{R_0^2 R_1^2} \qquad \text{(equation II.1)}$$

where M is the applied torque, L the length of the cylinder and R_0 and R_1 the radii of the cylinders and the shear rate:

$$\dot{\gamma} = \frac{R_1 \Omega}{e} \qquad \text{(equation II.2)}$$

With Ω the macroscopic angular velocity i.e. the velocity imposed by the device and $e = R_0 - R_1$, the width of the annular space containing the fluid usually called the gap.

The cone and plate geometry is most of the time used for highly viscous and concentrated fluids. It is composed of an inverted cone and a fixed flat plate. Either the upper or lower surface may rotate depending on the instrument design. The tested fluid is constrained in the narrow gap between the two surfaces. The cone is usually designed with an angle of less than 4°.

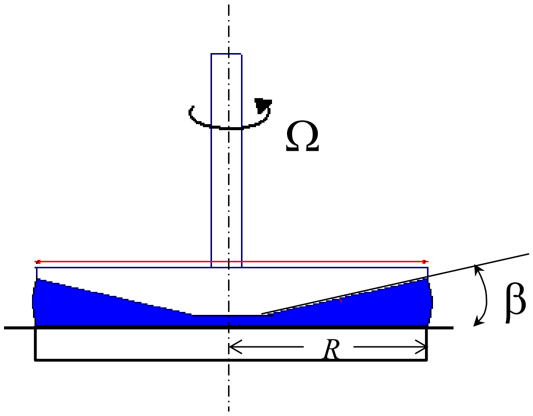

Figure II.4 Cone and plane rheometer

In this geometry, the shear stress and shear rate are very nearly constant in the whole gap.

In the ideal cell, we get $\sigma = \frac{3M}{2\pi R^3}$ and $\dot{\gamma} = \frac{\Omega}{\beta}$. (equation II.3 and II.4)

The rheometers operating the shearing devices are of two kinds: RFS 3 (TA Instruments) and the Physica MCR 501 (Anton Paar). With both apparatus, the temperature of the sample is kept constant within ± 0.05 °C with a circulating bath or a Peltier regulator; a solvent trap is used to minimize the evaporation.

- RFS 3 (TA Instruments) working in strain controlled mode. The measurements are conducted in a cone-plate cell (cone diameter = 50 mm, cone angle = 0.02 rad and a gap = 50 μm)

RFS3
Rheometric Scientific

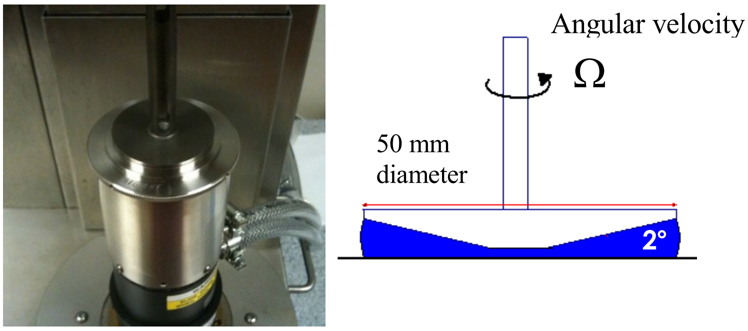

Figure II.5 Rheometer RFS 3 (TA Instruments) with cone and plate geometry

- Physica MCR 501 (Anton Paar): working either in stress or strain controlled mode. The MCR is well-suited to perform measurements at very low deformation rates, which are typically required in our experiments. It was used to study the steady and dynamic properties of the various samples. The MCR can access steady shear rates as low as 10^{-6} s^{-1} and as high as 10^{3} s^{-1} and conduct dynamic oscillatory measurements as low as 10^{-4} rad/s. Both cone-and-plate (cone diameter = 50 mm, cone angle = 1° and gap = 103 μm) and Couette geometries were used, and temperature control can be achieved with a circulating water bath, or a Peltier regulator.

Anton Paar
Physica

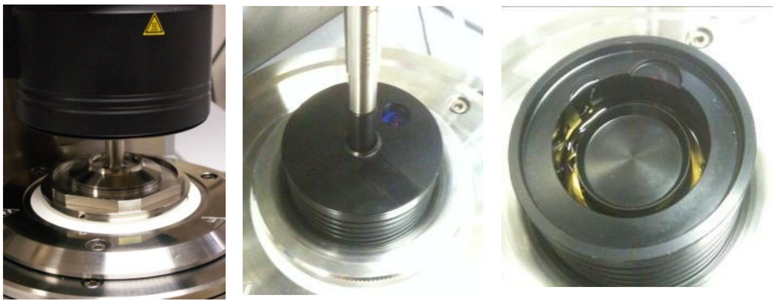

Figure II.6 Rheometer Physica MCR 501 (Anton Paar) with cone-plate and Couette geometries

2.2.2 Flow experiments

The samples were subjected to two kinds of flows in order to characterize their viscoelastic properties: steady state shear rate sweep and dynamic oscillations in the linear regime.

Measurements in steady-state conditions.

During a steady state test, the sample is subjected to a series of increasing values of the shear rate $\dot{\gamma}$ (in strain controlled mode) or of the shear stress σ (in stress controlled experiments) for a finite time interval (usually 60 to 120s). Once the steady state is reached, the ratio $\eta = \sigma / \dot{\gamma}$ leads to the apparent viscosity. From these results, the viscosity curve $\eta(\dot{\gamma})$ or the flow curve $\sigma(\dot{\gamma})$ are drawn and the rheological characteristics of the sample deduced.

Stress cycles

Stress cycles were also applied to the samples in order to follow the time variation of the viscosity under a constant stress. These cycles consist of a decreasing stress branch starting at a maximum value σ_{M} down to a minimum σ_{m}, followed by a constant stress at σ_{m} with recording of the viscosity as a function of time . Finally during the last branch, the stress is increased again up to σ_{M}. This last stress sweep allows checking for the importance of the evaporation.

2.2.3 Zero shear viscosity measurement

The zero shear viscosities are measured as a function of the mass fraction of surfactant ϕ_{mass} for the temperatures of 10 and 20°C. The values can be extrapolated from the non linear rheological measurements, or from the real part of the complex viscosities $\eta' = G''/ \omega$ at $\omega = 0$ in the linear measurements.

To complete the measurements at low concentration, we measured the viscosity of the sample for mass fractions ϕ_{mass} less than 5 wt% with capillary viscometers. The capillary viscometers of Ubbeohlde type of internal diameters 0.36, 0.58 and 0.77 mm are used to cover the range of explored viscosities. The viscometer is immersed in a water bath stabilised at the desired temperature (±0.2°C). The viscosity of the surfactant solution is then given by measuring the flow time of pure water (t_w) and the flow time of the solution (t_s) between two points of the tube at the same temperature. t_s and t_w were determined with an uncertainty of the order of 0.5 s. The flow time t_s is proportional to the kinematic viscosity of the solution $\nu = \eta / \rho$ (where ρ is the density of the fluid) with a constant of proportionality intrinsic to the viscometer, which is determined by measuring the flow time t_w of pure water. Assuming that the surfactant solution has the same density as pure water (a reasonable assumption since we work at low concentration) we have $t_w / t_s = \eta_w / \eta_s$ which gives $\eta_s = \eta_w . t_s / t_w$, where η_s and η_w are the viscosities of the surfactant solution and water, respectively.

2.2.4 Dynamic viscoelastic measurement

The experiments performed in dynamical mode by subjecting the sample to sinusoidal oscillations allow the study of the linear viscoelastic behaviour of the sample (if the sinusoidal strain is small) and to characterize its intrinsic properties i.e. its moduli G', G'' and , τ_R relaxation time.

A sinusoidal time dependent strain, γ , is applied to the sample:

$$\gamma = \gamma_0 \sin \omega t \qquad \text{(equation II.6)}$$

In the linear domain, the response of the solution to this strain is also a sinusoidal function of time with the same frequency but out of phase by the angle δ.

$$\sigma = \sigma_0 \sin(\omega t + \delta) = \sigma_0 \cos\delta \sin\omega t + \sigma_0 \sin\delta \cos\omega t \qquad \text{(equation II.7)}$$

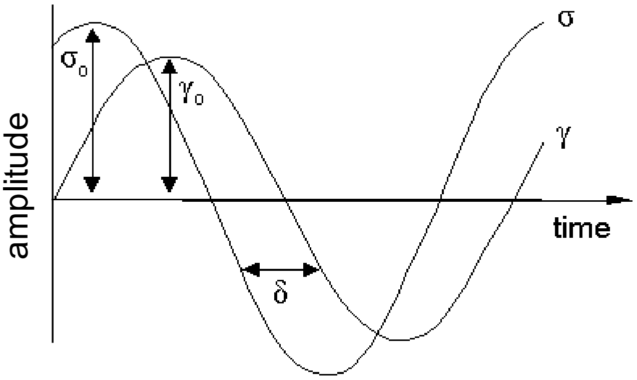

Figure II.7 Sinusoidal wave forms for stress and strain functions

This behaviour is intermediate between an ideally elastic material and a true Newtonian liquid where the stress is respectively in phase [5] and 90° out of phase with the strain.

Dividing the two time-independent coefficients of the stress by the strain amplitude γ_0, defines two dynamic moduli G' and G'':

$$G' = \frac{\sigma_0}{\gamma_0}\cos\delta \text{ and } G'' = \frac{\sigma_0}{\gamma_0}\sin\delta \qquad \text{(equation II.8)}$$

G' is the storage modulus in phase with the strain. It represents the elastic component of the system. G'' is the loss modulus, 90° out of phase with γ. It corresponds to the viscous character of the sample and is proportional to the energy dissipated.

G' is proportional to the energy stored during deformation. On a molecular basis, the magnitude of G' is dependent upon what rearrangements can take place within the period of oscillation [6] and is regarded as an indication of the solid or elastic character of the material.

The loss modulus (G'') is a measure of the energy dissipated or lost (as heat) per cycle of a sinusoidal deformation. It is, therefore, taken as an indication of the liquid or viscous behaviour of the medium.

Another parameter which is often useful in indicating the physical behaviour of a system is the loss tangent ($\tan\delta = G''/G'$). It represents the ratio of the energy lost to the energy stored for each cycle of the deformation. This ratio is a useful indicator of the relative contribution of the viscous (G'') and elastic (G') components to the viscoelastic properties of a material. The logarithmic plot of the loss tangent gives rise to several characteristics. If $\tan\delta$ is high (>> 1), these materials behaves rather like viscous fluids, but when $\tan\delta$ is low (<< 1), the materials have a solid-like behaviour.

The Maxwellian fluid model is often used to interpret data from dynamic testing of polymeric liquids. If the strain input is harmonic, solving Maxwell's constitutive equation will lead to:

$$G' = G_0\frac{\omega^2\tau_R^2}{1+\omega^2\tau_R^2} \text{ and } G'' = G_0\frac{\omega\tau_R}{1+\omega^2\tau_R^2} \qquad \text{(equation II.8 and II.9)}$$

$\tau_R = \eta_0 / G_0$ is the relaxation time (also called the characteristic time) of the Maxwellian fluid.

Eliminating the angular frequency in G' and G'', one gets the equation of a circle:

$$G''^2 + G'^2 = \frac{G_0^2}{4} \qquad \text{(equation II.10)}$$

This simple result will be used to check the Maxwellian character of the fluorinated surfactant solutions studied.

Like every experimental measurements, stress or strain experiments are always subjected to errors due to various reasons. In order to minimize their importance, a flow experiment is always repeated at least three times and the results too far from an average behaviour are systematically discarded.

2.3 Polarized light microscopy

A polarizing microscope is equipped with two linear polarizers free to rotate about the microscope axis, the directions of polarization of which can thus be set perpendicular. In that case, an isotropic sample placed between the two polarizers will not change the incident polarization (see Figure II.8 top line) and the field of observation will remain black. On the other hand, for light travelling through an anisotropic sample, the incident polarization will usually change from linear to elliptical and the field of observation will again appear clear (bottom diagram in Figure II.8).

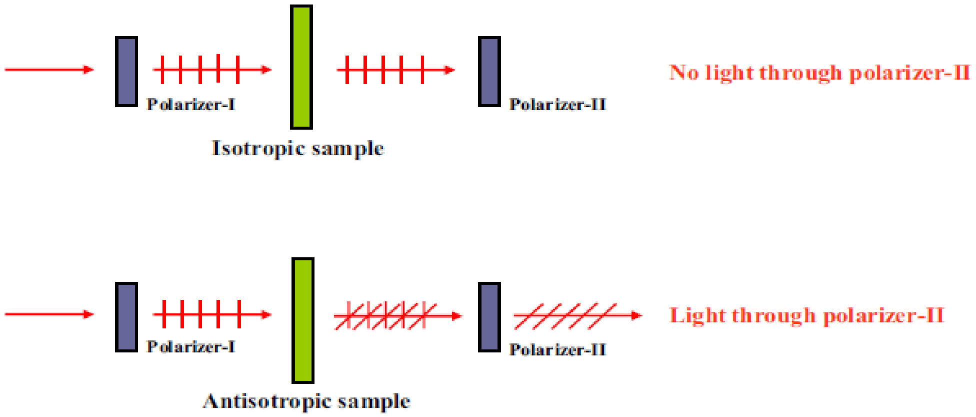

Figure II.8 Optical properties of isotropic and anisotropic materials under polarized light.

Thus, optical anisotropy or birefringence of a sample can easily be checked with this simple technique. Liquid crystal phases placed between crossed polarizing filters also reveal their characteristic birefringent textures because of defects in the liquid crystal phases; the liquid properties of these compounds lead to stacking faults at regular intervals on a micrometer scale and pattern typical of these crystal phases appear in the microscope field.

2.4 Flow birefringence

Under the action of orientating shearing flows, solutions of non symmetrical particles often become birefringent. This phenomenon is called “flow birefringence” and include intrinsic and shape birefringence. The first kind of anisotropy is related to the intrinsic optical anisotropy of the particles (here the micelles) while the second is due to the difference of the refraction index of the particle and the solvent. In this work, we are only concerned with the first kind of birefringence.

Flow birefringence results from the orientation of particles under flow. This is the case with surfactant solutions which can form micelles which are easily orientated in the hydrodynamical field. From an optical point of view, the solution is then equivalent to a biaxial crystal with three principal refraction indices. Two quantities of interest characterize a birefringent material: the angle of extinction χ and the birefringence intensity $\Delta n = n_1 - n_2$. The angle of extinction or orientation angle quantifies the average orientation of the particles and the birefringence intensity, the difference of two of the three principal refraction indexes. These two quantities are deduced from measurements performed on a polarimetric bench.

2.4.1 The polarimetric bench

The polarimetric bench used for flow birefringence experiments was designed in our laboratory [7] and is shown schematically in Figure II.9. In all the experiments, a linearly polarized light beam (a laser beam at 6328 Å for the quantitative measurements) propagates along the vorticity axis ($\vec{\omega}$), probing the birefringence in the $(\vec{v}, \nabla\vec{v})$ plane.

The beam of a He-Ne laser (λ = 6328 Å) passes successively through a hole D_1, a total reflection prism P_1, and a second diaphragm D_2 a lens L_1; a polarizer P defines the polarization state of the incident light beam before it crosses the sample. At the exit of the Couette cell, the polarization state of the beam emerging from the flowing medium is analyzed using a second polarizer A. The propagation takes place parallel to the axis of the cylinders.

The output signal is recovered by the detector which is a microscope, a photodiode, a camera or the eye. This element is appropriately chosen depending on the desired information we want to get of the sample. Any experiment requires an optimum positioning of the various elements: the vertical beam having been established previously, alignment and balance are performed at each stage by self-collimation (superposition of spots and back convergence spots out of a point at infinity).

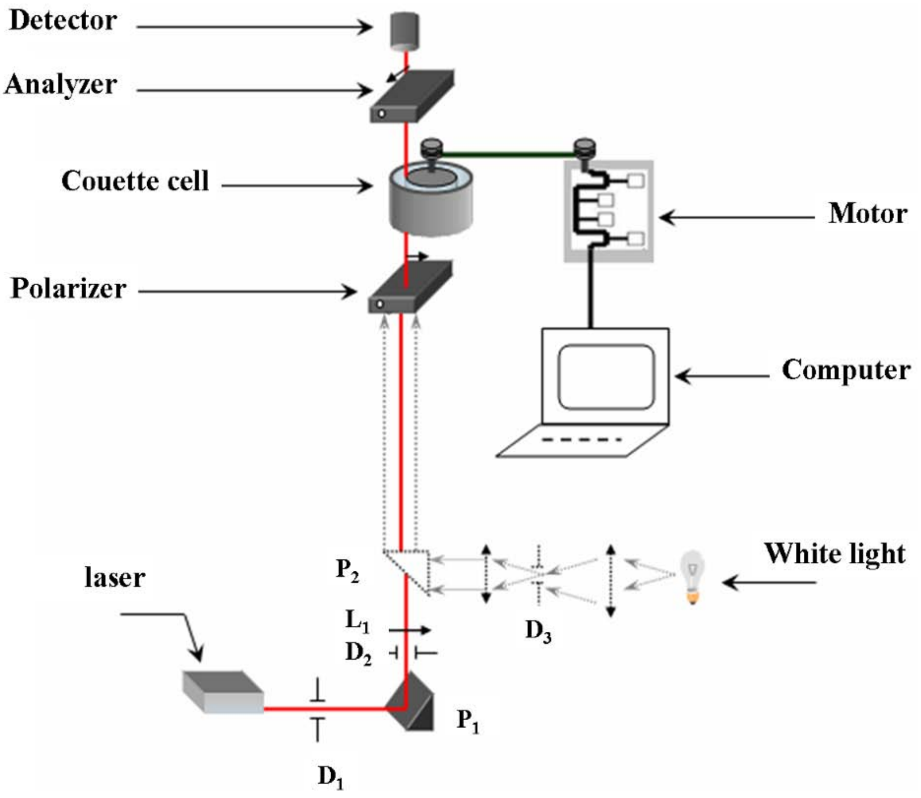

Figure II.9 Schematic diagram of the polarimetric bench

2.4.2 The measuring cell

All the experiments were realized in a conventional cell of Couette type. In practical way, the measurements are made by placing the medium or the solution in the gap between the two coaxial cylinders. The outer cylinder is fixed; the inner one is subjected to a rotational motion which creates the velocity gradient $\dot{\gamma}$ in the medium

$$\dot{\gamma}=\frac{2\Omega R_e^2 R_i^2}{R_e^2-R_i^2}\frac{1}{r^2} \qquad \text{(equation II.11)}$$

where Ω is the angular velocity of the moving wall, R_e and R_i respectively the radius of the outer and inner cylinder, and *r* the distance to the centre of the cell. Due to the curvature of the walls, the shear rate and consequently the shear stress are not strictly constant in the gap.

However, when the gap *e* between the cylinders is sufficiently small compared to the radius of cylinders, the velocity gradient is substantially constant across the gap

$$\dot{\gamma}=\frac{R_i\Omega}{e}, \qquad \text{(equation II.12)}$$

Taking into account the radii of the cylinders (R_e = 25mm and R_i = 23.5mm), the relative variation of the shear rate is approximately equal to 13%.

Cells of different heights can be used to vary the optical path through the liquid through (10, 30, 73 mm). All the results of this work are given for a cell height of 10 mm.

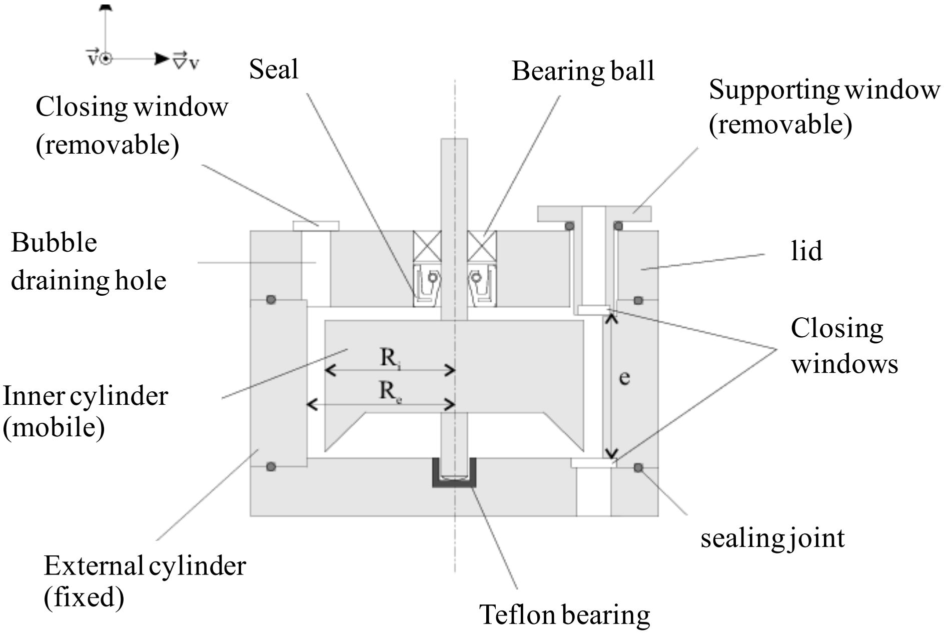
$\vec{v}$
$\vec{\nabla}v$
Seal
Bearing ball
Closing window (removable)
Supporting window (removable)
Bubble draining hole
lid
Closing windows
R_i
R_e
e
Inner cylinder (mobile)
sealing joint
External cylinder (fixed)
Teflon bearing

Figure II.10 Couette cell

2.4.3 The optical measurements: Principle of flow birefringence measurement

The Couette cell is placed between crossed polarizers; analyser (A) and polarizer (P). The gap is directly observed. At rest the solution is isotropic and the field appears black. Under shear, the sample becomes anisotropic and light reappears except in four radial regions forming the two branches of the isocline cross. The branches are the loci of the points where the average orientation of the particles is parallel to one of the polarization directions (see Figure II.11). These two peculiar directions of the polarizers (eigenpolarizations) are named the neutral lines of the medium; a linearly polarized light beam with its $\vec{E}$ vector parallel to one of these directions will suffer no change in its polarization state while travelling through the medium but will just propagate with a different velocity or “see” a different refraction index: n_1 or n_2.

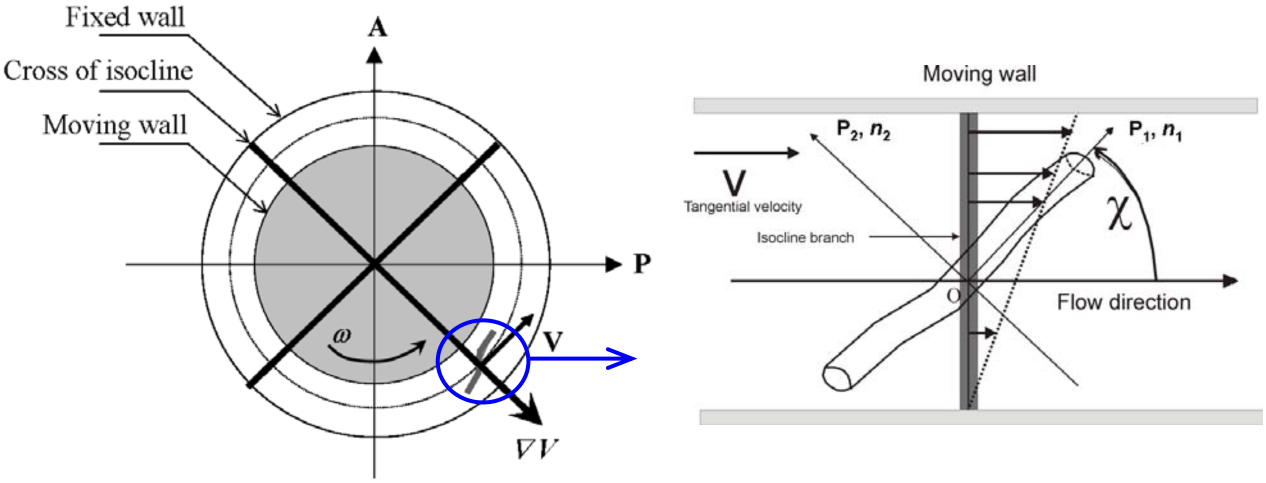

Figure II.11 Couette cell and cross of isoclines under cross polarizers

One branch of the cross of isoclines makes the angle χ with the flow direction. The birefringence intensity $\Delta n = n_2 - n_1$ is not a quantity that can be measured directly but the phase difference or retardation δ introduced by the solution can. Thus, a thickness of sample e introduces a phase shift or a retardance δ, between the two eigenpolarizations of the medium:

$$\delta = \frac{2\pi e}{\lambda}(n_2 - n_1) = \frac{2\pi e}{\lambda}(\Delta n) \qquad \text{(equation II.13)}$$

where λ the wavelength of the light and e is the thickness of the medium.

2.4.4 Measurement protocols

In this section, we shall describe the way to obtain χ and Δn from birefringence experiments. The sample, placed in the Couette cell, is subjected to increasing values of the shear rates. After a few minutes, the steady state is reached and measurements are performed. As in the rheological protocol, several experiments are realized with each sample in order to check for the coherence of our results.

2.4.4.1 Determination of the angle of extinction

The medium is placed between the two polarizers OP_1 and OP_2 which are crossed and the neutral line OX_1 makes the angle α with OP_1.
In that case, the transmitted intensity writes as:

$$I_\alpha = I_0 \sin^2 \frac{\phi}{2} \sin^2 2(\chi - \alpha) \qquad \text{(equation II.14)}$$

I_0 is the incident light intensity. It can readily be seen that $I_\alpha = 0$ when $\alpha = \chi$. The extinction is thus realized when the pair polarizer/analyzer is rotated by the angle α. The measurements are performed at different values of shear rate ($\dot{\gamma}$).

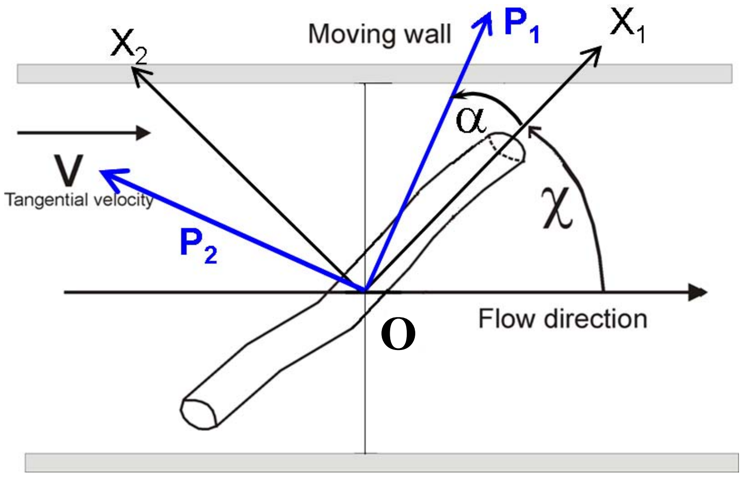

Figure II.12 Extinction angle determination.

The values of the angles red on a digital counter are not the true value of χ, since the zero of counter is arbitrary (arbitrary origin). In order to know the true value of χ, one has to identify the flow direction at first. To do this, we have to make the measurements of the angles α for both rotational directions of the inner cylinder for different values of velocity gradient. The curves $\alpha(\dot{\gamma})$ obtained for each rotation [$\alpha^{+}(\dot{\gamma})$ and $\alpha^{-}(\dot{\gamma})$] are symmetric with respect to the line of flow (see Figure II.13).

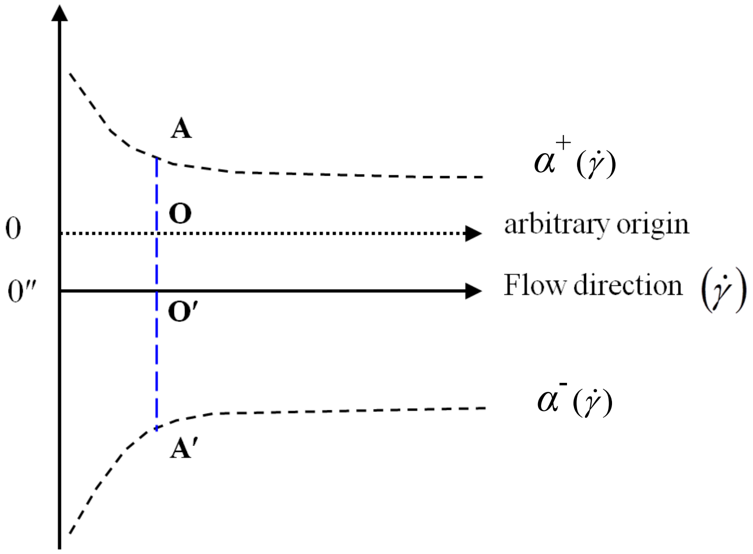
A
$\alpha^{+}(\dot{\gamma})$
0
O
arbitrary origin
0″
Flow direction $(\dot{\gamma})$
O′
$\alpha^{-}(\dot{\gamma})$
A′

Figure II.13 Determination of the true extinction angle ($\overline{O'A}$)

The y coordinate at the origin of the symmetry axis ($\overline{OO''}$) allows the calculation of the true values of the extinction angle χ.

2.4.4.2 Determination of the birefringence intensity

After having found the true evolution of χ, we can make use of the classical method of Sénarmont [8] to determine the retardation δ and then the birefringence intensity Δn. In this method, the polarizer OP is oriented at 45° from a neutral line OX, a quarter-wave plate, the principal axis of which is directed along OP, is added between the cell and the linear analyzer.

After crossing the solution, the light is elliptically polarized with the major axis of the ellipse parallel to the direction of incident polarization OP (see Figure II.14).

The quarter-wave plate changes the elliptic polarization back to linear along (OR) oriented at the angle ϕ with respect to OA.

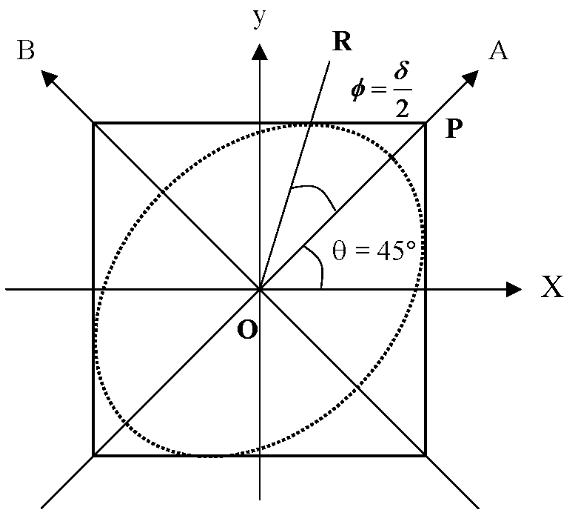

Figure II.14 The method of Sénarmont for measuring the phase shift

The transmitted intensity is:

$$I = \frac{I_0}{4}\left[1 - \cos(2\phi - \delta)\right] \qquad \text{(equation II.15)}$$

The analyzer OB is then rotated by the same angle ϕ in order to establish the extinction again and the induced phase shift is: $\delta = 2\phi$.

2.5 Small Angle Neutron scattering

2.5.1 Devices and experiments

Small angle neutron scattering technique (SANS) is a powerful tool for characterizing the structure of materials and in particular the shape and size of particles in colloidal systems.

In SANS (Figure II.15a), the sample is illuminated by a monochromatic neutron beam with wave vector $\vec{q}_i$. The interaction between this radiation and the nuclei of the sample results in a beam scattered in the direction of the wave vector $\vec{q}_f$. A more convenient parameter for the description of the scattered patterns is the scattering vector:

$$\vec{q} = \vec{q}_f - \vec{q}_i \qquad \text{(equation II.16)}$$

with $$q = |\vec{q}| = \frac{4\pi}{\lambda}\sin\left(\frac{\theta}{2}\right)$$ (equation II.17)

Remark: small angle neutron scattering implies that the angle θ *remains small* $(2\theta \leq 5°)$.

The experimental scattering curves are a combination of a form factor related to the shape of one particle (size and geometry) and a structure factor which describes the interactions between the particles, and which is negligible for very diluted samples. Thus different structural parameters, such as the geometry and size of aggregates, the conformations of the hydrophobic and hydrophilic chains and other parameters describing the system can be obtained by fitting the experimental data with theoretical models.

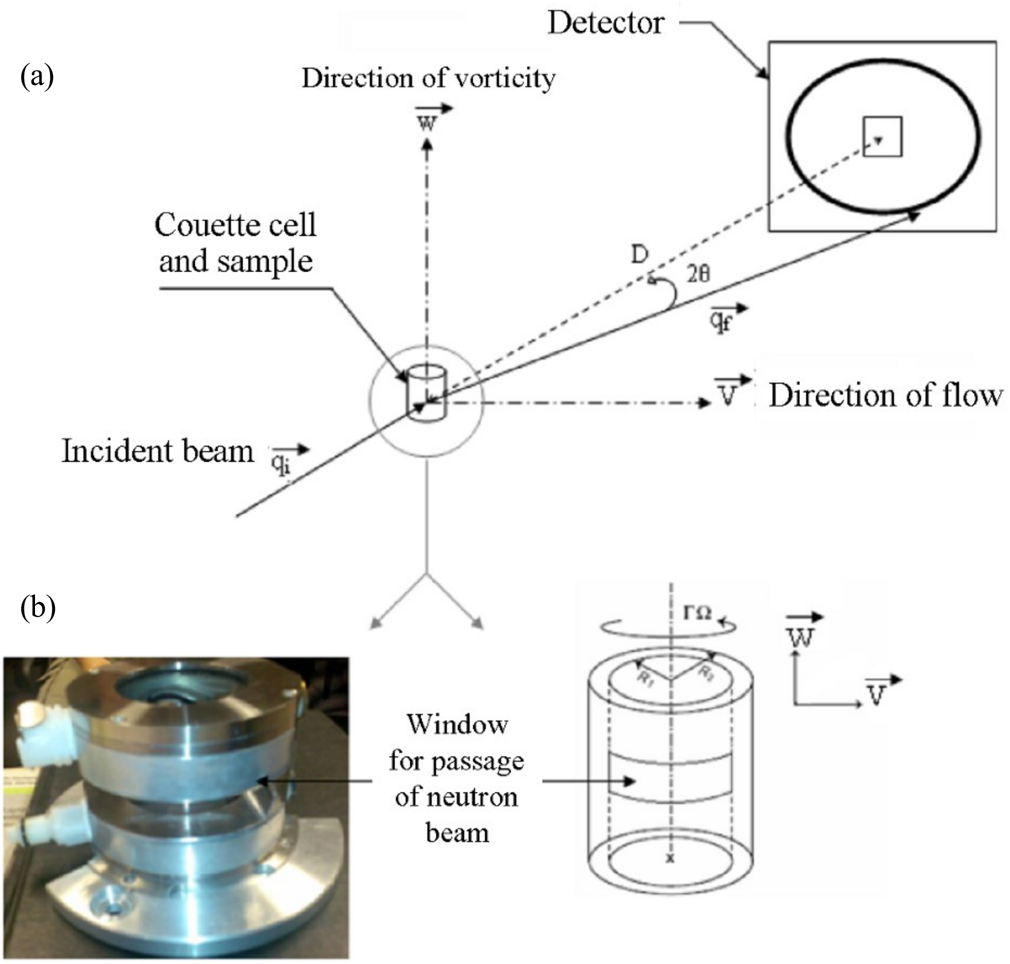
(a)
Detector
Direction of vorticity
W
Couette cell and sample
D
2θ
qf
V
Direction of flow
Incident beam
qi
(b)
rΩ
R1
R2
W
V
Window for passage of neutron beam
x

Figure II.15 (a) Principal scheme of the SANS experiment (b) Photograph and diagram of the Couette cell used

Our experiments were conducted on the D11 line at the Institut Laue-Langevin in Grenoble (ILL). The experimental setup is detailed in [9]. The device scheme is presented in Figure II.16. The neutron wavelength was set at 6 Å with a resolution $\Delta\lambda / \lambda = 10\%$. The raw data are collected on the XY 100x100cm detector with a resolution of 128 points in each direction. The detector is parallel to the plane ($\vec{\omega}$,$\vec{V}$), $\vec{\omega}$ lies in the vorticity direction and $\vec{V}$ defines the direction of the tangential velocity in the shearing device. Two sample-detector distances were chosen at 2.5m and 8m thus allowing the wave vector to scan the interval [$8.84\times10^{-3} – 2.71\times10^{-1}$ Å^{-1}].

The sample is subjected to the neutron beam in a Couette cell. The cup and bob, manufactured in quartz, respectively have a diameter of 50 and 48 mm forming a 1mm gap (Figure II.15b). The Couette cell was operated in strain controlled mode on a Bohlin apparatus (CVO120) with the inner cylinder rotating. The shear rates $\dot{\gamma}$ are chosen in the range [0.1 – 150 s^{-1}] similar to the ones used during rheological and flow birefringence experiments.

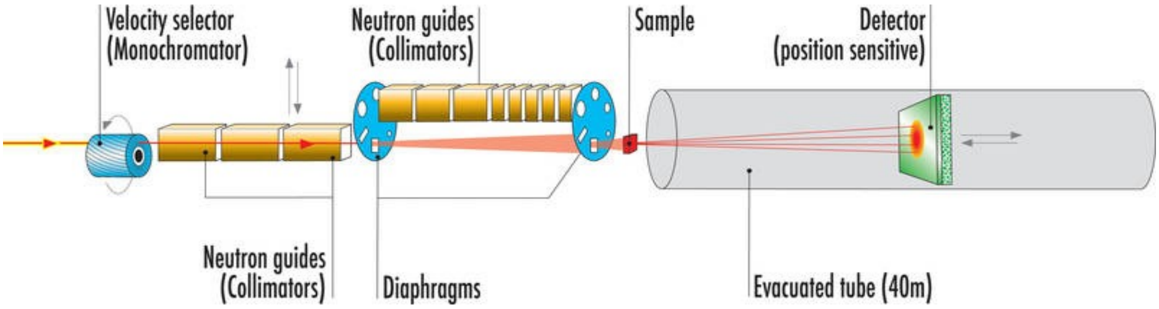

Figure II.16 The D11 line, archetype of a long, pinhole geometry instrument for SANS [10].
(http://www.ill.eu/instruments-support/instruments-groups/instruments/d11/)

2.5.2 Definition of the measured quantities in a SANS experiment

The amplitude of the signal scattered by N atoms *i* at individuals positions $\vec{r}_i$ results from the interference of the spherical waves scattered by each individual atoms. In the single-scattering approximation, the total scattering amplitude at a distance *R* of the scattering volume can be written as:

$$A(\vec{q}) = \frac{A_0}{R}\int_V \rho(\vec{r})\exp(i\vec{q}\vec{r})d\vec{r} \qquad \text{(equation II.18)}$$

where V is the scattering volume, A_0 the amplitude of the incident wave and $\rho(\vec{r})$ is the *scattering length density* of the atom located at $\vec{r}$. The amplitude of the scattered signal is thus proportional to the Fourier transform of the scattering length density distribution. The scattering length density is the number of atoms of a given isotope i per unit volume, weighted by a characteristic length called *scattering length* b_i which quantifies the core-neutron interaction of that isotope. It contains the structural information of the probed sample.

In any scattering experiment, the measured quantity is the average of the intensity of the scattered signal. The normalization of the scattered intensity by the intensity of the incident wave A_0^2 and by $1/R^2$ leads to the differential scattering cross section per unit solid angle $d\Omega$ = area of detector/R ; this quantity expressed per unit volume of sample reads :

$$\frac{d\Sigma}{d\Omega}(\vec{q}) = \frac{1}{V}\left|\int_V \rho(\vec{r})\exp(i\vec{q}\vec{r})d\vec{r}\right|^2 \qquad \text{(equation II.19)}$$

$\frac{d\Sigma}{d\Omega}$ represents the probability of a neutron of the incident beam to be scattered out of the scattering volume into the solid angle $d\Omega$. Its unit is cm^{-1}.

2.5.3 Extraction of the spectra

In practice we will consider only the coherent part of the differential scattering cross section per unit volume, which contains the structural information. We have thus performed all the preliminary measurements necessary to compute the correct cross section. Scattered as well as transmitted intensities through light and heavy water, empty cell and Cd sheet are recorded and used to correct and normalize the intensity signals. The scattered pattern collected at the detector is a two-dimensional distribution, which is reduced to a single set of data by an averaging process. The wave vector modulus q is then given by: $q = \sqrt{(X^2 + Y^2)}$.

When the intensity distribution is isotropic, the data are grouped using the circular averaging procedure on the whole pattern. When the pattern is anisotropic, the averaging is done in an angular sector of 45°; the whole pattern is thus reduced to six series of intensity data, two of which are of particular importance: $I_{\parallel}$ (parallel to the tangential velocity $\vec{V}$) and $I_{\perp}$ (parallel to the vorticity $\vec{\omega}$) which enter the calculation of the alignment factor $A_{\mathrm{f}}(q)$. All these computations are done with the software written at the ILL.

References

[1] F. Michaux in *Contribution des tensioactifs fluorés à la synthèse de matériaux mésoporeux : Application à la conception d'un bioréacteur*, *Ph.D thesis* UHP - Université Henri Poincaré, Nancy, **2009**.

[2] R. G. Larson, *The structure and Rheology of Complex Fluids*, Oxford University Press, New York, **1999**.

[3] J. F. Steffe, *Introduction to rheology. In J. F. Steffe, Rheological Methods in Food Process Engineering* Freeman Press., East Lansing, MI, **1996**, p. 1-91.

[4] C. W. Macosko, *Rhelogy: Principles, measurements, and applications*, Wiley-VCH, Inc., **1994**.

[5] S. A. El-Safty and J. Evans, *Journal of Materials Chemistry* **2002**, *12*, 117-123.

[6] J. D. Ferry, *Viscoelastic Properties of Polymers* John Wiley & Sons, Canada, **1980**.

[7] J. Dehmoune, J. P. Decruppe, O. Greffier, H. Xu and P. Lindner, *Langmuir* **2009**, *25*, 7271-7278.

[8] H. d. Senarmont, *Ann. Chim. Phys.* **1840**, *73*, 337.

[9] P. Lindner and T. Zemb, *Neutrons, X-Rays and Light: Scattering Methods Applied to Soft Condensed Matter* North-Holland, **2002**.

[10] P. Lindner and R. C. Oberthür, *Rev. Phys. Appl. (Paris)* **1984**, *19*, 759-763.

Chapitre III. Diagramme de phase des systèmes à base de $R_7^F(EO)_8$ et $R_8^F(EO)_9$

Dans ce troisième chapitre, on s'attache à la description des diagrammes de phase de solutions aqueuses préparées avec les deux tensioactifs fluorés $R_7^F(EO)_8$ et $R_8^F(EO)_9$. Il est d'importance primordiale de connaître la structure de la phase micellaire servant de modèle dans la synthèse des matériaux mésoporeux car leur propre structure en dépend.

3.1 Diagramme de phase de $R_7^F(EO)_8$ dans l'eau

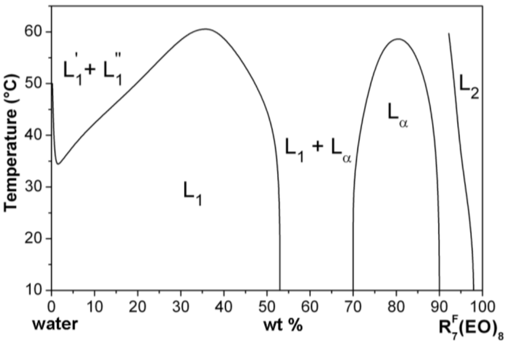

Figure III.1 Diagramme du système $R_7^F(EO)_8/H_2O$. L_1: phase micellaire directe, L_2: phase micellaire inverse, L_α: phase lamellaire, $L'_1 + L''_1$: domaine diphasique.[1]

Les solutions étudiées forment une phase unique du type L_1 et appartiennent au domaine de concentration [0, 50 wt %].

3.2 Diagramme de phase de $R_7^F(EO)_8$ en présence de sel NaI dans l'eau

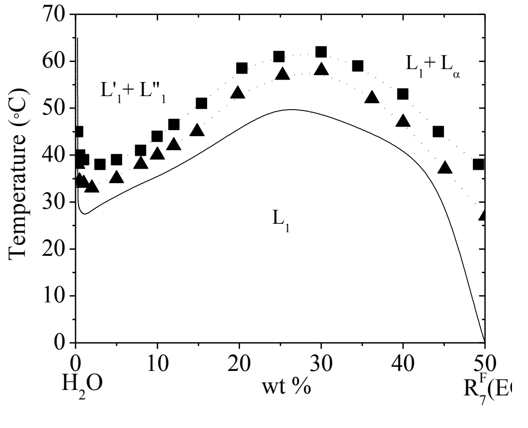

Figure III.2 Diagramme de phase partiel de $R_7^F(EO)_8$ dans (a) H_2O, dans NaI à (b) ▲ 0.5 M and (c) ■ 1 M ,dans le domaine de concentration 0.5-50 wt % en tensioactif.

Le système $R_7^F(EO)_8/H_2O$ ne conduit qu'à la synthèse de matériaux mésoporeux ayant un faible degré d'organisation tandis que l'ajout de sel NaI le favorise car l'ordre est perdu lorsque la température à laquelle la silice est ajoutée est trop proche de la température de séparation des phases. L'ajout de sel déplace la courbe de solubilité vers les hautes températures.

3.3 Diagramme de phase de $R_8^F(EO)_9$ dans l'eau

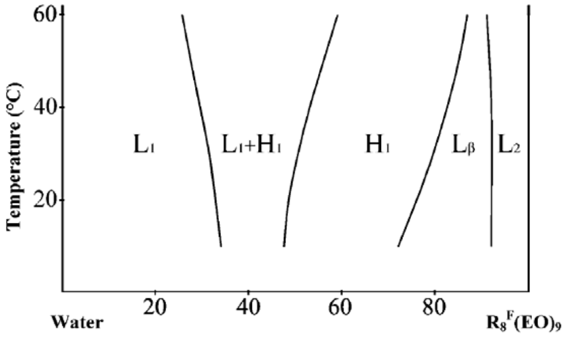

Figure III.3 Diagramme de phase de $R_8^F(EO)_9$ dans H_2O

Le système $R_8^F(EO)_9/H_2O$ est connu pour conduire à la formation de matériaux mésoporeux hexagonaux réguliers à partir d'une solution micellaire de type L_1 dans le domaine de concentration 5 and 20 wt %. Pour ce système, nous n'avons pas été en mesure de mettre en évidence la courbe de miscibilité même en portant la température à 90°C.

3.4 Diagramme de phase de $R_8^F(EO)_9$/NaCl dans l'eau

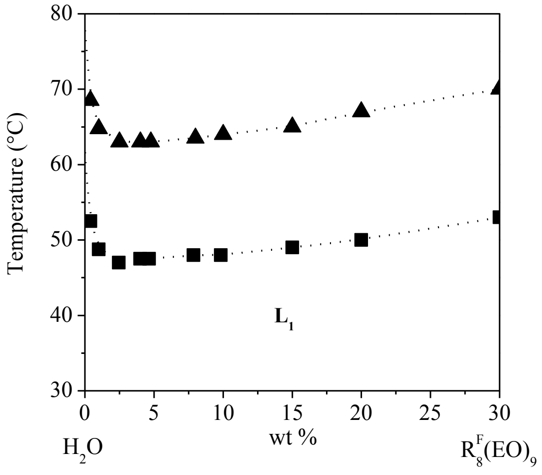

Figure III.4 Diagramme de phase partiel de $R_8^F(EO)_9$ dans une solution de NaCl à : (a) ▲ 1.5 M and (b) ■ 3 M dans le domaine de concentration 0.5-30 wt % en tensioactf.

L'ajout de sel NaCl abaisse la courbe de miscibilité qui sépare la phase isotrope L_1 du domaine diphasique vers des températures plus basses. Les ions chlorures Cl^- favorisent l'association des molécules d'eau par liaisons hydrogènes diminuant ainsi l'hydratation du tensioactif et par conséquent sa solubilité.

Chapter III. Phase diagram of $R_7^F(EO)_8$ and $R_8^F(EO)_9$ surfactant-based systems

3.1 $R_7^F(EO)_8$ surfactant based system

3.1.1 Phase diagram of $R_7^F(EO)_8$ in water

The structure of the mesoporous material is related to the behaviour of the surfactant in the synthesis solvent used as structure directing agent. It is thus of primary importance to know the structure of the micelles present in the initial liquid phase prior to any attempt to synthesize a well organized mesoporous material. Before, the phase diagram of the binary systems should be determined.

The complete phase diagram of the binary system $R_7^F(EO)_8$/water is presented in Figure III.1[1]. The full lines separate single phase domains from biphasic regions. The diagram has been established between 10 and 60°C as a function of the surfactant concentration; a miscibility curve is found with a particular cloud point (critical point CP) at 34°C for a concentration of 1 wt % in surfactant. This miscibility curve in the lower concentration range ($[R_7^F(EO)_8] < 50$ wt %) separates the isotropic L_1 phase from two biphasic domains. The two phases L'_1 and L''_1, respectively rich and poor in micelles coexist in the low concentration range. In the middle range (between 55 – 70 wt %), the L_1 phase appears with a lamellar phase L_α. In the concentration range [70 – 90 wt %], a pure L_α phase is found. As the temperature is increased, the concentration range of the L_α phase is gradually narrowing and the phase disappears around 60° C. At very high surfactant concentrations, a reverse micellar phase (L_2) is formed (see Figure III.1 rightmost part of the diagram).

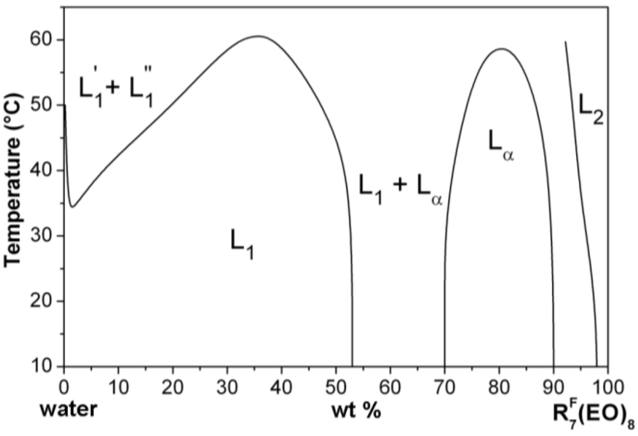

Figure III.1 Binary phase diagram of $R^F_7(EO)_8$/water system. L_1: direct micellar phase, L_2: reverse micellar phase, L_α: lamellar phase, $L'_1 + L''_1$: biphasic phase [1].

Since the phase diagram changes slightly between the different batches of surfactant, we found it necessary to redraw the diagram in the limited concentration range we are interested in i.e [0, 50 wt %].

To do so, a series of 16 samples in the concentration range 0.5-50 wt% of surfactant (Figures III.2) is prepared with the new $R^F_7(EO)_8$ batch.

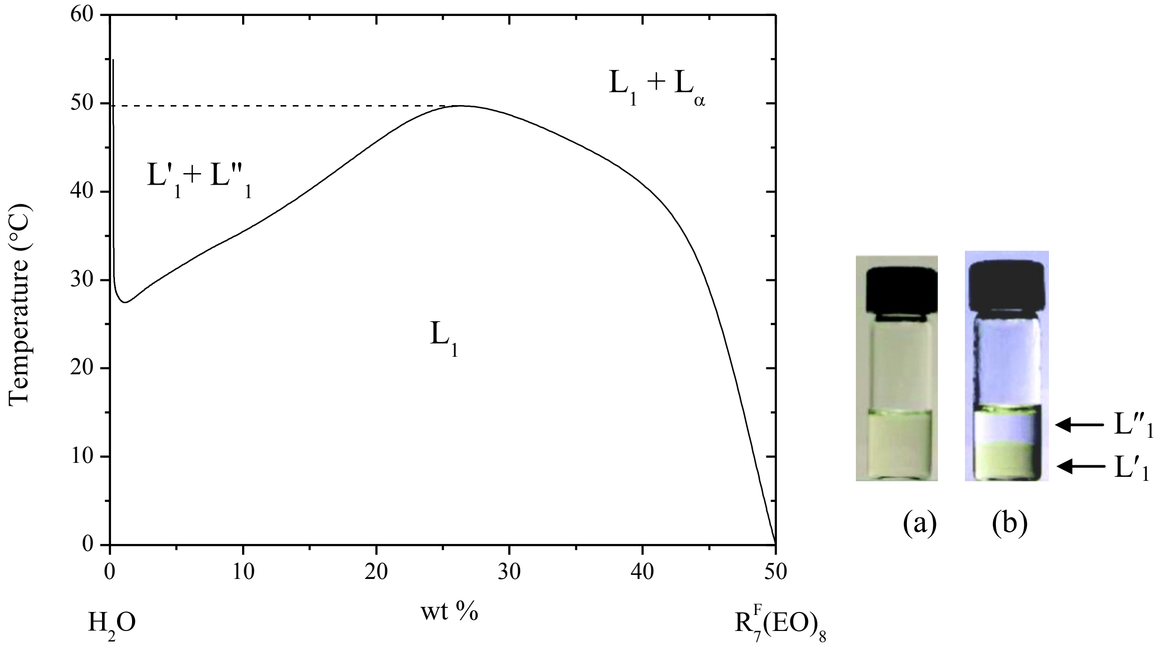

Figure III.2 Partial binary phase diagram of $R^F_7(EO)_8$/water system in the range [0.5-50 wt%]. L_1: direct micellar phase (tube III.2a), L_α: lamellar phase, $L'_1 + L''_1$: biphasic phase (tube III.2b): rich and poor in micelles.

It turns out that the critical point (CP) is at 27°C for a 1 wt % of surfactant. The two small pictures besides the graph show the sample in the L_1 phase (tube III.2a) and in the biphasic domain (tube III.2b). L'_1 and L''_1 respectively stand for the phase rich and poor in micelles. We are particularly interested in the L_1 phase which exists in a wide range of concentrations and temperatures; the micelles forming this phase are known to form mesoporous materials, but with a poor degree of order [1] compared to other fluorinated surfactant also forming a L_1 phase [2].

Consequently, the well prepared samples within the L_1 phase of $R_7^F(EO)_8$ will be considered to study the rheological and rheo-optical properties by using rheology, flow birefringence, and small-angle neutron scattering techniques.

3.1.2 Phase diagram of $R_7^F(EO)_8$ in sodium iodine (NaI)

As quoted before, the preparation of mesoporous material via the CTM mechanism with the nonionic fluorinated surfactant, the $R_7^F(EO)_8$/ water system is known to form materials with a poor degree of order. As mentioned in a previous work [3], only the disordered mesostructure are recovered from the $R_7^F(EO)_8$/water system, meanwhile the well-ordered mesostructure is synthesized from an aqueous solution of surfactant and sodium iodide (NaI). However, the pore ordering is lost if the temperature at which the silica precursor is added is close to the phase separation temperature. Therefore, it is very interesting to investigate the influence of salt addition on the lower consolute boundary of the fluorinated micellar surfactant solutions. This understanding can be useful to design, control or even improve the synthesis method via a CTM mechanism to obtain the well-ordered mesoporous material.

Besides the phase diagram of $R_7^F(EO)_8$ in water (shown in figure III.2), the partial phase diagram of the surfactant/NaI binary system is also established in the same surfactant concentration range (Figure III.3), in aqueous solutions (0.5 and 1 M). With the increase of the NaI concentration, the lower consolute boundary (LCB) is shifted toward higher temperatures (salting in effect). For example, the 10% surfactant /water solution presents a phase separation temperature of 35 °C (Figure IIII.3a); when NaI is present in the system, the temperature is shifted from 35 °C to 40 and then 44 °C, when the NaI concentration is raised from 0 to 0.5 (Figure III.3b) and 1.0 M (Figure III.3c), respectively.

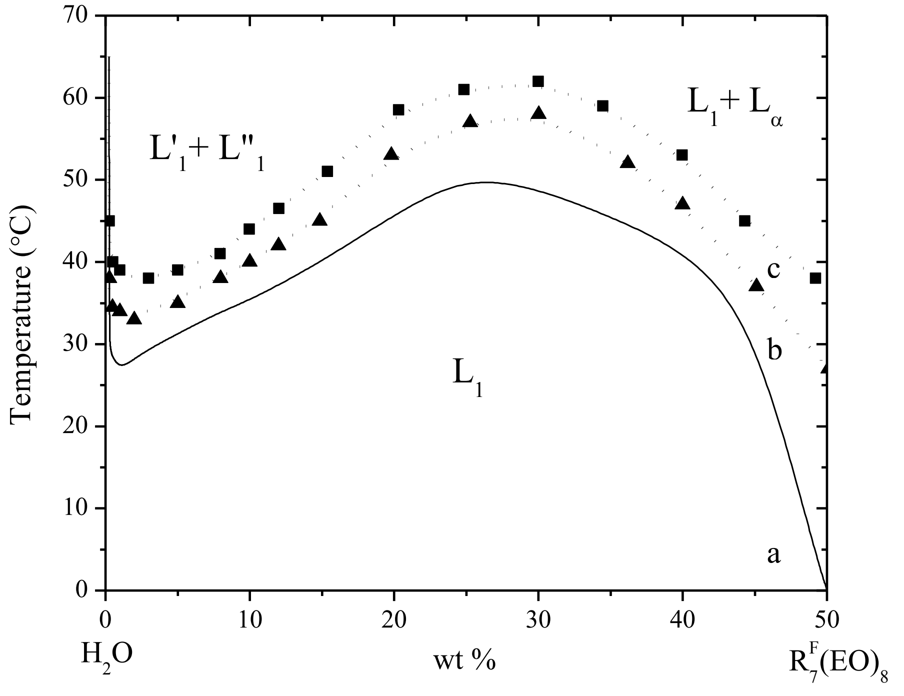

Figure III.3 Partial temperature-composition phase diagram of the $R_7^F(EO)_8$ surfactant in (a) water (same as figure III.2), (b) ▲ 0.5 M and (c) ■ 1 M NaI aqueous solutions, in the range 0.5-50 wt % surfactant.

The changes in the LCB location are mainly attributed to the influence of the anion of the added salts. Indeed, cations are known to be smaller and to bind more hydration water than anions. Therefore, the LCB shifts are not caused primarily by competition between the ions for free water, but by a more specific anion effect. Iodin$^-$ belongs to the chaotropic family of chemicals. Due to its low electronegativity, high polarizability, and weak electrostatic field, iodin$^-$ disrupts the association of water molecules that surround the micelles of surfactant. This kind of anion increases the concentration of single water molecules, which are able to form hydrogen bonds with the ethylene oxide groups of nonionic surfactants. Hence, NaI salt raises the CP [4].

3.2 $R_8^F(EO)_9$ surfactant based system

3.2.1 Phase diagram of $R_8^F(EO)_9$ in water

In the opposite way, the $R_8^F(EO)_9$ surfactant in pure water has been known to be a more effective template. It has been reported to give the ordered hexagonal molecular sieves in the final product, when the preparation is carried out from the direct micellar solution L_1 phase with the concentration of $R_8^F(EO)_9$ between 5 and 20 wt % [2]; conversely, the presence of sodium chloride (NaCl) in the system leads to the loss of pore ordering [3].

The phase diagram of $R_8^F(EO)_9$ surfactant/water system in Figure III.4 was already reported by Stébé and co-workers [2]; in the investigated temperature range, and up to 30 wt% of surfactant, a direct micellar L_1 phase is detected. When the surfactant concentration is increased (30 ≤ wt % ≤ 50), they found the biphasic domain (L_1 + H_1) of direct micellar and direct hexagonal phase detected by an optically anisotropic phase. When the weight percentage of surfactant is increased up to 75 wt %, the existence of the pure direct hexagonal phase (H_1) is considered. If the surfactant concentration is further increased (>75 wt %), the texture of the gel phase appears. If the temperature is increased, the overall phase limits are shifted toward higher surfactant concentrations.

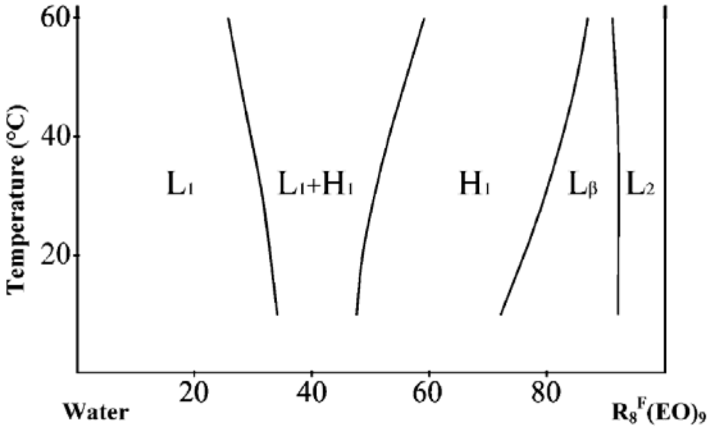

Figure III.4 Temperature-composition (wt%) phase diagram of $R_8^F(EO)_9$ in water [2].

For our study, we investigate the L_1 phase. In the $R_8^F(EO)_9$ surfactant- pure water system, the isotropic micellar phase L_1 is found to be present in the range of 0.5-30 wt % $R_8^F(EO)_9$.

The miscibility curve has yet not been observed even when we raise the temperature up to 80 °C, (thus there is no LCB line for $R_8^F(EO)_9$/water sample in figure III.5).

3.2.2 Phase diagram of $R_8^F(EO)_9$ in sodium cloride (NaCl)

In order to study the influence of NaCl on the shift of the phase separation curves in $R_8^F(EO)_9$ surfactant system, we have prepared samples focusing on the range where direct micelles are formed (L_1 phase), according to the phase diagram appearing in figure III.4. A series of 10 samples in the range [0.5-30 wt %] $R_8^F(EO)_9$ in water and in NaCl aqueous solutions (1.5 and 3 M) is thus prepared and the partial phase diagrams are established and drawn in Figure III.5.

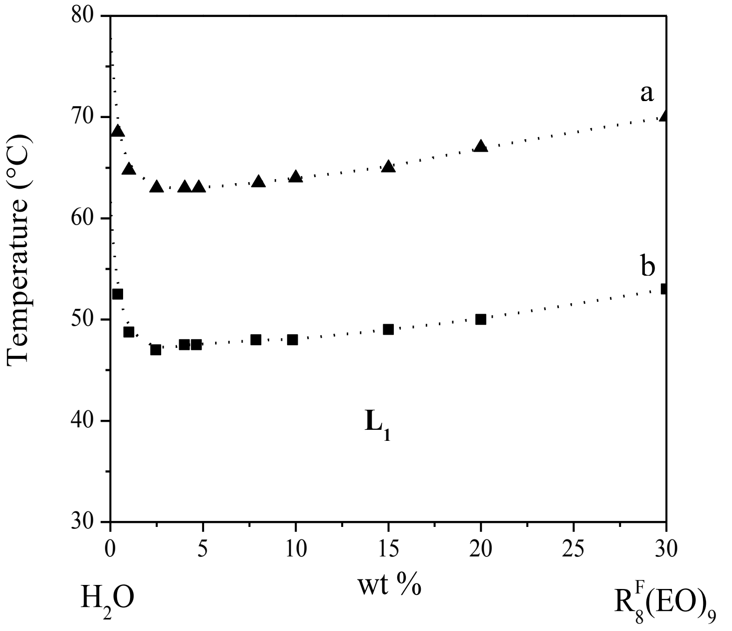

Figure III.5 Partial temperature-composition phase diagram of the $R_8^F(EO)_9$ surfactant in (a) ▲ 1.5 M and (b) ■ 3 M NaCl aqueous solutions, in a range of 0.5-30 wt % surfactant.

The addition of NaCl in the system leads to the emergence of the phase separation curve, the lowest point of which is the critical temperature (CP). The isotropic micellar L_1 phase is located under the miscibility curve, meanwhile the biphasic domain is observed above this curve. This result clearly shows that the LCB is shifted toward lower temperatures when the salt concentration is increased. As seen in this diagram, the phase separation temperature at 10 wt% for $R_8^F(EO)_9$ drops to 63 and 47°C, when NaCl is added at the concentration of 1.5 M (Figure III.5a) and 3 M (Figure III.5b), respectively.

This result confirmed that the LCB of $R_8^F(EO)_9$ surfactant- pure water system is located at high temperatures; the CP is being at a temperature higher than 90 °C [2]. A shift of the LCB toward lower temperatures is thus proved with the addition of NaCl (salting out effect) [3]. The Cl- is in the Hofmeister series, which is known to be a kosmotropic anion [4]. Therefore, it enhances the association of water molecules by hydrogen bonds instead of their association with the surfactant. Thus, it reduces the surfactant hydration and solubility, lowering the CP temperature.

References

[1] R. Bleta, J. L. Blin and M. J. Stebe, *The Journal of Physical Chemistry B* **2006**, *110*, 23547-23556.

[2] J. L. Blin, P. Lesieur and M. J. Stébé, *Langmuir* **2004**, *20*, 491-498.

[3] F. Michaux, J. L. Blin and M. J. Stebe, *Langmuir* **2008**, *24*, 1044-1052.

[4] H. Schott, *Journal of Colloid and Interface Science* **1997**, *189*, 117-122.

Chapitre IV. Rhéophysique des solutions des tensioactifs fluorés $R_7^F(EO)_8$ et $R_8^F(EO)_9$

Le quatrième chapitre est consacré à la présentation et à l'analyse des résultats obtenus à l'aide des différentes techniques expérimentales utilisées dans ce travail à savoir : la rhéologie, la biréfringence d'écoulement et la diffusion de neutrons aux petits angles.

Il est divisé en quatre grandes parties qui correspondent à des solutions aqueuses des deux tensioactifs $R_7^F(EO)_8$ et $R_8^F(EO)_9$ et des mélanges $R_7^F(EO)_8$/NaI et $R_8^F(EO)_9$/NaCl. Pour les quatre systèmes, les données de la rhéologie sont analysées quantitativement à l'aide d'un modèle à deux paramètres du type Ostwald pour l'écoulement permanent et du modèle de Maxwell pour l'écoulement oscillatoire. Les résultats de biréfringence sont interprétés dans le cadre de la théorie de l'orientation de particules et ceux de SANS à l'aide du modèle théorique de J.C. Ravey.

4.1 Système I - $R_7^F(EO)_8/H_2O$

Les paramètres de cette étude sont la température et la concentration en masse de tensioactif ; quatre températures (10, 20, 30 et 40°C) ainsi que quatre concentrations (10, 20, 30 et 40%) ont été choisies. Les systèmes sont soumis à différents types de sollicitations : écoulement permanent, dynamique et cycle de contrainte. On s'intéresse aux variations de la viscosité apparente en fonction du taux de cisaillement, des modules *G*' et *G*'' en fonction de la fréquence des oscillations et de la viscosité apparente en fonction du temps sous contrainte constante.

En écoulement permanent et dans le domaine de taux de cisaillement [0.1 – 10^2 s^{-1}], le comportement rhéologique qualitatif dépend fortement des conditions de température et de concentration. On pourra ainsi observer un comportement classique à savoir, Newtonien aux bas cisaillements puis rhéofluidifiant mais également une décroissance constante de la viscosité apparente η sur tout le domaine de cisaillement sans palier Newtonien aux faibles taux. Cette seconde évolution est particulièrement marquée lorsque, pour une concentration donnée, la température est proche de celle de la courbe de miscibilité.

On s’assure du caractère Maxwellien de la solution en la sollicitant de manière dynamique dans le domaine linéaire. A la température de 20°C, G et G'' suivent avec une bonne approximation les comportements théoriques : $G' \sim \omega^2$ et $G'' \sim \omega$; mais $G'' > G'$ sur toute l’étendue des pulsations : le caractère visqueux est toujours prépondérant. A la température de 10°C, et pour les concentrations de 20, 30, 40%, G' et G'' suivent encore le modèle théorique de Maxwell et se coupent dans l’intervalle de fréquences accessibles permettant ainsi le calcul du temps de relaxation τ_R qui diminue avec la température. Du module plateau G_0 et du minimum de G'' dans la représentation Cole-Cole, on détermine le temps de cassure et recombinaison τ_b des micelles ainsi que la longueur de corrélation hydrodynamique ξ_H.

Soumise à une contrainte constante et faible (0.01, 0.1 Pa), la viscosité apparente croît dans le temps ; on émet ainsi l’hypothèse que cet accroissement est dû à la formation d’une structure plus complexe de type agrégats formés par des attractions faibles entre les micelles.

La biréfringence induite sous écoulement est également étudiée. On détermine l’évolution des deux grandeurs caractéristiques : l’angle d’extinction χ et l’intensité de la biréfringence Δn. Les variations de l’angle d’extinction en fonction du taux de cisaillement $\dot{\gamma}$ ne suivent pas les prédictions de la théorie de l’orientation des particules sous écoulement. En effet χ croît avec $\dot{\gamma}$, passe par un maximum avant de décroître à nouveau. Ce comportement inhabituel aux faibles $\dot{\gamma}$ est expliqué par la présence d’agrégats de micelles liées par des forces faibles graduellement compensées par l’action du champ hydrodynamique. Aux plus forts taux de cisaillement, χ suit la théorie classique et la valeur relativement grande de l'angle (35 – 40°) atteste de la présence de micelles dont le rapport d’aspect est petit.

Les résultats de diffusion de neutrons au repos ont permis de déterminer les dimensions moyennes des micelles en se donnant un modèle de particule ellipsoïdale développé par J.C. Ravey. Sous cisaillement, une anisotropie apparaît dans les spectres de diffusion traduisant une orientation moyenne des particules. L’allure des courbes d’intensité diffusée $I_{\parallel}(q)$ et $I_{\perp}(q)$ est caractéristique de solutions dans lesquelles les particules sont en interaction ; elles présentent toutes deux un pic de corrélation pour un vecteur d’onde particulier q^* à partir duquel on calcule la distance de corrélation ξ,

4.2 Système II - $R_7^F(EO)_8/NaI/H_2O$

Les paramètres de l'étude, concentration massique et température, sont identiques à ceux utilisés pour le système I. L'addition de sel NaI à la solution de tensioactif a pour effet de déplacer la courbe de miscibilité vers des températures plus élevées. Toutes les solutions forment une phase L_1 située sous la courbe de miscibilité.

Qualitativement la rhéologie sous cisaillement permanent est identique à celle des solutions sans sel. A 20°C et pour toutes les concentrations le comportement est quasi Newtonien sur toute l'étendue du domaine de cisaillement ; il en est de même à 10% pour toutes les températures. Lorsque la concentration croît et à basse température (10°C), la solution est rhéofluidifiante aux grands cisaillements; à la température de 40°C, on observe une rhéofluidification aux faibles cisaillements suivi d'un palier Newtonien. Aux températures intermédiaires (20 et 30°C), la viscosité est pratiquement constante sur tout le domaine de cisaillement. En sollicitation sinusoïdale, le caractère Maxwellien est observé à la température de 10°C. L'abscisse du crossover décroît avec la concentration. Pour les deux solutions à 30 et 40%, il est possible de calculer les grandeurs microscopiques τ_{break} et ξ_H.

La biréfringence d'écoulement apporte des résultats semblables à ceux du système I. Dans le domaine des faibles cisaillements, l'angle d'extinction χ ne suit pas la théorie classique de l'orientation sous cisaillement.

4.3 Système III - $R_8^F(EO)_9/H_2O$

Ce tensioactif conduit toujours à la synthèse de matériaux mésoporeux réguliers. L'étude est restreinte à deux solutions de concentration massique 20 et 30 %, la température varie entre 10 et 40°C. La solution à 20% est Newtonienne pour toutes les températures ; à 30%, un comportement rhéofluidifiant apparaît aux faibles cisaillements et son importance croît avec la température. A 40°C, le palier Newtonien a complètement disparu et la viscosité apparente décroît sur toute l'étendue du cisaillement.

Les expériences de biréfringence d'écoulement effectuées sur cette solution n'ont pas permis d'obtenir de résultats quantitatifs dans le domaine de taux de cisaillement utilisé. Le manque de tensioactif ne nous a pas permis d'utiliser une cellule présentant un chemin optique plus grand. Néanmoins, on peut en conclure que les micelles en solution sont certainement petites avec un rapport d'aspect et une forme proche de celle d'une sphère.

4.4 Système IV - $R_8^F(EO)_9$ /NaCl/H_2O

L’ajout de sel a pour effet de déplacer la courbe de miscibilité vers les températures plus basses. Les solutions appartiennent toujours au domaine L_1 ; deux concentrations massiques (20 et 30%) sont étudiées à différentes températures entre 10 et 50°C.

Dans le domaine des faibles cisaillements, la viscosité apparente de la solution à 20% décroît lentement jusqu’à un taux critique au-delà duquel le caractère Newtonien prévaut. Le comportement qualitatif est le même pour la solution à 30% en masse sauf pour la température maximale (50°C) pour laquelle le système est fortement rhéofluidifiant dans le domaine des faibles cisaillements puis devient Newtonien. L’addition de sel conduit à la perte du caractère Maxwellien pour les deux concentrations.

En biréfringence d’écoulement, l’angle d’extinction χ décroît à partir de 45° aux faibles γ conformément à la théorie de l’orientation. La loi tensio-optique est vérifiée pour les deux solutions. On vérifie que le coefficient tensio-optique C varie en inverse de la température absolue.

Chapter IV. Rheophysics of nonionic fluorinated surfactant based system

This chapter is dedicated to the description of three rheophysical properties (rheology, flow birefringence and neutron scattering under shear) of nonionic fluorinated surfactant systems. The study concerns four systems of two surfactants. The first is the pure $R_7^F(EO)_8$ in water and we report the solution properties under the L_1 phase by using rheology, flow birefringence and neutron scattering measurements. The second system is $R_7^F(EO)_8$ in the presence of the salt NaI, in order to investigate the influence of NaI on the rheological and flow birefringence properties of $R_7^F(EO)_8$. Besides the $R_7^F(EO)_8$ system, another nonionic fluorinated surfactant $R_8^F(EO)_9$ has also been studied. The third part contains the results of the rheological and flow birefringence properties of $R_8^F(EO)_9$ in water under the L_1 phase. The influence of NaCl on shifting down the miscibility curve of $R_8^F(EO)_9$, will be presented as the fourth system.

4.1 SYSTEM I - $\mathbf{R_7^F(EO)_8}$ in water

4.1.1 Rheological properties

The quantitative analysis of the steady state measurements is done in the frame of the theoretical model with two parameters (Ostwald's law):

$$\sigma = \kappa\, \dot{\gamma}^{\,n} \qquad \text{(equation IV.1)}$$

Or if we introduce the apparent viscosity (η):

$$\eta = \kappa\, \dot{\gamma}^{\,n-1} \qquad \text{(equation IV.2)}$$

σ is the shear stress, $\dot{\gamma}$ the shear rate; κ and n are both constants.

Experiments performed in dynamic mode lead to the elastic and loss modulii G' and G''. For a Maxwellian fluid, G' and G'' read:

$$G' = G_0 \frac{\omega^2 \tau_R^2}{1+\omega^2\tau_R^2} \qquad \text{(equation IV.3)}$$

$$G'' = G_0 \frac{\omega \tau_R}{1+\omega^2\tau_R^2} \qquad \text{(equation IV.4)}$$

τ_R is the relaxation time of the solution and ω the angular frequency. Eliminating the product $\omega\tau_R$ in G' and G'' leads to the equation of a circle (Cole-Cole plot) and the Maxwellian character of the fluid can be appreciate by plotting G' vs G''.

4.1.1.1 Steady state rheological behaviour

The two parameters of this study are the surfactant concentration $[R_7^F(EO)_8]$ and the temperature T. The points representing the different solutions used for this study appear in the partial phase diagram (Figure IV.1a). Most of experiments are situated in the L_1 micellar phase domain, and some conditions are close to or beyond the miscibility curve. Figure IV.1b describes the variations of the apparent viscosity η as a function of the shear rate in a log-log scale. Four solutions of concentrations 10, 20, 30 and 40 wt% are subjected to increasing shear rates in the range $[0.1-10^2]\,s^{-1}$ and the temperature is kept constant within the interval 20.00 ± 0.05 °C.

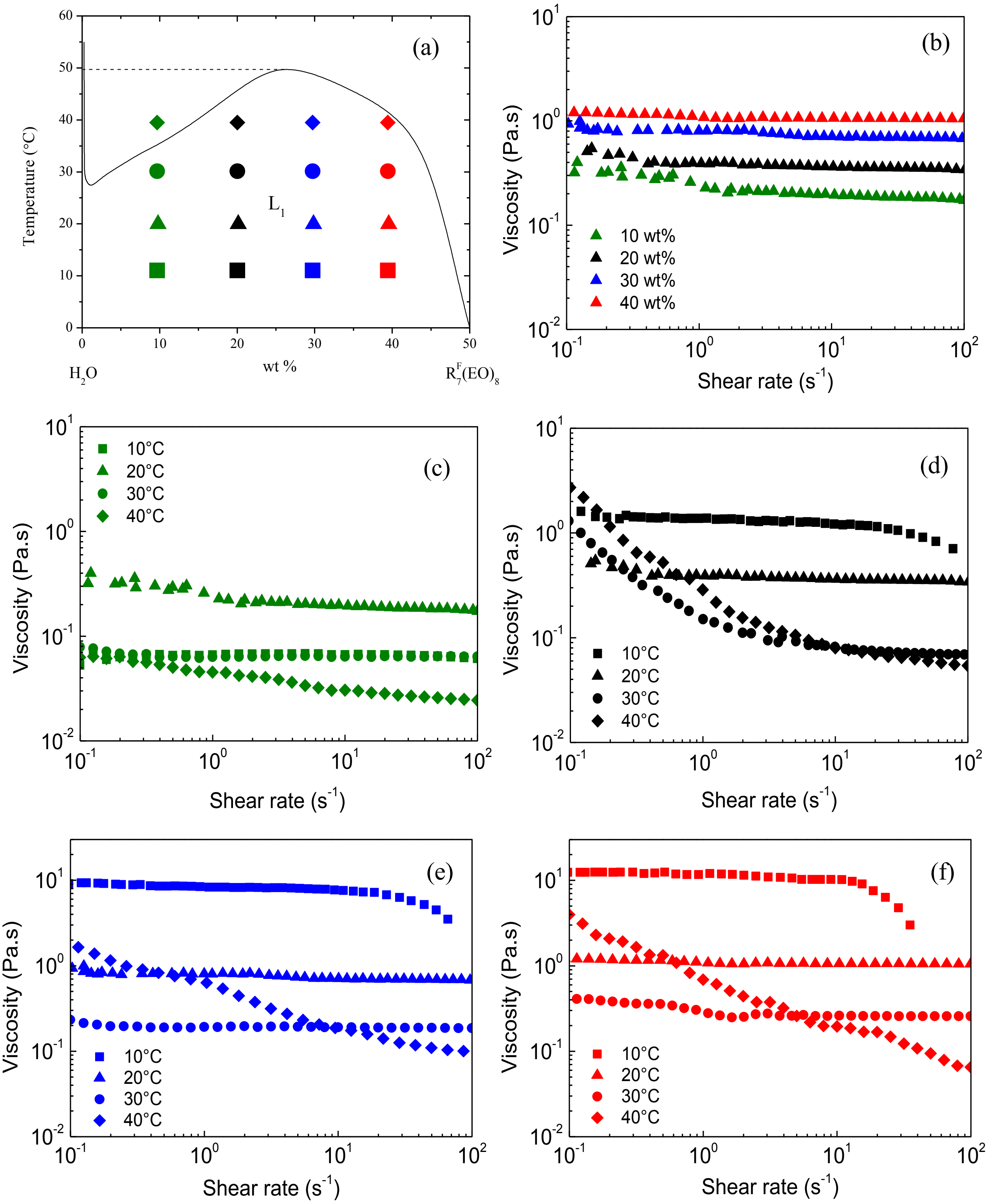

Figure IV.1 Rheological behaviour in steady state shearing mode. (a) miscibility curve (solid line), the symbols pointing out the solutions under investigation; (b) viscosity curves at 20°C of different wt% $R_7^F(EO)_8$ concentrations. The viscosity curves (c-f) for the concentrations of (c) 10, (d) 20, (e) 30 and (f) 40 wt% at different temperatures; 10°C (square), 20°C (triangle), 30°C (circle), 40°C (diamond).

Table IV.1 The Ostwald's law parameters for $R_7^F(EO)_8$ in water at different concentrations and temperatures.

Conditions		Rheological characters from flow curves fitting	$\dot{\gamma}_c$ (s^{-1})	Ostwald's law parameters		
$R_7^F(EO)_8$ in H_2O				κ (Pa s^n)	n (-)	R^2
10% wt	10°C	Newtonian	-	0.077	0.952	0.999
	20°C	(1) Shear-thinning (2) Newtonian*	2.0	0.198	0.981	0.998
	30°C	Newtonian	-	0.065	0.996	0.999
	40°C	Shear-thinning	-	0.038	0.905	0.999
20% wt	10°C	(1) Quasi-Newtonian* (2) viscosity decreases at high $\dot{\gamma}$	24.5	1.419	0.932	0.999
	20°C	(1) Shear-thinning (2) Newtonian*	0.7	0.392	0.970	0.999
	30°C	Shear-thinning	-	0.085	0.950	0.999
	40°C	Shear-thinning	-	0.135	0.780	0.990
30% wt	10°C	(1) Quasi-Newtonian* (2) viscosity decreases at high $\dot{\gamma}$	16.8	8.872	0.933	0.999
	20°C	Newtonian	-	0.760	0.975	0.999
	30°C	Newtonian	-	0.195	0.991	1.000
	40°C	Shear-thinning	-	0.387	0.686	0.993
40% wt	10°C	(1) Quasi-Newtonian* (2) viscosity decreases at high $\dot{\gamma}$	13.3	11.88	0.927	0.999
	20°C	Newtonian	-	1.078	0.994	1.000
	30°C	Newtonian	-	0.268	0.988	0.999
	40°C	Shear-thinning	-	0.685	0.492	0.984

κ, consistency coefficient (Pa s^n); n, flow behaviour index (dimensionless). $\dot{\gamma}_c$, critical shear rate (s^{-1}) at the juxtaposition of two approximately linear segments on the viscosity curves; (1) and (2) are the first and second segments, respectively. In the case of curves formed by the juxtaposition of two segments, the fitting has been done only over the nearly Newtonian segment.

A qualitative observation of the distribution $\eta(\dot{\gamma})$ in Figure IV.1b shows at first an increase of the apparent viscosity with the concentration. Two types of rheological behaviour can be distinguished. For the more concentrated solutions (30 and 40 wt %), the quasi-Newtonian behaviour is found over the whole shear rates range. As shown in Table IV.1, fitting the experimental results with Ostwald's law (equation IV.1) leads to $n = 0.994$ and $\kappa = 1.078$ for a concentration of 40 w% and $n = 0.975$ and $\kappa = 0.760$ for the 30 wt% sample. The value of n close to 1 confirms the highly Newtonian character of these two solutions. In the case of the two lowest concentrations (10 and 20 wt %), the variation of apparent viscosity η as a function of shear rate is discontinuous. As a matter of fact, the viscosity curve appears as formed by the juxtaposition of two approximately linear segments with different slopes in the log-log system; therefore a simple model with two parameters cannot explain on its own the rheological behaviour over the entire shear rates range. The change of the slope appears at a critical shear rate $\dot{\gamma}_c$ all the smaller as the surfactant concentration is larger: $\dot{\gamma}_c \approx 0.7\ s^{-1}$ for $[R_7^F(EO)_8] = 20$ wt% and $\dot{\gamma}_c \approx 2\ s^{-1}$ for $[R_7^F(EO)_8] = 10$ wt%. In the low shear rates range, $\dot{\gamma} \in [0.1\text{-}\dot{\gamma}_c]\ s^{-1}$, the viscosity decreases and the shear thinning character is more important for the 10 wt% solution. In the highest gradients domain, the values of the two constants n and κ are computed by fitting the experimental data to the two parameters model; one gets: $n = 0.97$ and $\kappa = 0.392$ for the 20 wt% solution and $n = 0.98$ and $\kappa = 0.198$ for the 10 wt% sample. Again the constant n is close to 1 in good agreement with the Newtonian character observed at the highest shear rate (see Figure IV.1b).

In order to compare the influence of the temperature, the variations of the apparent viscosity as a function of the shear rate for the four solutions at different temperatures (10, 20, 30 and 40°C), are reported in Figures IV.1c to IV.1f. Upon increasing the temperature, there are two obvious trends of changing in the evolution of the $R_7^F(EO)_8$ in water solutions. At the three largest concentrations (20, 30, 40 wt%, see Figure IV.3d, 3e, 3f), the point representing the solutions moves closer and closer to the miscibility curve. The temperature increase leads to a significant qualitative change in the viscosity curves.

At 10°C, a quasi-Newtonian behaviour is observed over a wide range of shear rates; the apparent viscosity η, almost constant in the range of low shear rates, decreases afterwards at higher shear rates (after a certain critical shear rate, $\dot{\gamma}_c$). The beginning of this decreasing segment is found to occur at a critical shear rate $\dot{\gamma}_c$ all the smaller as the concentration is higher. For example, for the 20 wt% solution $\dot{\gamma}_c \approx 24.5$ s^{-1} while, for the 30 wt% and 40 wt% samples $\dot{\gamma}_c \approx 16.8$ s^{-1} and ≈ 13.4 s^{-1}, respectively. The apparent viscosity also increase with the concentration; κ = 1.419, 8.872 and 11.88 Pa.s^n. Then as the temperature is increased, the initial Newtonian character disappears, the solution is shear thinning at low shear rates and this character is the stronger for the highest temperatures. This change in the rheological behaviour related to the temperature rise is significant of a structural change of the particles in solution. If we focus on the temperature increase from 20 up to 40°C for the 20, 30, 40 wt% samples, the change from the Newtonian to the shear thinning behaviour is first noticed at 20°C for the 20 wt% $R_7^F(EO)_8$ (n = 0.970), until getting the strongest shear thinning curve at 40°C (n = 0.780). Meanwhile, the 30 and 40 wt% solutions keep the Newtonian character until 30°C (n = 0.991 and 0.998 respectively for the 30 and 40 wt% solutions), and finally turn to be strongly shear thinning at 40°C. This change of the rheological behaviour from Newtonian to shear thinning suggests that the temperature has a less important effect in the system with the larger surfactant concentration. In the low shear rates range, the apparent viscosity η of 20 wt% solution at 40°C is greater than at 10, 20°C and 30°C (Figure IV.1d), whereas it only exceed the viscosity of the solutions at 30 and 40 wt% for the two temperatures 20°C and 30°C (Figure IV.1e and f).

Shrestha et al.[1] reported that an increase of the temperature results in an increase of the size of nonionic surfactants micelles and that one can expect the formation of long cylindrical micelles at higher temperatures. This hypothesis is consistent with the solution behaviour at 40°C; as a matter of fact, the fast decrease of the viscosity η under weak shearing reflects an easy orientation of the particles and the average orientation is all the faster as the micellar length is large.

On the other hand, another trend is revealed at the lowest concentration tested of 10 wt% (Figure IV.1c). The Newtonian behaviour is found at 10°C, the viscosity remains quite low and almost constant at 0.06 Pa.s without decreasing at higher shear rates, unlikely the behaviour of the other solution having a higher surfactant concentration. Upon increase the temperature to 20°C, the viscosity value increases with discontinuous manner (initial shear thinning character then Newtonian as describe above). At 30°C, the viscosity curve becomes Newtonian again then turns to shear-thinning behaviour at 40°C.

4.1.1.2 Dynamic rheological behaviour

For this type of rheological experiment, the solutions are subjected to a sinusoidal deformation in the linear strain region. The maximum angular frequency is 500 rad/s. The effect of the surfactant concentration at 20°C is summarized in Figure IV.2a.

At the given temperature of 20°C (Figure IV.2a), the overall behaviour of the four solutions is the same: the storage modulus *G*' is always smaller than the loss modulus *G*''; the viscous character prevails over the entire frequency range. Apart from some fluctuations of the storage modulus *G*' at low frequencies probably due to the limitations of the equipment, the experimental distribution is close to the line of slope 2 (see Figure IV.2a), the dashed straight line); it is a corroboration of the viscoelastic characteristic of the solution. The loss modulus *G*'' distribution gather remarkably well around the line of slope 1.

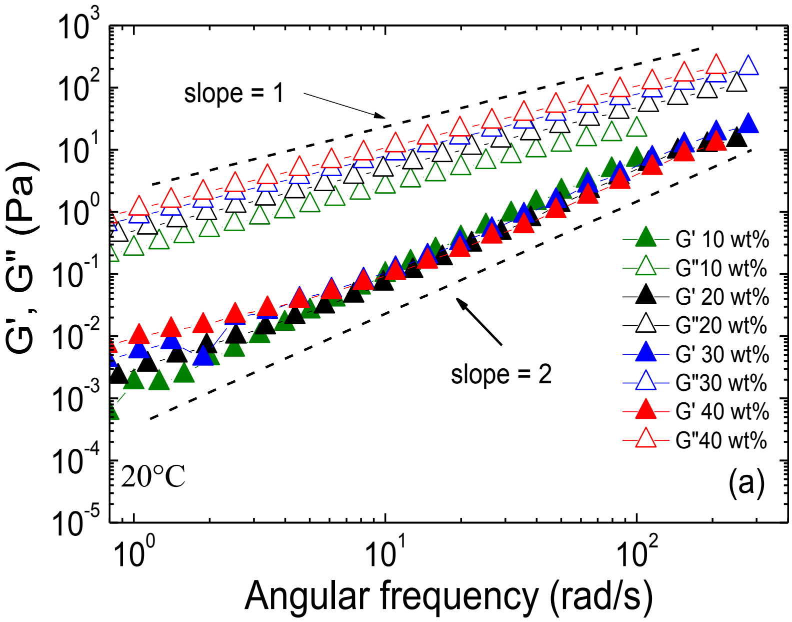

Figure IV.2 Storage modulus *G*' (solid symbols) and loss modulus *G*'' (open symbols) as a function of the angular frequency ω: (a) at a constant temperature 20°C.

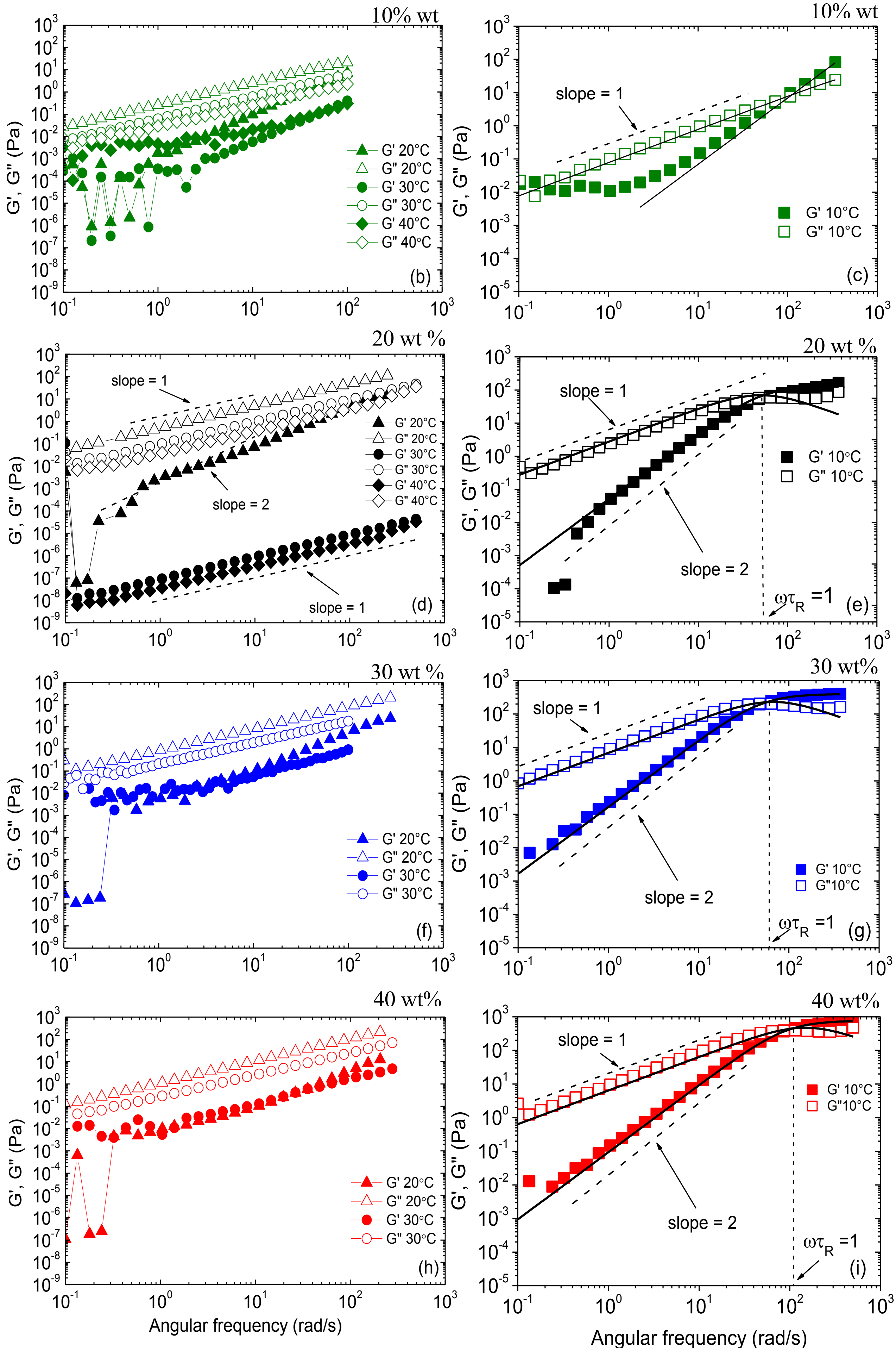
10% wt
10% wt
G', G" (Pa)
G' 20°C
G" 20°C
G' 30°C
G" 30°C
G' 40°C
G" 40°C
(b)
slope = 1
G' 10°C
G" 10°C
(c)
20 wt %
20 wt %
slope = 1
slope = 2
slope = 1
(d)
slope = 1
slope = 2
$\omega\tau_R$ =1
(e)
30 wt %
30 wt%
(f)
slope = 1
slope = 2
G"10°C
$\omega\tau_R$ =1
(g)
40 wt%
40 wt%
(h)
slope = 1
slope = 2
$\omega\tau_R$ =1
(i)
Angular frequency (rad/s)
Angular frequency (rad/s)
10^{-9} … 10^{3}
10^{-5} … 10^{3}
10^{-1} 10^{0} 10^{1} 10^{2} 10^{3}

Figure IV.2 (continued) Storage modulus *G*' (solid symbols) and loss modulus *G*'' (open symbols) as a function of the angular frequency ω: at different $\mathrm{R}_7^{\mathrm{F}}(\mathrm{EO})_8$ concentrations in water; at the various concentrations of (b) 10, (d) 20, (f) 30 and (h) 40 wt% at different temperatures (20, 30 and/or 40°C). At the constant 10°C of (c) 10 wt%, (e) 20 wt%, (g) 30 wt%, (i) 40 wt%; *G*' and *G*'' intersect at the "crossover" point for which $\omega\tau_{\mathrm{R}} = 1$, except for 10 wt%. From the intersection coordinates, the computed relaxation time (τ_{R}) turns out to be 0.02s. The solid curves represent the Maxwell's theoretical model. Two dashed lines of slope 1 and 2 are added to serve as a visual guide.

Note: The result of the 30 and 40 wt% solutions at 40°C have not been shown, because of a too narrow linear region range during amplitude sweep tests.

In the case of a single concentration and different temperatures, the loss moduli *G*'' are generally prevailing over *G*' (Figure IV.2b-2i); both moduli increase with increasing the angular frequency in different degrees. In order to consider the influence of the temperature increase on the behaviour of *G*' and *G*'', the surfactant concentration of 20 wt% $\mathrm{R}_7^{\mathrm{F}}(\mathrm{EO})_8$ has been chosen for interpretation here. The experimental distributions of *G*' and *G*'' as a function of the angular frequency ω are reported in Figures IV.2d and IV.2e. For the two highest temperatures (30 and 40°C), the viscous character of the solution always predominates; the elastic modulus *G*', always very small, ranges between $10^{-8} < G' < 10^{-6}$ Pa. For the two lowest temperatures (10 and 20°C) and particularly at 10°C (see Figure IV.2e), the variations of *G*' and *G*'' under sinusoidal strain are reminiscent of a Maxwellian fluid: $G''(\omega)$ is a linearly increasing (in a log-log scale) function of ω within the interval $5\times10^{-1} < \omega < 4\times10^{1}$ rad/s and $G'(\omega) \sim \omega^{n}$ with a slope n ~ 2.

In addition, at the temperature of 10°C for the 20, 30 and 40 wt % of $\mathrm{R}_7^{\mathrm{F}}(\mathrm{EO})_8$ solutions (Figure IV.2e, 2g, 2i), *G*' and *G*'' intersect ("crossover" point) at an angular frequency ω of 55, 60 and 102 rad/s. At these particular positions, the product $\omega\tau_{\mathrm{R}} = 1$; $\tau_{\mathrm{R}} = [\tau_{\mathrm{break}}\tau_{\mathrm{rep}}]^{1/2}$ is the terminal relaxation time, while τ_{break} is the breaking time of the micelles and τ_{rep} is the reptation time. From the "crossover" point, we easily calculate the relaxation time τ_{R} which turns out to be ≈ 0.018, 0.017 and 0.010 s, respectively.

In the range of high angular frequencies ($\omega > 10^2$ rad/s), G' converges to the plateau modulus G_0, which is related to the zero shear viscosity and the relaxation time by:

$$\eta_0 = G_0.\tau_R \qquad \text{(equation IV.5)}$$

By averaging G' over the last few values obtained at high frequency, we obtain $G_0 \sim G'_{\text{average}} = 117$, 382 and 702 Pa in the case of 20, 30 and 40 wt% solutions. Taking into account the calculated value of the relaxation time, we obtain for η_0 a value of 2.11, 6.49 and 7.02 Pa.s. These calculated zero shear viscosity values are close to the value extrapolated from the viscosity curve at low shear rates, within the same order of magnitude. (see Figure IV.1d, 1e, 1f; symbol ■ 🟦 🟥).

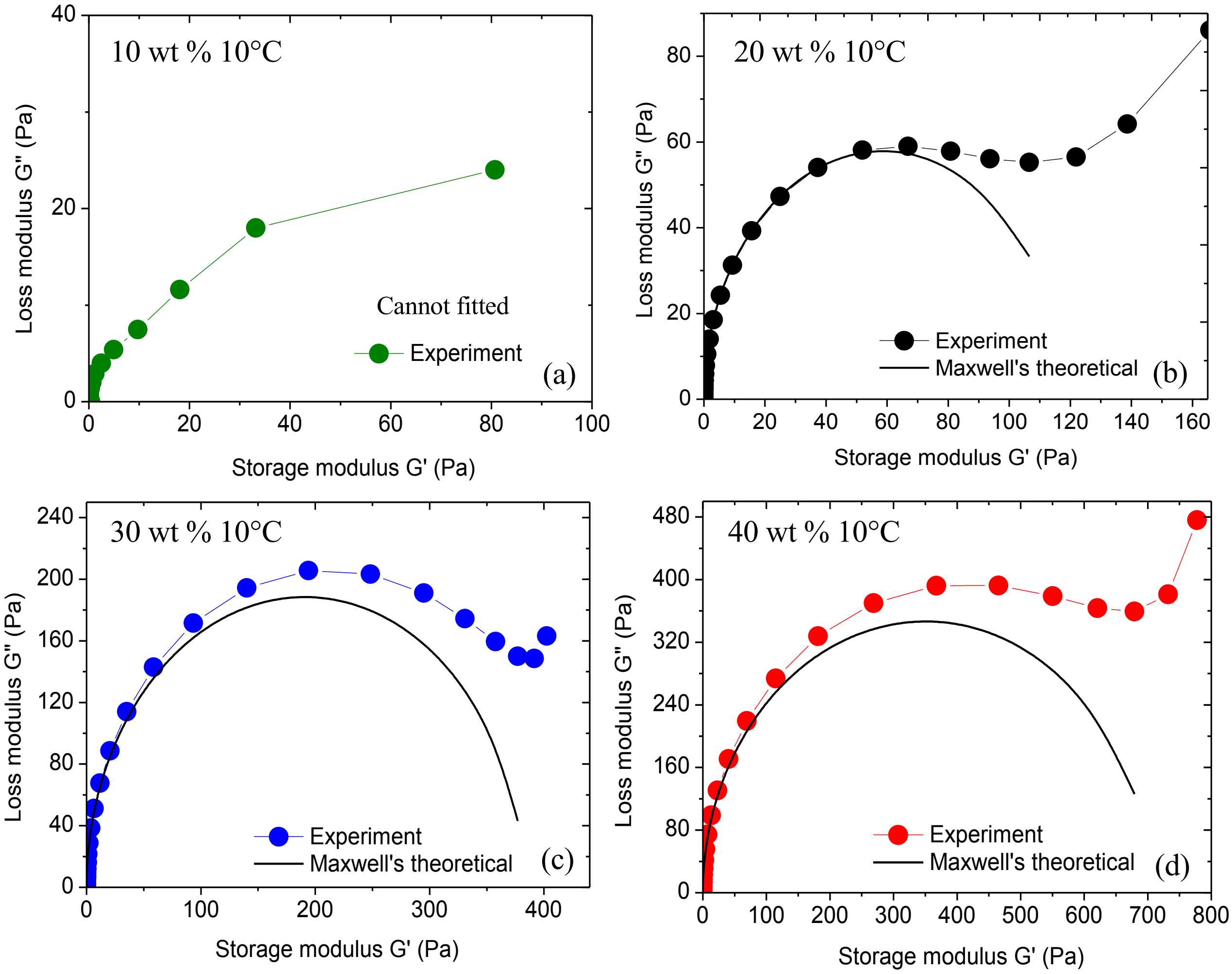

Figure IV.3 Cole-Cole plot $G''(G')$ at 10°C of $R_7^F(EO)_8$ (a) 10, (b) 20, (c) 30 and (d) 40 wt % in water. The circle symbols correspond to the experimental points and, in each graph, the black continuous curve represents the computed Maxwell's theoretical model taking for the plateau modulus G_0: 117, 382 and 702 Pa respectively for the 20, 30 and 40 wt % $R_7^F(EO)_8$ solutions.

In each graph of Figure IV.3, the black continuous curve represents Maxwell's theoretical model computed with G_0 = 117, 382 and 702 Pa respectively for the 20, 30 and 40 wt % $R_7^F(EO)_8$ solutions.

At 20 wt% $R_7^F(EO)_8$, the experimental results fit well to Maxwell's theoretical curve. In the low frequency range, the theoretical curve is in good agreement with the experimental values; however, at high frequencies, G'' departs significantly from the circle, decreasing to a minimum $G''_{\min}$ before increasing again. Upon increasing the concentration to 30 and 40 wt%, the deviation from the model becomes more and more obvious and at 10°C, for the 10 wt% solution even disappears.

Based on a wormlike micelle model [2], we can calculate some characteristic values like τ_{break} and G_0.

At 20 wt% $R_7^F(EO)_8$, the minimum $G''_{\min}$ occurs for the angular frequency $\omega = \omega^* = 207$ rad/s from which we can compute the breaking time τ_{break} of the micelles [3]:

$$\tau_{break} \approx 1/\omega^* = 5ms \qquad \text{(equation IV.6)}$$

Also, from the plateau modulus G_0, one can compute the hydrodynamic correlation length ξ_H which can be regarded as the average entanglement length [4]:

$$G_0 = k_B T/\xi_H^3 \qquad \text{(equation IV.7)}$$

Where k_B stands for Boltzmann's constant. Taking for: G_0 = 117 Pa, T = 283 K and k_B = 1.38 10^{-23} SI, one finds: ξ_H = 32 nm.

As described above, we can also calculate these parameters from Maxwell's model applied to the 30 and 40 wt % $R_7^F(EO)_8$ solution. The results are summarized in Table IV.2.

Table IV.2 The calculated parameters from Maxwellian theoretical model at T= 283K.

$R_7^F(EO)_8$/water	τ_R (s)	G_0 (Pa)	η_0 (Pa.s)	ω^* (rad/s)	τ_{break} (ms)	ξ_H (nm)
10 wt%	-	-	-	-	-	-
20 wt%	0.018	117	2.11	207	4.8	32.2
30 wt%	0.017	382	6.49	242	4.1	21.6
40 wt%	0.010	702	7.02	286	3.5	17.6

τ_R, relaxation time (s); G_0, plateau modulus (Pa); η_0; zero shear viscosity (Pa.s); ω^*, angular frequency at the minimum G''_{min}; τ_{break}, breaking time of the micelles, ξ_H, hydrodynamic correlation length. (The results at 10 wt% $R_7^F(EO)_8$ are not presented, because of a poor agreement with the model).

At this low temperature of 10°C, the increase of the concentration leads to an increase of the macroscopic parameters G_0 and η_0, but to a decrease of the microscopic quantities τ_{break} and ξ_H.

4.1.1.3 Stress cycle

Starting from σ_M = 10 Pa, the sample is at first subjected to a decreasing shear stress σ down to different minima σ_m (step 1); σ is then kept constant during 60 mn (step 2) and finally the stress is gradually brought back to the maximum σ_M (step 3). The temperature is kept constant at 20°C, the concentration is 20 wt% and the duration of a whole cycle is 4020s.

Figure IV.4 displays the variations of the apparent viscosity vs. the stress during the three steps cycle experiment for two temperatures: 20°C (Figure IV.4a) and 10°C (Figure IV.4b). During the first step, the apparent viscosity η is constant over the entire stresses range: the solution is clearly Newtonian; during step 2, σ is kept constant, η increases sharply and reaches a value much larger than the constant apparent viscosity of step 1; finally during the last step, η decreases again and, in the high stresses range, both viscosity curves $\eta(\sigma)$ superimpose again.

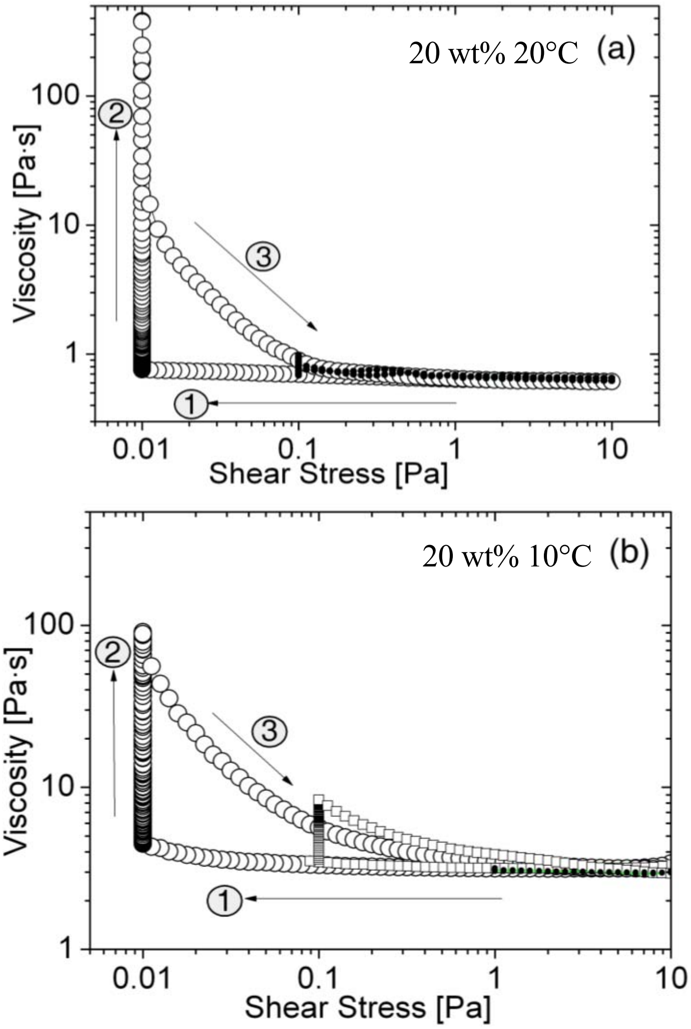

Figure IV.4 Apparent viscosity η as a function of the shear stress σ during the three steps cycle for a sample at 20 wt% $R_7^F(EO)_8$ in water; step 1: decreasing stress from σ_M = 10 Pa to σ_m, step 2: constant stress at σ_m, step 3: increasing stress up to σ_M ; (a) T = 20°C, σ_m = 0.1Pa (●), 0.01Pa (○); (b) T= 10°C, σ_m = 0.01Pa (○), 0.1Pa (☐), 1Pa (●).

The highest stress value σ_M is always the same (10 Pa) as well as the duration of step 2 (3600s), but different values have been chosen for σ_m: 1, 0.1 and 0.01Pa. Although the whole cycle is rather long, no significant increase of the apparent viscosity due to evaporation is seen in the high stresses range after step 3 since the two distributions are well superimposed. We also noticed that the viscosity increase in step 2 depends, for a given temperature, on the value of σ_m and the larger σ_m, the smaller value gives rise to the larger increase of the viscosity. For a temperature of 10°C and σ_m = 1 Pa, step 2 even disappears, it thus seems that it exist a yield stress between 1 and 0.1 Pa. It should be emphasized that the highest values of η in step 2 do not have any physical meaning; they are the results of the computation of the ratio $\sigma / \dot{\gamma}$ with $\dot{\gamma}$ getting very small and unreliable as the viscosity increases. We thus formulate the hypothesis that the increase of the viscosity is due to the building up of aggregates, due to weak forces between the micelles.

4.1.1.4 Evolution of the zero shear viscosity with the concentration of surfactant

The zero shear viscosities are plotted as a function of the mass fraction of surfactant ϕ_{mass} Figure IV.5 for the temperatures of 10 and 20°C. Both definitions; the zero shear viscosities (non linear measurements) and the complex viscosities (linear measurements), give rise to the same values as expected (Figure IV.5). The measurements at low concentration are also performed by capillary viscometers (see in Chapter 2.2.3).

For very dilute concentrations (dilute regime), the zero shear viscosity varies linearly according to $\eta_0 = \eta_w (1 + k\phi_{mass})$ where ϕ_{mass} is the mass fraction of the dispersed phase, and k a coefficient that is sensitive to the shape of the micelles [5]. The best fit of the experimental data with the relation $\eta_0 = \eta_w (1 + k\phi_{mass})$ is obtained for k = 46 (dotted curve on Figure IV.5).

As the concentration increases, the data deviates from the linear model for both temperatures, indicating the semi-dilute regime is reached. Above 2% mass fraction of surfactant, the η_0 values keep increasing with a power law of 3.5 for both temperatures. This power law is valid up to the highest concentration tested at 10°C while at 20°C, a linear regime is encountered for concentrations larger than 5 wt% of surfactant. At 20°C, fits of the data in the range [5-40 wt%] indicate that the viscosity increases linearly as $\eta_0 = 2.5\phi_{mass}$ and $\eta_0 = 2.6\phi_{mass}$ for non-linear and linear rheology measurements respectively.

The power law of 3.5 (solid line) observed at both temperatures in the semi-dilute regime is reminiscent of the model proposed by Cates for the stress relaxation of wormlike micelles [6] [7]. This model is based on the Maxwellian behaviour of the wormlike micelles, and confirms the Maxwellian character observed in linear rheology at 10°C. However at 20°C, the viscosity for samples of concentration larger than 5 wt% increases linearly and the scaling law of 3.5 is lost. This suggests that the Maxwellian character of the solution at 20°C is lost for those concentrations.

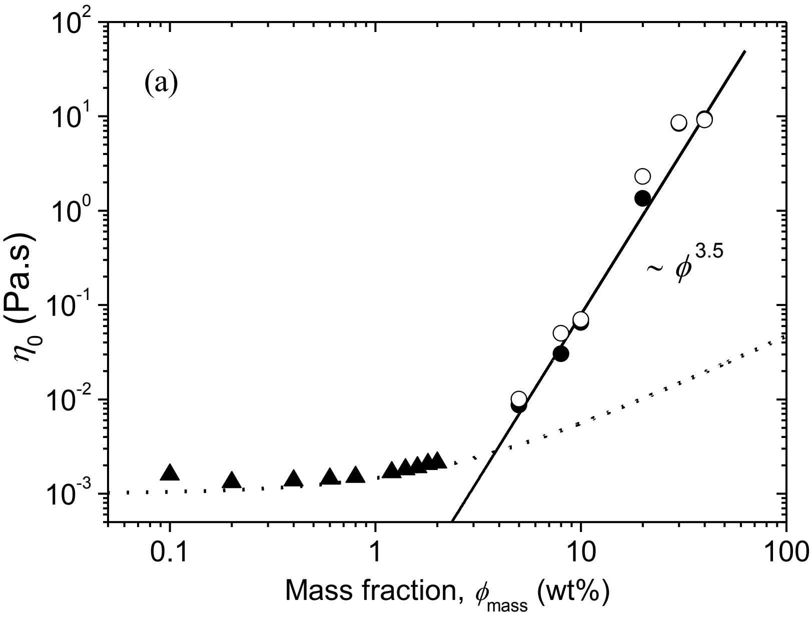

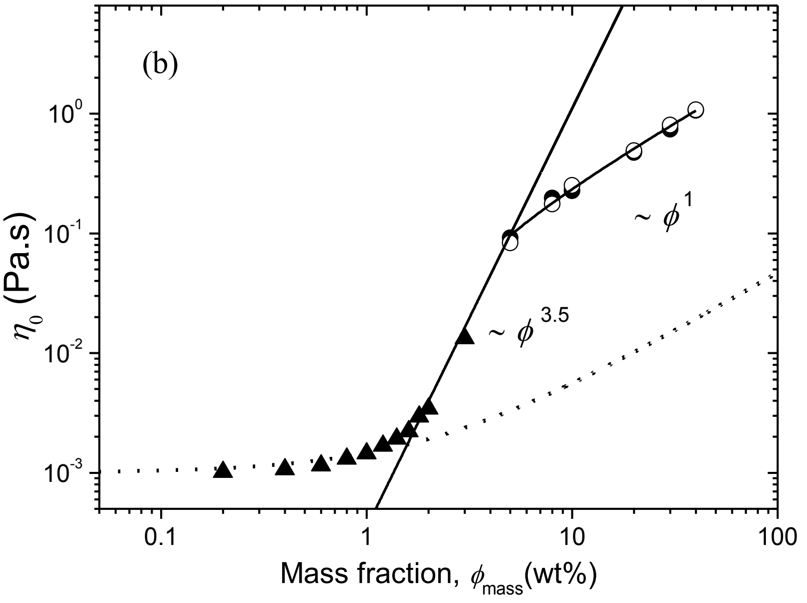

Figure IV.5 Zero-shear viscosity η_0 as a function of mass fraction ϕ_{mass} of $R_7^F(EO)_8$ in water at (a) 10 and (b) 20°C. The η_0 values are obtained from non linear rheology (solid circles), linear rheology (empty circles) and capillary viscometry (solid triangle). The dotted line is the fit of the data in the dilute regime $\eta_0 = \eta_w (1 + 46\phi_{mass})$, the solid line indicates a power law of 3.5 and the dashed lines are linear fits of the data in the interval of mass fraction [5-40 wt%] giving slopes respectively of 2.5 and 2.6 for non-linear and linear rheology measurements.

These results suggest that at least in the semi-dilute region the micelles start to grow as $\phi_{mass}^{0.5}$[6] [7]. However at a temperature of 20°C it seems that this regime of growing micelles is terminated at concentrations larger than 5 wt% and reaches a regime where the viscosity grows linearly with a slope of 2.5 to 2.6.

The rheological and structural study of our system was performed in the concentration range of 10 to 40 wt%. In this concentration range, the variation of the zero-shear viscosity with the concentration depends on the temperature: it increases linearly at 20°C and with a power law of 3.5 at 10°C. This shows that we work in a different regime for each temperature. This is coherent with the modification of the rheological behaviour observed as the temperature increases from 10 to 20°C.

From these studies, we can summarize the three rheological properties of the L_1 phase behaviour in Figure IV.6. The micellar solutions behave either like Newtonian fluids, shear thinning ones or even like Maxwellian fluids depending on the thermodynamical conditions. In the next sections, we propose to carry out further experiments by birefringence and small angle neutron scattering technique, with solutions in the L_1 domain.

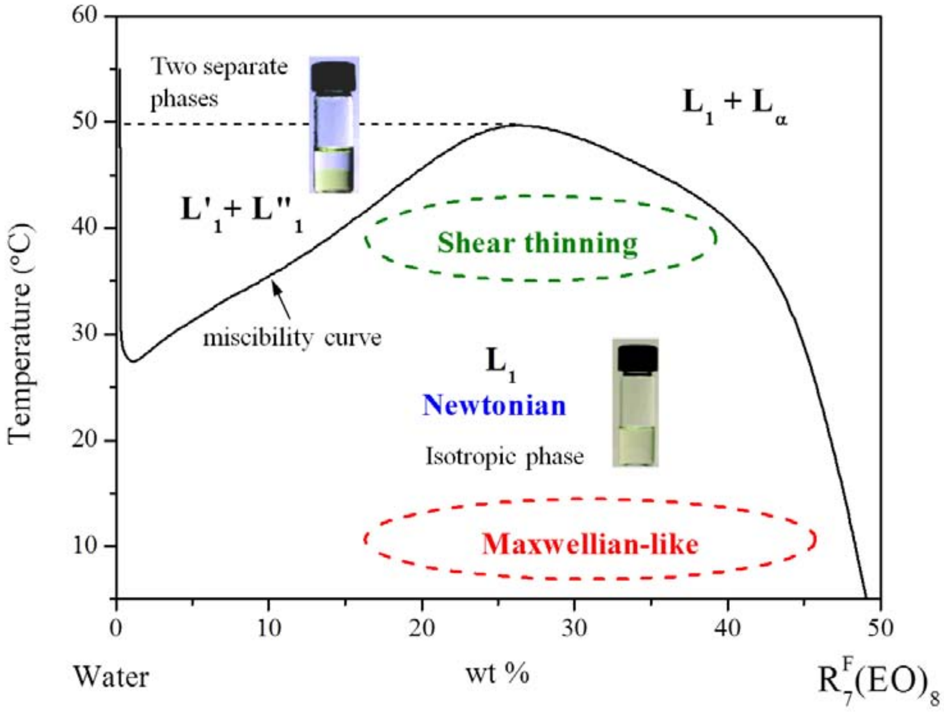

Figure IV.6 The three rheological behaviours of $R_7^F(EO)_8$ in water under L_1 phase.

4.1.2 Flow birefringence

As quoted before in chapter 2, the flow birefringence experiments are performed on a polarimetric bench and the two quantities of interest, i.e. χ and Δn merely computed from the measurements done using the method of Sénarmont [8].

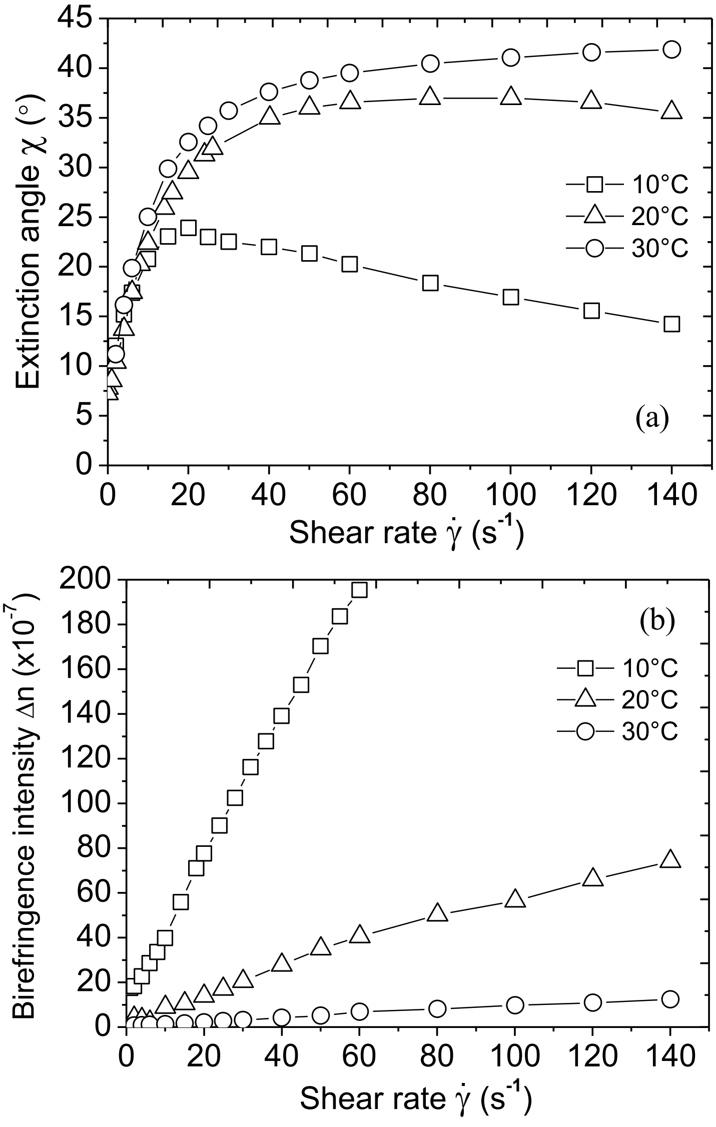

Figure IV.7 Flow birefringence experiments: (a) extinction angle χ, (b) birefringence intensity Δn vs. the shear rate. The concentration is 20 wt % $R_7^F(EO)_8$ in water and the temperature 10°C (□), 20°C (△) and 30°C (○).

Figures IV.7a and 7b respectively report the variations of the extinction angle χ and of the birefringence intensity Δn versus the shear rate for three temperatures 10, 20 and 30°C.

Starting from a few degrees, χ increases at first in the low shear rates range with the same evolution for the three temperatures. Upon increasing the shear rate, the angle of the solution at 10°C reaches a sharp maximum at $\dot{\gamma}_c \approx 20\ s^{-1}$, before decreasing again in a quasi linear way; for the two highest temperatures, the evolution is slightly different. At 20°C, the maximum is broader, occurs approximately for $\dot{\gamma}_c \approx 80\ s^{-1}$ and χ decreases slowly in the high shear rates domain. Finally at 30°C, no clear maximum is observed but the angle tends smoothly toward a plateau value close to 40°. This peculiar evolution of the extinction angle χ completely disagrees with the orientation theory of the streaming birefringence which states that the angle should decrease from 45° towards 0° with the shear rate. A similar unexpected evolution of χ has already been reported in aluminium soap solutions subjected to shear flows[9] and in amylase in ethylenediamine-glycol[10]. In the orientation theory of birefringence, a value of the extinction angle close to 45° is an indication of small particles poorly orientated in the flow. The birefringence intensity Δn is increasing linearly in the whole shear rates range for the three temperatures and for a given shear rate, Δn is all the smaller as the temperature is the higher. As a matter of fact, this is merely the result of the increasing influence of the Brownian motion at high temperature probably due to the existence of smaller micelles as suggested by the high value of χ. At moderate shear rates ($\dot{\gamma}_c \approx 25\ s^{-1}$) and 10°C, the order of magnitude of Δn is $\approx 10^{-5}$; this value can be regarded as very high for liquids. Δn is also found to be negative, thus the main contribution comes from the intrinsic birefringence of the particles.

However, as the rheological experiments in Figure IV.1, a Newtonian behaviour is usually characteristic of a fluid containing small asymmetrical particles oriented more or less at random. Thus there is no preferred orientation in the medium and the extinction angle χ should remain close to 45° at least in the low shear rate range where the shearing stresses are weak; at higher values of the shear rate $\dot{\gamma}$, χ should decrease with the shear rate. Therefore, the birefringence measurements are in opposition with the results of the rheology experiments. This unexpected result will be discussed later in the manuscript.

Although the sample is isotropic at rest, a simple impulse on the rotor of the shearing device induces birefringence which relaxes over several minutes. The medium is then anisotropic with an average orientation of ~5°. This result seems to indicate that large anisotropic objects exist at low shear rates and are gradually broken as $\dot{\gamma}$ is increased. Then as the shear rate is increased, χ increases for the two highest temperatures before leveling off; at 10°C, when $\dot{\gamma}$ approximately reaches 20 s^{-1}, χ reaches a maximum before decreasing again with $\dot{\gamma}$ as would a shear thinning fluid do.

4.1.3 Small angle scattering experiments

The SANS experiments were recorded on the D11 line of the Institut Laue-Langevin in Grenoble (ILL). The differential scattering cross section per unit volume $\frac{d\Sigma}{d\Omega}(q)$ curves are built from the results gathered at two distances of the pair sample-detector: 2.5 and 8m; with a wavelength of 6 Å, the scattering vector length thus lies in the range of 0.008 - 0.267 $Å^{-1}$. (For more details, see Chapter II, section 2.5.1)

Modelling program by J.C. Ravey

In order to interpret the experimental spectra $\frac{d\Sigma}{d\Omega}(q)$, a theoretical spectrum calculated for the model particles is compared to our data thanks to a program developed in SRSMC laboratory in Nancy by Jean-Claude Ravey. The model particles have a centrosymmetric structure consisting of 2 layers: a hydrophobic core and a hydrophilic corona (Figure IV.8). The composition of the samples and the masses, molar volumes and scattering lengths of the water and of the surfactant are known. The contribution of monomers to the total scattered intensity is neglected since the CMC is very weak ~10^{-5} $mol.l^{-1}$, thus all surfactant molecules are considered to be involved in the micelles. Based on a previous study on the same system at rest [11], we choose to adjust the experimental spectra with a model of elongated ellipsoidal particles (Figure IV.9).

Based purely on geometrical constraints, this is a probable shape of the micelles. The conformations of the hydrophilic and hydrophobic chains defined by the thicknesses of the hydrophilic (L_A) and hydrophobic (L_B) parts as well as the aggregation number (N_{ag}) of the micelles are adjustable, but geometrical constraints make them interdependent. The theoretical calculation of the scattered intensity leads to the determination of the area per polar head (S), the penetration of water into the surfactant film (α) and the dimensions of the particle (A and B) and hydrophobic core (A_{phobe} and B_{phobe}) (Figure IV.8), which provide the ellipticity p. As the used systems are not diluted, interaction potential which modifies the scattered intensity should be taken into account.

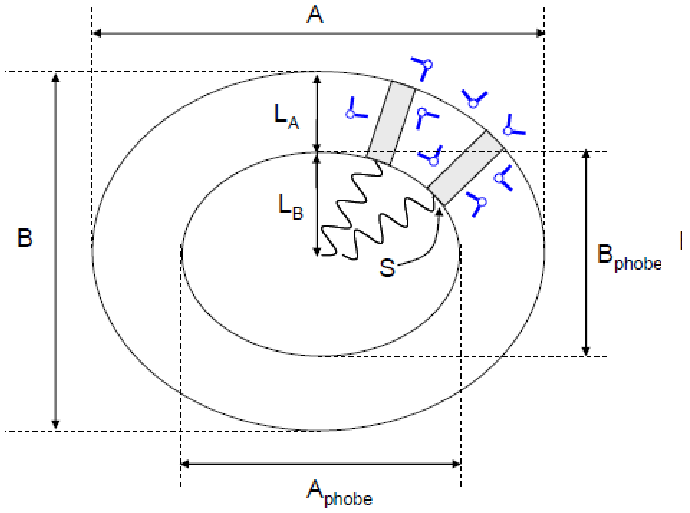

Figure IV.8 Schematic diagrams showing the various parameters defining the geometry of a micelle solution with A, B: size of the particle, A_{phobe}, B_{phobe}: dimensions of the hydrophobic core, L_A, L_B: hydrophilic and hydrophobic parts of the micelle and S polar head surface at the hydrophilic / hydrophobic interface.

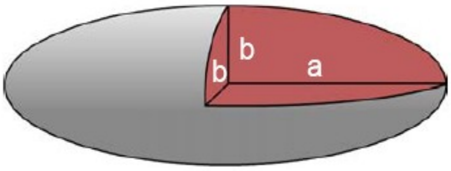

Figure IV.9 Representation of elongated ellipsoidal particle

The repulsive interactions are taken into account by using a hard sphere potential based on the Percus Yevick approximation. The hard sphere volume fraction is characterized by the parameter CET. If CET = 1, the hard sphere volume corresponds to the total volume of the particle; and if CET = 0, the hard sphere volume is calculated from the volume occupied by the hydrophobic chains of the surfactant. To this potential, an attractive interaction of Van der Waals origin is added. It is modelled by a potential well of width 1 to 2 Angstroms and which depth, of a few kT, constitutes a parameter quantifying the intensity of the attraction[12]. The adjustment of theoretical and experimental curves is obtained using a least squares method.

The characteristics of the surfactant $R_7^F(EO)_8$ studied are gathered in the following Table IV.3 (density, b, M, V, chain lengths).

Table IV.3 The characteristics of the constituting molecules in the studied system, described in F. Michaux thesis [11].

		Density	b (10^{-12} cm)	M ($g.mol^{-1}$)	V ($cm^3.mol^{-1}$)	Chain length (nm)
H_2O		1	-0.169	18	18	
D_2O		1.1	1.909	20	18	
$R_7^F(EO)_8$	Surfactant	1.35	16.438	744	551.1	
	Hydrophilic chain	1.13	3.331	347	307.1	2.80
	Hydrophobic chain	1.60	13.107	397	248.1	1.26

Density, coherent scattering length (b), molecular weight (M), molar volume (V) and length of hydrophilic and hydrophobic chains (extended) of molecules.

The experiments were performed for one concentration of the $R_7^F(EO)_8$ solution (20 wt% in heavy water (D_2O) at two temperatures: 10 and 20°C. The results obtained in birefringence experiments and linear rheology suggest that the micelles are not isotropic, even at rest. To obtain information about the structure of the sample, we thus performed preliminary experiments at rest. SANS experiments under flow were then conducted thanks to a Couette device set on a Bohlin rheometer on the D11 line. The evolution of the scattered spectra as a function of the shear rate $\dot{\gamma}$ could be then described. The sample was subjected to increasing values of the shear rate and measurements performed after duration of 120 and 300s respectively for the two sample-detector distance: 2.5 and 8m.

4.1.3.1 SANS at rest

The spectra were recorded at rest for the temperature T = 20°C, and at a $\dot{\gamma}$ = 0.1 s^{-1} sufficiently low to consider it did not modify the structure of the sample for the temperature T = 10°C (as will be confirmed by SANS experiments conducted under shear).

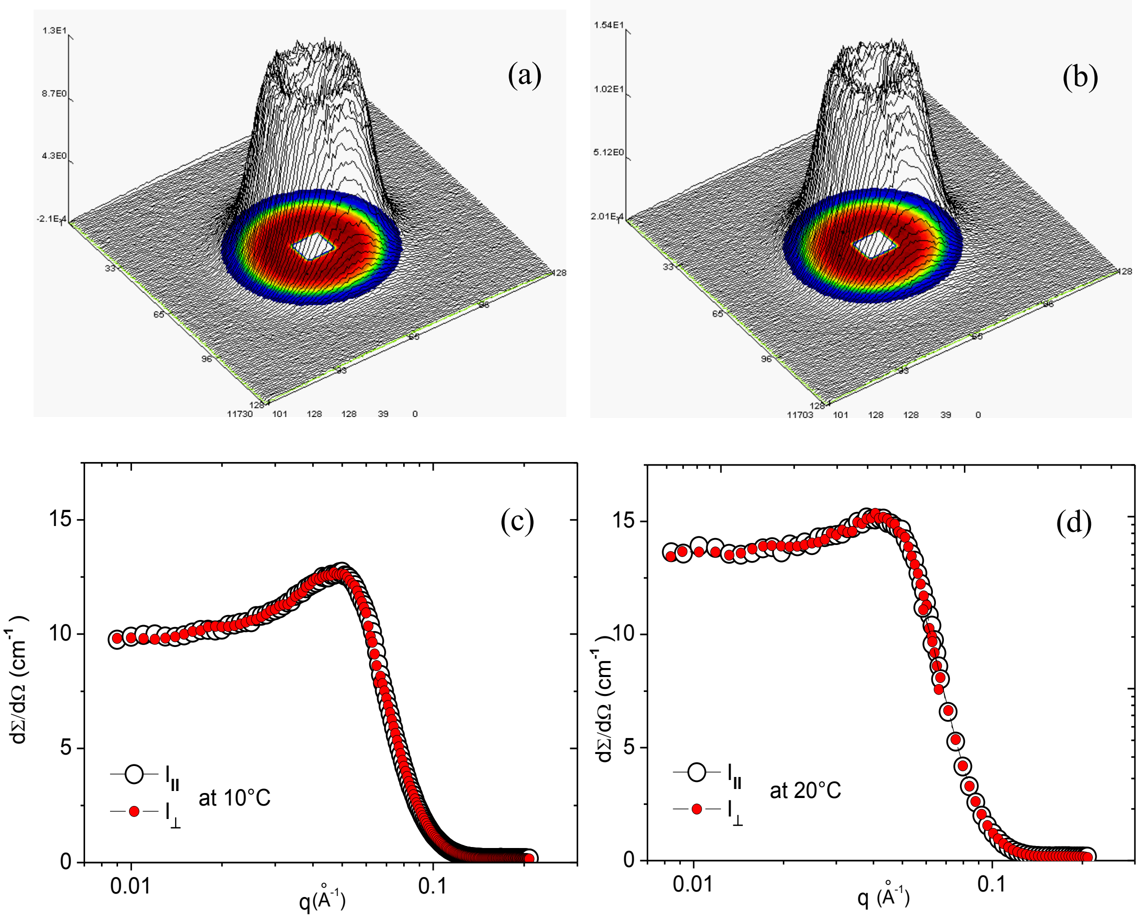

Figure IV.10 Absolute contour plot 3D for the 20 wt % $R_7^F(EO)_8$ micellar solution (in heavy water) at (a) 10°C at $\dot{\gamma}$ 0.1 s^{-1} and (b) 20°C at rest. The scattered intensity $I_{\parallel}$ *(q)* and $I_{\perp}(q)$, at (c) 10°C at $\dot{\gamma}$ 0.1 s^{-1} and (d) 20°C at rest.

Figure IV.10 (a and b) shows the tridimensional representations of the differential scattering cross-section contour plot represented as a function of the $q_{//}$ and $q_{\perp}$ plane coordinates for both temperatures. A linear color scale is used to code the values of the differential scattering cross-sections and superimposed on the 3D representations. Both spectra appear to be isotropic. This is confirmed by Figure IV.10 (c and d) which presents the differential scattering cross-sections $I_{\parallel}$ *(q)* and $I_{\perp}(q)$ averaged over 45° angular sectors centered respectively in the tangential velocity $\vec{V}$ and the vorticity $\vec{\omega}$ directions (see chapter II section 2.5). It is found that in the whole *q* range, and for both temperatures, $I_{\parallel}$ *(q)* and $I_{\perp}(q)$ superimpose perfectly. The $I_{\parallel}$ *(q)* and $I_{\perp}(q)$ curves are characteristic of a solution in which particles interactions are present: both intensity curves show a correlation peak which occurs respectively at $q^* = 0.041$ Å^{-1} at T=20°C and $q^* = 0.050$ Å^{-1} at T=10°C. A characteristic distance ξ, one can see as a correlation distance, can be deduced from the simple equation:

$$\xi = \frac{2\pi}{q^*} \qquad \text{(equation IV.8)}$$

It turns out that $\xi \approx 153$ Å at T = 20°C and $\xi \approx 125$ Å at T = 10°C.

The total scattering cross-sections for both temperatures, obtained by a circular average over the whole spectra, are compared in Figure IV.10. The increase of temperature from 10°C to 20°C leads to an increase of the scattering cross-section in the low q range ($q < 0.06$ A^{-1}), and in particular, to a higher value of the correlation peak $I(q^*_{10°C} = 12.6\ \text{cm}^{-1}) < I(q^*_{20°C} = 15.1\ \text{cm}^{-1})$. On the other hand, in the high q range ($q \in [q^*, 0.1$ Å^{-1}) the intensity curves for both temperatures superimpose indicating that the local structure of the micelles remains unchanged.

In order to obtain quantitative informations about the structure of the sample and interactions between particles, we used Jean-Claude Ravey modelling program to fit our experimental data. For the fits, we concentrated on the low q part of the curves, because that is where we observe a difference between 10 and 20°C. As previously mentioned, the size and shape of particles are determined on geometrical considerations N_{ag}, L_A and L_B. By adjusting the parameters of local structure, it is possible to deduce information about the interactions between the micelles. The blue and red lines in Figure IV.11 represent the best fits obtained for different parameters summarized in Table IV.4.

The theoretical fits fail to fit the experimental data over the whole q range: theoretical curves differ from the experimental data for q larger than 0.12 Å^{-1}. For both temperatures, the best agreement between the model and the data (at least in the low q range) was obtained for elongated particles of dimensions of about 20 by 7 nm, with no penetration of water into the surfactant film. The dimension B_{Phobe} of the hydrophobic core is almost twice the length of the hydrophobic chain of the surfactant (2 × 1.26 nm) which shows the hydrophobic chains are elongated. On the other hand the dimension of the hydrophilic corona given by $L_A = (B - B_{\text{phobe}})/2$ is about 1.7 nm, half the length of the hydrophilic chain of the surfactant: the hydrophilic chains are thus completely folded [11].

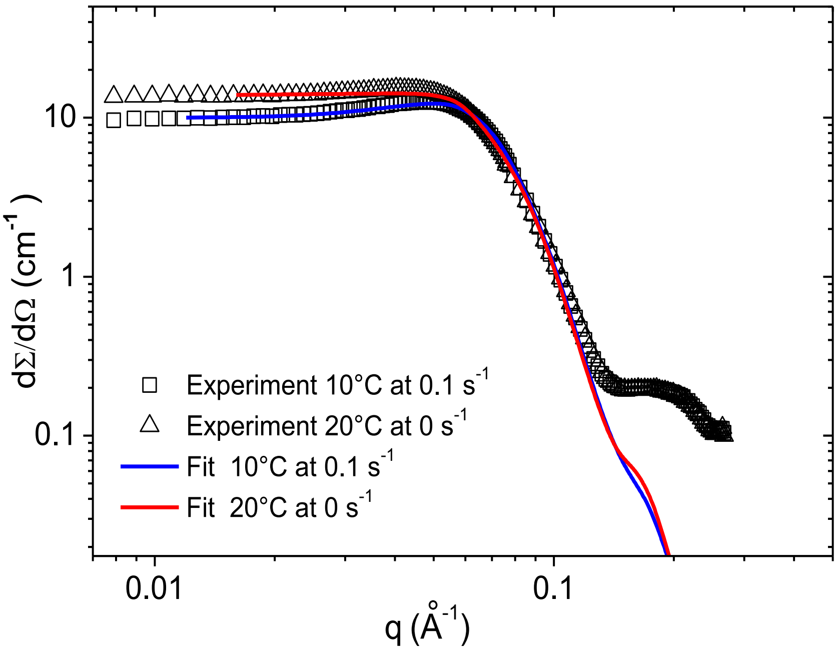

Figure IV.11 The scattering cross section, for the 20 wt % micellar solution at two temperatures: 10°C at 0.1 s^{-1} (□) and 20°C at rest (△).The best data fits by Ravey's model are also shown in the blue and red lines. All three case fits at 20°C show the same pattern as in the red line.

As the temperature is increased from 10 to 20°C, it is possible to fit the data with a fixed set of structural parameters of the individual micelles (including ellipticity and dimensions) by modifying only the interactions between the micelles: the effect of the interaction parameters are indeed limited to the low *q* range [11] (Figure fits, case 1 and 3). The results of the fits suggest that interactive attractions between the micelles (corresponding to either an increase of the absolute value of attractive potential or decrease of repulsive potential) increase with the temperature. This effect accounts for the observed increase of the scattering cross-section in the low *q* range and could be related to an increase of the number density of scattering centres with the temperature.

However changing the ellipticity of the micelles from p=5 to p=4 from 10 to 20°C (case2), all interaction parameters being left unchanged, also lead to a good fit of the experimental data, showing that the shift of the spectra in the low *q* range could originates in a structural modification of the micelles. This observation points out the limitations of the SANS experiments to draw a definitive conclusion about the structure of the micelles at both temperatures.

Table IV.4 Jean-Claude Ravey modeling parameters for 20 wt % $R_7^F(EO)_8$ /water micellar solution at 10 and 20 °C.

Conditions	N_{ag}	L_A (nm)	L_B (nm)	α	p	Repulsive potential	Attractive potential (kT)	A (nm)	B (nm)	A_{phobe} (nm)	B_{phobe} (nm)	S (nm^2)
10°C	260	1.68	1.26	0	5	0.7	-1.6	20.2	6.7	16.8	3.4	0.59
20°C (case 1)	260	1.68	1.26	0	5	0.7	-2.0	20.6	6.8	17.3	3.4	0.57
20°C (case 2)	260	1.68	1.26	0	4	0.7	-1.6	18.2	7.1	14.9	3.7	0.54
20°C (case 3)	260	1.68	1.26	0	5	0.6	-1.6	20.6	6.8	17.3	3.4	0.57

N_{ag} : aggregation number, α: number of water molecule per surfactant molecule (the penetration of water into the surfactant film), p: ellipticity, A, B: size of the particle, A_{phobe}, B_{phobe}: dimensions of the hydrophobic core, L_A, L_B: Length of the hydrophilic and hydrophobic parts of the surfactant and S polar head surface at the hydrophilic / hydrophobic interface.

4.1.3.2 SANS under flow

In order to compare the birefringence experiments with the SANS results, the same shear rates were applied for both experiments.

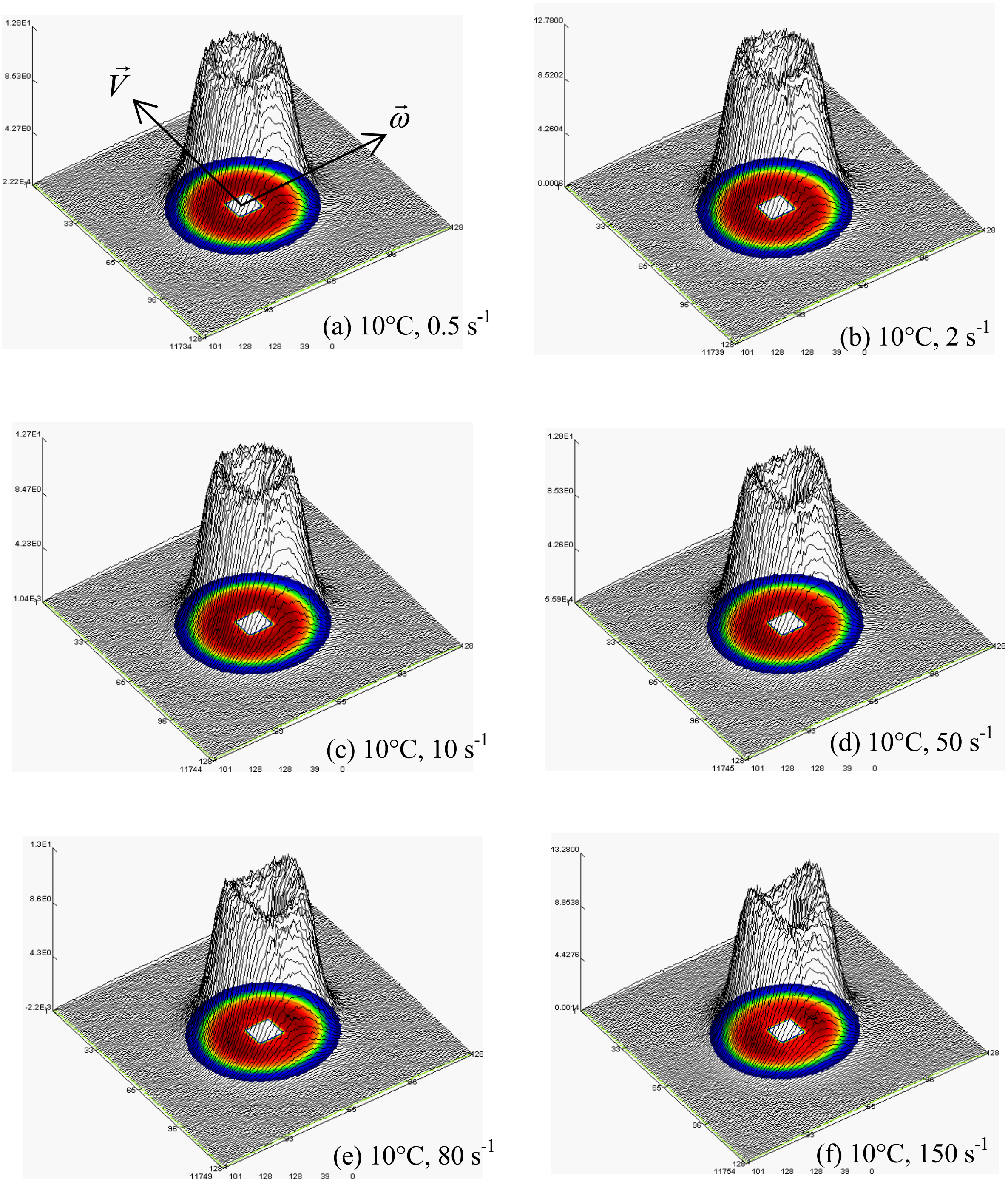

(a) 10°C, 0.5 s^{-1}

(b) 10°C, 2 s^{-1}

(c) 10°C, 10 s^{-1}

(d) 10°C, 50 s^{-1}

(e) 10°C, 80 s^{-1}

(f) 10°C, 150 s^{-1}

Figure IV.12 Iso-intensity surface plots at the temperature of 10°C for the 20 wt % micellar solution (in heavy water). Six values of the shear rates $\dot{\gamma}$ were used: (a) 0.5 s^{-1}, (b) 2 s^{-1}, (c) 10 s^{-1}, (d) 50 s^{-1}, (e) 80 s^{-1} and (f) 150 s^{-1}.

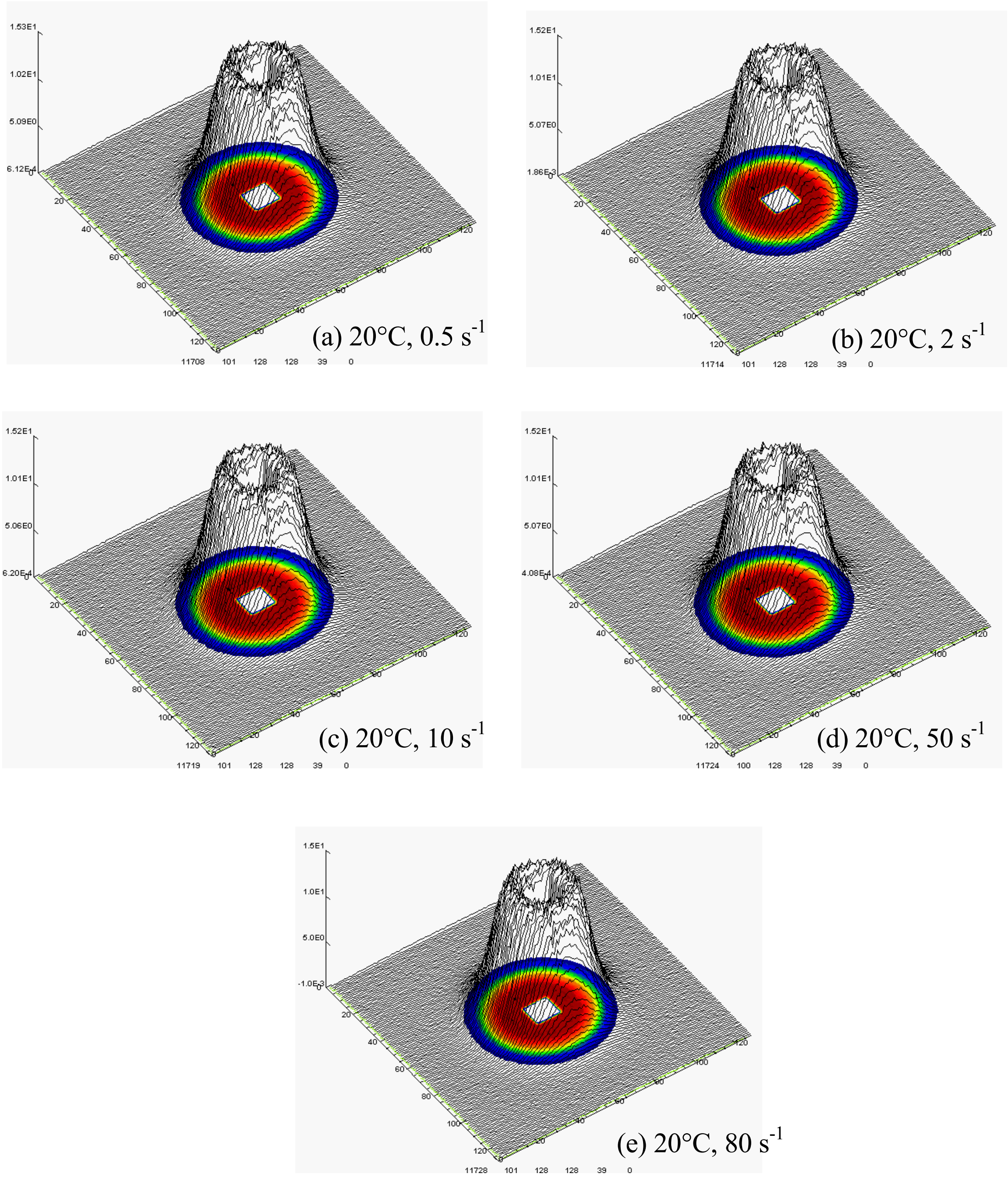

(a) 20°C, 0.5 s^{-1}

(b) 20°C, 2 s^{-1}

(c) 20°C, 10 s^{-1}

(d) 20°C, 50 s^{-1}

(e) 20°C, 80 s^{-1}

Figure IV.13 Iso-intensity surface plots at the temperature of 20°C for the 20 wt % micellar solution (in heavy water). Five values of the shear rates $\dot{\gamma}$ were used: (a) 0.5 s^{-1}, (b) 2 s^{-1}, (c) 10 s^{-1}, (d) 50 s^{-1} and (e) 80 s^{-1}.

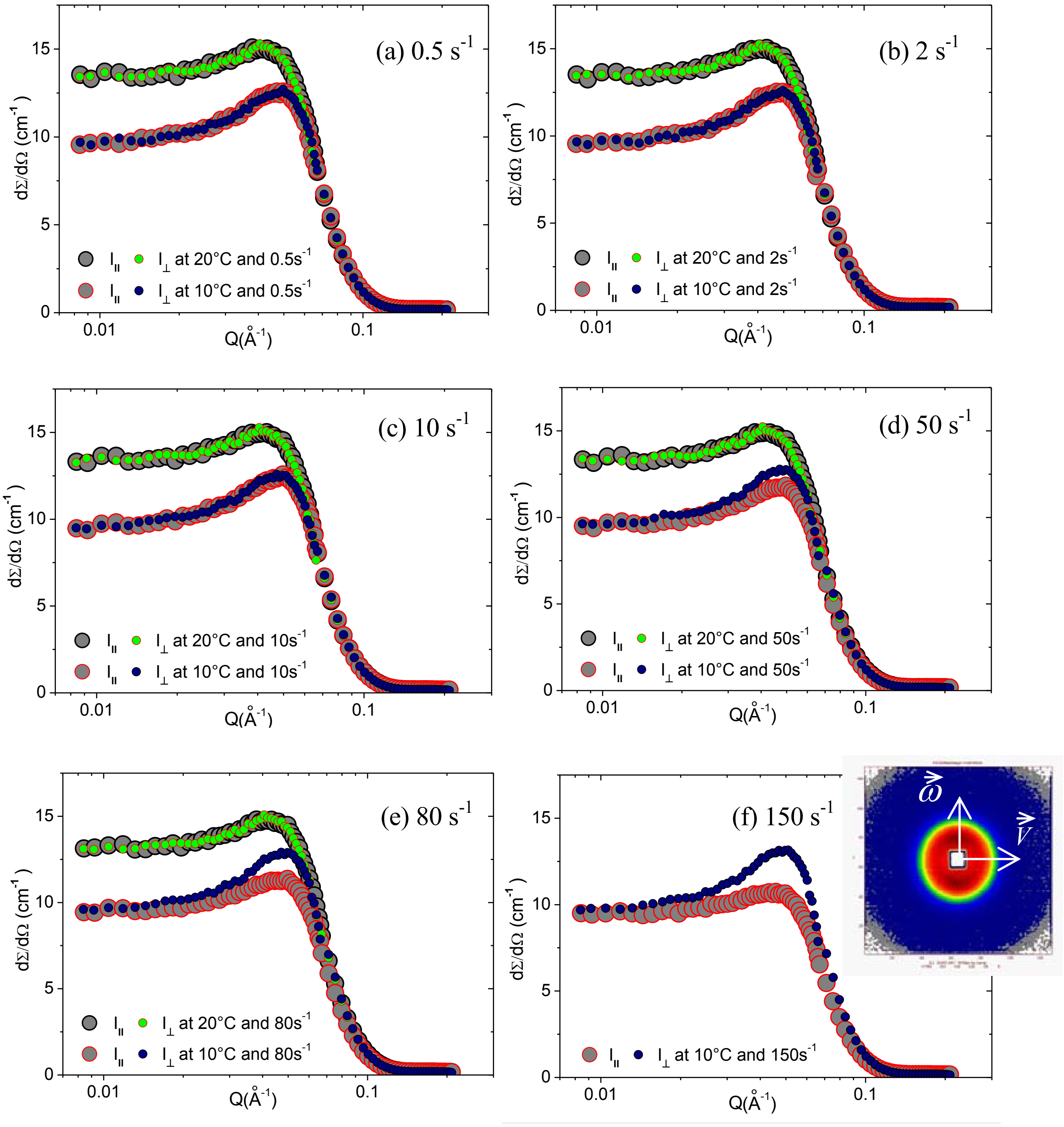

Figure IV.14 The scattered intensity $I_{||}(q)$ and $I_{\perp}(q)$ for the 20 wt.% micellar solution (in heavy water) at two temperatures: 10°C and/or 20°C. Six values of the shear rates $\dot{\gamma}$ were applied: (a) 0.5 s^{-1}, (b) 2 s^{-1}, (c) 10 s^{-1}, (d) 50 s^{-1}, (e) 80 s^{-1} and/or (f) 150 s^{-1}.

(a) Results at T = 10°C

Figure IV.12 represents the tridimensional representations of the differential scattering cross-section contour plot recorded at T = 10°C. The scattering patterns remain symmetrical for the lowest shear rates ($\dot{\gamma}$= 0.5, 2 and 10 s^{-1}) (Figure IV.12 a-c). Meanwhile, for the higher applied shear rates ($\dot{\gamma}$ = 50, 80 and 150 s^{-1}), anisotropy can be observed in the vorticity $\vec{\omega}$ direction (Figure IV.12 d-f) indicating an orientation of the structure in the flow direction. The isotropic nature of the sample at low shear rates also appears in the intensity curves $I_{\parallel}(q)$ and $I_{\perp}(q)$ which perfectly superimpose in the whole range of q at the lowest shear rates (Figure IV.14), while they clearly not superimpose anymore at $\dot{\gamma}$ = 50, 80 and especially at 150 s^{-1}.

q^* is easily found from the derivative of the $I_{\parallel}(q)$ and $I_{\perp}(q)$ curves. The computed results of its value under different shear rates are gathered in Table IV.5 No variations of q^* are observed as the shear is increased; moreover, q^* and thus the correlation distance in the sample remains close to its value at rest.

The total scattering cross-sections are plotted for all explored shear rates in Figure IV.15 in order to observe the qualitative characteristics of curves at different applied shear rates. The whole curve at low q shifts down obviously when the shear rate goes from 0.1 (nearly at rest) to 1 s^{-1}. Then, the differential scattering cross-section decreases gradually as a function of increasing shear rate in the range $0.02 < q < 0.07$ Å^{-1} (Figure IV.15c). This shift down of the correlation peak could suggest a loss of the correlation in the sample as the shear rate increases.

(b) Results at T = 20°C

The scattering cross-section spectra recorded at T = 20°C for different shear rates all appear isotropic and present a similar aspect to the spectrum recorded at rest (Figure IV.13). Figure IV.14 shows the intensity curves $I_{\parallel}(q)$ and $I_{\perp}(q)$ which perfectly superimpose in the whole range of q for all explored shear rates, demonstrating that the sample stays isotropic under shear.

The values of q^*, obtained from the $I_{||}(q)$ and $I_{\perp}(q)$ curves, are gathered Table IV.5. Again, the correlation distance in the sample remains close to its value at rest for the whole range of explored shear rates.

The total scattering cross-sections are plotted for all explored shear rates in Figure IV.15d. At 20°C, the differential scattering cross-section decreases in the whole range of the low q, showing a different behaviour than at 10°C.

Table IV.5 q^* ($Å^{-1}$) for the two components $I_{||}(q)$ and $I_{\perp}(q)$ of the 20 wt % $R_7^F(EO)_8$ in water under different shear rates at 10°C and 20°C.

Shear rate (s^{-1})	$0.5\ s^{-1}$		$2\ s^{-1}$		$10\ s^{-1}$	
q*	$I_{\|\|}$	$I_{\perp}$	$I_{\|\|}$	$I_{\perp}$	$I_{\|\|}$	$I_{\perp}$
T = 10°C	0,048 ± 0,0013	0,048 ± 0,0013	0,048 ± 0,0013	0,048 ± 0,0013	0,048 ± 0,0013	0,047 ± 0,0013
T = 20°C	0,042 ± 0,0013	0,041 ± 0,0013	0,041 ± 0,0013	0,041 ± 0,0013	0,041 ± 0,0013	0,042 ± 0,0013
Shear rate (s^{-1})	$50\ s^{-1}$		$80\ s^{-1}$		$150\ s^{-1}$	
q*	$I_{\|\|}$	$I_{\perp}$	$I_{\|\|}$	$I_{\perp}$	$I_{\|\|}$	$I_{\perp}$
T = 10°C	0,047 ± 0,0013	0,047 ± 0,0013	0,045 ± 0,0013	0,050 ± 0,0013	0,045 ± 0,0013	0,050 ± 0,0013
T = 20°C	0,041 ± 0,0013	0,041 ± 0,0013	0,042 ± 0,0013	0,041 ± 0,0013	nd	nd

nd = not determined.

(c) Discussion

For both temperatures, we found that the SANS results under shear differ from the results of birefringence experiments which already show optical anisotropy and alignment at the lowest value of the shear rate ($0.1\ s^{-1}$). But one has to remember that neutrons and visible light probe the sample on a completely different length due to the large difference in the wavelength of the beam (6 Å for neutrons and 6328 Å for the laser light). At that length scale, the behaviour of the sample under shear differs in for both temperatures: anisotropy is observed only at 10°C, for the highest shear rates, while the sample at 20°C stays isotropic. At 20°C, the effect of the shear rate is weaker than at 10°C. The effect of shearing is comparable to a decrease in temperature, and could be due to a structural change; for example a change in ellipticity.

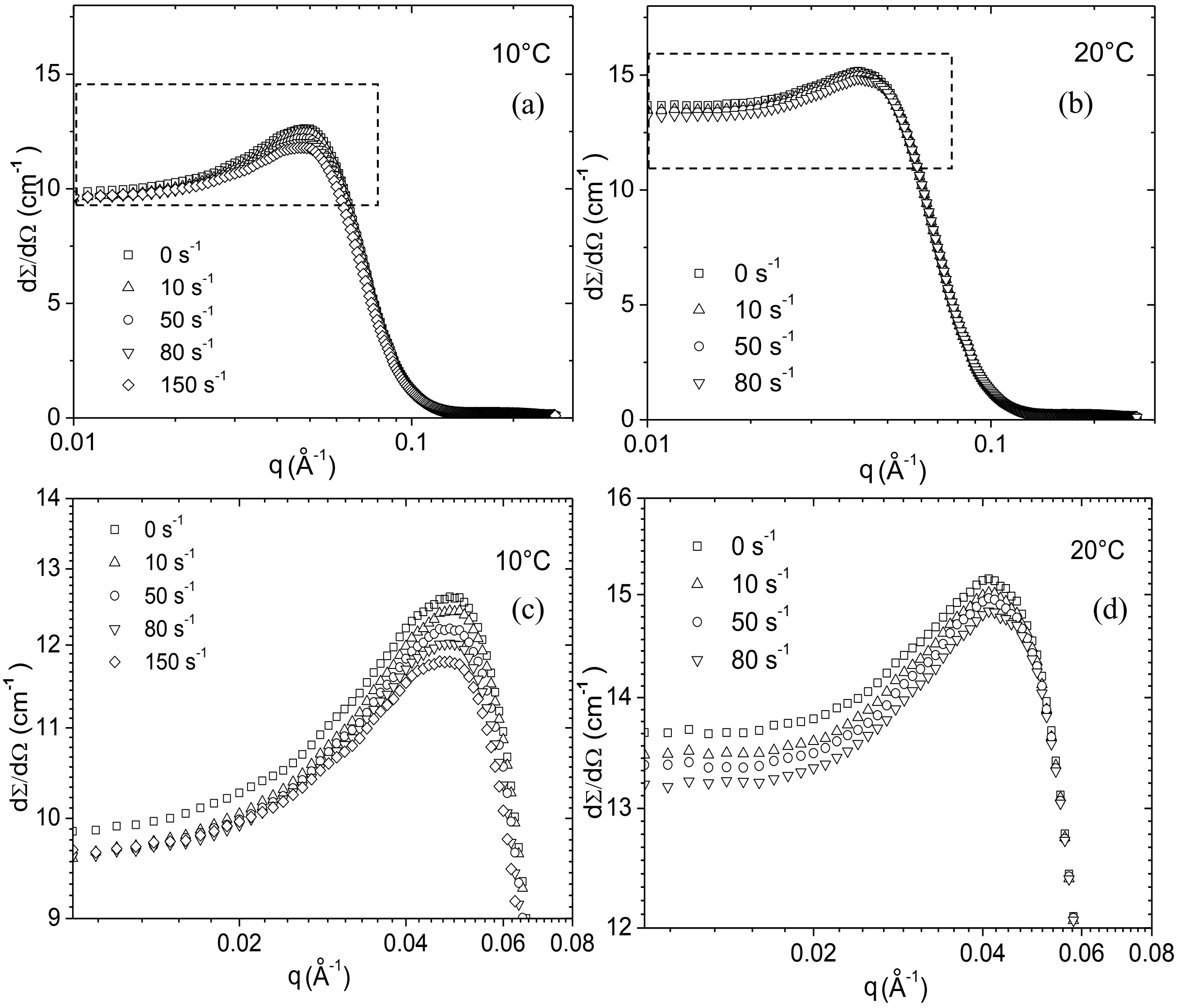

Figure IV.15 The linear-log experimental absolute scattered intensity, for the 20 wt % micellar solution (in heavy water) at (a) 10°C at 0.1, 10, 50, 80 and 150 s^{-1}; (b) 20°C at 0, 10, 50 and 80 s^{-1}. The figures (c) and (d) are the expanded graphs within the dash square frame in each figure a and b, respectively.

4.2 SYSTEM II - $R_7^F(EO)_8$ in NaI

4.2.1 Rheological properties

To study the influence of the NaI salt addition on the rheological behaviour of the $R_7^F(EO)_8$ system, the steady shear and dynamic measurements have also been performed in the same manner, compared with the $R_7^F(EO)_8$ in H_2O system (see in Chapter 4.1.1). The addition of NaI at the concentration of 1M was chosen, because the previous study shows that we can obtain the well-ordered hexagonal mesoporous material in the final product by using 10%wt $R_7^F(EO)_8$-1 M NaI system as a template (see in appendix A1) [11].

4.2.1.1 Steady state rheological behaviour

The rheological characterization of the system $R_7^F(EO)_8$ in 1 M NaI solution was performed under steady state conditions. All measurements are conducted with solutions containing the L_1 phase with some samples close to the miscibility curve. The viscosity curves will reveal the general rheological behaviour. The variations of the apparent viscosity η appear as a function of the shear rate ($\dot{\gamma}$ range = 0.1-10^2 s^{-1}) with different surfactant concentrations and temperature in the different graphs of Figure IV.16. The quantitative analysis of the steady state measurements has been performed in the frame of Ostwald's model. The results are gathered in Table IV.6. The measurements are again conducted with solutions containing the L_1 phase.

The viscosity of four solutions at the concentration of 10, 20, 30 and 40 wt% $R_7^F(EO)_8$ in 1 M NaI solution at 20.00 ± 0.05 °C is plotted in Figure IV.16b (30 and 40 wt% solutions are superimposed). At 20°C, the variations of the apparent viscosity as a function of the shear rate show similar behaviour for all solutions. The value of the viscosity decreases with the concentration. Two types of rheological behaviours can be observed. The lowest concentration of 10 wt% $R_7^F(EO)_8$ exhibited the Newtonian over the range of shear rates used, the flow behaviour index $n = 0.988$ and consistency coefficient $\kappa = 0.052$ Pa s^n. The value of n close to 1 confirms the Newtonian behaviour, the κ value reflects the lowest apparent viscosity for this concentration.

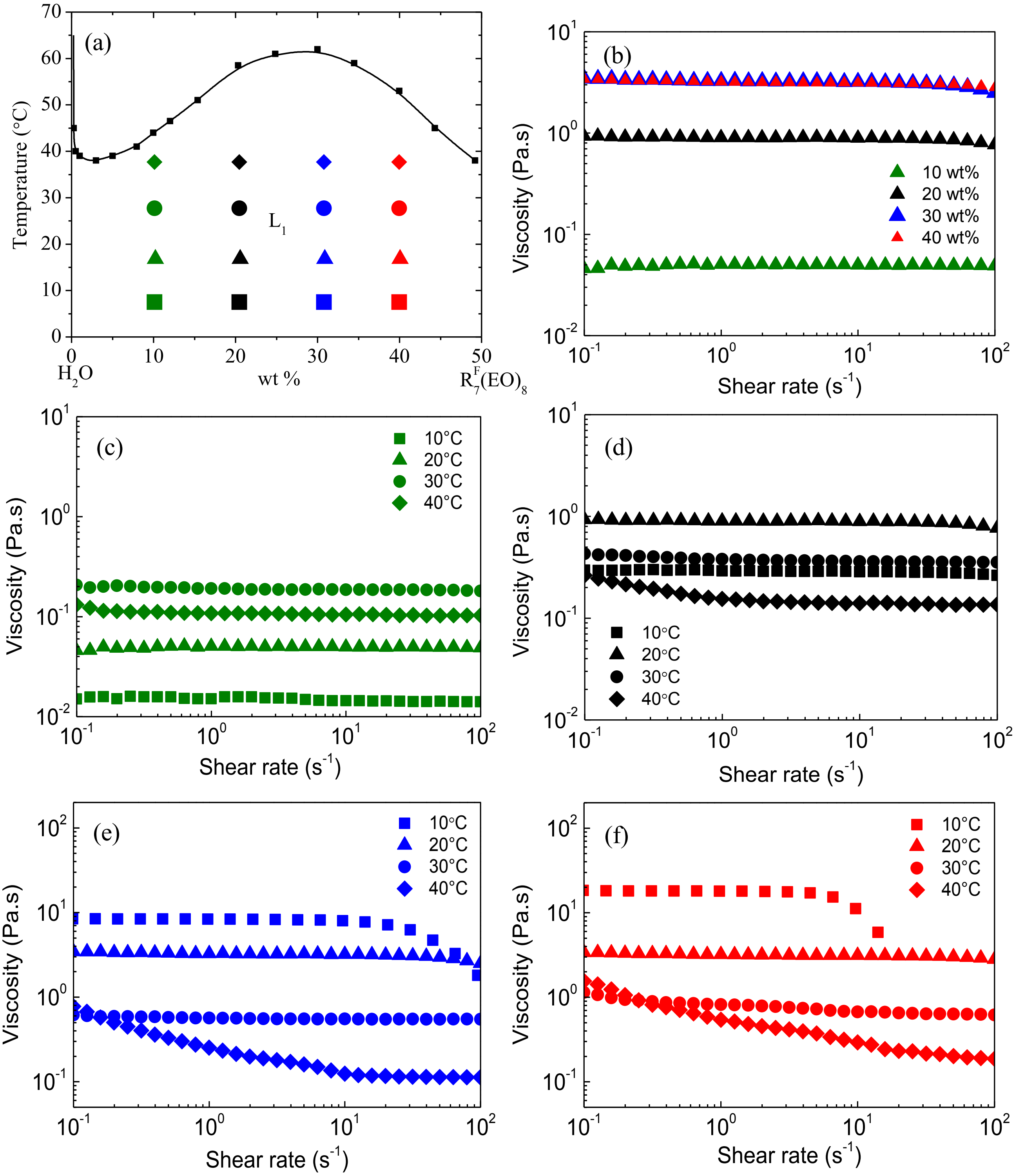

Figure IV.16 Rheological behaviour in steady state shearing mode. (a) miscibility curve (solid line), the symbols pointing out the solutions under investigation; (b) viscosity curves at 20°C for different wt% $R_7^F(EO)_8$ concentrations in 1M NaI solution. The viscosity curves (c-f) for the concentrations of (c) 10, (d) 20, (e) 30 and (f) 40 wt% $R_7^F(EO)_8$ concentrations in 1M NaI at different temperatures; 10°C (square), 20°C (triangle), 30°C (circle), 40°C (diamond).

Table IV.6 Ostwald's law parameters for $R_7^F(EO)_8$ in 1 M NaI solution at different concentrations and temperatures.

Conditions		Rheological characters from flow curves fitting	$\dot{\gamma}_c$ (s^{-1})	Ostwald's law parameters		
$R_7^F(EO)_8$ in 1 M NaI				κ (Pa s^n)	n (-)	R^2
10% wt	10°C	Newtonian	-	0.015	0.989	0.999
	20°C	Newtonian	-	0.052	0.988	0.999
	30°C	Newtonian	-	0.197	0.982	0.999
	40°C	(1) Shear-thinning (2) Newtonian*	0.2	0.106	0.993	0.999
20% wt	10°C	Newtonian	-	0.328	0.955	0.999
	20°C	(1) Quasi-Newtonian* (2) η decreases at high $\dot{\gamma}$	46.8	0.938	0.980	0.999
	30°C	(1) Shear-thinning (2) Newtonian*	1.3	0.366	0.993	1.000
	40°C	(1) Shear-thinning (2) Newtonian*	1.0	0.143	0.989	0.999
30% wt	10°C	(1) Quasi-Newtonian* (2) η decreases at high $\dot{\gamma}$	26.9	9.540	0.910	0.999
	20°C	(1) Quasi-Newtonian* (2) η decreases at high $\dot{\gamma}$	40.0	3.381	0.952	0.999
	30°C	Newtonian	-	0.552	0.998	1.000
	40°C	(1) Shear-thinning (2) Newtonian*	17.2	0.121	0.985	0.999
40% wt	10°C	(1) Quasi-Newtonian* (2) η decreases at high $\dot{\gamma}$	6.8	19.089	0.897	0.997
	20°C	(1) Quasi-Newtonian* (2) η decreases at high $\dot{\gamma}$	40.0	3.603	0.970	0.999
	30°C	(1) Shear-thinning (2) Newtonian*	10.0	0.717	0.969	0.999
	40°C	Shear-thinning	-	0.418	0.820	0.998

κ, consistency coefficient (Pa s^n); n, flow behaviour index (dimensionless). $\dot{\gamma}_c$, critical shear rate (s^{-1}) at the juxtaposition of two approximately linear segments on the viscosity curves; (1) and (2) are the first and second segments, respectively. In the case of curves composed of two segments, the fitting has been done only over the nearly Newtonian segment.

The more concentrated solutions (20, 30 and 40 wt%) show a quasi-Newtonian behaviour. The apparent viscosity η appears to be almost constant in the low shear rate range ($\dot{\gamma} < \dot{\gamma}_c$) then decreased afterwards. The critical shear rate $\dot{\gamma}_c$ is equal to 46.8 s^{-1} for the 20% solution; meanwhile $\dot{\gamma}_c$ values are obtained at 40 s^{-1} for 30 and 40 wt% solutions (Table IV.6). The fitting of the experimental data in the almost constant viscosity range before $\dot{\gamma}_c$ leads to n = 0.980 and κ = 0.938 for 20 wt%, n = 0.952 and κ = 3.381 for 30 wt%, n = 0.970 and κ = 3.603 for 40 wt% sample.

The effect of the temperature on the apparent viscosity is also studied as a function of the shear rate for four concentrations. The chosen temperatures are 10, 20, 30 and 40°C. The results obtained for the system $R_7^F(EO)_8$/NaI (1M) at 10, 20, 30 and 40 wt%, are presented in Figures IV.16c to IV.16f.

Three kinds of the distribution of $\eta(\dot{\gamma})$ are observed upon increasing the temperature. At 10 wt% (Figure IV.16c), the sample behaves like a Newtonian fluid at 10, 20, 30 and 40°C. The lowest value of η is obtained at 10°C (κ = 0.015): then, upon increasing the temperature, η increases, reaches a maximum at 30°C before decreasing again at 40°C. When the temperature reaches 40°C, the initial Newtonian character disappears and is replaced by a shear thinning one until $\dot{\gamma} = \dot{\gamma}_c \sim 0.18$ s^{-1}.

The evolution of the viscosity curves at different temperatures (10, 20, 30 and 40°C) and concentration (10, 20, 30 or 40 wt %) is presented in Figure IV.16c, 16d, 16e, 16f. The parameters of Ostwald's model are listed in Table IV.6.

For the 10 wt% solution (Figure IV.16c), the Newtonian character dominates at 10, 20 and 30°C over the whole range of shear rates. The lowest apparent viscosity is found at 10°C (κ = 0.015), then upon increasing the temperature at 20°C (κ = 0.052) and 30°C (κ = 0.197), the viscosity increases before decreasing again at 40°C.

Increasing the concentration to 20 wt % (Figure IV.16d), leads to an increase of the apparent viscosity at all temperatures; especially large shifts are observed at 10 and 20°C. A quasi perfect Newtonian behaviour is observed at 10°C and 20°C. For the two highest temperatures (30 and 40°C), the initial behaviour in the low shear rates domain is shear thinning but the Newtonian character is found again when $\dot{\gamma} > \dot{\gamma}_c$ with $\dot{\gamma}_c$ = 1.3 and 1.0 s^{-1}, respectively for 30 and 40°C. The highest value of the viscosity is obtained at 20°C ($\kappa = 0.938$), then η decreases and reaches its minimum at 40°C

At the two highest concentrations (30 and 40 wt%, Figure IV.16e and 16f), the rheological behaviour is similar to the one of $R_7^F(EO)_8$ without NaI (Figure IV.1e and 1f). At 10°C, the solutions show a quasi-Newtonian behaviour; a shear thinning character appears at high shear rates beyond a critical shear rate $\dot{\gamma}_c$ respectively ≈ 26.9 s^{-1} for 30 wt% and $\dot{\gamma}_c \approx$ 6.8 s^{-1} for 40 wt%. At 20°C, the solutions are less viscous than at 10°C. At 40°C, the viscosity η in the low shear rates is as expected lower than the one at 10 and 20°C but larger than the viscosity at 30°C. At 40°C for solutions containing 1M NaI, the shear thinning character is less pronounced than in pure water systems as the miscibility curve is shifted toward higher temperatures.

4.2.1.2 Dynamic rheological behaviour

The dynamical rheological studies of the $R_7^F(EO)_8$ in a presence of 1M NaI are illustrated in Figure IV.17. The measurements were conducted in the linear viscoelastic region in the same way as with the $R_7^F(EO)_8$-H_2O system (Chapter 4.1.1.2). The effect of the surfactant concentration in 1M NaI solution at 20°C with four concentrations (10, 20, 30 and 40 wt%) is shown in Figure IV.17a.

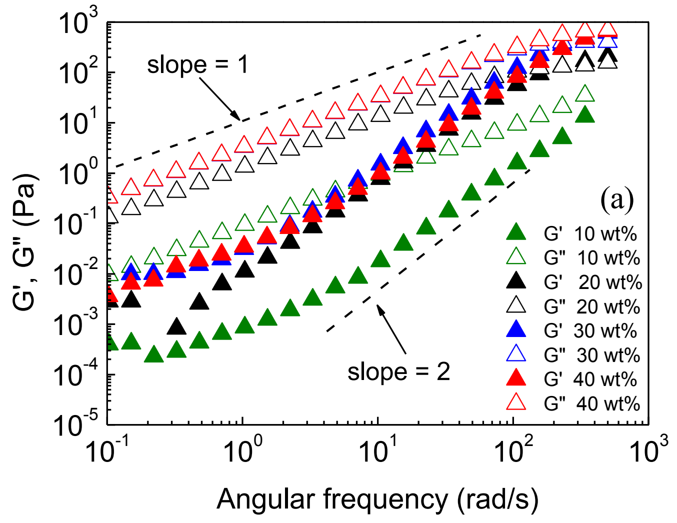

Figure IV.17 Storage modulus *G'* (solid symbols) and loss modulus *G"* (open symbols) as a function of the angular frequency ω: (a) at a constant temperature 20°C.

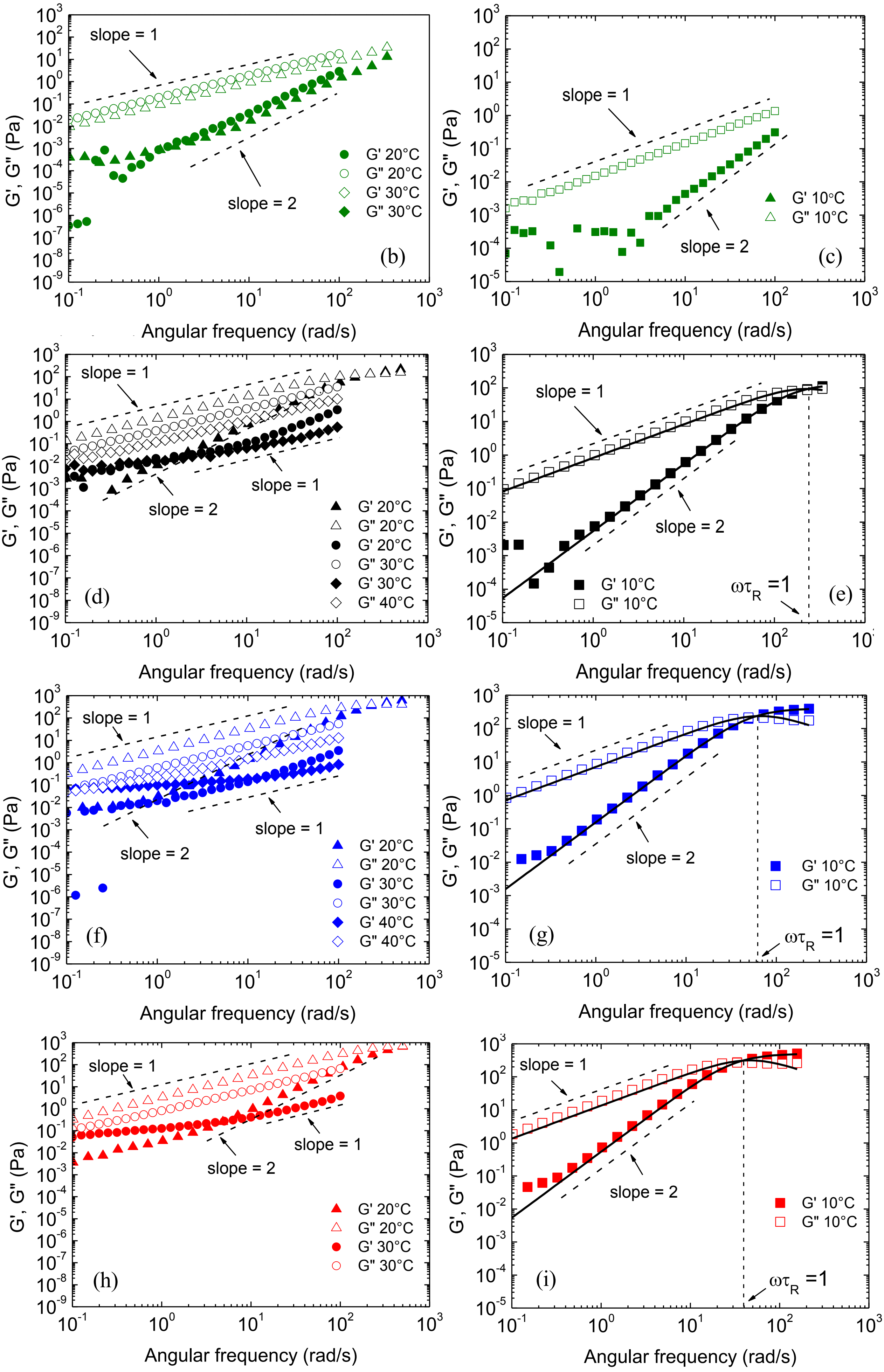
(b)
slope = 1
slope = 2
G' 20°C
G" 20°C
G' 30°C
G" 30°C
(c)
slope = 1
slope = 2
G' 10°C
G" 10°C
(d)
slope = 1
slope = 2
slope = 1
G' 20°C
G" 20°C
G' 20°C
G" 30°C
G' 30°C
G" 40°C
(e)
slope = 1
slope = 2
G' 10°C
G" 10°C
ωτ$_R$ =1
(f)
slope = 1
slope = 2
slope = 1
G' 20°C
G" 20°C
G' 30°C
G" 30°C
G' 40°C
G" 40°C
(g)
slope = 1
slope = 2
G' 10°C
G" 10°C
ωτ$_R$ =1
(h)
slope = 1
slope = 2
slope = 1
G' 20°C
G" 20°C
G' 30°C
G" 30°C
(i)
slope = 1
slope = 2
G' 10°C
G" 10°C
ωτ$_R$ =1
G', G" (Pa)
Angular frequency (rad/s)
10^{-1} 10^{0} 10^{1} 10^{2} 10^{3}
10^{-9} 10^{-8} 10^{-7} 10^{-6} 10^{-5} 10^{-4} 10^{-3} 10^{-2} 10^{-1} 10^{0} 10^{1} 10^{2} 10^{3}

Figure IV.17 (Continued) Storage modulus *G*' (solid symbols) and loss modulus *G*'' (open symbols) as a function of the angular frequency ω : at different $R_7^F(EO)_8$ concentrations in 1M NaI solution; at the concentrations of (b) 10, (d) 20, (f) 30 and (h) 40 wt% and at different temperatures (20, 30 and/or 40°C). At the constant temperature 10°C of (c) 10 wt%, (e) 20 wt%, (g) 30 wt%, (i) 40 wt%; *G*' and *G*'' intersect at the "crossover" point for which $\omega\tau_R$ = 1, except for 10 wt%. The solid curves represent Maxwell's theoretical model. Two dashed lines of slope 1 and 2 are added to serve as a visual guide.

Note: The result for the 10 and 40 wt% solutions at 40°C have not been shown, because of a too narrow linear region range during amplitude sweep tests.

For all concentrations at 20°C (Figure IV.17a) the storage modulus *G*' is always smaller than the loss modulus *G*''; the viscous character prevails over the entire angular frequency range. Both moduli linearly increase almost linearly with the angular frequency in a log-log scale. The distribution of the experimental values of the storage modulus is close to the line of slope 2 (dash straight line drawn as a visual guide). The values of the loss modulus *G*'' gather well on a line of slope 1. These experimental distributions reveal the Maxwellian character of the sample.

The intersection or crossover between *G*' and *G*'' is observed for the samples at 20, 30 and 40 wt%; it occurs at the angular frequency ω of 274, 286 and 481 rad/s, respectively for the solutions at 20, 30 and 40 wt%. At these particular positions; $\omega\tau_R$ = 1; it thus becomes possible to calculate the relaxation time τ_R which turns out to be ≈ 0.0036, 0.0035 and 0.0021 s.

For a solution at different temperatures, the loss modulus *G*'' generally is larger than the storage modulus *G*' (Figure IV.17b-17i); both magnitudes increase as a function of angular frequency in different degrees. The tendency of *G*'' to increase with a slope of 1 and *G*' with a slope of 2, usually is the sign of the Maxwellian character of the system.

To study the influence of the temperature on the dynamical rheological behaviour of $R_7^F(EO)_8$ in the presence of NaI salt, the 20 wt % solution has been selected. The experimental distributions of G' and G'' as a function of the angular frequency ω are reported in Figures IV.17d and IV.17e. For the two highest temperatures (30 and 40°C), $G'(\omega)$ and $G''(\omega)$ increase with a slope close to 1, the viscous character of the solution always predominates. For the two lowest temperatures (10 and 20°C) and particularly at 10°C (see Figure IV.2e), the variations of G' and G'' under sinusoidal strain are reminiscent of a Maxwellian fluid: $G'(\omega)$ is a linearly increasing (in a log-log scale) function of ω within the interval $1\times10^{-1} < \omega < 10^{1}$ rad/s and $G'(\omega) \sim \omega^{n}$ with a slope n ~ 2.

At low temperature (10°C) for the 20, 30 and 40 wt % $R_7^F(EO)_8$/1M NaI solutions (Figure IV.17e, 17g, 17i), G' and G'' intersect at the angular frequency ω respectively equal to 243, 62 and 40 rad/s. The relaxation time τ_R can be calculated from the crossover coordinates and is equal to ≈ 0.004, 0.016 and 0.025 s respectively for the 20, 30 and 40 wt % solutions.

In the range of high angular frequencies ($\omega > 10^2$ rad/s), G' tends to the plateau value G_0 only for the sample at 30 and 40 wt%. G_0, is related to the zero shear viscosity and to the relaxation time by the equation: $\eta_0 = G_0.\tau_R$ (equation IV.5). By averaging G' over the last few values obtained at high frequency, we obtain $G_0 \sim G'_{\mathrm{average}} = 391$ and 462 Pa in the case of 30 and 40 wt% solutions. Taking into account the calculated value of the relaxation time, we obtain for η_0 a value of 6.26 and 11.55 Pa.s. These calculated zero shear viscosity values are close to the value extrapolated from the viscosity curve at low shear rates (see Figure IV.16e, 16f; symbol 🟦 🟥).

The variations of G'' as a function of G' (Cole-Cole) plot are presented in Figure IV.18. The semi-circle $G'' = \sqrt{G_0 G' - G'^2}$ of Maxwell's model is drawn using the previously calculated values of G_0; the adjustment of the experimental data to this curve allows to appreciate the quality of the Maxwellian character of the different samples. In the low frequencies range, the experimental data gather well on the theoretical curve but G'' departs significantly from the circle at the higher frequencies, decreasing to a minimum G''_{min} before increasing slightly again.

The minimum G''_{min} occurs for the angular frequency $\omega = \omega^* = 231$ and 107 rad/s, from which we can compute the breaking time τ_{break} of the micelles (by equation IV.6); 4.3 and 9.3 ms for 30 and 40 wt%, respectively. From the plateau modulus G_0, the hydrodynamic correlation length ξ_H, regarded as the average entanglement length, can be computed by equation IV.7. In summary, we list the calculated parameters from Maxwell's model applied to the 30 and 40 wt % $R_7^F(EO)_8/1$ M NaI solutions, in the Table IV.7.

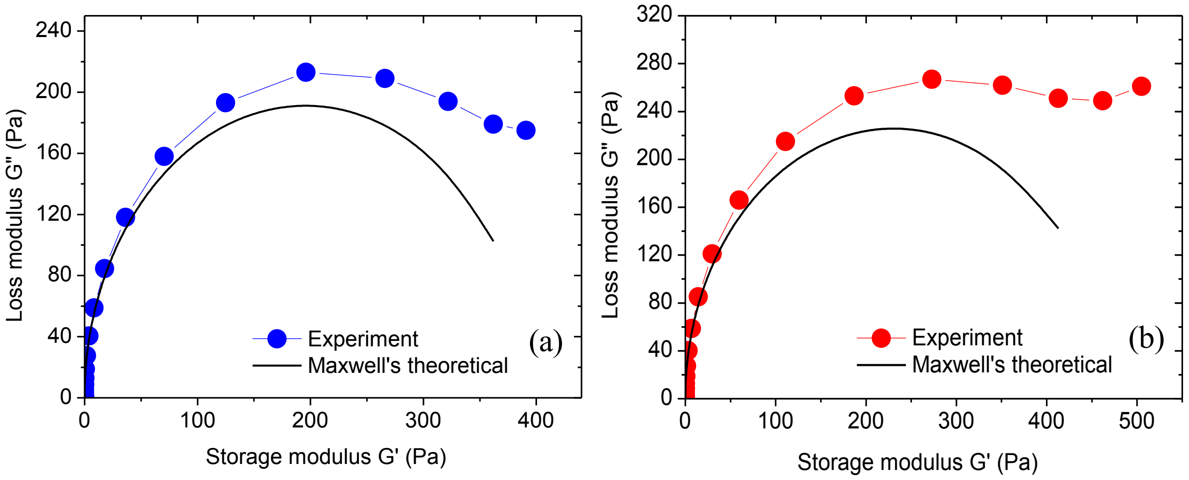

Figure IV.18 Cole-Cole plot *G*''(*G*') at 10°C of $R_7^F(EO)_8$ (a) 30, and (b) 40 wt % in 1M NaI solution. The circle symbols correspond to the experimental points and, in each graph, the black continuous curve represents the computed Maxwell's theoretical model taking for the plateau modulus G_0: 391 and 462 Pa respectively for the 30 and 40 wt %.

Table IV.7 The calculated parameter from Maxwellian theoretical models at T = 283K, of the $R_7^F(EO)_8$ surfactant in 1M NaI solution.

$R_7^F(EO)_8/1$M NaI	τ_R (s)	G_0 (Pa)	η_0 (Pa.s)	ω^* (rad/s)	τ_{break} (ms)	ξ_H (nm)
10 wt%	-	-	-	-	-	-
20 wt%	0.004	-	-	-	-	-
30 wt%	0.016	391	6.26	231	4.3	22.0
40 wt%	0.025	462	11.55	107	9.3	20.0

τ_R, relaxation time (s); G_0, plateau modulus (Pa); η_0; zero shear viscosity (Pa.s); ω^*, angular frequency at the minimum G''_{min}; τ_{break}, breaking time of the micelles, ξ_H, hydrodynamic correlation length. (The results at 10 and 20wt% $R_7^F(EO)_8$ are not presented, because of a poor agreement with the model).

For the $R_7^F(EO)_8$-1M NaI solutions at 10°C, the increase of the concentration also leads to an increase of the macroscopic parameters G_0 and η_0. We found an increase in microscopic quantitiy of τ_{break}, but a decrease in ξ_H.

4.2.2 Flow birefringence

Flow birefringence experiments were also performed on the system $R_7^F(EO)_8$/NaI in water. The variations of the optical quantities (χ and Δn) are studied at three specific temperatures (10, 20, 30°C) as a function of the shear rate.

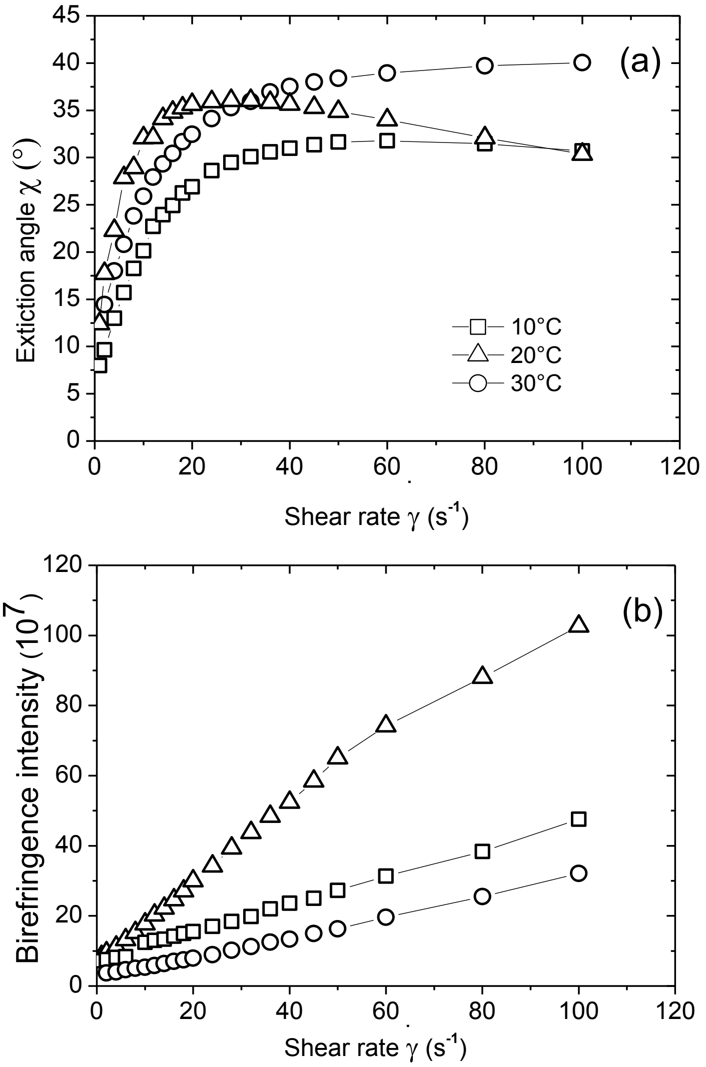

Figure IV.19 Flow birefringence experiments: (a) extinction angle χ, (b) birefringence intensity Δn vs. the shear rate $\dot{\gamma}$. The concentration is 20 wt % $R_7^F(EO)_8$ 1M NaI solution and the temperatures: 10°C (□), 20°C(△) and 30°C (○).

As in the case of the solution $R_7^F(EO)_8$ with salt, the extinction angle χ (see Figure IV.19a) does not follow the variations predicted by the orientation theory of small particles subjected to a shearing flow: χ increases in the low shear rate domain, goes through a maximum before decreasing or approaching a plateau depending on the temperature set for the experiment. On the other hand, the birefringence intensity Δn (Figure IV.19b) is a linear function of the shear rate in the entire shear rate domain. The straight lines representing $\Delta n\,(\dot{\gamma})$ do not intersect at the origin of the coordinates system due to a small non vanishing birefringence at zero shear rate. The behaviour of the extinction angle is qualitatively the same with and without salt even if at 10°C, the angle χ does not decrease as quickly as with the solution without salt.

4.3 SYSTEM III - $R_8^F(EO)_9$ in water

A second nonionic fluorinated system, $R_8^F(EO)_9$, has also been the aim of our work. With this surfactant, ordered mesoporous materials are always synthesized. The small differences in molecular structure and physico-chemical characteristics are gathered in Table II.2. The physical properties of $R_8^F(EO)_9$ in the L_1 phase in water are studied using rheology and flow birefringence. The influence of the NaCl salt on shifting down the miscibility curve of $R_8^F(EO)_9$, will be presented in the system IV.

4.3.1 Steady state rheological behaviour

The steady state flow characteristics of pure $R_8^F(EO)_9$ in water at 20 and 30 wt% are presented in Figure IV.20. The micelles in solution form the L_1 phase as emphasized in the partial phase diagram (Figure IV.20a).

For the 20 wt% $R_8^F(EO)_9$ solution, the flow curve $\eta\,(\dot{\gamma})$ for all temperatures (10 to 40°C) is characteristic of a Newtonian fluid (Figure V20.b). The temperature has no effect on the flow behaviour at this concentration. The fitting of the data with Ostwald's model confirm the Newtonian character, as the *n* values for the different temperatures are close to 1 (Table IV.8). The apparent viscosities are quite low.

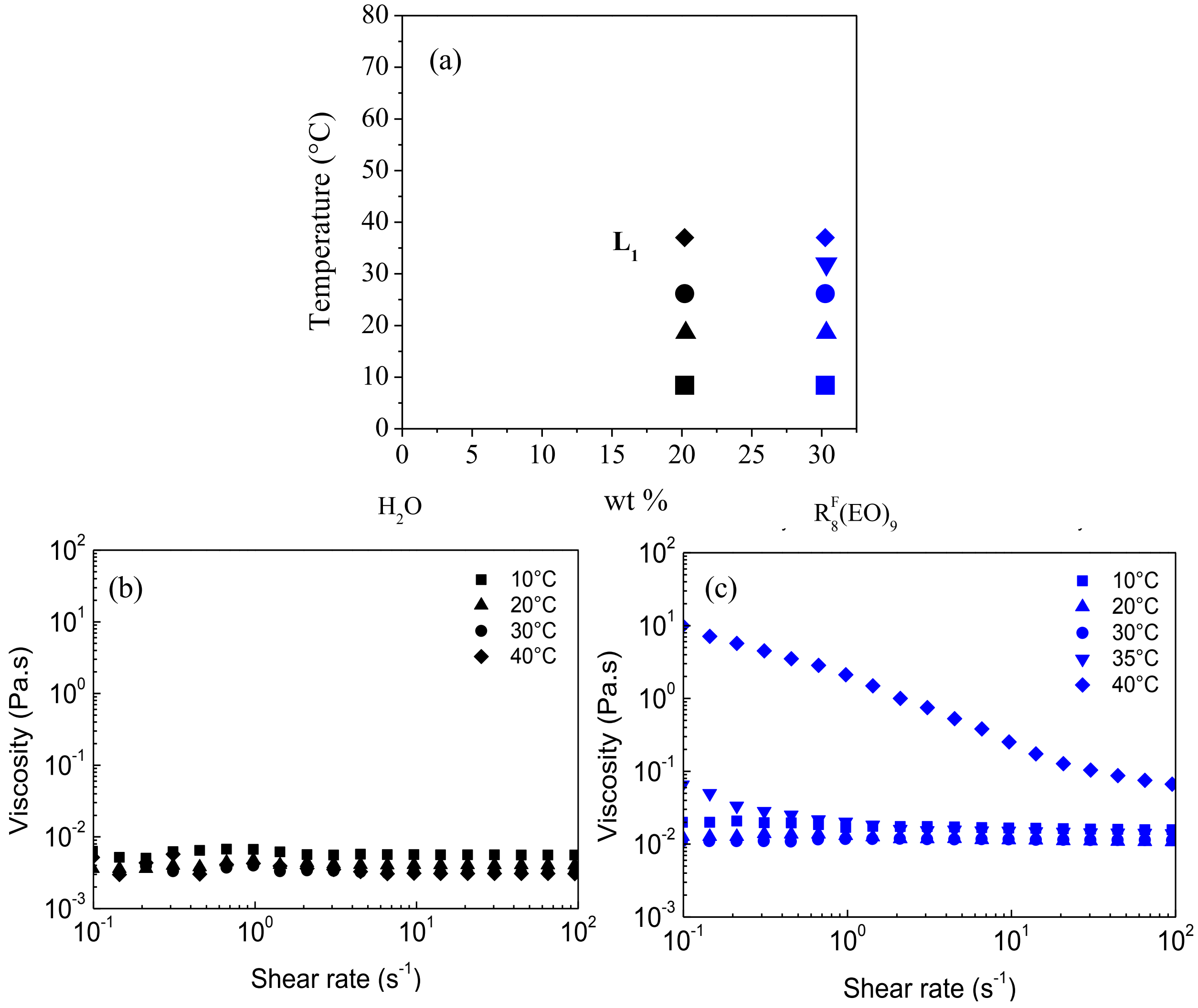

Figure IV.20 Rheological behaviour in steady state shearing mode. (a) The partial phase diagram of $R_8^F(EO)_9$ in water, the symbols pointing out the solutions under investigation. The viscosity curves for the concentrations of (b) 20 and (c) 30 wt% $R_8^F(EO)_9$ in water at different temperatures; 10°C (square), 20°C (triangle), 30°C (circle), 35°C (reverse triangle) and 40°C (diamond).

Table IV.8 Ostwald's law parameters for $R_8^F(EO)_9$ in water at different concentrations and temperatures.

Conditions		Rheological characters from flow curves fitting	$\dot{\gamma}_c$ (s^{-1})	Ostwald's law parameters		
$R_8^F(EO)_9$ in H_2O				κ (Pa s^n)	n (-)	R^2
20% wt	10°C	Newtonian	-	0.006	0.995	1.000
	20°C	Newtonian	-	0.004	0.994	1.000
	30°C	Newtonian	-	0.003	0.993	0.999
	40°C	Newtonian	-	0.003	0.980	0.999
30% wt	10°C	Newtonian	-	0.017	0.977	1.000
	20°C	Newtonian	-	0.012	0.980	0.999
	30°C	Newtonian	-	0.012	0.991	0.999
	35°C	(1) Shear-thinning (2) Newtonian*	2.1	0.016	0.967	1.000
	40°C	Shear-thinning	-	0.783	0.482	0.926

κ, consistency coefficient (Pa s^n); n, flow behaviour index (dimensionless). $\dot{\gamma}_c$, critical shear rate (s^{-1}) at the juxtaposition of two approximately linear segments on the viscosity curves; (1) and (2) are the first and second segments, respectively. In the case of the curves composed of two nearly linear segments, the fitting has been done only over the Newtonian part.

Figure IV.20c shows the change in apparent viscosity of 30 wt% $R_8^F(EO)_9$ in water, as a function of the temperature from 10 to 40°C. The curves are fitted with Ostwald's model and the results are listed in the Table IV.8. The quantitative results show the Newtonian character of the sample. The apparent viscosities appear to be higher than the viscosity of the 20 wt% samples. When raising the temperature to 35°C, the initial Newtonian character at low shear rate is lost. The critical shear rater $\dot{\gamma}_c$ is found at $\approx 2.1\ s^{-1}$. Once the temperature reaches 40°C, the solution turns to be completely shear thinning. This change in viscosity curves at 40°C may occur because the sample is closer to the miscibility curve (referred in Figure III.4)

4.3.2 Dynamic rheological behaviour

We have also studied the dynamic rheological behaviour of the pure $R_8^F(EO)_9$ solutions. Strain amplitude sweep tests are performed in order to find the linear viscoelastic region (LVR) of the samples. A low amount of strain equal to 1% in the LVR was chosen to perform the frequency sweeps in the LVR . The maximum angular frequency is 500 rad/s. The experimental data for two concentrations (20 and 30 wt%) at various temperatures (10 to 40°C) are presented in Figure IV.21.

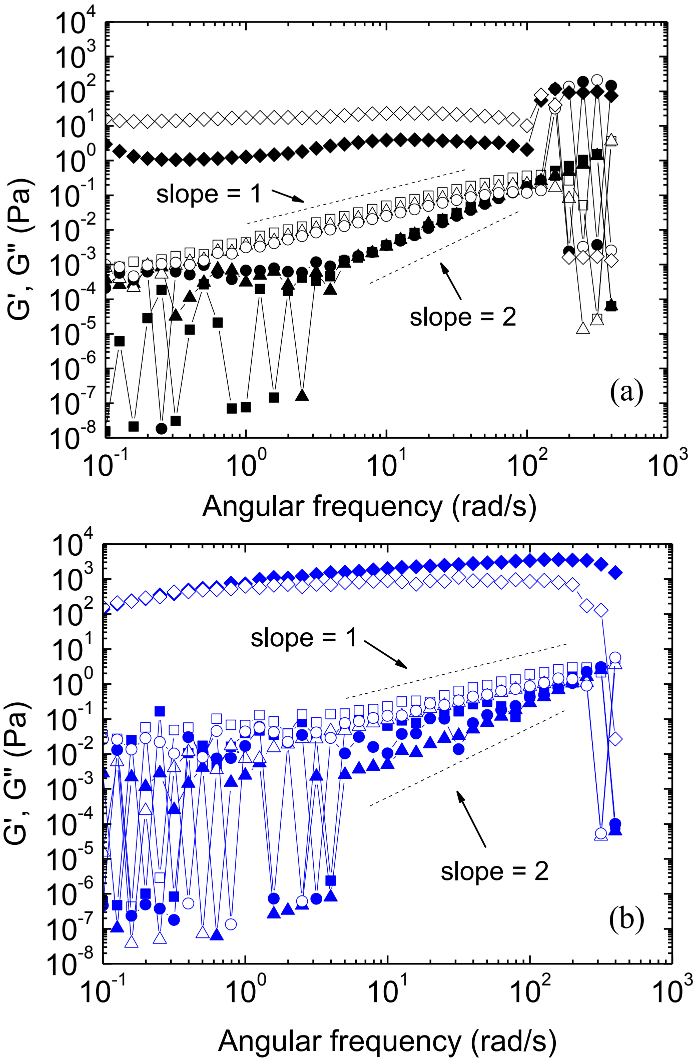

Figure IV.21 Storage modulus *G*' (solid symbols) and loss modulus *G*'' (open symbols) as a function of the angular frequency ω for pure $R_8^F(EO)_9$ solutions. (a): concentrations of 20 wt%, (b) 30 wt% at different temperatures; 10 (square), 20 (triangle), 30 (circle) and 40°C (diamond). Two dashed lines of slope 1 and 2 are added to serve as a visual guide.

G' and *G*'' show large fluctuations at low and high frequencies, probably due to the low viscosity of the solutions and to the limitations of the equipment; even if the large oscillations at high frequencies are more difficult to explain.

For both concentrations at 10 to 30°C, the storage modulus *G*' is smaller than the loss modulus *G*''; the viscous character of the solutions (Figure IV.21) is thus prevailing. The storage modulus *G*' varies as ω^2; while the loss modulus *G*'' varies as ω. This tendency is the signature of a Maxwellian character of the solutions.

The Maxwellian character however disappears upon increasing the temperature to 40°C.

4.3.3 Flow birefringence

Flow birefringence experiments were also performed on a 30 wt% solution free of salt at the temperature of 20°C. The optical path of the Couette cell is 10 mm, the same as the one used with the other systems. No measurable values of the extinction angle χ or of the retardation δ could be realized by the conventional method of Sénarmont. Although the quantitative result is negative, the fact that no appreciable birefringence can be measured under the shearing conditions used for the other systems tells us that the micelles in solution are probably small with a shape close to a sphere.

The difficulty to obtain a new batch of surfactant prevented us from performing further experiments with $R_8^F(EO)_9$ in a shearing device having a larger optical path (70mm).

4.4 SYSTEM IV - $R_8^F(EO)_9$ in 3M NaCl

4.4.1 Steady state rheological behaviour

We have seen in Figure III.5 that the miscibility curve of the $R_8^F(EO)_9$ surfactant can be shifted down by adding the NaCl salt into the system. In this part, we present the effect of NaCl addition on the rheological properties of the $R_8^F(EO)_9$ in 3M NaCl solution. The measurements are still performed within the L_1 phase (Figure IV.22a), for the sample of 20 and 30 wt%, at 10 to 50°C.

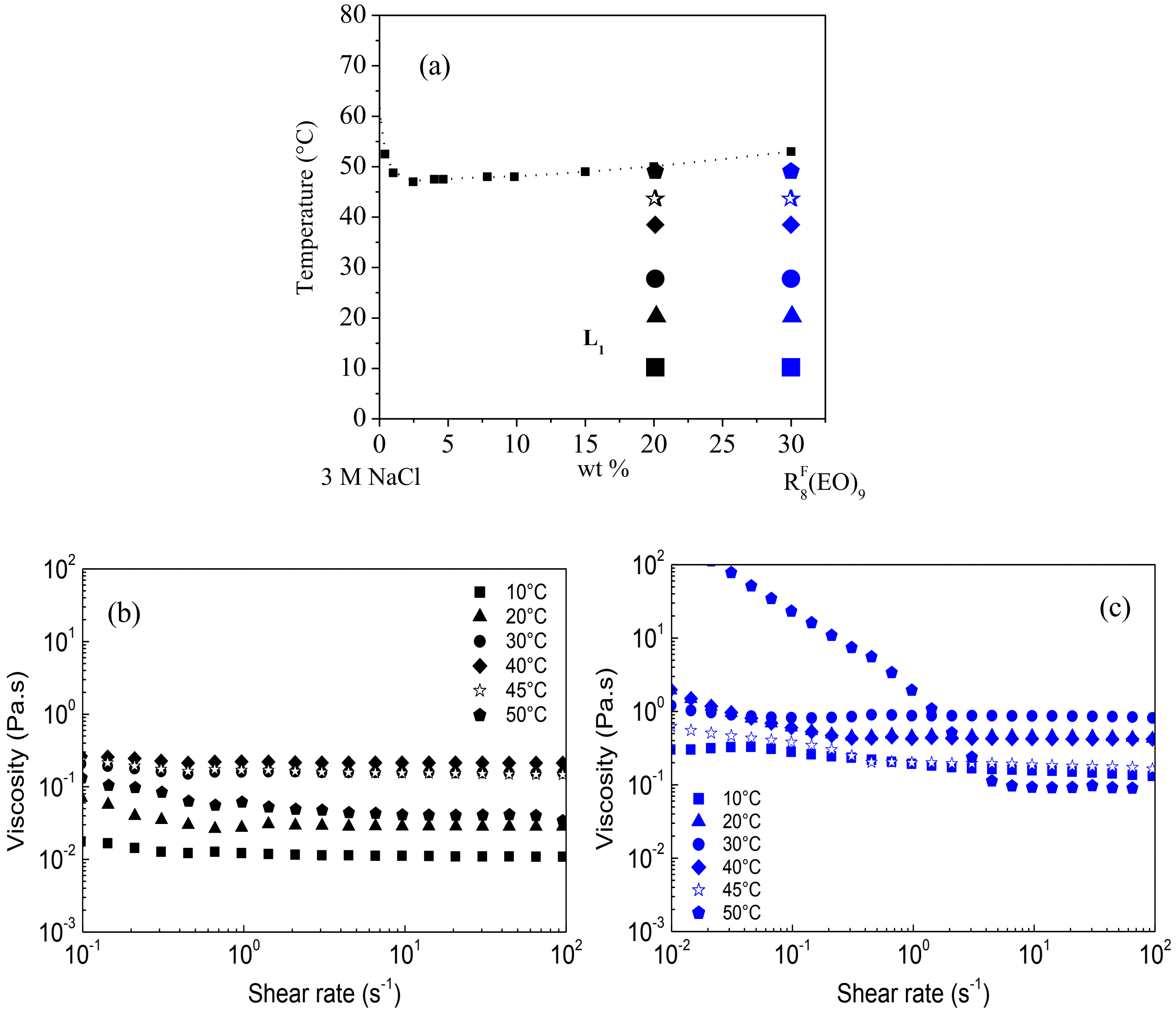

Figure IV.22 Rheological behaviour in steady state shearing mode. (a) miscibility curve, the symbols pointing out the solutions under investigation. The viscosity curves for the concentrations of (b) 20 and (c) 30 wt% $R_8^F(EO)_9$ concentration in 3 M NaCl solution at different temperatures; 10°C (square), 20°C (triangle), 30°C (circle), 40°C (diamond), 45°C (empty star) and 50°C (pentagone).

Table IV.9 The parameters of Ostwald's law for $R_8^F(EO)_9$ in 3M NaCl at different concentrations and temperatures.

Conditions		Rheological characters from flow curves fitting	$\dot{\gamma}_c$ (s^{-1})	Ostwald's law parameters		
$R_8^F(EO)_9$ in 3M NaCl				κ (Pa s^n)	n (-)	R^2
20% wt	10°C	(1) Shear-thinning (2) Newtonian*	0.3	0.011	0.991	0.999
	20°C	(1) Shear-thinning (2) Newtonian*	1.0	0.029	0.997	1.000
	30°C	Newtonian	-	0.164	0.986	0.999
	40°C	Newtonian	-	0.216	0.997	1.000
	45°C	Newtonian	-	0.164	0.976	1.000
	50°C	(1) Shear-thinning (2) Newtonian*	4.5	0.044	0.980	0.999
30% wt	10°C	(1) Shear-thinning (2) Newtonian*	3.1	0.195	0.915	0.999
	20°C	(1) Shear-thinning (2) Newtonian*	0.2	0.527	0.956	0.999
	30°C	Newtonian	-	0.963	0.963	0.999
	40°C	(1) Shear-thinning (2) Newtonian*	0.3	0.430	0.993	1.000
	45°C	(1) Shear-thinning (2) Newtonian*	0.5	0.223	0.934	0.999
	50°C	(1) Shear-thinning (2) Newtonian*	6.6	0.154	0.841	0.981

κ, consistency coefficient (Pa s^n); n, flow behaviour index (dimensionless). $\dot{\gamma}_c$, critical shear rate (s^{-1}) at the juxtaposition of two approximately linear segments on the viscosity curves; (1) and (2) are the first and second segments, respectively. In the case of curves formed by two segments, the fitting has been done only over the nearly Newtonian segment.

The flow curves $\eta(\dot{\gamma})$ of the 20 wt% $R_8^F(EO)_9$ in 3M NaCl solution at 10, 20, 30, 40, 45 and 50°C are described in Figure IV.22b. In the low shear rate range, the viscosity decreases slightly (shear thinning character) until the critical shear rate $\dot{\gamma}_c \approx 0.3$ s^{-1} at 10°C and 1 s^{-1} at 20°C. The curves beyond $\dot{\gamma}_c$ show a Newtonian behaviour. They can be fitted by Ostwald's model (see in Table IV.9). Increasing the temperature to 30°C and 45°C, the solutions are Newtonian. At 30 and 40°C, the η values increase slightly then decrease again when the temperature is raised to 45°C. At the highest value of 50°C, the solution develops a shear thinning behaviour for shear rates smaller than the critical shear rate $\dot{\gamma}_c$ (≈ 4.5 s^{-1}). At this temperature, the solution is very close to the miscibility curve.

The rheogram of the 30 wt% $R_8^F(EO)_9$ in 3M NaCl solution is presented in Figure IV.22c for different temperatures. At 10 and 20°C, the solutions are shear thinning in the low shear rates range and Newtonian beyond a critical shear rate. On the whole range of shear rate, the viscosity at 20°C is about five times the viscosity at 10°C. At 30°C, the solution becomes Newtonian with the highest value of η in the high shear rate plateau. Then at the higher temperatures 40, 45 and 50°C, the solution are again shear thinning at low shear rates up to a critical value $\dot{\gamma}_c$ respectively $\approx$ 0.3, 0.5 and 6.6 s^{-1}. The apparent viscosity after $\dot{\gamma}_c$ decreases with the temperature. The strong change of the shear behaviour at 50°C could result from a phase transition induced due to the proximity to the miscibility curve.

4.4.2 Dynamic rheological behaviour

The dynamical rheological results of the $R_8^F(EO)_9$ in 3M NaCl solution are shown in Figure IV.23, for two concentrations (20 and 30 wt%) at 10°C. A narrow linear viscoelastic region is determined by amplitude sweep tests and a low amount of strain (0.1%) was also chosen to perform the frequency sweeps.

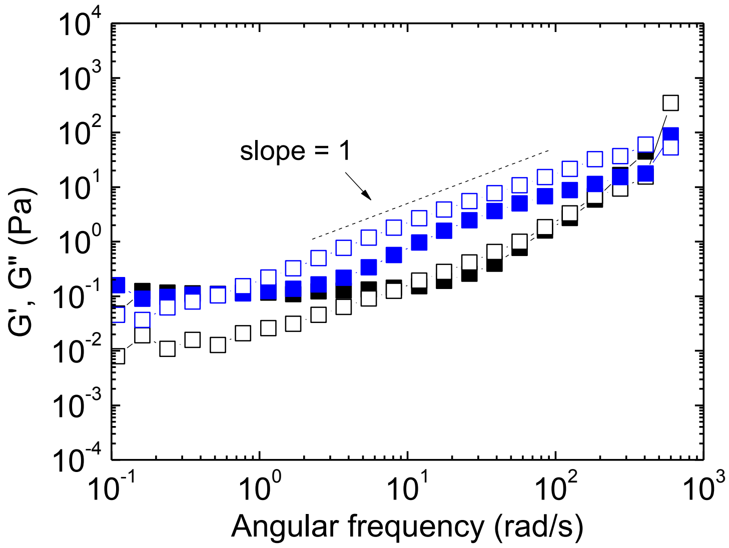

Figure IV.23 Storage modulus *G*' (solid symbols) and loss modulus *G*" (open symbols) as a function of the angular frequency ω. The concentrations are: 20 (■,□) and 30 (■,□) wt% of $R_8^F(EO)_9$ in 3M NaCl solution at the constant temperature 10°C.

The variations of G'' and G' with the frequency do not agree with the theoretical Maxwellian model. In the case of the 20 wt% sample, the distribution of the moduli is too far away from the model to determine a specific behaviour. The 30 wt% solution shows a slope of 1 for both moduli in the intermediate range of ω. These results suggest that the Maxwellian character is lost with the addition of NaCl salt into the system.

4.4.3 Flow birefringence

Figures IV.24a and b report the variations of the extinction angle χ and of the birefringence intensity Δn for two concentrations (20 and 30 wt %) at different temperatures. On the contrary to the $\mathrm{R}_7^\mathrm{F}(\mathrm{EO})_8$ systems and apart from a few points in the low shear rates range (see Figure IV.24a, open circles and triangles) which are above the angle limit (45°), the extinction angle decreases smoothly with the shear rate from 45° according to the orientation theory of small rigid particles. For both solutions, the birefringence intensity is a linearly increasing function of $\dot{\gamma}$.

For both concentrations, the evolution of the angle χ is found to be very closely the same for the two temperatures 25 and 30°C, the temperature difference being probably too small to induce important structural changes which would affect the physical properties of the micellar solutions. At the temperature of 40°C, χ remains close to 45° with a relative variation of only 3% over the entire shear rates range. For the 20 wt% solution, the extinction angle remains quite large (~ 40°) even for the largest values of the shear rates (100 s^{-1}). This is a sign of the existence of rather small micelles difficult to orientate by the flow.

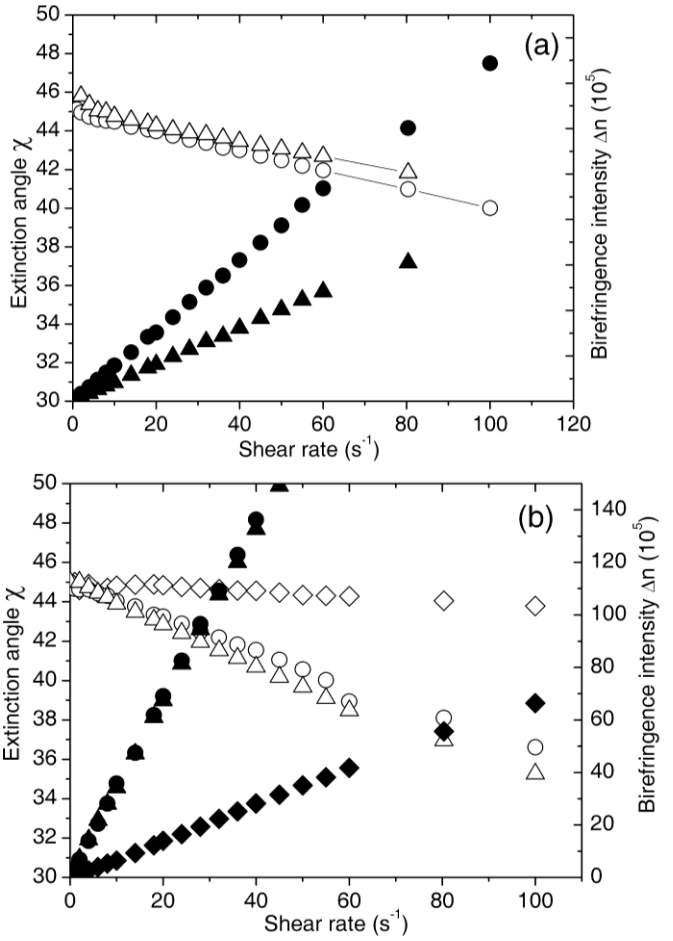

Figure IV.24 Extinction angle (open symbol) and birefringence intensity (full symbols) for the concentrations of 20 (a) and 30 (b) wt% of $R_8^F(EO)_9$ in 3 M NaCl solution at different temperatures; 25°C (triangle), 30°C (circle), 40°C (diamond).

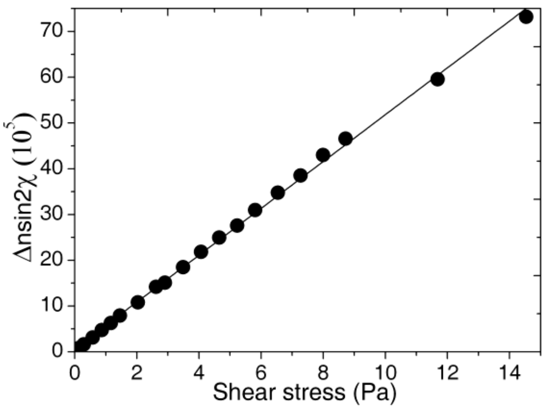

Figure IV.25 Stress optical law $\Delta n\sin2\chi = 2C\sigma$ for $R_8^F(EO)_9$ 20 wt% in 3M NaCl at the temperature of 30°C. The straight line (slope: 2C = 5.12.10^{-5}) represents a linear fit of the experimental values

Since χ and Δn seem to follow the orientation theory, it thus becomes possible to check the validity of the stress optical law [13] [14] [15] which simply relates the tangential stress σ to the birefringence quantities χ and Δn.

$$\Delta n\sin2\chi = 2C\sigma$$

Figure IV.25 is the graphical representation of the stress optical law for $R_8^F(EO)_9$ in 3M NaCl at the temperature of 30°C. The experimental data gather well on the straight line in the entire range of stress. From the slope, one easily computes the stress optical coefficient C. It turns out that:

$$C = 2.56.10^{-5}\ \mathrm{Pa}^{-1}$$

Similar calculations are performed for 30wt% $R_8^F(EO)_9$ in 3M NaCl at different temperatures (25, 30, 40°C). Again the distribution of the experimental data as a function of the stress is linear (see Figure IV.26); the slope of the straight lines gives the optical coefficient C for the different temperatures (Table IV.10, three values of the coefficient C which are multiplied by the factor 10^5 for convenience)

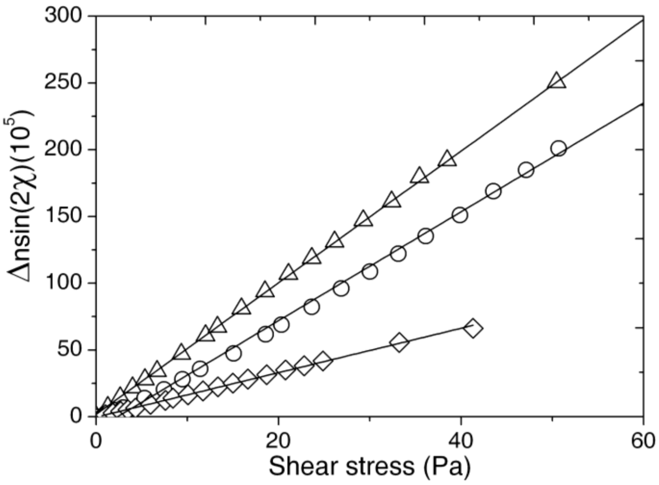

Figure IV.26 Stress optical law $\Delta n\sin2\chi = 2C\sigma$ for $R_8^F(EO)_9$ 30 wt% in 3M NaCl at three temperatures: 20°C (triangle △), 30°C (circle ○), 40°C (diamond

◇). The straight line (slope: 2C) represents a linear fit of the experimental values.

Table IV.10 Stress optical coefficient for $R_8^F(EO)_9$ 30wt% in 3M NaCl at different temperatures.

Temperature (°C)	Stress optical coefficient (x10^5)
25	2.46
30	2.03
40	0.83

According to the theory developed by Doi et al. [15], C is a linear function of the inverse of the Kelvin temperature T. The function C(1/T) is drawn in Figure IV.27.

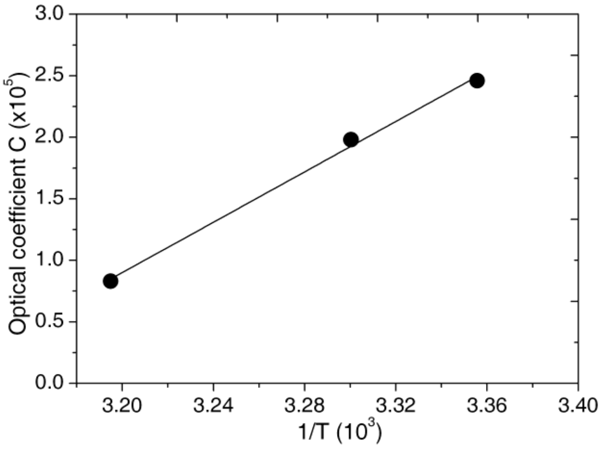

Figure IV.27 Stress optical coefficient C versus the inverse or the Kelvin temperature T.

Although the number of experimental data is relatively small, the three experimental points fit well on a single straight line.

References

[1] R. G. Shrestha, L. K. Shrestha, S. C. Sharma and K. Aramaki, *The Journal of Physical Chemistry B* **2008**, *112*, 10520-10527.
[2] F. Lequeux, *Current Opinion in Colloid &amp; Interface Science* **1996**, *1*, 341-344.
[3] M. E. Cates and S. J. Candau, *Journal of Physics: Condensed Matter* **1990**, *2*, 6869-6892.
[4] M. E. Doi, S.F., *The theory of Polymer Dynamics* Clarendon Press, Oxford, **1986**.
[5] C. El Moujahid, J. C. Ravey, V. Schmitt and M. J. Stébé, *Colloids and Surfaces A: Physicochemical and Engineering Aspects* **1998**, *136*, 289-297.
[6] M. E. Cates, *Macromolecules* **1987**, *20*, 2289-2296.
[7] J. F. Berret, J. Appell and G. Porte, *Langmuir* **1993**, *9*, 2851-2854.
[8] H. d. Senarmont, *Ann. Chim. Phys.* **1840**, *73*, 337.
[9] V. R. Gray and A. E. Alexander, *J. Phys. Chem.* **1949**, *53 (1)*, 9-22.
[10] J. F. Foster and D. Zucker, *J. Phys Chem.* **1952**, *56 (2)*, 174-177.
[11] F. Michaux in *Contribution des tensioactifs fluorés à la synthèse de matériaux mésoporeux : Application à la conception d'un bioréacteur*, *Ph.D thesis* UHP - Université Henri Poincaré, Nancy, **2009**.
[12] C. Regnaut and J. C. Ravey, *J. Chem. Phys.* **1989**, *91*, 1211-1221.
[13] A. S. Lodge, *Trans. Far. Soc.* **1956**, *52*, 120.
[14] L. R. G. Treolar, *The physics of Rubber elasticity*, Clarendon Press, Oxford, **1975**.
[15] M. Doi and S. F. Edwards, *J. Chem. Soc. Far. Trans* **1978**, *2*, 418.

Chapitre V. Discussion (résumé)

Le cinquième chapitre est consacré à la discussion des résultats expérimentaux obtenus à l'aide des différentes techniques expérimentales. Il est divisé en cinq parties principales plus une sixième qui est un tableau récapitulatif et comparatif des propriétés des deux tensioactifs.

Les résultats de rhéologie, confirmés par les expériences de biréfringence d'écoulement montrent que les objets en solution subissent un changement de structure lorsque les conditions de température et de concentration sont modifiées.

5.1. Système $R_7^F(EO)_8$ et $R_7^F(EO)_8$/NaI

Pour une température donnée (20°C), la viscosité apparente croît lorsque la concentration augmente par suite de l'accroissement des forces de friction entre particules. Aux températures basses et intermédiaires, on observe un comportement Newtonien dans de nombreuses solutions dont la concentration est éloignée de celle de la courbe de miscibilité. Lorsque la température augmente, le caractère Newtonien disparaît graduellement à un taux de cisaillement d'autant plus petit que la température est proche de la courbe de miscibilité. Pour les deux concentrations les plus élevées (30 et 40%), un accroissement de la température conduit à un élargissement du domaine Newtonien qui finit par couvrir tout le domaine de cisaillement.

Le caractère Maxwellien du système est mis en évidence à basse température (~10°C). Les modules G' et G'' se coupent au crossover et varient conformément au modèle théorique. Le comportement Maxwellien disparaît à plus hautes températures.

Les expériences de biréfringence effectuées sur ce système montrent que l'angle d'extinction χ ne suit pas les prédictions de la théorie de l'orientation qui prévoit une décroissance monotone de 45° vers 0° en fonction du taux de cisaillement. Ce comportement inhabituel est attribué à la présence en solution de larges structures micellaires détruites lorsque le cisaillement croît.

On retrouve un comportement rhéologique qualitatif similaire pour le système $R_7^F(EO)_8/NaI/H_2O$ avec, cependant un caractère Maxwellien plus prononcé dans un domaine de concentration et température plus étendu. Il en est de même pour l'évolution des caractéristiques optiques : angle d'extinction χ et intensité de la biréfringence Δn.

5.2. Formation de la phase hybride hexagonale

L'obtention de matériaux mésoporeux ordonnés par CTM repose sur la formation, au préalable, d'une phase hydride hexagonale formée par la solution micellaire et le précurseur inorganique. Les solutions micellaires satisfaisant à cette condition montrent un comportement Maxwellien plus ou moins prononcé ; ce critère n'est cependant pas suffisant, il faut de plus que les conditions de concentration et de température ne soient pas trop proches de la courbe de miscibilité.

5.3. Comparaison $R_7^F(EO)_8/H_2O$ et $R_7^F(EO)_8/H_2O/NaI$

Globalement le comportement rhéologique qualitatif est le même pour les deux solutions.
A 10°C, les deux solutions sont Newtoniennes à faible cisaillement puis au-delà d'un taux critique $\dot{\gamma}_c$ apparaît le régime rhéofluidifiant ; $\dot{\gamma}_c$ est d'autant plus petit que la concentration en tensioactif est grande. L'addition de sel conduit à une diminution de la viscosité apparente des solutions à 10 et 20% et le comportement Newtonien est conservé sur tout l'intervalle de cisaillement. Les deux systèmes présentent un caractère Maxwellien plus ou moins prononcé. Les modules G' et G'' se coupent au crossover dont l'abscisse permet le calcul du temps de relaxation τ_R; de plus $G''(G')$ présente un minimum pour certaines conditions de température et concentration dont on peut tirer la longueur de corrélation hydrodynamique ξ. L'addition de sel NaI a pour effet de déplacer le crossover vers les pulsations plus basses ce qui conduit à un temps de relaxation plus grand.

5.4. Comparaison entre rhéologie, biréfringence d'écoulement et diffusion de neutrons.

Pour le système $R_7^F(EO)_8/H_2O$ dans le domaine des faibles cisaillements, biréfringence et rhéologie sont en désaccord : l'augmentation de l'angle χ est expliqué par une importante modification de la structure des objets en solution ce que ne traduit pas le comportement Newtonien. Par contre au-delà du maximum de χ, la décroissance de l'angle est en accord avec la rhéofluidification. Un comportement similaire est observé pour le système $R_7^F(EO)_8/H_2O/NaI$.

L'orientation préférentielle dans une direction moyenne quantifiée par l'angle χ en biréfringence est également mise en évidence par l'analyse des spectres de diffusion de neutrons. Les variations d'intensités diffusées $I_{\parallel}(q)$ et $I_{\perp}(q)$ présentent toutes deux un pic attribué aux interactions entre micelles. Lorsque le taux de cisaillement croît, les deux composantes initialement superposées se séparent et un écart significatif apparaît pour un cisaillement de $50s^{-1}$ à la température de 20°C. Le cisaillement critique pour lequel les deux composantes $I_{\parallel}(q)$ et $I_{\perp}(q)$ se séparent est situé entre 10 et 50 s^{-1} en accord qualitatif large avec les résultats de rhéologie et de biréfringence.

5.5. Système $R_8^F(EO)_9$/H2O et $R_8^F(EO)_9$/NaI/H_2O

On observe un changement progressif du comportement rhéologique en fonction de la concentration en tensioactif. A 20%, la solution est Newtonienne à toutes les températures ; à 30%, le caractère Newtonien disparaît aux faibles cisaillements à 35°C pour disparaître complètement à 40°C. Il n'a pas été possible de quantifier les deux grandeurs caractérisant la biréfringence d'écoulement dans les conditions de l'expérience. Ceci laisse supposer que l'on est en présence de petites particules faiblement asymétriques.

L'addition de sel provoque un abaissement de la courbe de miscibilité et entraine une modification du comportement rhéologique. Les deux solutions à 20 et 30% en masse sont rhéofluidifiantes aux faibles cisaillements à 10 et 20°C puis Newtoniennes au-delà d'un taux critique. Entre 30 et 45°C, la solution à 20% est Newtonienne mais redevient rhéofluidifiante à 50°C. A 30%, le caractère Newtonien prévaut à 30°C, puis, aux températures les plus hautes 40, 45 et 50°C, la viscosité apparente décroît à nouveau. Les deux grandeurs caractérisant la biréfringence, χ et Δn sont en accord avec la théorie de l'orientation.

5.6 Tableau récapitulatif des propriétés des quatre systèmes.

Systèmes	Comportement rhéologique de la phase L_1	Evolution de l'angle d'extinction χ	SANS	Matériau mésoporeux ordonné
Système I: $R_7^F(EO)_8$ dans H_2O	Newtonien/rhéofluidifiant au voisinage de la courbe de miscibilité - Maxwellien aux basses temperatures.	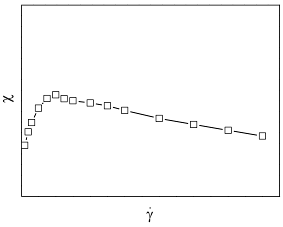	- isotrope au repos - Les micelles sont orientées sous écoulement à basse température	non
Système II: $R_7^F(EO)_8$ dans NaI 1M	- décalage vers le haut de la courbe de miscibilité - Newtonien rhéofluidifiant au voisinage de la courbe de miscibilité - Extension du domaine Maxwellien	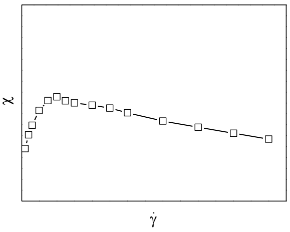	nd	oui
Système III: $R_8^F(EO)_9$ dans H_2O	- Maxwellien/ rhéofluidifiant au voisinage de la courbe de miscibilité	Pas de mesures significatives	nd	oui
Système IV: $R_8^F(EO)_9$ dans NaCl 3M	- décalage vers le bas de la courbe de miscibilité - Domaine Newtonien plus restreint. rhéofluidifiant au voisinage de la courbe de miscibilité	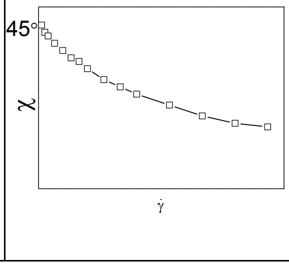	nd	non

= non déterminé

Chapter V. Discussion

5.1 Molecular organization of $R_7^F(EO)_8$ system at equilibrium

5.1.1 $R_7^F(EO)_8$ in water

In chapter four, the rheophysical characteristics of solutions containing micelles of the surfactant $R_7^F(EO)_8$ in the L_1 phase have been studied with the temperature and concentration of the solution as parameters.

The rheological experiments show that the objects in solutions undergo a structural change as a function of the temperature and concentration.

For a given temperature (20°C), the apparent viscosity η increases, as expected, with the concentration (Figure IV.1 b) as the consequence of the increase of the inter-particular friction forces.

At low and intermediate temperatures, a Newtonian behaviour is observed in a wide range of solutions the composition of which is far from the miscibility curve at a given temperature. As the temperature is increased, the Newtonian character gradually disappears at a shear rate all the lower than the temperature is close to the miscibility curve; the shear thinning behaviour then prevails.

Shear thinning usually is associated with the orientation of the particles by the flow and occurs after a Newtonian regime in the low shear rates domain. The curve $\eta(\dot{\gamma})$ at 10°C (Figure IV.1 d black square) clearly follows this behaviour.

For the two largest concentrations (30 and 40 wt %) and as the temperature is raised, the Newtonian domain enlarges and even covers the entire shear rates domain. This is particularly noticeable at 20°C for the 30 and 40wt % sample.

If the temperature is further increased, a shear thinning domain emerges at low shear rates and the Newtonian character completely disappear at 40°C for both samples. This behaviour is the sign of a structural change of the micelles as the temperature gets closer to the miscibility curve.

The dynamic rheological measurements reveal the Maxwellian behaviour at low temperature (~10°C) with an intersection of the moduli *G*' and *G*" at the crossover and typical variations of *G*' and *G*" with *ω*. Upon increasing temperature to ~20°C, the solutions still show a Maxwellian character, but the crossover occurs at a frequency out of the range of angular frequency. The Maxwellian behaviour is eventually lost at higher temperatures (30 and 40°C). Additionally, the modification of Maxwellian behaviours with increasing temperature is reported in Chapter 4.1.1.4 (Figure IV.5). As already observed in the literature, a Maxwellian behaviour seems to indicate the presence of entangled wormlike micelles.

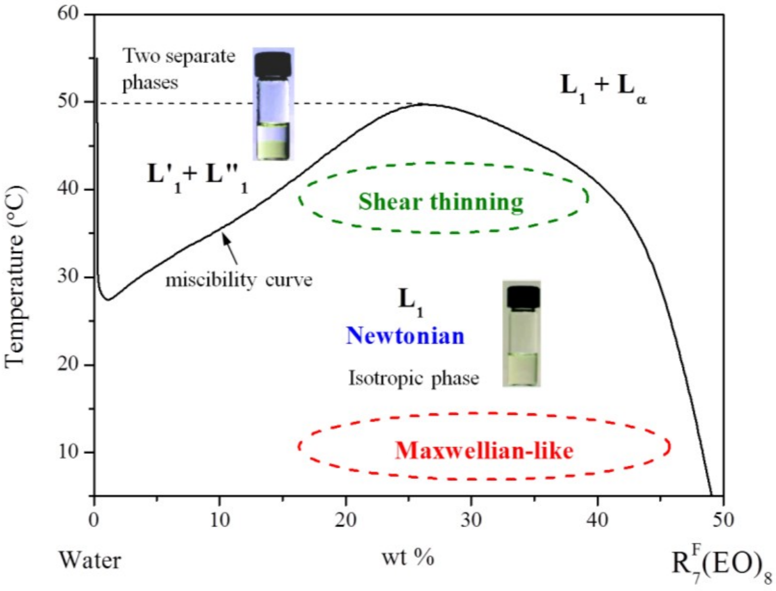

However an unexpected evolution of the extinction angle χ has been found in the flow birefringence experiment (Figure IV.7). The results do not follow the orientation theory of the streaming birefringence for the Newtonian fluid containing asymmetrical particles which states that the extinction angle should remain close to 45° at least in the low shear rate range, and then decrease towards 0° with the shear rate. Therefore, the tested solution cannot be described as a solution containing wormlike micelles.

Some literature reviews have reported the existence of wormlike micelles in nonionic fluorinated system, but we have to keep in mind that they have never determined the extinction angle of those surfactants [1] [2] [3] . Their results are mainly interpreted on the base of their rheological properties.

At rest, the $R_7^F(EO)_8$ in water solutions are optically isotropic but the slightest shearing motion induces birefringence which relaxes slowly. Therefore, a structure at equilibrium of $R_7^F(EO)_8$ in water can be proposed.

Although the sample is isotropic at rest, the extinction angle shows the value of ~5° at the beginning of the test. This result seems to indicate that large anisotropic objects exist at low shear rates. These objects may consist of small micelles linked as a chain by a weak force. These large structures are orientated at random since the solution is isotropic at rest. The weak links are easily counteracted by the hydrodynamical forces.

Once applying a small amount of shear, the weak links are easily broken into smaller objects. Increasing slightly the shear rate (but still remaining small) leads to a sharp increase of the angle χ. The angle increases until reaching a maximum value at the critical shear rate $\dot{\gamma}_c$, at which the system contains smaller asymmetrical micelles which then start to align in an average direction.

The existence of large aggregates at equilibrium is also evidenced in the stress cycle test (Chapter 4.1.1.3). The increase of the viscosity at rest suggests a building up of aggregates exists, due to weak forces between the micelles.

5.1.2 $R_7^F(EO)_8$ in 1M NaI solution

For the $R_7^F(EO)_8$/NaI(1M) solution, the change in rheological behaviour also depends on the concentrations and temperatures (Figure IV.16). When salt is added, the critical concentration corresponding to the transition from Newtonian to shear thinning behaviour is shifted toward higher values (from 20 wt % to 30 wt %).

The Maxwellian character with a crossover of *G*' and *G*" is found at both temperatures of 10 and 20°C and appears more clearly than in the pure $R_7^F(EO)_8$/water system. It is gently lost when increasing the temperature from 30 to 40°C. In general, this peculiar character is found in a wider concentrations and temperatures range when compared to pure $R_7^F(EO)_8$ systems.

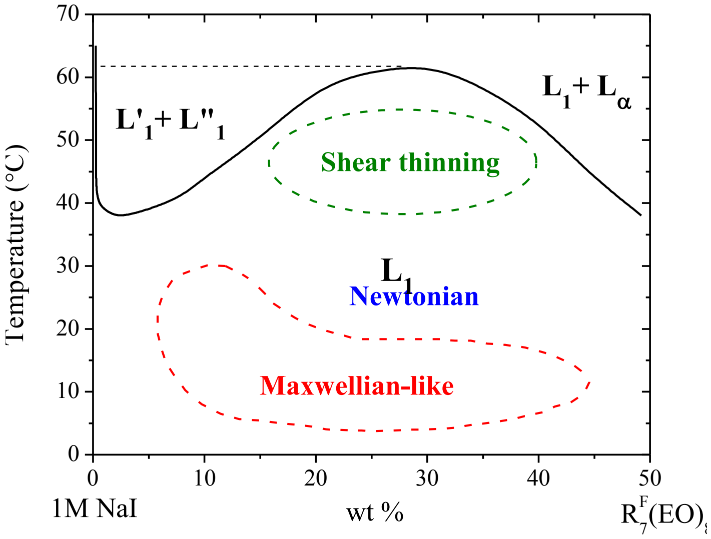

For the sample containing salt, the evolution of the extinction angle is qualitatively the same as for pure $R_7^F(EO)_8$ systems. A micellar organization similar to the one suggested previously is thus plausible. In the presence of NaI salt at 10°C, the maximum of χ is broader and followed by a smoothly decreasing branch.

At 20°C, after reaching its maximum approximately for $\dot{\gamma} = 25$ s^{-1}, χ decreases to superimpose with the curve obtained at 10°C in the high shear rates range. The NaI salt does not change the angle evolution at 30°C.

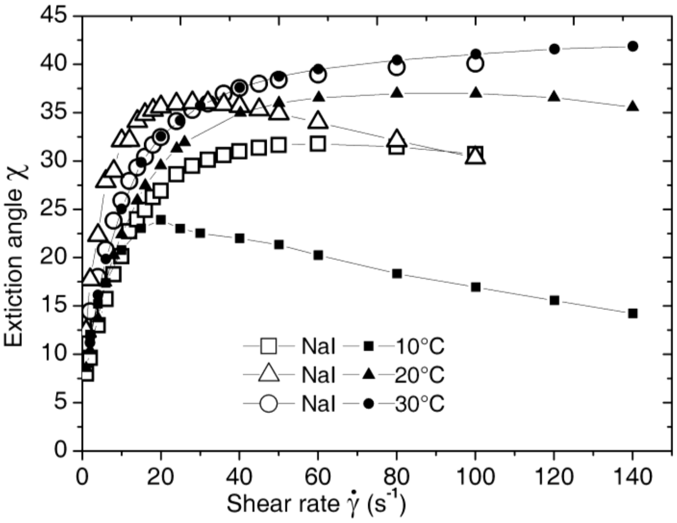

Figure V.1 Comparison of the evolution of the extinction angle for the solutions with salt (open symbols) and without salt (full symbols).

5.2 Formation of hybrid hexagonal mesophase: link to the rheological behaviours

5.2.1 $R_7^F(EO)_8$ in water

For the preparation of mesoporous materials with $R_7^F(EO)_8$ surfactant-based system, the CTM is not favoured if the cloud point is too low [4]. If we aim at preparing materials in conditions of concentration and temperature far from the miscibility curve, the hybrid hexagonal mesophase should be efficiently formed. The hybrid structure can occur and leads to the ordered mesoporous material in the final product.

As mentioned earlier, the $R_7^F(EO)_8$-water solutions show a Maxwellian behaviour at low temperature (10°C). This Maxwellian behaviour becomes "weaker" when increasing the temperature towards the miscibility curve.

Therefore, we can suggest that the Maxwellian character of the solution might be a significant property of the micellar template used for the preparation of the mesoporous materials. In the pure $R_7^F(EO)_8$/water solutions (system I), the Maxwellian character takes place in all concentrations (10 to 40 wt%) at 10 and even 20°C. From a previous study [5], an hybrid ordered structure can be observed. However, this structure collapses during the hydrothermal treatment; therefore, a wormhole-like material is finally obtained.

5.2.2 $R_7^F(EO)_8$ in 1M NaI solution

When NaI is added (system II), the miscibility curve is shifted toward higher temperatures resulting from the salting in effect of NaI. The Maxwellian character can be found at the temperatures of 10 and 20°C and appears more clearly than in the pure $R_7^F(EO)_8$/water system. However, when the temperature is increased to 30 and 40°C, the Maxwellian character is lost. Nevertheless, the Maxwellian behaviour can apparently be used to predict the formation of hybrid ordered structure in this system. The previous mentioned work reports that an ordered mesoporous material is successfully synthesized, without loss of structure during hydrothermal treatment. The addition of NaI salt shifts the miscibility curve of the system $R_7^F(EO)_8$/NaI/water toward higher temperatures. In the range of concentrations and temperature investigated, the solutions with NaI show a better tendency to form hybrid hexagonal structure during the synthesis.

5.3 $R_7^F(EO)_8$ -water vs $R_7^F(EO)_8$-1M NaI systems

Based on the steady shear and dynamic measurements, the rheological properties of $R_7^F(EO)_8$ surfactant solutions at different temperatures are further discussed.

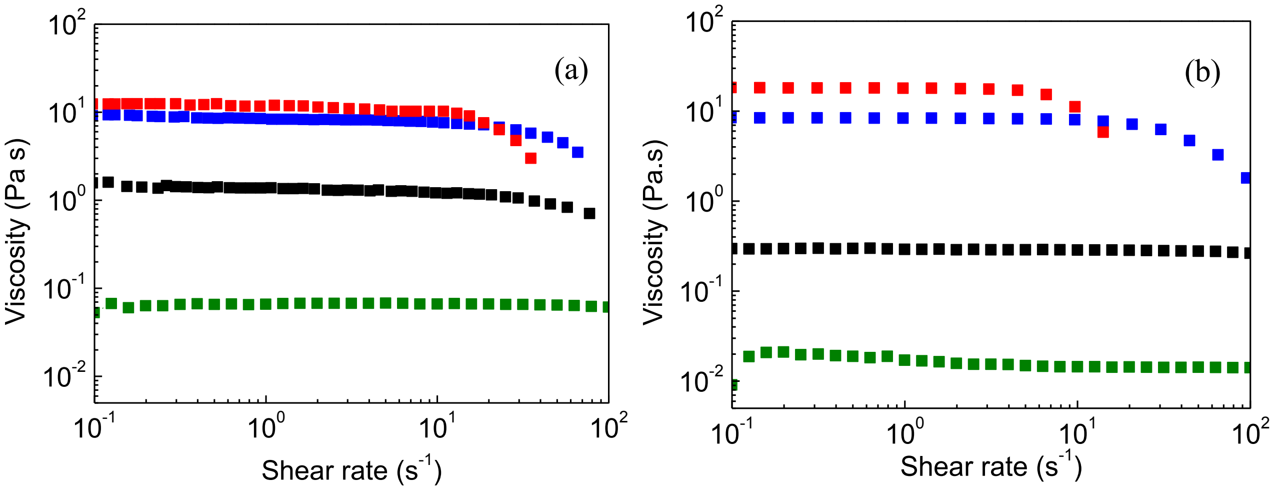

Figure V.2 The viscosity curves as a function of shear rate of $R_7^F(EO)_8$ at 10°C; (a) with NaI solution (b) without NaI salt. At various concentrations 10 wt% (🟩 green), 20 wt% (⬛ black), 30 wt% (🟦 blue) and 40 wt% (🟥 red).

At 10°C, the flow tests of the $R_7^F(EO)_8$ solution generally show the Newtonian character at low shear rates. Then, above a critical shear rate $\dot{\gamma}_c$, the solutions become shear thinning; the decrease of the apparent viscosity is usually explained by the alignment of the particles under the action of the shear flow. In the case of aqueous solutions of surfactant, shear thinning requires the existence of asymmetrical micelles which can be orientated by the flow. The viscosity decrease begins at a critical shear rate $\dot{\gamma}_c$ all the smaller than the geometrical anisotropy is larger.

The $\dot{\gamma}_c$ values for the pure $R_7^F(EO)_8$ at 10°C are summarized in Table IV.1. The critical shear rate $\dot{\gamma}_c$ is all the smaller than the concentration is larger for a given temperature. For micelles in the L_1 phase, increasing the concentration at constant temperature leads to the growth of the micellar length and thus to a decrease of $\dot{\gamma}_c$.

Increasing the concentrations from 20 to 40 wt%, leads to a shift of $\dot{\gamma}_c$ towards lower values. In the same time, the increase of viscosity can suggest that the system is getting more structured. This behaviour is typical of systems consisting of a structured network as found in wormlike micellar solution [6]. When the network structure is deformed by shear, shear thinning occurs because the aggregates brake and get aligned by the flow. This can occur when the time required for the equilibrium network structure to rebuilt is longer than the characteristic time of the shearing flow. The decrease in $\dot{\gamma}_c$ may be related to an increasing network density in the system.

In the presence of 1 M NaI salt (Table IV.6), the critical shear rate $\dot{\gamma}_c$ is also decreasing on increasing the concentration. Compared with the pure $R_7^F(EO)_8$ solution, the addition of NaI salt leads to a decrease in the apparent viscosity of the solutions at 10 and 20 wt% and the behaviour remains Newtonian over the whole range of shear rates.

At high concentrations (30 and 40 wt%), the apparent viscosities turns to increase slightly. The addition of NaI shifts the $\dot{\gamma}_c$ values toward a higher value in the case of the 20 and 30 wt% solutions; the alignment is made more difficult due to the existence of smaller particles. Meanwhile, the 40 wt% solution has the lowest $\dot{\gamma}_c$, which could be explained by an increase in micellar size when adding NaI salt.

At the temperature of 10 and 20°C, the results of the fitting with Maxwell's model applied to $R_7^F(EO)_8$ are discussed (see in Figure V.3).

For the $R_7^F(EO)_8$/water solutions at 10°C, the crossover is shifted toward higher ω on increasing the concentration from 20 to 40 wt %, leading to a shorter relaxation time τ_R (Figure V.3a ■). An increase of the concentration also leads to an increase of the macroscopic parameters: plateau modulus (Figure V.3b G_0, ■) and zero shear viscosity (Figure V.3b η_0, ▲), but to a decrease of the microscopic quantities: breaking time (Figure V.3b τ_{break}, ●) and hydrodynamic correlation length (Figure V.3b ξ_H, ◆).

Adding 1M NaI into the solutions at 10°C (symbol □ on figure V.3a) changes the behaviour of the relaxation time which increases with the concentration; thus the crossover coordinates are shifted toward lower ω : on figure V.3a: compare the gap between the τ_R's at 10°C for the 20 and 30% solutions. In contrast, NaI shifts the crossover toward low ω for the solution at 40 wt%.

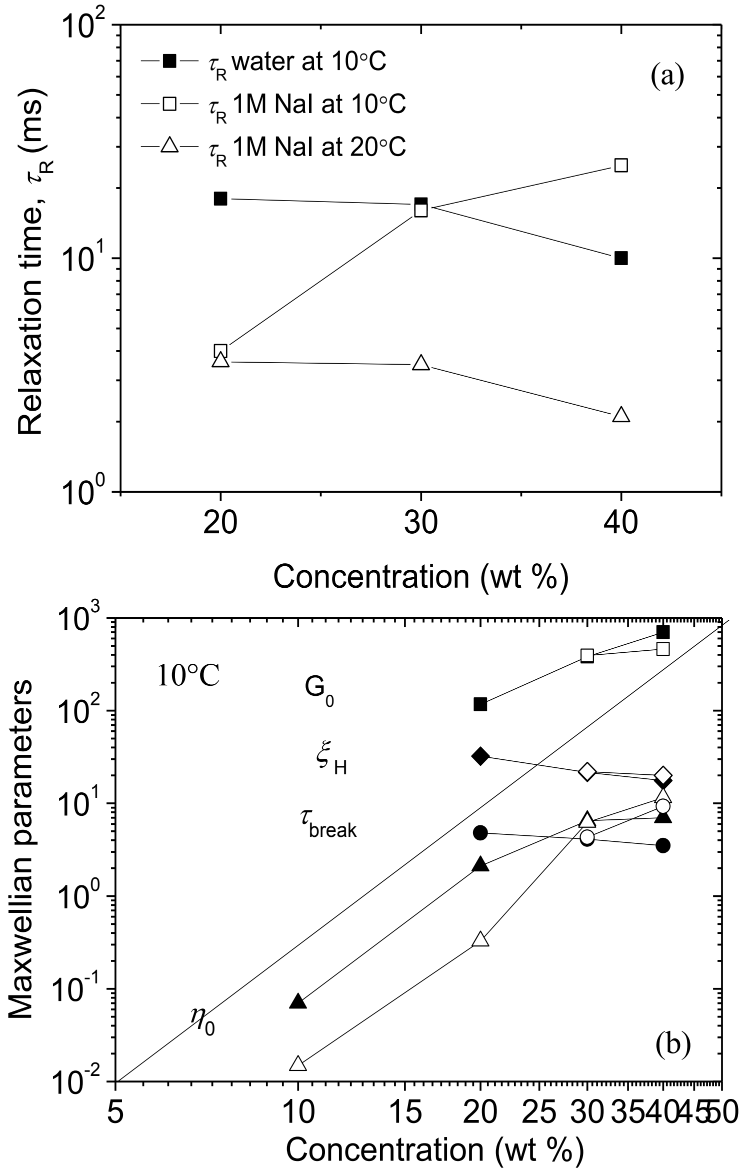

Figure V.3 The calculated Maxwellian parameters as a function of the concentrations (20, 30 and 40 wt%). The pure $R_7^F(EO)_8$ system is plotted in solid symbols; $R_7^F(EO)_8$ with 1M NaI is shown in empty symbols. (a) The relaxation time τ_R (ms) at 10°C (square) and 20°C (triangle). (b) The Mawellian parameters at 10°C, plateau modulus G_0 (Pa) (square); zero shear viscosity η_0 (Pa.s) (triangle); breaking time τ_{break} (ms) (circle); hydrodynamic correlation length ξ_H (nm) (diamond).

Note: In Figure V.3a, the τ_R curve for $R_7^F(EO)_8$/water solution is missing because no crossover is found in the tested frequency range at the temperature of 20°C. In Figure V.3b, the Maxwellian parameters values cannot be calculated for the 20 wt% $R_7^F(EO)_8$/ NaI solution since no plateau of *G*' is observed.

In both solutions (with and without salt), G_0 and η_0 increase with the concentration. In both cases, from the evolution of G_0, we can assume that the number density of entanglement points or the interactions between the objects increase. On the other hand, the variation of η_0 is related to an increase of the number of objects.

The correlation length ξ_H, regarded as the average entanglement length of the chain (the mesh size of the micellar network), decreases as in the case of the solution without salt (Figure V.3b ◆); the values of ξ_H are of the same order of magnitude between 20 and 30nm. Assuming a wormlike micellar system, it is the sign of an entangled structure. The breaking time τ_{break} varies in opposite direction: τ_{break} decreases for the solution without salt (Figure V.3b ●) and increases for the salted solution (Figure V.3b ○).

Under steady shear flow, the wormlike micelles normally exhibit a low-shear Newtonian plateau followed by the shear thinning at $\dot{\gamma} > \dot{\gamma}_c$. The inverse of the critical shear rate $\dot{\gamma}_c$ can also give an estimate of the longest micellar structural relaxation time τ_R [7]. This calculated τ_R values of the $R_7^F(EO)_8$ solutions at 10°C from steady shear test (Table IV.1 and IV.6), are of the same order of magnitude as the τ_R values from dynamic measurement (Table IV.2 and IV.7).

5.4 Comparison between flow birefringence, rheology and SANS

5.4.1 $R_7^F(EO)_8$ in water

In order to see the correlation between the different techniques, the experimental results of the pure $R_7^F(EO)_8$ solution at 20 wt% are shown again in Figure V.4.

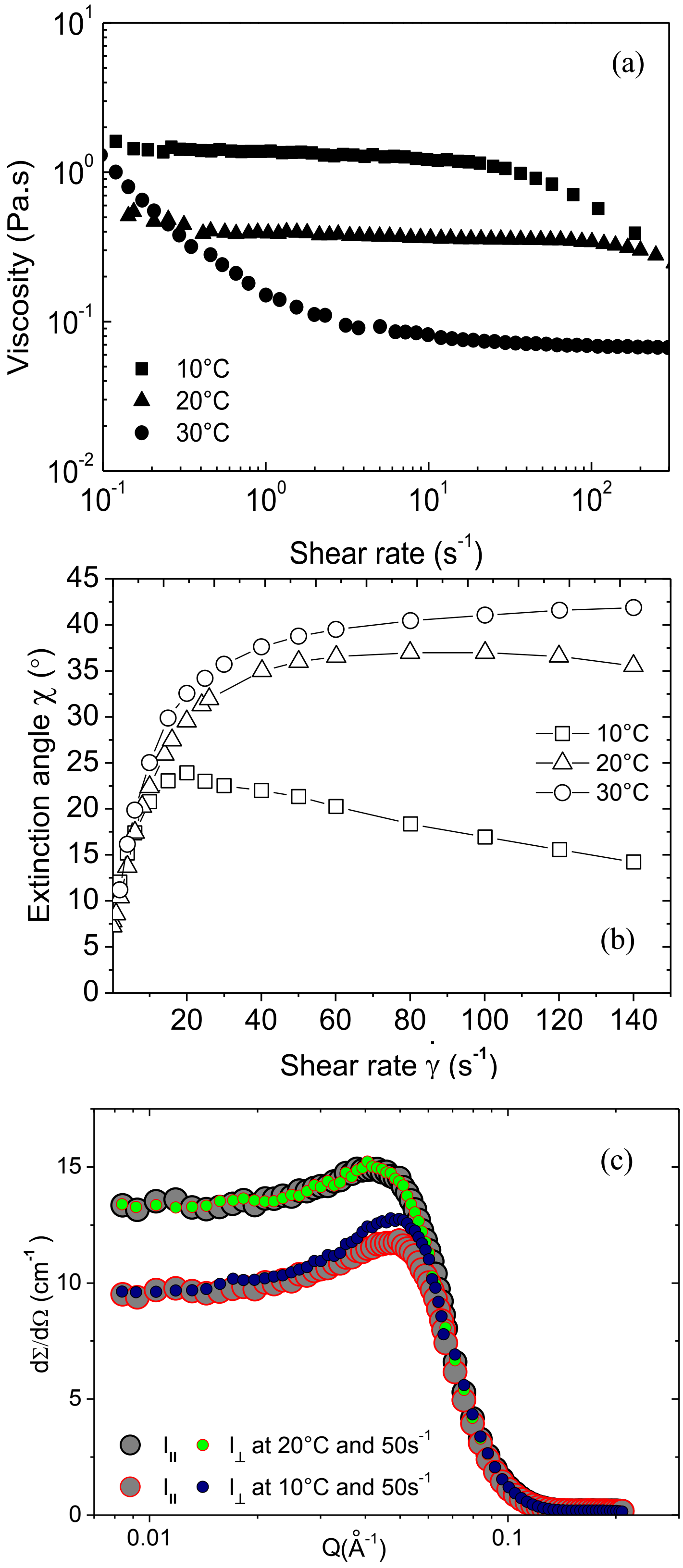

Figure V.4 Pure $R_7^F(EO)_8$ solution at 20 wt%. (a) Viscosity curve as a function of the shear rate (range of 0.1 – 300 s^{-1}) at 10, 20 and 30°C. (b) Evolution of the extinction angle as a function of the shear rate (range of 0 – 140 s^{-1}) at 10, 20 and 30°C. (c) Scattered intensity $I_{\parallel}(q)$ and $I_{\perp}(q)$ at 10°C and 20°C at the shear rate of 50 s^{-1}.

As the low values of the extinction angle in the range of low shear rates let assume, (see chapter 4.1.2), the initial 20 wt% $R_7^F(EO)_8$ solution may contain large anisotropic objects at rest orientated at random. The increase of the angle χ with the shear rate until its maximum at $\dot{\gamma}_c$ is a sign of disorganization in the sample; for $\dot{\gamma} > \dot{\gamma}_c$, the slow decreasing branch at 20 °C toward an angle $\chi \cong 35°$ and the plateau levelling at 30 °C with an angle $\cong 40°$ is characteristic of small Brownian particles poorly orientated by the flow.

However, we further discuss the results for one part in the low shear rates range ($\dot{\gamma} < \dot{\gamma}_c$), and for the other, in the high shear rates range ($\dot{\gamma} > \dot{\gamma}_c$).

(1) At low shear rates before $\dot{\gamma}_c$, the gradual break of the large objects occurs when a small amount of shear is applied. However, the variations of χ do not correlate with the results from the rheological measurements. As a matter of fact, the Newtonian plateau observed at low shear rate is in contradiction with the increase of χ, sign of a huge change of the objects.

(2) Above the critical shear rate value $\dot{\gamma}_c$, the decreasing or levelling off evolution of χ can be related to the shear thinning behaviour. The orientation effect or structural change can be explained by the action of the hydrodynamic field in the high shear rate range on the objects.

At 10°C, the critical shear rates deduced from the flow and extinction angle curves, are respectively $\dot{\gamma}_c \approx 24.5\ s^{-1}$ and $\dot{\gamma}_c \approx 20\ s^{-1}$. For $\dot{\gamma} > \dot{\gamma}_c$, the viscosity η and the angle χ decrease upon increasing the shear rate. The same evolution is found for the sample at 20°C with a critical shear rate $\dot{\gamma}_c$ at $\approx 80 s^{-1}$.

The higher critical shear rate of the solution at 20°C indicates that the orientation of the micelles begins at a higher shear rate, thus suggesting the existence of particles smaller at 20°C than at 10°C. At the temperature of 30°C, closer the miscibility curve, a strong decrease of the apparent viscosity η is observed before a low plateau value; the maximum of χ is not clearly observed and the angle tends smoothly toward a plateau value close to 40°. At this temperature, the particles are supposed to be small and, consequently, difficult to orientate within the applied shear rates range.

Rheo-SANS experiments were also performed in order to study the emergence of anisotropy under flow. Due to a short allocation of beam time, all the SANS experiments were performed on a unique system: 20 wt% $R_7^F(EO)_8$ in D_2O (Figure V.5). Two quantities of interest are computed from the raw data: $I_{\parallel}(q)$ and $I_{\perp}(q)$: respectively components of the intensity parallel and perpendicular to the wave vector. The variations of $I_{\parallel}(q)$ and $I_{\perp}(q)$ for the 20 wt% $R_7^F(EO)_8$-D_2O solution are reported in Figure V.4c.

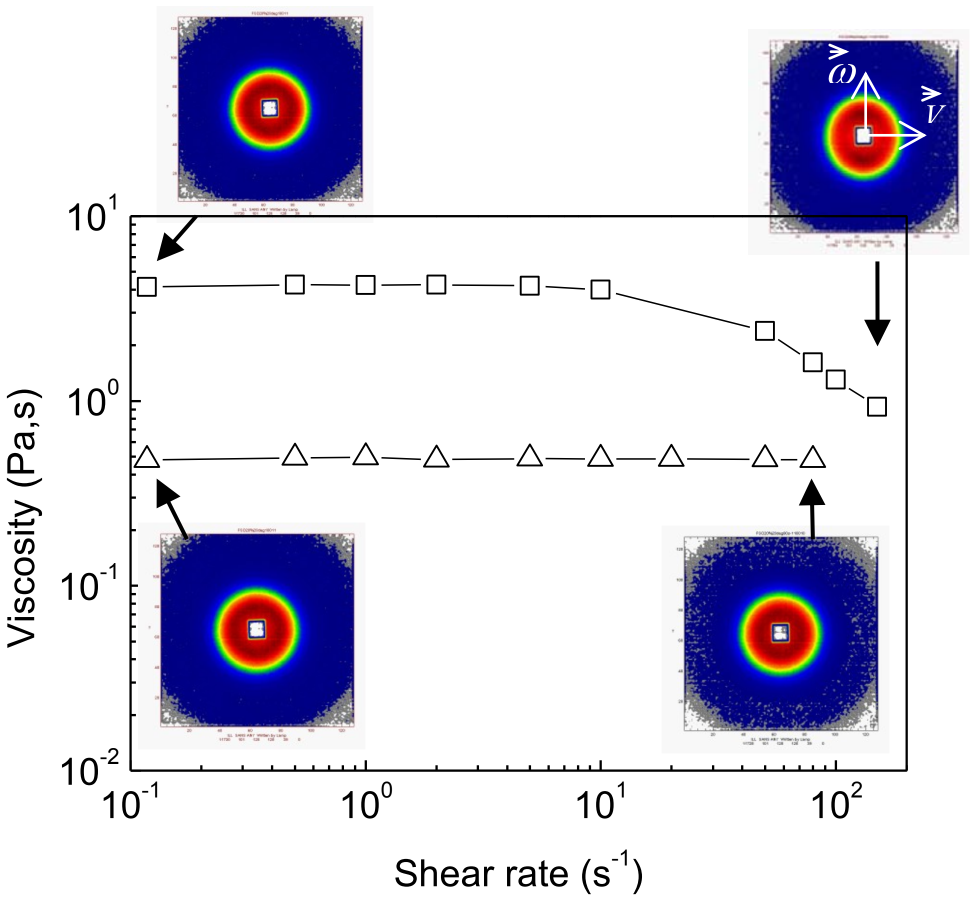

Figure V.5 Viscosity of the 20 wt% pure $R_7^F(EO)_8$-D_2O solution as a function of the shear rate measured at 10 (empty square) and 20°C (empty triangle). The corresponding contour plots from SANS at 10°C are shown at $\dot{\gamma} = 0.1$, 50 and 150 s^{-1}. At 20°C, the contour plots are presented at $\dot{\gamma} = 0.1$ and 80 s^{-1}. The viscosity curves are drawn from the data given by the Bohlin apparatus (CVO120) operating on the D11 line.

A significant gap between the intensity curves $I_{\parallel}(q)$ and $I_{\perp}(q)$ appears at $\dot{\gamma} = 50\ s^{-1}$ (as shown again in Figure V.4c). The shear rate at which the SANS patterns become anisotropic, is thus situated in the range 10 – 50 s^{-1} in agreement, at least approximately, with the results of rheology and flow birefringence. It corresponds to the emergence of the shear thinning character in the viscosity curve when $\dot{\gamma} > \dot{\gamma}_c \approx 20\ s^{-1}$.

At 20°C, the two components superimpose well, neutrons "see" no anisotropy for $\dot{\gamma} \leq 80\ s^{-1}$; the solution is Newtonian. If one compares this result with the steady state and extinction angle measurements, this value (80 s^{-1}) does not appear as a critical value corresponding to a change in the behaviour of the sample under flow. One reason may be found in the ability of heavy water to change quantitatively the rheophysical properties of the sample as previously observed in other micellar systems [8].

5.4.2 $R_7^F(EO)_8$ / 1M NaI solution

The results from steady state rheological (Figure IV.16d) and flow birefringence (Figure IV.19a) measurements are compared at three temperatures: 10, 20 and 30°C. No correlation between the values of $\dot{\gamma}_c$ is found at 10°C: the viscosity curve is Newtonian over nearly the entire range of shear rates while the angle χ starts to decrease when $\dot{\gamma} > 60\ s^{-1}$. At 20°C, the critical shear rate is estimated at $\dot{\gamma}_c \approx 46\ s^{-1}$ from the rheological data and $\approx 40\ s^{-1}$ from the extinction angle variations. For the highest values of $\dot{\gamma}$, χ is the same for both temperatures; we can assume that the geometry of the micelles is nearly the same. At 30°C, the maximum of χ is not clearly observed and the angle still increases slowly toward a plateau value close to 40°. It is the signature of particles with a small geometrical anisotropy hardly orientated by the flow.

5.5 Molecular orientation of $R_8^F(EO)_9$ system

5.5.1 $R_8^F(EO)_9$ in water

Within the direct micellar L_1 phase, the rheological properties of pure $R_8^F(EO)_9$ in water at 20 and 30 wt% concentrations are investigated from 10 to 40°C. The solution at 20 wt%

shows a Newtonian character at all tested temperatures. The change in apparent viscosity occurs at higher concentration (30 wt %). The solution exhibits a Newtonian behaviour, then loses its initial Newtonian character at 35°C, and finally turns to be shear thinning at 40°C. This change may occur because the solution approaches to the miscibility curve. For the flow birefringence results of 30 wt% pure $R_8^F(EO)_9$ at 20°C, there are no measurable values of the extinction angle χ or of the retardation δ. The fact that no appreciable birefringence can be measured under the shearing conditions used for the other systems tells us that the micelles in solution are probably small with a shape close to a sphere.

5.5.2 $R_8^F(EO)_9$ in 3M NaCl solution

The addition of NaCl (3M) into the $R_8^F(EO)_9$ system induces a shift down of the miscibility curve and leads to a change of the flow behaviour for both concentrations, as a function of temperatures from 10 to 50°C. The 20 and 30 wt% solutions at 10 and 20°C, are shear thinning in the low shear rates range and Newtonian beyond a critical shear rate. For the 20 wt% solution between 30 to 45°C, the solutions are Newtonian, but turn to shear thinning again when temperature is raised to 50°C. For higher concentration at 30 wt%, the Newtonian character is only found at 30°C, and then becomes shear thinning again at 40, 45 and 50°C.

The evolution of χ is in agreement with the rheological results. In the presence of NaCl salt, the angle χ is very close to the upper limit of the angle χ (45°) at low shear rates; on further increasing the shear rate, the extinction angle decreases smoothly according to the orientation theory of rigid particles (Figure IV.24). For the 20 wt% solution, the extinction angle remains quite large (~ 40°) even for the largest values of the shear rates (100 s^{-1}). This is a sign of the existence of micelles with a small aspect ratio which are difficult to be orientated by the flow. The addition of NaCl in the $R_8^F(EO)_9$ solutions suggests a change in the structure of the objects from spherical to asymmetrical particles, so that they can be orientated by the flow in an average direction. Normally an increase of the temperature leads to an increase of the Brownian motion of the particles, resulting in a poorer organization of the particles. That is a reason we get a decrease in birefringence intensity with increasing temperature. This is not the case for the 20% solution.

5.6 Comparison between two nonionic fluorinated surfactant systems

For both systems, the rheo-optical properties of micellar solutions in the L_1 phase depend on the concentration and temperature. The ordered hybrid mesophase structure cannot always be obtained although the template used is always an L_1 micellar phase. Without looking at the phase diagram, a shear thinning behaviour over the entire shear rates domain is the sign telling that the thermodynamical conditions are close to the miscibility curve; these conditions are not satisfactory for obtaining ordered mesoporous materials.

Addition of NaI salt (1M) shifts the lower consolute boundary (LCB) of $R_7^F(EO)_8$ based systems toward higher temperatures by a salting in effect. The shear thinning character is also shifted to higher temperatures. In the opposite way, addition of NaCl salt (3M) shifts the LCB of $R_8^F(EO)_9$ systems toward lower temperature by salting out effect.

The Maxwellian character seems to be a pre-requisite condition of the micellar solution for obtaining ordered mesoporous materials.

For both nonionic surfactant systems (with and without salt), the change in behaviour to shear thinning is generally obtained when the experimental condition approaches the miscibility curve. The emergence of the shear thinning phenomenon is supposed to happen because the system gains energy under shear. It may induce the nucleation of the other phase in the region near the miscibility curve, where the fluctuation of concentration normally exists.

The general behaviour of the four systems at the ambient temperature (20°C) is presented in the table V.1. To provide a link between the rheophysical properties of the micellar phase and the mesoporous material, the results will be explained in the conclusion.

Table V.1 The general behaviour of the four systems at the ambient temperature (20°C).

Systems	Phase behaviour and rheological behaviour within the L_1 phase	Evolution of the extinction angle (χ)	SANS	Ordered mesoporous materials*
System I: $R_7^F(EO)_8$ **in water**	**-Newtonian to shear thinning close to the miscibility curve.** **- Maxwellian character**	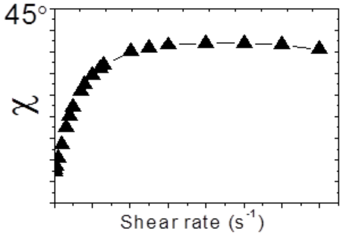	**- isotropic at rest** **- Micelles orient under high shear rate**	**no**
System II: $R_7^F(EO)_8$ **in 1M NaI**	**-Shift up the miscibility curve** **-Newtonian to shear thinning close to the miscibility curve.** **- Maxwellian character with crossover**	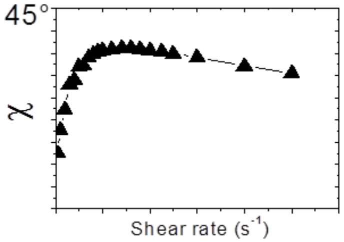	**nd**	**yes**
System III: $R_8^F(EO)_9$ **in water**	**-Newtonian** **-Maxwellian character**	**No measurable values with the experimental device**	**nd**	**yes**
System IV: $R_8^F(EO)_9$ **in 3M NaCl**	**- Shift down the miscibility curve** **- Narrower Newtonian domain, shear thinning near the miscibility curve.**	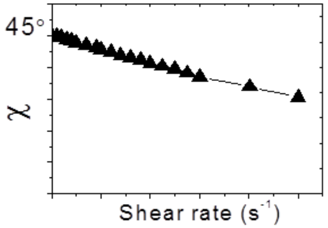	**nd**	**no**

nd = not determined

*** From the previous studies/ reports: Can the ordered mesoporous material be successfully obtained in the final products?**

References

[1] K. S. Sharma, S. R. Patil and A. K. Rakshit, *Colloids and Surfaces A: Physicochemical and Engineering Aspects* **2003**, *219*, 67-74.

[2] D. P. Acharya, S. C. Sharma, C. Rodriguez-Abreu and K. Aramaki, *The Journal of Physical Chemistry B* **2006**, *110*, 20224-20234.

[3] R. G. Shrestha, L. K. Shrestha, S. C. Sharma and K. Aramaki, *The Journal of Physical Chemistry B* **2008**, *112*, 10520-10527.

[4] J. L. Blin, R. Bleta and M. J. Stébé, *Journal of Colloid and Interface Science* **2006**, *300*, 765–773.

[5] F. Michaux in *Contribution des tensioactifs fluorés à la synthèse de matériaux mésoporeux : Application à la conception d'un bioréacteur*, *Ph.D thesis* UHP - Université Henri Poincaré, Nancy, **2009**.

[6] S. C. Sharma, D. P. Acharya and K. Aramaki, *Langmuir* **2007**, *23*, 5324-5330.

[7] C. A. Dreiss, *Soft Matter* **2007**, *3*, 956-970.

[8] J. P. Decruppe and S. Lerouge, *Colloid & Polymer Science* **1999**, *277*, 891-894.

Conclusion

L'objectif principal de ce travail a consisté en l'étude des propriétés rhéophysiques de solutions micellaires à base de tensioactifs fluorés. Ces solutions sont utilisées comme modèles dans la préparation de matériaux mésoporeux qui peuvent avoir une structure bien ordonnée ou pas. Des études précédentes ont établi l'existence d'une relation entre la position de la courbe de miscibilité et l'obtention de matériaux mésoporeux ordonnés.

Deux surfactants de la famille des éthers polyoxyéthylène fluoroalkyl, $R_7^F(EO)_8$ et $R_8^F(EO)_9$ ont été utilisés pour la préparation des solutions. Les paramètres de l'étude à l'équilibre et hors équilibre sont la température, la concentration en tensioactif et en sel. Les expériences effectuées apportent des informations sur les caractéristiques des systèmes micellaires à la première étape de la préparation des matériaux mésoporeux et qui favorisent la formation de structures hexagonales ordonnées.

Le diagramme de phases des deux tensioactifs montrent qu'une phase micellaire L_1 existe dans une large gamme de températures et concentrations. La position de la courbe de miscibilité dépend des caractéristiques de chaque système. La phase L_1 est optiquement isotrope au repos. L'addition de sel NaI au système $R_7^F(EO)_8$ conduit à un déplacement de la courbe de miscibilité vers les hautes températures tandis que l'ajout de sel NaCl à $R_8^F(EO)_9$ conduit à un abaissement de la courbe de miscibilité. On peut ainsi contrôler la position de cette courbe.

Les propriétés de la phase micellaire L_1 de $R_7^F(EO)_8$ dans H_2O (système I) ont été étudiées hors équilibre par les techniques de rhéologie et de rhéooptique avec, comme paramètres, la température et la concentration. On observe une évolution claire du comportement sous écoulement en modifiant ces paramètres. En général, les solutions présentent un caractère Maxwellien à basses températures (conditions éloignées de la courbe de miscibilité). Aux températures intermédiaires, un grand nombre de solutions présentent un comportement Newtonien qui devient rhéofluidifiant lorsque la température se rapproche de la courbe de miscibilité.

L'accroissement de la viscosité apparente avec la concentration peut être dû à une augmentation de la taille des micelles ou du nombre de particules en solution. Différentes études suggèrent l'existence de micelles vermiculaires dans ces systèmes mais nos nouvelles expériences sont en contradiction avec cette hypothèse.

Considérant les résultats de biréfringence et de cycles de contrainte obtenus avec la solution à de $R_7^F(EO)_8$ à 20%, un modèle structural simple est proposé ; il suppose l'existence de petites micelles allongées liées par des forces faibles pour former une chaine aisément rompue par un cisaillement croissant. L'évolution de l'angle d'extinction avec le taux de cisaillement et le rhéoépaississement sous contrainte constante conforte cette hypothèse. Une faible augmentation du cisaillement conduit à un accroissement important de χ qui croît jusqu'à un maximum atteint pour $\dot{\gamma} = \dot{\gamma}_c$ avant de décroître a nouveau. Le système contient alors de petites particules qui s'orientent dans une direction moyenne. Ceci est confirmé par l'émergence de la rhéofluidification qui apparaît alors pour $\dot{\gamma} > \dot{\gamma}_c$.

L'effet de la température sur la taille des particules asymétriques peut également être observé en considérant l'orientation des micelles sous cisaillement dans le domaine $\dot{\gamma} > \dot{\gamma}_c$. En effet, la solution $R_7^F(EO)_8/H_2O$ à 20% présente un taux de cisaillement critique $\dot{\gamma}_c$ à 20°C plus grand qu'à 10°C. Ceci indique que l'orientation des micelles débute à un cisaillement critique plus grand à 20°C et donc que les particules sont plus petites à 20°C qu'à 10°C. A 30°C, température proche de la courbe de miscibilité, on n'observe plus de maximum dans l'évolution de χ; ceci laisse supposer que les particules sont faiblement asymétriques avec un rapport d'aspect petit et par conséquent difficiles à orienter.

Des expériences de diffusion de neutrons aux petits angles ont été réalisées sur la solution à 20% en masse aux températures de 10 et 20°C au repos et sous écoulement. Un pic de corrélation apparaît dans les courbes d'intensité diffusée en fonction du vecteur d'onde ; c'est la signature de l'existence d'interactions entre les objets diffusants. Un modèle centrosymétrique à deux couches, un cœur hydrophobe et une couronne hydrophile est utilisé pour interpréter quantitativement les résultats.

Au repos, un accroissement de la température (de 10 à 20°C) n'affecte pas la structure locale des micelles. L'ajustement des données expérimentales au modèle théorique suggère l'existence de particules allongées d'environ 20nm de longueur pour un rayon de 7nm sans pénétration de molécules d'eau dans le film de tensioactif. Les dimensions du cœur hydrophobe sont environ 17 nm pour la longueur et 3.4nm pour le diamètre.

Sous écoulement, un écart significatif apparaît entre les intensités $I_{\|}(q)$ et $I_{\perp}(q)$ pour le taux de cisaillement de $50s^{-1}$; cette séparation traduit l'apparition d'une orientation préférentielle dans une direction moyenne, mais cette valeur du cisaillement n'est pas en accord avec les résultats de rhéologie et de biréfringence d'écoulement.

L'addition de sel NaI à $R_7^F(EO)_8$ (système II) décale la courbe de miscibilité vers les hautes températures. Ainsi, dans les mêmes conditions de concentration et de température les systèmes avec sel sont plus éloignés de la courbe et, bien qu'ils forment toujours une phase L_1 , leurs propriétés rhéologiques n'en sont pas moins modifiées.

La concentration critique qui correspond à la transition Newtonien- rhéofluidification est déplacée vers des valeurs plus grandes (de 20% à 30%). Le caractère Maxwellien apparaît dans un domaine de températures et concentration plus large que pour le système $R_7^F(EO)_8/H_2O$. Les résultats de biréfringence d'écoulement, qualitativement similaires à ceux obtenus avec $R_7^F(EO)_8/H_2O$ laissent également supposer l'existence de la même structure micellaire : de petites micelles liées par des forces faibles.

Les paramètres du modèles de Maxwell ont été calculés pour les deux systèmes $R_7^F(EO)_8$ avec et sans sel. Le module plateau croît avec la concentration car la densité en nombre de points d'enchevêtrements ou interactions entre les objets, augmentent. La longueur de corrélation hydrodynamique ξ_H décroît comme dans le cas de la solution sans sel et reste du même ordre de grandeur entre 20 et 30nm.

Les solutions aqueuses L_1 formées avec le second tensioactif $R_8^F(EO)_9$ (système III) présentent des propriétés différentes car $R_8^F(EO)_9$ est plus hydrophile que $R_7^F(EO)_8$.

Les propriétés rhéologiques du système III à 20 et 30.% sont déterminées entre 10 et 40°C. Les modifications du comportement de la viscosité apparente apparaissent plus clairement à la concentration de 30%. La solution est initialement Newtonienne, perd ensuite ce caractère pour finalement devenir rhéofluidifiante à 40°C. Pour la solution de $R_8^F(EO)_9$ à

30% et à 20°C, l'angle d'extinction χ ou la différence de phase δ n'ont pu être mesurés avec précision ; ceci laisse supposer que les particules ont une forme proche de la sphère.

L'addition du sel NaCl à $R_8^F(EO)_9$ induit un décalage vers le bas de la courbe de miscibilité et une modification du comportement en écoulement pour les deux concentrations dans le domaine de température s'étendant entre 10 et 50°C. L'évolution de χ est en accord avec les résultats de rhéologie. χ, qui est très proche de la limite supérieure (45°) aux faibles cisaillements décroît de manière monotone avec le cisaillement conformément à la théorie de l'orientation des particules rigides. Cette évolution laisse supposer que l'ajout de sel entraine une modification de la forme des particules, probablement un accroissement qui facilite l'orientation.

Tous les résultats obtenus laissent supposer que le caractère Maxwellien des solutions semble être une propriété pertinente des solutions micellaires utilisées comme modèles dans la fabrication des structures hybrides hexagonales. Dans le domaine de température et concentrations utilisés, les solutions contenant le sel NaI ont une meilleure propension à former des structures hybrides hexagonales. Elles présentent également un caractère Maxwellien plus marqué que les solutions $R_7^F(EO)_8/H_2O$.

Les solutions micellaires à base de $R_8^F(EO)_9$ sont également Maxwelliennes mais elles perdent ce caractère avec l'adjonction du sel NaCl.
Pour les quatre systèmes, le caractère Maxwellien disparaît en général lorsque les conditions sont proches de celles de la courbe de miscibilité. Ce résultat conforte l'hypothèse selon laquelle : pour préparer des matériaux mésoporeux ordonnés, les conditions thermodynamiques de la solution à laquelle le précurseur est ajouté, ne doivent pas être trop proche de la courbe de miscibilité. Dans ce cas les solutions sont Maxwelliennes.

Afin de mieux comprendre l'organisation à l'échelle moléculaire dans ces deux tensioactifs, il est souhaitable d'utiliser d'autres techniques expérimentales complémentaires. Ainsi la diffusion de lumière sous écoulement et la cryo miscroscopie électronique à transmission apporteraient sans doute une réponse partielle aux questions qui restent en suspens.

Conclusion

The main objective of this study consisted in studying the rheophysical properties of micellar solutions of nonionic fluorinated surfactants. These solutions are used as templates in the preparation of mesoporous materials which can have a well-ordered structure or not. Previous studies have shown a link between this property and the distance to the lower consolute boundary.

Two surfactants of the polyoxyethylene fluoroalkyl ether family, $R_7^F(EO)_8$ and $R_8^F(EO)_9$, in aqueous systems have been used to prepare the samples. The influence of the temperature, concentration of surfactant and salt addition on the rheophysical properties has been taken into account under equilibrium and out-of-equilibrium conditions. The experiments performed during this work bring more information on the characteristics of the micellar systems at the initial stage of the mesoporous preparation which promotes the formation of hexagonal ordered structures in the final product.

The phase diagrams of both surfactants show that a direct micellar phase (L_1) exists in a wide range of concentrations and temperatures; the position of the lower consolute boundary (LCB) depends on the characteristics of the different systems. This phase is optically isotropic at rest. The addition of NaI salt into $R_7^F(EO)_8$ system results in a shift of the miscibility curve toward higher temperatures by a “salting in” effect. In the opposite way, the NaCl salt can shift the miscibility curve of $R_8^F(EO)_9$ toward lower temperatures by a “salting out” effect. Salt is added in order to control the distance to the LCB

The properties of the micellar phase (L_1) of $R_7^F(EO)_8$ in water have been studied (system I) by out-of-equilibrium techniques (rheology and rheo-optics) with the temperature and concentration as parameters. A clear evolution of the rheological behaviour is seen when the temperature and concentration are changed. The solutions generally show a Maxwellian character at low temperatures (conditions far from the miscibility curve). At low and intermediate temperatures, a Newtonian behaviour is observed for a wide range of solutions which becomes shear thinning when the temperature is raised toward the miscibility curve.

The increase of the apparent viscosity with the concentration may be due to the increase of the micelles size or of the number of particles in the solution. Different publications suggest that the system must contain wormlike micelles. But these newer experiments update new proofs in contradiction with this hypothesis.

Considering the results of the flow birefringence and stress cycles experiments obtained with the 20 wt% $R_7^F(EO)_8$ solutions, a simple structural model is proposed: we assume that small elongated micelles are linked by weak forces to form a chain easily broken as the shear rate is increased. This assumption is supported by the evolution of the extinction angle χ in the low shear rates range and the increase of the apparent viscosity η under a small constant stress. These experiments reveal the existence of large anisotropic structures, which could be disorganized by the increasing shear rate. Moreover, the shear thickening phenomenon at constant shear stress in stress cycle test could result from the emergence and a building up of aggregates, due to weak forces between the micelles.

The large aggregates are easily broken into smaller objects with a very small shear rate indicating the presence of weak links. Increasing slightly the shear rate (but still remaining small) leads to a sharp increase of the angle χ. This angle increases until a maximum is reached at the critical shear rate $\dot{\gamma}_c$; the system then contains smaller asymmetrical micelles which align on average in the same direction. The alignment of asymmetrical micelles under the action of shear flow is also confirmed during steady shear measurements, when we observe the decrease of the apparent viscosity (shear thinning) at $\dot{\gamma} > \dot{\gamma}_c$.

The effect of temperature on the size of the asymmetrical particles out of equilibrium (at non-equilibrium) can also be observed by considering the orientation of the micelles under shear within the range $\dot{\gamma} > \dot{\gamma}_c$. As a matter of fact, the 20 wt% $R_7^F(EO)_8$/water solution has a critical shear rate $\dot{\gamma}_c$ at 20°C higher than at 10°C; it indicates that the orientation of the micelles begins at a higher shear rate at 20°C suggesting the existence of particles smaller at 20°C than at 10°C. At the temperature of 30°C, closer to the miscibility curve, the maximum of χ is not clearly observed. The particles are supposed to be small and, consequently, difficult to orientate within the applied shear rates range.

SANS experiments were also performed on the 20 wt% $R_7^F(EO)_8$/ water solution at the temperatures of 10 and 20 °C at rest and under shear. A peak appears in the intensity versus the wave vector curves, it is the signature of interactions between the scattering objects. A centrosymmetric model consisting of 2 layers: a hydrophobic core and a hydrophilic corona is used to fit the data. At rest, an increase of the temperature (from 10 to 20°C) does not affect the local structure of the micelles. The fitting of the experimental data suggested the existence of elongated particles about 20nm long with a radius of 7 nm, with no penetration of water into the surfactant film. The dimensions of the hydrophobic core are about 17 by 3.4 nm. Under flow, a significant gap between the intensity curves $I_{\|}(q)$ and $I_{\perp}(q)$ appears at $\dot{\gamma} = 50\ s^{-1}$ indicating the emergence of anisotropy; but the shear rate value is in fair agreement with the results of rheology and birefringence.

The addition of NaI into the $R_7^F(EO)_8$ system (system II) shifts up the miscibility curve. Thus, in the same conditions of concentration and temperature, the systems with salt are further away from the miscibility curve and, although the micellar phase still is a L_1 phase, their rheological behaviour is changed.

The critical concentration corresponding to the transition from the Newtonian to the shear thinning behaviour is shifted toward higher values (from 20 wt % to 30 wt %). The Maxwellian character is found in a concentrations and temperatures range wider than in the pure $R_7^F(EO)_8$/water system. The flow birefringence results which are qualitatively similar to those obtained with the pure $R_7^F(EO)_8$/water system suggest the existence of the same micellar organization, i.e. micelles linked by weak forces.

The Maxwellian parameters have been calculated for the two systems ($R_7^F(EO)_8$ with and without salts. In both systems, G_0 increases with the concentration: we can assume that the number density of entanglement points or the interactions between the objects increase. The hydrodynamic correlation length ξ_H decreases as in the case of the solution without salt; it is of the same order of magnitude between 20 and 30nm.

The aqueous solutions in the L_1 phase of the second surfactant, $R_8^F(EO)_9$ have different micellar properties as it is a more hydrophilic surfactant than $R_7^F(EO)_8$ (see the phase diagram).

In system III, the rheological properties of the 20 and 30 wt% $R_8^F(EO)_9$/water systems are determined from 10 up to 40°C. The change in the apparent viscosity occurs more clearly at higher concentration (30 wt %) than at 20 wt%. The solution exhibits a Newtonian behaviour, then loses it and finally turns to be shear thinning at 40°C. For the 30 wt% pure $R_8^F(EO)_9$ solution at 20°C, no measurable values of the extinction angle χ or of the retardation δ could be obtained, suggesting that the micelles in solution are probably small with a shape close to a sphere.

For system IV, the addition of NaCl (3M) into the $R_8^F(EO)_9$ system induces a shift down of the miscibility curve and a change of the flow behaviour for both concentrations in the temperature range between 10 and 50°C. The evolution of χ is in agreement with the rheological results. The angle χ which is very close to the upper limit (45°) at low shear rates, decreases smoothly with increasing the shear rate according to the orientation theory of rigid particles. This evolution suggests that the addition of salt induces a change in the shape of the objects from spherical to asymmetrical particles, so that they can be more easily orientated by the flow.

All the results obtained suggest that the Maxwellian character of the solution might be a significant property of the micellar template used for obtaining the hybrid hexagonal structure. In the range of concentrations and temperature investigated, the solutions with NaI show a better tendency to form hybrid hexagonal structure; they also have a stronger Maxwellian character than the pure $R_7^F(EO)_8$/water system.

The $R_8^F(EO)_9$ micellar solutions also behave like Maxwellian fluids but this feature disappears with the addition of NaCl (system IV).

From all four systems, the loss of the Maxwellian character is generally observed when the conditions approach the miscibility curve. This result consolidates the following assumption: in order to prepare ordered mesoporous materials, the thermodynamical conditions at which the silica precursor is added to the micellar solution should not be close to the miscibility curve. Therefore, this study suggests that the Maxwellian character seems to be a pre-requisite condition of the micellar solution for obtaining ordered mesoporous materials.

In order to better understand the molecular organization of both surfactants, further experiments should be performed using other techniques, such as light scattering under shear and Cryo- transmission electron microscopy.

Appendix

Appendix I

For mesoporous material preparation in our laboratory, the concentration of 10wt% $R_7^F(EO)_8$ is commonly used as a template. In order to study the influence of NaI salt, the mesoporous materials are synthesized by using 10wt% $R_7^F(EO)_8$ in NaI aqueous solutions by the following method: Firstly, the micellar solution of $R_7^F(EO)_8$ at 10wt% in water at pH 7 for different NaI concentrations (0.25, 0.5 and 1 M) is prepared. Then, the silica source (Tetramethoxysilane, TMOS) is added drop wise into the micellar solution at room temperature under stirring during 1 hour. The surfactant/silica molar ratio (n_{TA}/n_{TMOS}) is adjusted to 0.5. The hydrothermal treatment is then performed by sealing the obtained samples in Teflon autoclaves and heated during 24h at 80°C. The final products are recovered after removal of the surfactant by ethanol extraction with a Soxhlet apparatus during 2 days.

The cloud point temperature of these prepared micellar solutions 10wt% $R_7^F(EO)_8$ in water and in NaI aqueous solutions (0.25, 0.5 and 1 M) are plotted as a function of NaI concentration (Figure A.1). It suggested that the cloud point temperature increases with increasing the NaI concentration. The characteristics of the obtained mesoporous material from the $R_7^F(EO)_8$ prepared under these conditions are then measured by X-ray, Nitrogen adsorption-desorption measurements and pore size distribution determination. The results showed that the well ordered hexagonal materials can be obtained with a NaI concentration equal to 1M (data not shown). This is the reason why we decided to use the concentration of 1M NaI aqueous solution to continue studying on the influence of NaI salt on the phase behaviour and rheological properties of this micellar solution.

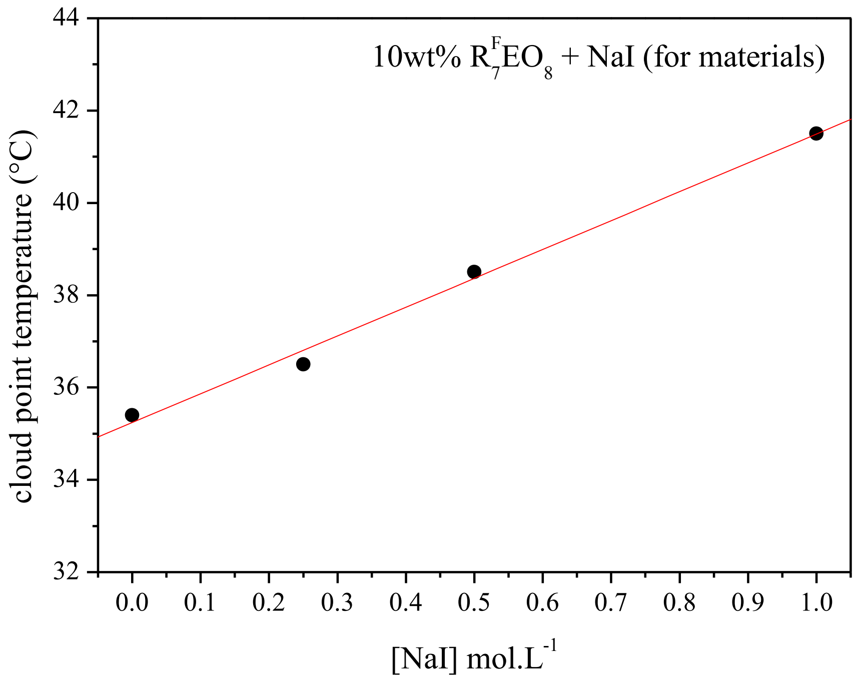

Figure A.1 The change in cloud point temperature (CP) between the solutions without and with salt of the 10wt% $R_7^F(EO)_8$ solution as a function of the NaI concentration (0.25, 0.5 and 1 M).

Appendix II

As described in chapter II, we use the rheology, flow birefringence and SANS under shear methods for studying the properties of $R_7^F(EO)_8$ in water system. Generally, when different methods of investigation are used, care must be taken to operate under exactly the same conditions. Since SANS experiments require heavy water (D_2O) for sample, we did prepare our SAN sample by D_2O. Meanwhile, the rheology and flow birefringence were operated under normal water (H_2O) conditions. Though, we were concerned that the experiments must be taken to operate under exactly the same conditions, when different methods of investigation are used.

In order to compare and analyse the properties of $R_7^F(EO)_8$ in this work, we had to confirm the rheological behaviours of this surfactant, if D_2O was used for the sample preparation. Therefore, we have presented the rheological properties of $R_7^F(EO)_8$ samples in D_2O, operating by the two different methods; here in this index.

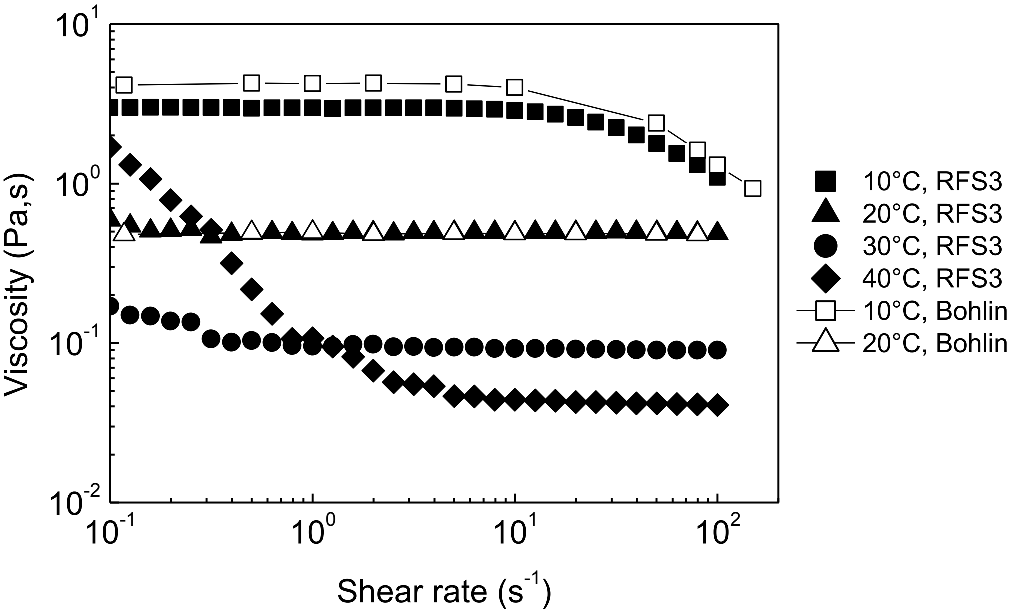

Figure A.2 The apparent viscosities of 20 wt% $R_7^F(EO)_8$ in D_2O as a function of shear rate $\dot{\gamma}$, operating by the rheometer RFS3 (rheological studies; 10°C ■, 20°C ▲, 30°C ●, 40°C ◆) and the Bohlin apparatus; CVO120 (SANS experiment; 10°C □, 20°C △).

For the steady shear measurement, the 20 wt% $R_7^F(EO)_8$ samples in heavy water (D_2O); in Figure A.2, have revealed the change in rheological behaviours as can be obtained from the $R_7^F(EO)_8$ samples in water (H_2O); in Figure IV.1d. All apparent viscosity curves of 20 wt% in D_2O system show the same qualitative flow behaviours, and similar values of the apparent viscosity as in H_2O system. The highest apparent viscosity is found at 10°C with the quasi-Newtonian behaviour in the wide range of tested shear rate. Once the curve reaches the critical shear rate $\dot{\gamma}_c$, the shear thinning character occurs. At 20°C, the Newtonian is observed. The initial Newtonian character is lost; defines as the shear thinning, when raising the temperature to 30°C and eventually stronger character at 40°C.

Between the two instruments (the RFS3 and Bohlin apparatus), the results of $R_7^F(EO)_8$ samples in heavy water (D_2O) at 10 and 20°C indicate the similar behaviours and also in the quantitative values of the apparent viscosity.

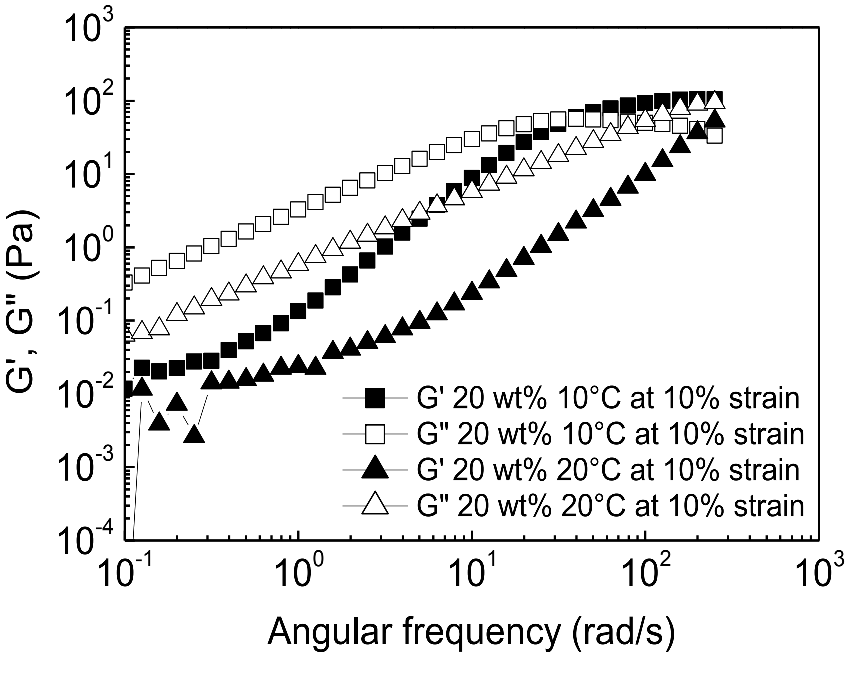

Figure A.3 Storage modulus *G*' (solid symbols) and loss modulus *G*" (open symbols) as a function of the angular frequency ω by using RFS3: (a) at a constant temperature 20°C and different $R_7^F(EO)_8$ concentrations in D_2O; at the concentrations of 20 wt% at 10 and 20°C.

The dynamic rheological behaviours of 20 wt% $R_7^F(EO)_8$ samples in heavy water (D_2O) at 10 and 20°C are also confirmed. The magnitudes of G' and G'' are linearly increased as a function of angular frequency ω. Both temperatures pronounced the Maxwellian character, G' and G'' increase with slope of 1 and 2, respectively. At the constant 10°C, G' and G'' intersect are also found at 38.5 rad/s, the "crossover" point at for which $\omega\tau_R = 1$; while can not be observed at 20°C.

From this part of experiment, the results are in agreement even we use H_2O or D_2O for sample preparation. Therefore, it is admitted to compare and analyse the results from the different used measurements, within this work.

However, the rheological behaviours of H_2O and D_2O can be quantitatively varied. It may because of the physical properties of the deuterium compound in the heavy water. It can exhibit significant kinetic isotope effects and other physical and chemical property differences from the hydrogen analogs; for example, D_2O is more viscous than H_2O [1]. Chemically, deuterium behaves similarly to ordinary hydrogen, but there are differences in bond energy and length for compounds of heavy hydrogen isotopes which are larger than the isotopic differences in any other element.

[1] D. R. Lide CRC Handbook of Chemistry and Physic, **2005**.

List of Tables

I.1 Surfactant packing parameter g,
expected structure and examples for such structures 25
I.2 Synthesis routes to mesoporous materials with the emphasis on silicates 27
II.1 Physical- data of the fluorinated surfactants 55
IV.1 The Ostwald's law parameters for $R_7^F(EO)_8$ in water at different
concentrations and temperatures 96
IV.2 The calculated parameters from Maxwellian theoretical models at T= 283K 104
IV.3 The characteristics of the constituting molecules in the studied system 113
IV.4 Jean-Claude Ravey Modeling parameters for
20 wt% $R_7^F(EO)_8$ /water micellar solution at 10 and 20 °C 117
IV.5 q^* (Å^{-1}) for the two components $I_{\|}(q)$ and $I_{\perp}(q)$ of the 20 wt % $R_7^F(EO)_8$
in water under different shear rates at 10°C and 20°C 122
IV.6 Ostwald's law parameters for $R_7^F(EO)_8$ in 1 M NaI solution
at different concentrations and temperatures 126
IV.7 The calculated parameter from Maxwellian theoretical models at T = 283K,
of the $R_7^F(EO)_8$ surfactant in 1M NaI solution 132
IV.8 Ostwald's law parameters for $R_8^F(EO)_9$ in water
at different concentrations and temperatures 136
IV.9 The parameters of Ostwald's law for $R_8^F(EO)_9$ in 3M NaCl
at different concentrations and temperatures 140
IV.10 Stress optical coefficient for $R_8^F(EO)_9$ 30wt% in 3M NaCl
at different temperatures 145
V.1 The general behaviour of the four systems at the ambient temperature (20°C) 166

List of Figures

I.1 Schematic and curvature of OMS:
the sequence- of weight percentage dependent phase of surfactant in water. 12
I.2 Onset of micellization observed by sudden change
in measured properties of solution at characteristic surfactant concentration,
critical micellization concentration (CMC) 13
I.3 Schematic models and texture of hexagonal phase 14
I.4 Schematic model and texture of lamellar phase 15
I.5 Bicontinuous cubic phases (*Ia3d* and *Pn3m*), *Im3m* 16
I.6 The ideal phase diagram of a mostly hydrophilic surfactant
as a function of temperature and HLB values 17
I.7 Phase diagram of hydrogenated surfactants a) $C_{16}(EO)_{12}$ and b) $C_{16}(EO)_8$ 18
I.8 Packing shapes of surfactants and the structure they form 20
I.9 Illustrations of mesoporous M41S materials:
a) MCM-41 b) MCM-48 and c) MCM50 23
I.10 Two synthesis strategies of mesoporous materials:
(a) cooperative self-assembly, (b) “true” liquid-crystal templating process 24
I.11 Molecular structure of perfluoroalkyl sulfonamide ethoxylate, $C_8F_{17}EO_n$ 32
I.12 The influence of salt on the shift of the lower consolute boundary 38
I.13 Temperature-composition phase diagram of
$C_7F_{15}C_2H_4(OC_2H_4)_8OH$, $R^F{}_7(EO)_8$ in water 44
I.14 Temperature-composition (wt%) phase diagram of $R_8^F(EO)_9$ 45
II.1 Simple classification of rheological behaviours 57
II.2 Schematic diagram of basic tools for the rotational rheometer:
(a) coaxial cylinders, (b) cone-plate, (c) parallel plates 58
II.3 Schematic view of a concentric cylinder rheometer 58
II.4 Cone and plane rheometer 59
II.5 Rheometer RFS 3 (TA Instruments) with cone and plate geometry 60
II.6 Rheometer Physica MCR 501 (Anton Paar)
with cone-plate and Couette geometries 60
II.7 Sinusoidal wave forms for stress and strain functions 62

II.8 Optical properties of isotropic and anisotropic materials under polarized light ... 64

II.9 Schematic diagram of the polarimetric bench 66

II.10 Couette cell 67

II.11 Couette cell and cross of isoclines under cross polarizers 68

II.12 Extinction angle determination 69

II.13 Determination of the true extinction angle ($\overline{O'}\,\overline{A}$).. 70

II.14 The method of Sénarmont for measuring the phase shift 71

II.15 (a) Principal scheme of the SANS experiment, (b) Photograph and diagram of the Couette cell used 72

II.16 The D11 line, archetype of a long, pinhole geometry instrument for SANS 73

III.1 Binary phase diagram of $R_7^F(EO)_8$/water system. L_1: direct micellar phase, L_2: reverse micellar phase, L_α: lamellar phase, $L'_1 + L''_1$: biphasic phase.............. 82

III.2 Partial binary phase diagram of $R_7^F(EO)_8$/water system in the range [0.5-50 wt %]. L_1: direct micellar phase (tube III.2a), L_α: lamellar phase, $L'_1 + L''_1$: biphasic phase (tube III.2b): rich and poor in micelles 82

III.3 Partial temperature-composition phase diagram of the $R_7^F(EO)_8$ surfactant in (a) water, (b) 0.5 M and (c) 1 M NaI aqueous solutions, in the range 0.5-50 wt % surfactant... 84

III.4 Temperature-composition (wt%) phase diagram of $R_8^F(EO)_9$ in water................. 85

III.5 Partial temperature-composition phase diagram of the $R_8^F(EO)_9$ surfactant in (a) 1.5 M and (b) 3 M NaCl aqueous solutions, in a range of 0.5-30 wt % surfactant... 86

IV.1 Rheological behaviour in steady state shearing mode. (a) miscibility curve, the symbols pointing out the solutions under investigation; (b) viscosity curves at 20°C of different wt% $R_7^F(EO)_8$ concentrations. The viscosity curves for the concentrations of (c) 10, (d) 20, (e) 30 and (f) 40 wt% at different temperatures; 10°C, 20°C, 30°C, 40°C 95

IV.2 Storage modulus G' and loss modulus G'' as a function of the angular frequency ω: (a) at a constant temperature 20°C and different $R_7^F(EO)_8$ concentrations in water; at the various concentrations of (b) 10, (d) 20, (f) 30 and (h) 40 wt% at different temperatures (20, 30 and/or 40°C) 99

IV.3 Cole-Cole plot $G''(G')$ at 10°C of $\mathrm{R}_7^{\mathrm{F}}(\mathrm{EO})_8$ (a) 10, (b) 20, (c) 30 and (d) 40 wt % in water 102

IV.4 Apparent viscosity η as a function of the shear stress σ during the three steps cycle for a sample at 20 wt% $\mathrm{R}_7^{\mathrm{F}}(\mathrm{EO})_8$ in water 105

IV.5 Zero-shear viscosity η_0 as a function of mass fraction ϕ_{mass} of $\mathrm{R}_7^{\mathrm{F}}(\mathrm{EO})_8$ in water at (a) 10 and (b) 20°C 107

IV.6 The three rheological behaviours of $\mathrm{R}_7^{\mathrm{F}}(\mathrm{EO})_8$ in water under L_1 phase.............108

IV.7 Flow birefringence experiments: (a) extinction angle χ, (b) birefringence intensity Δn vs. the shear rate The concentration is 20 wt % $\mathrm{R}_7^{\mathrm{F}}(\mathrm{EO})_8$ in water and the temperature 10°C, 20°C and 30°C 109

IV.8 Schematic diagrams showing the various parameters defining the geometry of a micelle solution..112

IV.9 Representation of elongated ellipsoidal particle 112

IV.10 Absolute contour plot 3D for the 20 wt % $\mathrm{R}_7^{\mathrm{F}}(\mathrm{EO})_8$ micellar solution (in heavy water) at (a) 10°C at $\dot{\gamma}$ 0.1 s^{-1} and (b) 20°C at rest. The scattered intensity $I_{\parallel}(q)$ and $I_{\perp}(q)$, at (c) 10°C at $\dot{\gamma}$ 0.1 s^{-1} and (d) 20°C at rest 114

IV.11 The scattering cross section, for the 20 wt % micellar solution at two temperatures: 10°C at 0.1 s^{-1} and 20°C at rest. The best data fits by Ravey's model are also shown in the blue and red lines.................................116

IV.12 Iso-intensity surface plots at the temperature of 10°C for the 20 wt % micellar solution (in heavy water). Six values of the shear rates $\dot{\gamma}$ were used: (a) 0.5 s^{-1}, (b) 2 s^{-1}, (c) 10 s^{-1}, (d) 50 s^{-1}, (e) 80 s^{-1} and (f) 150 s^{-1} 118

IV.13 Iso-intensity surface plots at the temperature of 20°C for the 20 wt % micellar solution (in heavy water). Five values of the shear rates $\dot{\gamma}$ were used: (a) 0.5 s^{-1}, (b) 2 s^{-1}, (c) 10 s^{-1}, (d) 50 s^{-1} and (e) 80 s^{-1} 119

IV.14 The scattered intensity $I_{\parallel}(q)$ and $I_{\perp}(q)$ for the 20 wt.% micellar solution (in heavy water) at two temperatures: 10°C and/or 20°C. Six values of the shear rates $\dot{\gamma}$ were applied: (a) 0.5 s^{-1}, (b) 2 s^{-1}, (c) 10 s^{-1}, (d) 50 s^{-1}, (e) 80 s^{-1} and/or (f) 150 s^{-1}...120

IV.15 The linear-log experimental absolute scattered intensity, for the 20 wt %

micellar solution (in heavy water) at (a) 10°C at 0.1, 10, 50, 80 and 150 s^{-1}; (b) 20°C at 0, 10, 50 and 80 s^{-1}. The figures (c) and (d) are the expanded graphs within the dash square frame in each figure a and b, respectively 123

IV.16 Rheological behaviour in steady state shearing mode. (a) miscibility curve, the symbols pointing out the solutions under investigation; (b) viscosity curves at 20°C for different wt% $R_7^F(EO)_8$ concentrations in 1M NaI solution. The viscosity curves for the concentrations of (c) 10, (d) 20, (e) 30 and (f) 40 wt% $R_7^F(EO)_8$ concentrations in 1M NaI at different temperatures; 10°C, 20°C, 30°C, 40°C (diamond). 125

IV.17 Storage modulus G' and loss modulus G'' as a function of the angular frequency ω: (a) at a constant temperature 20°C and different $R_7^F(EO)_8$ concentrations in 1M NaI solution; at the concentrations of (b) 10, (d) 20, (f) 30 and (h) 40 wt% and at different temperatures (20, 30 and/or 40°C 128

IV.18 Cole-Cole plot $G''(G')$ at 10°C of $R_7^F(EO)_8$ (a) 30, and (b) 40 wt % in 1M NaI solution 132

IV.19 Flow birefringence experiments: (a) extinction angle χ, (b) birefringence intensity Δn vs. the shear rate $\dot{\gamma}$ The concentration is 20 wt % $R_7^F(EO)_8$ 1M NaI solution and the temperatures: 10°C, 20°C and 30°C 133

IV.20 Rheological behaviour in steady state shearing mode. (a) The partial phase diagram of $R_8^F(EO)_9$ in water, the symbols pointing out the solutions under investigation. The viscosity curves for the concentrations of (b) 20 and (c) 30 wt% $R_8^F(EO)_9$ in water at different temperatures;10°C, 20°C, 30°C (circle), 35°C and 40°C 135

IV.21 Storage modulus G' and loss modulus G'' as a function of the angular frequency ω for pure $R_8^F(EO)_9$ solutions. (a): concentrations of 20 wt%, (b) 30 wt% at different temperatures; 10, 20, 30 and 40°C 137

IV.22 Rheological behaviour in steady state shearing mode. (a) miscibility curve,

the symbols pointing out the solutions under investigation.
The viscosity curves for the concentrations of (b) 20 and (c) 30 wt%
$R_8^F(EO)_9$ concentration in 3 M NaCl solution at different temperatures;
10°C, 20°C, 30°C, 40°C, 45°C and 50°C 139
IV.23 Storage modulus *G*' and loss modulus *G*" as a function of the
angular frequency ω. The concentrations are: 20 and 30 wt% of $R_8^F(EO)_9$
in 3M NaCl solution at the constant temperature 10°C 141
IV.24 Extinction angle and birefringence intensity for the concentrations of
20 (a) and 30 (b) wt% of $R_8^F(EO)_9$ in 3 M NaCl solution
at different temperatures; 25°C, 30°C, 40°C..143
IV.25 Stress optical law $\Delta n \sin 2\chi = 2C\sigma$ for $R_8^F(EO)_9$ 20 wt% in 3M NaCl
at the temperature of 30°C..143
IV.26 Stress optical law $\Delta n\sin 2\chi = 2C\sigma$ for $R_8^F(EO)_9$ 30 wt% in 3M NaCl
at three temperatures: 20°C, 30°C, 40°C 144
IV.27 Stress optical coefficient C versus the inverse or the Kelvin temperature T 145
V.1 Comparison of the evolution of the extinction angle
for the solutions with salt and without salt 154
V.2 The viscosity curves as a function of shear rate of $R_7^F(EO)_8$ at 10°C;
(a) with NaI solution (b) without NaI salt. At various concentrations
10 wt%, 20 wt%, 30 wt% and 40 wt% 156
V.3 The calculated Maxwellian parameters as a function of the concentrations
(20, 30 and 40 wt%). The pure $R_7^F(EO)_8$ system is plotted in solid symbols;
$R_7^F(EO)_8$ with 1M NaI is shown in empty symbols. (a) The relaxation time
τ_R (ms) at 10°C and 20°C. (b) The Mawellian parameters at 10°C,
plateau modulus G_0 (Pa); zero shear viscosity η_0 (Pa.s);
breaking time τ_{break} (ms); hydrodynamic correlation length ξ_H (nm) 158
V.4 Pure $R_7^F(EO)_8$ solution at 20 wt%. (a) Viscosity curve as a function of
the shear rate (range of 0.1 – 300 s^{-1}) at 10, 20 and 30°C.
(b) Evolution of the extinction angle as a function of the shear rate
(range of 0 – 140 s^{-1}) at 10, 20 and 30°C. (c) Scattered intensity
$I_{\parallel}(q)$ and $I_{\perp}(q)$ at 10°C and 20°C at the shear rate of 50 s^{-1} 160

V.5 Viscosity of the 20 wt% pure $R_7^F(EO)_8$-D_2O solution as a function of the shear rate measured at 10 and 20°C. The corresponding contour plots from SANS at 10°C are shown at $\dot{\gamma} = 0.1$, 50 and 150 s^{-1}. At 20°C, the contour plots are presented at $\dot{\gamma} = 0.1$ and 80 s^{-1}.
The viscosity curves are drawn from the data given by the Bohlin apparatus (CVO120) operating on the D11 line 162

A.1 The change in cloud point temperature (CP) between the solutions without and with salt of the 10wt% $R_7^F(EO)_8$ solution as a function of the NaI concentration (0.25, 0.5 and 1 M) 180

A.2 The apparent viscosities of 20 wt% $R_7^F(EO)_8$ in D_2O as a function of shear rate $\dot{\gamma}$, operating by the rheometer RFS3 (rheological studies; 10°C, 20°C, 30°C, 40°C) and the Bohlin apparatus; CVO120 (SANS experiment; 10°C, 20°C) 181

A.3 Storage modulus G' and loss modulus G'' as a function of the angular frequency ω by using RFS3: (a) at a constant temperature 20°C and different $R_7^F(EO)_8$ concentrations in D_2O; at the concentrations of 20 wt% at 10 and 20°C 182

« PROPRIETES RHEOPHYSIQUES DE PHASES MICELLAIRES FLUOREES NON IONIQUES : LIEN AVEC LES MATERIAUX MESOPOREUX »

Résumé :

Afin d'établir un lien entre les solutions servant de modèles dans la préparation de matériaux mésoporeux, on étudie les propriétés physiques à l'équilibre et hors équilibre de solutions micellaires aqueuses à base de deux tensioactifs fluorés : $C_8F_{17}C_2H_4(OC_2H_4)_9OH$, $[R^F_8(EO)_9]$ and $C_7F_{15}C_2H_4(OC_2H_4)_8OH$, $[R^F_7(EO)_8]$. Cette étude devrait nous aider à comprendre pourquoi on obtient des matériaux mésoporeux bien ordonnés à partir de solutions micellaires du tensioactif $R^F_8(EO)_9$ et des structures désordonnées lorsque l'on utilise $R^F_7(EO)_8$. Les expériences sont menées sur quatre systèmes de deux surfactants: $R^F_7(EO)_8/H_2O$, $R^F_7(EO)_8/NaI/H_2O$, $R^F_8(EO)_9/H_2O$ et $R^F_8(EO)_9/NaCl/H_2O$. Plusieurs techniques expérimentales sont utilisées: rhéologie, biréfringence d'écoulement et diffusion de neutrons aux petits angles dans le but de décrire ces quatre systèmes. Les diagrammes de phase des deux tensioactifs montrent qu'une phase micellaire L_1 existe dans une large gamme de température et concentration. Mais dans tous les cas, la distance à la courbe de miscibilité a une influence sur les caractéristiques rhéologiques bien que toutes les solutions soient une phase L_1. La biréfringence d'écoulement des deux systèmes apporte des informations complémentaires quant à la taille et la forme des micelles. Pour les deux systèmes, avec et sans sel, les résultats suggèrent l'existence de petites micelles allongées liées en chaines par des forces faibles excepté pour le système $R^F_8(EO)_9$ qui ne présente pas de biréfringence notable; les micelles sont probablement petites avec une forme voisine de la sphère. Pour les quatre systèmes, on observe une perte du caractère Maxwellien lorsque les conditions de concentration et de température se rapprochent de la courbe de miscibilité. Ces résultats confortent l'idée selon laquelle : les conditions thermodynamiques choisies pour l'addition de la silice ne doivent pas être trop proches de la courbe de miscibilité, afin d'obtenir des matériaux mésoporeux ordonnés. Dans ces conditions, les solutions sont Maxwelliennes et les matériaux mésoporeux synthétisés sont ordonnés.

Mots-clé *: Rhéologie, Micelle, Matériaux mésoporeux, Tensioactif, Biréfringence, Caractère Maxwellien.*

« RHEOPHYSICAL PROPERTIES OF FLUORINATED NONIONIC MICELLAR PHASES : LINK WITH MESOPOROUS MATERIALS »

Abstract :

To provide a link between the micellar templates and the mesoporous material characteristics in the final product, the physical properties of aqueous systems prepared with two kinds of fluorinated surfactants are described and analyzed under equilibrium and out-of-equilibrium conditions: the surfactants are $C_8F_{17}C_2H_4(OC_2H_4)_9OH$, $[R^F_8(EO)_9]$ and $C_7F_{15}C_2H_4(OC_2H_4)_8OH$, $[R^F_7(EO)_8]$. This study may help us to understand why the ordered mesoporous materials are recovered only when $R^F_8(EO)_9$ micellar solutions are used as building blocks while $R^F_7(EO)_8$ solutions give rise to wormhole like structure. The distance to the lower consolute boundary (LCB) and a shift in position by salt additions are also taken into account. The experiments concern four systems of two surfactants; 1) pure $R^F_7(EO)_8$ in water, 2) $R^F_7(EO)_8$ in the presence of the NaI salt, 3) pure $R^F_8(EO)_9$ in water, and 4) $R^F_8(EO)_9$ in the presence of the NaCl salt. Several experimental techniques have been used (rheology, flow birefringence, neutron scattering) to shed light on the physical difference between the four systems. The phase diagrams of both surfactants show that a direct micellar phase (L_1) exists in a wide range of concentrations and temperatures. In any cases, the distance to the LCB is a parameter which influences rheological behaviour although the micellar phase still is a L_1 phase. The flow birefringence experiments performed on both systems bring complementary information of the size and shape of the micelles. For both systems, with and without salt, the results suggest the existence of small elongated micelles linked by weak forces except for the $R^F_8(EO)_9$ system which shows no birefringence; the micelles in solution are probably small with a shape close to a sphere. From all four systems, the loss of the Maxwellian character is generally observed when the conditions approach the miscibility curve. These results consolidate the assumption that in order to prepare ordered mesoporous materials, the thermodynamical conditions at which the silica precursor is added to the micellar solution should not be too close to the miscibility curve. Therefore, this study suggests that the Maxwellian character seems to be a pre-requisite condition of the micellar solution for obtaining ordered mesoporous materials.

Keywords *: Rheology, Surfactants, Micelle, Mesoporous material, Birefringence, Maxwellian character.*